

**Bio-Compounds as Reducing Agents of Reforming Catalyst
and their Subsequent Steam Reforming Performance**

Feng Cheng

Submitted in accordance with the requirements for the degree of
Doctor of Philosophy

The University of Leeds
Energy Research Institute
School of Chemical and Process Engineering

October, 2014

The candidate confirms that the work submitted is her own, except where work which has formed part of jointly-authored publications has been included. The contribution of the candidate and the other authors to this work has been explicitly indicated below. The candidate confirms that appropriate credit has been given within the thesis where reference has been made to the work of others.

Chapter 6 within this thesis is based on the work that has formed one jointly-authored paper:

Feng Cheng*, Valerie Dupont. Nickel catalyst auto-reduction during steam reforming of bio-oil model compound acetic acid. *International Journal of Hydrogen Energy*. 2013; 38: 15160-15172.

In this paper, the experimental work, data processing and paper writing up are directly attributable to the candidate. The candidate's supervisor Dr. Valerie Dupont contributed to the section of 'thermodynamic equilibrium calculation' and gave comments and edits on the whole paper.

This copy has been supplied on the understanding that it is copyright material and that no quotation from the thesis may be published without proper acknowledgement.

The right of Feng Cheng to be identified as Author of this work has been asserted by her in accordance with the Copyright, Designs and Patents Act 1988.

© <2014> The University of Leeds and Feng Cheng

Acknowledgements

I would like to express my sincere appreciation and thanks to my supervisor Dr. Valerie Dupont. Thank you for giving me this opportunity to start my PhD. Thanks for your supervision on my research throughout the past three years. You always gave me encouragement and support. Both your insistence on scientific rigor and your easy-going personality affected me a lot.

I would also like to thank Dr. Adrian Cunliffe, Dr. Tim Comyn, Sara Dona, and Stuart Micklethwaite for their technical support on TGA-FTIR, XRD and SEM-EDX tests. I also want to thank our industrial collaborator Dr. Martyn V. Twigg from TST Ltd. for his helpful discussion on Chapter 9. Thanks to Chinese Scholarship Council (CSC)-Leeds University Scholarship for financial support, to Johnson Matthey Plc. and TST Ltd. for providing catalyst materials.

Special thanks and gratitude are given to my parents and younger sister Ping Cheng for their support and love.

Abstract

At present, H₂ is mainly produced through catalytic steam reforming of natural gas. Sustainable H₂ production from renewable resources is of great significance to achieve a 'hydrogen economy' in the future. Aiming at exploring the potential of bio-derived fuel (e.g. bio-oil) for H₂ production via chemical looping reforming (CLR), this study investigated the direct reduction of a reforming catalyst (18 wt% NiO/Al₂O₃) with five bio-compounds (acetic acid, ethanol, acetone, furfural and glucose) and subsequent steam reforming (SR), which represented one half of a cycle in CLR.

First, thermodynamic analysis was conducted. Results indicated that for a system consisting of bio-compound, steam and NiO above 200 °C, the bio-compounds would preferably reduce NiO rather than react with steam or decompose. The reduction was hardly affected by temperature, pressure, or the presence of steam. The formation of carbon during reduction depended on temperature and the availability of NiO. Moreover, the dependence of SR performance (equilibrium yields, and carbon formation) on temperature, molar steam to carbon ratio (S/C) and the type of bio-compound was studied. Equilibrium yields of H₂, CO, CO₂ and CH₄ were successfully fitted into linear functions of the O/C and H/C ratios in bio-compound molecules. The wide suitability of these fitted equations made it possible to predict the potential of various feedstocks in H₂ production without doing repeated simulation work.

Moreover, the integrated catalyst reduction and SR process was experimentally investigated in a packed bed reactor over the temperature range of 500-750 °C and S/C range of 4.5-9 for glucose and 0-5 for the other bio-compounds at atmospheric pressure. The effects of temperature and S/C on reduction kinetics as well as the subsequent SR were systematically investigated. Kinetic modelling was performed within NiO conversion of 0-50% and two-dimensional nuclei growth model (A2) was found to fit very well except for glucose. For all the bio-compounds, the apparent activation energy of NiO reduction was between 30 and 40 kJ/mol. Their pre-exponential factors decreased in this order: CH₄>ethanol≈acetone>acetic

acid>furfural> glucose, probably due to the different activities of reducing species they produced. Optimal S/C values for reduction kinetics were found between 1 and 2. The main barrier for each bio-compound in SR process was summarised.

In addition, temperature programmed reduction (TPR) of the NiO catalyst with solid bio-compounds (glucose and citric acid) under N₂ was investigated by TGA-FTIR technique. It was found that the coke formed by bio-compound pyrolysis acted as the actual reductant for NiO reduction with CO₂ as main reduction product. The reduction extent depended on the initial loading of bio-compounds and their charring characteristics. The reduction kinetics was studied by the Kissinger method. A two-step reduction mechanism (initially solid-solid reduction, and then gaseous reduction with CO) was proposed to explain the multiple reduction phases observed.

Contents

Acknowledgements	i
Abstract	iii
Contents	v
List of Tables	xiii
List of Figures	xv
List of Abbreviations	xxiii
Chapter 1 Introduction: background, scope and objectives of the research	1
1.1 Research background	1
1.2 Research scope	8
1.3 Research objectives	9
Chapter 2 Literature review	11
2.1 Introduction	11
2.2 Thermochemical conversion of biomass.....	11
2.2.1 Pyrolysis.....	11
2.2.2 Gasification	12
2.2.3 Hydrothermal processing	14
2.2.4 Bio-oil properties and applications	15
2.2.4.1 Physical properties of bio-oil.....	15
2.2.4.2 Chemical composition of bio-oil	17
2.2.4.3 Applications of bio-oil.....	19
2.3 Hydrogen production via thermal processes	20
2.3.1 Hydrogen production from fossil fuels	22
2.3.1.1 Steam reforming (SR) of natural gas or naphtha	22
2.3.1.2 Partial oxidation (POX) of natural gas or heavy oil	24
2.3.1.3 Autothermal reforming (ATR).....	25

2.3.2 Hydrogen production from biomass.....	26
2.3.2.1 Steam reforming of bio-oil or its aqueous fraction.....	27
2.3.2.2 Steam reforming of acetic acid.....	29
2.3.2.3 Steam reforming of ethanol.....	32
2.3.2.4 Steam reforming of other oxygenates.....	35
2.4 Chemical looping technology.....	36
2.4.1 Reduction reactivity of oxygen carrier with fuel.....	38
2.4.2 Carbon deposition.....	40
2.5 Reduction of metal oxides.....	41
2.5.1 Application fields.....	41
2.5.2 Kinetic models of metal oxide reduction.....	43
2.5.2.1 Nucleation model.....	44
2.5.2.2 Shrinking core model.....	46
2.5.3 Reduction mechanism with H ₂ , CO or syngas.....	48
2.5.4 Reduction mechanism with CH ₄ and other light hydrocarbons.....	48
2.5.5 Reduction mechanism with solid carbonaceous materials.....	49
2.5.5.1 Pure carbon.....	49
2.5.5.2 Coal, biomass and other solids.....	50
2.6 Conclusions.....	51
Chapter 3 Experimental materials, reactor set-up and methodology.....	55
3.1 Experimental materials.....	55
3.1.1 Steam reforming catalyst.....	55
3.1.2 Bio-compounds.....	55
3.2 Packed bed reactor set-up and operation procedure.....	57
3.3 Elemental balance and definition of process outputs.....	60
3.4 Characterisation and analysis methods.....	63
3.4.1 TGA-FTIR.....	63
3.4.2 XRD and Rietveld Refinement.....	64

3.4.3 CHN elemental analysis.....	65
3.4.4 SEM-EDX.....	66
3.4.5 Adsorption/Desorption Isotherm.....	66
3.4.6 TOC.....	67
3.4.7 ICP-MS	67
3.5 Thermodynamic equilibrium calculation	68
3.5.1 Principles of thermodynamic equilibrium calculation.....	68
3.5.2 Calculation software (CEA from NASA)	68
3.5.3 Thermodynamic data.....	69
Chapter 4 Thermodynamics of NiO reduction with bio-compounds.....	71
4.1 Introduction.....	71
4.2 Thermodynamic feasibility of NiO reduction with bio-compounds.....	72
4.2.1 Competition of reduction, pyrolysis and steam reforming reactions	72
4.2.2 Ease of NiO reduction with different reducing agents.....	75
4.2.3 Other metal oxide reduction.....	77
4.3 Enthalpy changes (energy demand for NiO reduction).....	79
4.4 Influencing factors of equilibrium products.....	82
4.4.1 Temperature and pressure	82
4.4.2 The presence of steam.....	83
4.4.3 NiO/C ratio.....	84
4.5 Conclusions.....	88
Chapter 5 Thermodynamics of hydrogen production from steam reforming of bio-compounds	91
5.1 Introduction.....	91
5.2 Method and definition of outputs.....	91
5.3 Gibbs free energy changes for complete steam reforming.....	93
5.4 Influencing factors of equilibrium yields.....	95

5.4.1 Temperature	95
5.4.2 Molar steam to carbon ratio (S/C).....	98
5.4.3 Molecular formulas of feedstock.....	100
5.4.3.1 Hydrogen-containing products (H ₂ and CH ₄).....	100
5.4.3.2 Oxygen-containing products (CO ₂ and CO).....	102
5.4.4 Equilibrium system with Ni/NiO: SR with NiO reduction	104
5.5 Thermodynamic evaluation for carbon free region.....	106
5.5.1 Pyrolysis of bio-compounds.....	106
5.5.2 Dependence of carbon formation on temperature and S/C	107
5.6 Energy calculation.....	109
5.7 Conclusions	112
Chapter 6 Nickel catalyst auto-reduction during steam reforming of bio-	
compound acetic acid	115
6.1 Introduction	115
6.2 Experimental	115
6.2.1 Integrated catalyst reduction and steam reforming process	115
6.2.2 Conventional steam reforming process (using H ₂ to reduce catalyst) ...	117
6.2.3 Characterization	117
6.2.4 Thermodynamic equilibrium calculations.....	117
6.3 Results and discussion.....	118
6.3.1 Auto-reduction of NiO by HAc.....	118
6.3.1.1 Process analysis	118
6.3.1.2 Kinetics modelling.....	120
6.3.1.3 Apparent activation energy of NiO reduction	124
6.3.1.4 Effects of water content on NiO reduction	126
6.3.2 Steam reforming performance in the integrated process.....	129
6.3.2.1 Effects of temperature	130
6.3.2.2 Effects of S/C.....	131
6.3.2.3 Comparison of experimental data with thermodynamic equilibrium data...133	

6.3.2.4 HAc auto-reduced and H ₂ -reduced catalyst activities in steam reforming .	133
6.4 Conclusions	136
Chapter 7 Auto-reduction of nickel catalyst with a series of bio-compounds.	139
7.1 Introduction	139
7.2 Experimental	139
7.3 Reduction extent.....	140
7.4 Reduction rate curves	144
7.4.1 Explanation for the residual error of reduction rate	144
7.4.2 The conversion range selected for kinetic modelling	146
7.5 Kinetic modelling of NiO reduction	148
7.5.1 Mass transfer resistance	148
7.5.2 Model fitting	150
7.6 Apparent activation energy and pre-exponential factor	154
7.7 Effects of steam content on reduction rate	156
7.8 Conclusions	158
Chapter 8 Steam reforming of bio-compounds with auto-reduced nickel catalyst.....	159
8.1 Introduction	159
8.2 Comparison between auto-reduction and H ₂ reduction	159
8.3 Effects of temperature	161
8.3.1 Feedstock conversion	161
(1) Fuel conversion	161
(2) Water conversion	164
8.3.2 Gas product yields.....	165
(1) H ₂ yield	165
(2) Yields of C-containing products	167
8.4 Catalytic pyrolysis of bio-compounds (S/C=0)	169
8.4.1 Product composition	169

(1) Auto-reduction stage.....	170
(2) Catalytic pyrolysis stage	170
8.4.2 Comparison with equilibrium composition.....	172
8.5 Effects of S/C	173
8.5.1 Feedstock conversion	173
8.5.2 Gas product yields	174
(1) H ₂ yield	174
(2) Yields of C-containing products	175
8.6 Characterisation of carbon deposits	176
8.6.1 CHN elemental analysis	176
8.6.2 SEM imaging.....	178
8.6.2.1 Acetic acid, ethanol, acetone and furfural	178
8.6.2.2 Glucose	179
8.6.2.3 Methane	180
8.7 Conclusions	181
Chapter 9 Reduction of nickel catalyst using solid bio-compounds glucose and citric acid	183
9.1 Introduction	183
9.2 Experimental	184
9.2.1 Sample preparation.....	184
9.2.2 Temperature programmed reduction (TPR).....	184
9.2.3 Sample characterization	185
9.3 Results and discussion.....	185
9.3.1 TPR of glucose-impregnated NiO/ α -Al ₂ O ₃ (NiO-G)	185
9.3.2 TPR of citric acid-impregnated NiO/ α -Al ₂ O ₃ (NiO-CA).....	188
9.3.3 Coke characterisation	190
9.3.3.1 Carbon and hydrogen content during TPR (CHN results).....	190
9.3.3.2 Oxidation temperature of coke (TPO results).....	192

9.3.3.3 Distribution of coke in NiO/ α -Al ₂ O ₃ (SEM-EDX)	194
9.3.4 Reduction mechanism	195
9.3.5 Reduction kinetics	198
9.4 Conclusions	201
Chapter 10 Conclusions and future work	203
10.1 Conclusions	203
10.1.1 NiO catalyst reduction with bio-compounds (auto-reduction).....	203
10.1.1.1. Thermodynamic study	203
10.1.1.2 Kinetic investigation	204
10.1.2 SR of bio-compounds following the auto-reduction.....	205
10.1.2.1 Thermodynamic study	205
10.1.2.2 Experimental investigation	206
10.1.3 Reduction of NiO catalyst with solid bio-compounds	206
10.2 Future work	207
List of references	209
Appendix A	225
Appendix B	229
Appendix C	233
Appendix D	235

List of Tables

Table 2.1 Typical properties of wood pyrolysis bio-oil and heavy fuel oil [62].....	15
Table 2.2 Chemical composition of bio-oil from different feedstock and different processes (yield in wt% of dry biomass) [26].....	18
Table 2.3 Energy density of selected fuels (data from Wikipedia)	21
Table 2.4 Common kinetic models for solid state reaction [149-151].....	44
Table 3.1 Basic physical properties and suppliers of the liquid bio-compounds used in this work.....	56
Table 3.2 Basic physical properties and suppliers of the solid bio-compounds used in this work.....	56
Table 3.3 Flow rates of liquid feedstock into the packed bed reactor.....	59
Table 4.1 The Gibbs free energy change, the enthalpy change and the entropy change per mol of NiO reduced with different reducing agents at 650 °C.....	77
Table 4.2 The lower limit of the amount of NiO for no carbon formation at 650 °C and 1 atm, as well as the syngas yield (CO+H ₂) and H ₂ /CO ratio at this point	86
Table 5.1 Molecular composition of feedstock as well as equilibrium yields of H ₂ , CH ₄ , CO and CO ₂	100
Table 5.2 Comparison of the equilibrium yields obtained using the fitted equations (in black colour) and through CEA calculation (in red colour)	103
Table 5.3 The energy balance for the combustion of bio-compounds and the steam reforming of bio-compounds as well as NiO inventory for 1 mol of H ₂ produced in an autothermal CLR process at 650 °C and S/C=3.....	111
Table 6.1 Kinetic models of solid state reactions [149, 197, 198].....	121
Table 6.2 Reaction conditions for a set of comparative experiments.....	127
Table 6.3 H ₂ yield from steam reforming of HAC in the literature	132

Table 6.4 Comparison of the integrated process (using HAc as reductant) and conventional steam reforming process (using H ₂ as reductant)	134
Table 7.1 Calculated molar flux of gas reactants ($W_{A,r}$) and observed consumption rate (r_A) in mol m ⁻² s ⁻¹	149
Table 7.2 The m values obtained at different reduction temperatures.....	152
Table 7.3 R-squared values for fitting reduction kinetic data with the A2 model .	154
Table 7.4 Estimated kinetic parameters for NiO reduction with different reductants	155
Table 7.5 Ratios of rate constant k with respect to ethanol	156
Table 8.1 H ₂ yields (in mol/mol C feed) from different bio-compounds at 650 °C, S/C=6 for glucose and S/C=3 for the rest	167
Table 8.2 Height ratio of H ₂ O peak to CO ₂ peak	170
Table 8.3 Yields of CH ₄ , CO, CO ₂ and H ₂ (in mol/mol carbon feed) in the catalytic pyrolysis stage (yields below 0.05 were considered as measurement error)	171
Table 8.4 Elemental compositions (in wt%) of the sites marked in Figure 8.16 determined by EDX.....	180

List of Figures

Figure 1.1 Renewable energy share of global final energy consumption in 2011 (source: renewables 2013 global status report from REN 21)	2
Figure 1.2 Share of renewable energy in gross final energy consumption per member state of EU in 2012 (Source: Eurostat newsrelease, 37/2014-10 March 2014)	3
Figure 1.3 Global H ₂ production share by sources [4].....	4
Figure 1.4 Schematic diagrams of chemical looping combustion (left) and chemical looping reforming (right) (MeO: oxidized oxygen carrier, Me: reduced oxygen carrier, C _n H _m : fuel).....	5
Figure 2.1 Various applications of syngas produced from biomass gasification.....	13
Figure 2.2 Properties of bio-oil and their correlations	17
Figure 2.3 Scheme of pure H ₂ production by steam reforming of natural gas in a conventional system (up) and in a membrane reactor (down) [83]	24
Figure 2.4 Three types of reactor configuration for ATR process a) fixed bed reactor, b) fluidized bed reactor and c) two zone fluidized bed reactor [87]	26
Figure 2.5 Schematic diagram of acetic acid steam reforming reaction [93]	30
Figure 2.6 Thermal decomposition of acetic acid and subsequent secondary reactions [94].....	31
Figure 2.7 Reaction network during ethanol steam reforming proposed by ref. [106] and adapted from ref. [33].....	33
Figure 2.8 Molecular structures of bio-oil model compounds that were investigated in steam reforming processes in the literature.....	35
Figure 2.9 Schematic diagram of shrinking core model	47
Figure 3.1 Images of catalyst pellet (left) and catalyst particles (right) used in this project.....	55
Figure 3.2 Molecular structures of the bio-compounds investigated in this project	57
Figure 3.3 Schematic diagram of a packed bed reactor set-up.....	58

Figure 4.1 Comparison of Gibbs free energy changes for the reduction, steam reforming and pyrolysis reactions: (a) acetic acid, (b) ethanol, (c) acetone, (d) furfural, (e) glucose and (f) CH ₄	74
Figure 4.2 Comparison of Gibbs free energy change for NiO reduction with different agents (bio-compounds in solid line, traditional reducing agents in dash line).....	76
Figure 4.3 Gibbs free energy change for the reduction of different metal oxides with 1 mol reducing agents (a) CH ₄ , (b) ethanol, (c) solid carbon and (d) CO.....	78
Figure 4.4 Schematic diagram of enthalpy balance calculation	80
Figure 4.5 Enthalpy terms vs. temperature for the system of 1 mol NiO and stoichiometric amounts of reductant: (a) the enthalpy change of the reduction reaction, (b) the enthalpy change of heating each reactant to reaction temperature, and (c) the total enthalpy balance for 1 mol NiO reduced.	81
Figure 4.6 Yields of equilibrium products when 1 mol acetic acid reacts with the stoichiometric amount of NiO at different temperatures and 1 atm: (a) major products with the yield of Ni being zoomed in, (b) minor products	82
Figure 4.7 Changes in (a) the Ni yield and (b) the H ₂ yield when different amounts of steam are added to the system of acetic acid and NiO in a stoichiometric ratio at 1 atm.....	83
Figure 4.8 Equilibrium yields of products when 1 mol bio-compound reacts with different amounts of NiO at 650 °C and 1 atm	85
Figure 4.9 Thermodynamic domains (temperature and NiO/C ratio) for avoidance of carbon formation at the pressure of 1 atm	87
Figure 5.1 Gibbs free energy changes for the complete steam reforming reactions of the bio-compounds and CH ₄ as well as the water gas shift reaction.....	94
Figure 5.2 H ₂ yield versus reaction temperature for the bio-compound/steam system at S/C=3 (a) in mol/mol carbon feed, (b) in wt% of the bio-compound input.....	96
Figure 5.3 Carbon-containing product yields versus the reaction temperature for the bio-compound/steam system at S/C=3: (a) CO ₂ , (b) CO and (c) CH ₄	97

Figure 5.4 H ₂ yield versus the S/C ratio for the bio-compound/steam system at 650 °C: (a) in mol/mol carbon feed, (b) in wt% of the bio-compound input.....	98
Figure 5.5 Carbon-containing product yields versus the S/C ratio for the bio-compound/steam system at 650 °C: (a) CO ₂ , (b) CO and (c) CH ₄	99
Figure 5.6 Dependence of (a) H ₂ yield and (b) CH ₄ yield on the molecular formula of feedstock used for steam reforming process (the H ₂ yield was calculated at 650 °C and S/C=3, the CH ₄ yield was at 500 °C and S/C=3).....	101
Figure 5.7 Dependence of the CO and CO ₂ yields at 650 °C and S/C=3 on the molecular formula of feedstock used for steam reforming process	102
Figure 5.8 Effects of incorporating NiO reduction into the steam reforming system on the H ₂ yield using (a) acetic acid and (b) furfural as feedstock ('w' represents 'with NiO reduction' in solid line and 'wo' represents 'without NiO reduction' in dash line).....	104
Figure 5.9 Yields of solid carbon from bio-compound pyrolysis over temperature range of 100-850 °C at 1 atm.....	106
Figure 5.10 Thermodynamic domains (temperature and S/C ratio) for the avoidance of carbon formation at atmospheric pressure predicted by thermodynamic equilibrium calculation using CEA.....	107
Figure 5.11 Dependence of equilibrium carbon on the temperature and the S/C: (a) furfural and (b) CH ₄	108
Figure 5.12 Energy balance for the system of bio-compound and water at S/C =3: (a) energy demand for related reactions in steam reforming process, (b) energy demand for heating reactants (water and bio-compound) from room temperature to reaction temperature T, (c) the total energy demand ΔH_{total} , and (d) ΔH ratio	109
Figure 5.13 Schematic diagram of energy calculation for a chemical looping reforming system at 650 °C and S/C=3	111
Figure 6.1 An integrated catalyst reduction and steam reforming experiment at 650 °C with S/C=3 (a) yields of gaseous products; (b) feedstock conversion and (c) zoom in the onset of reactions.....	118

Figure 6.2 XRD patterns of the catalyst reacting for 360 seconds and the fresh catalyst: (∇) Ni characteristic peaks, (◆) NiO characteristic peaks, the other unmarked peaks are attributed to α -Al ₂ O ₃	119
Figure 6.3 NiO reduction with HAc during an integrated process at 650 °C with S/C=3 (a) the reduction rate of NiO vs. time and (b) the conversion of NiO to Ni vs. time.....	120
Figure 6.4 Change trend of m values and R ² values of kinetic models (A2 or R3) with (a) temperature, and (b) S/C (A2: two-dimensional nucleation model, R3: geometrical contraction model of sphere, R ² : R-squared value of linear fit).....	123
Figure 6.5 Arrhenius plot of NiO reduction by HAc solution with S/C=3 for the NiO to Ni conversion range of 0-50%	125
Figure 6.6 Influence of water content on the reduction rate constant and reduction time at 650 °C.....	126
Figure 6.7 CO ₂ chemigrams (2250-2400 cm ⁻¹) during the TPO of reacted catalysts (a) different reducing agents (b) different S/C ratios (c) NiO/ α -Al ₂ O ₃ catalyst and bare α -Al ₂ O ₃	127
Figure 6.8 Mechanism diagram of NiO/ α -Al ₂ O ₃ catalyst reduction with HAc solution.....	129
Figure 6.9 Effects of temperature on steam reforming performance at S/C=3 (a) conversion fractions of HAc and water as well as H ₂ yield in mol/mol C feed, (b) gaseous product concentration in dry outlet gas excluding N ₂ (solid line: experimental data, dash line: thermodynamic equilibrium data)	130
Figure 6.10 Effects of S/C ratio on steam reforming performance at 650 °C (a) conversion fractions of HAc and water as well as H ₂ yield in mol/mol C feed, (b) gaseous product concentration in dry outlet gas excluding N ₂ , (solid lines: experimental data, dash lines: thermodynamic equilibrium data).....	132
Figure 6.11 SEM images of used catalyst (a-c) different sites of catalyst reduced by HAc (d) catalyst reduced by H ₂ (under the same steam reforming condition S/C=1, 650 °C and for 45 min).....	135

Figure 7.1 XRD pattern of the catalyst reacted with ethanol solution (S/C=3) at 550 °C and its model by Rietveld refinement (84.8 wt% α -Al ₂ O ₃ , 11.5 wt% Ni and 3.8 wt% NiO, R_{wp} = 2.86 and GOF=2.00).....	141
Figure 7.2 XRD patterns and Rietveld refinement results of catalysts after reduction with (a) H ₂ and (b) ethanol solution (S/C=3).....	142
Figure 7.3 XRD patterns of catalysts after reduction with various reductants at 550 °C as well as Rietveld refinement results (a) CH ₄ , (b) acetone, (c) furfural, and (d) glucose. (S/C=3 for all these reductants except glucose, which is at S/C=6) ...	143
Figure 7.4 Plots of reduction rate vs. time at 650 °C and S/C=3	144
Figure 7.5 Reduction rate vs. time when subjecting fresh catalyst and pre-reduced catalyst to the atmosphere of acetic acid and steam with S/C=2 at 650 °C	145
Figure 7.6 Illustration for oxygen element balance during the auto-reduction of NiO catalyst with bio-compounds	146
Figure 7.7 Plots of conversion fraction vs. time when reduction rate was calculated using Eq. 3.7 and Eq. 7.2 (NiO catalyst reduction with acetic acid solution at S/C=2 and 650 °C)	147
Figure 7.8 Plots of $\ln[-\ln(1-\alpha)]$ vs. $\ln t$ for the reduction of NiO catalyst with furfural (S/C=3) at different temperatures	151
Figure 7.9 Comparison between the experimental data and A2 model for the reduction of NiO catalyst with (a) CH ₄ , (b) acetic acid, (c) ethanol, (d) acetone, (e) furfural and (f) A1.5 model with glucose (S/C=6 for glucose and S/C=3 for the other reductants).....	153
Figure 7.10 Arrhenius plots of NiO reduction with bio-compounds as well as CH ₄ at S/C=3 (S/C=6 for glucose).....	154
Figure 7.11 Influence of steam content on the reduction rate constant at 650 °C .	156
Figure 7.12 Illustration of the influence of S/C on reduction rate constant.....	157
Figure 8.1 SR performance comparison between auto-reduction (solid line) and H ₂ reduction (dotted line) at 650 °C, S/C=3: (a) ethanol, (b) acetone, and (c) furfural	160
Figure 8.2 Effects of temperature on the bio-compound conversion (S/C=6 for glucose, and S/C=3 for the rest).....	161

Figure 8.3 Photos of condensate samples collected from furfural experiments at different temperatures with S/C=3	162
Figure 8.4 Photos of reacted catalysts collected from glucose experiments at different reaction temperatures with S/C=6	163
Figure 8.5 Schematic diagram of the agglomeration of catalyst particles due to glucose coking during steam reforming of glucose	164
Figure 8.6 Effects of temperature on the water conversion obtained by experiments and thermodynamic equilibrium calculation (S/C=6 for glucose, S/C=3 for the rest, equilibrium data were indicated by ‘e’ in front of bio-compound name)	165
Figure 8.7 H ₂ yield vs. temperature from steam reforming of bio-compounds (S/C=6 for glucose and S/C=3 for the rest): (a) in mol/mol carbon feed, (b) in wt% of the bio-compound input	166
Figure 8.8 Yields of carbon-containing products vs. temperature from the steam reforming of bio-compounds (a) CO ₂ , (b) CO and (c) CH ₄	167
Figure 8.9 Pyrolysis of reforming fuel in the presence of fresh catalyst at 650 °C (a) acetic acid, (b) ethanol, (c) acetone, (d) furfural and (e) CH ₄	169
Figure 8.10 Comparison of pyrolysis product yields obtained by experiments at 650 °C (black solid square) with the equilibrium data (red solid triangle): (a) H ₂ yield, (b) CH ₄ yield, (c) CO yield, (d) CO ₂ yield, and (e) solid carbon yield	172
Figure 8.11 Effects of S/C on (a) fuel conversion and (b) water conversion efficiency at 650 °C (the water conversion efficiency at equilibrium was also shown in dashed line)	173
Figure 8.12 Variation of H ₂ yield with S/C (a) in mol/mol carbon feed, and (b) in wt% of the bio-compound used	174
Figure 8.13 Carbon-containing product yields vs. S/C at 650 °C (a) CO ₂ , (b) CO and (c) CH ₄	175
Figure 8.14 Yields of carbon deposits on the reacted catalyst at different temperatures with S/C=3 (for glucose, the S/C of 6 was used and the carbon yield calculation only considered the carbon deposited non-agglomerated catalyst particles)	176
Figure 8.15 SEM images of reacted catalysts from steam reforming of (a) acetic acid, (b) acetone, (c) ethanol, and (d) furfural	178

Figure 8.16 SEM images of (a-c) agglomerated catalyst particles and (d) non-agglomerated catalyst particles from steam reforming of glucose at 550 °C	179
Figure 8.17 SEM images (LA-BSE signals) of the catalyst collected from steam reforming of CH ₄ at 650 °C and S/C=3: (a) 20k magnification, (b) 70k magnification.....	180
Figure 9.1 TGA-FTIR results of NiO-G (solid line) and Al ₂ O ₃ -G (dashed line) under N ₂ at the heating rate of 5 °C/min: (a) TGA curve, (b) DTG curve, (c) CO ₂ evolution profile, (d) H ₂ O evolution profile and (e) formic acid evolution profile. DTG of fresh NiO is also shown in (b).....	186
Figure 9.2 XRD patterns of NiO-G-T samples and fresh NiO sample (T=420, 530, 770, 900 °C, unmarked peaks are attributed to α-Al ₂ O ₃)	187
Figure 9.3 TGA-FTIR results of NiO-CA (solid line) and Al ₂ O ₃ -CA (dashed line) under N ₂ at the heating rate of 5 °C/min: (a) TGA curve, (b) DTG curve, (c) CO ₂ evolution profile, (d) H ₂ O evolution profile and (e) anhydride evolution profile ..	189
Figure 9.4 XRD patterns of NiO-CA-T samples (T=280, 400, 480, 530 and 740 °C, unmarked peaks are attributed to α-Al ₂ O ₃).....	190
Figure 9.5 Carbon and hydrogen contents (wt%) from CHN analysis in (a) NiO-G-T samples and (b) NiO-CA-T samples, ‘T’ is the end temperature of TGA experiments, hydrogen content is multiplied by 12	190
Figure 9.6 TPO-FTIR results of (a) NiO-G-420, (b) NiO-CA-400, and (c) fresh NiO/α-Al ₂ O ₃ catalyst mixed with carbon black in air (50 ml/min) at a heating rate 5 °C/min	193
Figure 9.7 SEM image (left) and EDX mapping result (right) of fresh NiO/α-Al ₂ O ₃ catalyst.....	194
Figure 9.8 SEM image (left) and EDX mapping result (right) of the NiO-G-420 sample which was obtained by heating NiO-G under N ₂ at 5 °C/min up to 420 °C	194
Figure 9.9 TGA and DTG curves of the NiO/α-Al ₂ O ₃ catalyst under H ₂ flow at a heating rate of 5 °C/min	195
Figure 9.10 Mechanism diagram of NiO/α-Al ₂ O ₃ reduction with the coke deposited on both NiO sites and Al ₂ O ₃ sites	196

Figure 9.11 DTG of NiO-G under N₂ with excess glucose (the weight ratio of glucose and NiO/ α -Al₂O₃ is 1:1.4 in contrast to the ratio of 1:10 in the case of glucose not excess)..... 197

Figure 9.12 Evolution profiles of CO₂, H₂O and CO with respect to temperature for TPR of NiO-G with excess glucose under N₂ 198

Figure 9.13 DTG of (a) NiO-G and (b) NiO-CA under N₂ at different heating rates (*these reduction peaks are used for kinetics calculation)..... 198

Figure 9.14 Kissinger plots of NiO reduction by coke (a) the first reduction peak and (b) the last reduction peak 199

List of Abbreviations

LPG	liquefied petroleum gas including propane and butane
PEMFC	polymer electrolyte membrane fuel cell or proton exchange membrane fuel cell
EU	European Union
IPCC	the Intergovernmental Panel on Climate Change
S/C	molar steam to carbon ratio
WGS	water gas shift
RWGS	reverse water gas shift
SR	steam reforming
MSR	methane steam reforming
SESR	sorption enhanced steam reforming
CSR	complete steam reforming
POX	partial oxidation
ATR	autothermal reforming
CLC	chemical looping combustion
CLR	chemical looping reforming
SECLR	sorption enhanced chemical looping reforming
MeO	oxidized oxygen carrier
Me	reduced oxygen carrier
C_nH_m	generic expression of hydrocarbons
$C_nH_mO_k$	generic expression of oxygenated hydrocarbons
YSZ	yttria-stabilized zirconia
DRI	direct reduction of iron ore

TEM	Transmission Electron Microscope
XPS	X-ray Photoelectron Spectroscopy
TGA	Thermal Gravimetric Analysis
DTG	Differential Thermal Gravity
FTIR	Fourier Transform Infrared Spectroscopy
XRD	X-ray Diffraction
ICDD	International Centre for Diffraction Data
GOF	goodness of fit
R _{exp}	expected residual value
R _{wp}	weighted residual value
SEM	Scanning Electron Microscopy
EDX	Energy Dispersive X-ray Spectroscopy
TOC	Total Organic Carbon
NPOC	non-purgeable organic carbon
TC	total carbon
IC	inorganic carbon
ppm	parts per million (10 ⁻⁶)
ICP-MS	Inductively Coupled Plasma-Mass Spectrometry
BET	Brunauer-Emmett-Teller
BJH	Barrett-Joyner-Halenda
TGA-MS	Thermal Gravimetric Analysis-Mass Spectrometry
TPR	temperature programmed reduction
TPO	temperature programmed oxidation
CEA	Chemical Equilibrium with Application
NiO(cr)	NiO in crystal state

C_{gr}	graphite carbon
HAc	acetic acid
CD	carbon deposits
n/a	not applicable
NiO-G	glucose-impregnated NiO/ α -Al ₂ O ₃ catalyst
NiO-CA	citric acid-impregnated NiO/ α -Al ₂ O ₃ catalyst
Al ₂ O ₃ -G	glucose-impregnated α -Al ₂ O ₃
Al ₂ O ₃ -CA	citric acid-impregnated α -Al ₂ O ₃
A2	two-dimensional nucleation and nuclei growth model
R3	geometrical contraction model for sphere
R2	geometrical contraction model for cylinder
C_p°	heat capacity at standard state in J/mol·K
H°	enthalpy at standard state in J/mol
S°	entropy at standard state in J/mol·K
R	general gas constant, 8.314 J/mol·K
ΔH°	enthalpy change in kJ/mol
ΔG°	Gibbs free energy change in kJ/mol
ΔS°	entropy change in kJ/mol·K
ν_i	stoichiometric number of species i in a specified reaction
Δn	change in the moles of gas for per mol of NiO reduced
$n_{out,dry}$	flow rate of total dry outlet gas in mol/s
n_i	flow rate of specie i in mol/s
n_{eq}	total moles of equilibrium products
$y_{i,in}$	molar fraction of specie i in feedstock
$y_{i,eq}$	molar fraction of specie i at equilibrium

y_i	molar fraction of specie i in dry outlet gas
y_{C_2}	total molar fraction of C_2H_4 and C_2H_6
y_{C_3}	total molar fraction of C_3H_6 and C_3H_8
X_{bio}	conversion fraction of bio-compound
X_{H_2O}	conversion fraction of water
M_{bio}	molecular weight of bio-compound in gram
M_{H_2}	molecular weight of H_2 in gram
M_c	ratio of molar mass in gram to carbon number in bio-compound molecule
NiO/C ratio	molar ratio of NiO to carbon in bio-compound molecule
O/C	ratio of oxygen atoms to carbon atoms in bio-compound molecule
H/C	ratio of hydrogen atoms to carbon atoms in bio-compound molecule
$Y(CO_2)$	equilibrium yield of CO_2 in mol/mol carbon feed
$Y(CO)$	equilibrium yield of CO in mol/mol carbon feed
$Y(H_2)$	equilibrium yield of H_2 in mol/mol carbon feed
$Y(CH_4)$	equilibrium yield of CH_4 in mol/mol carbon feed
R^2	square of correlation coefficient
E_a	apparent activation energy
A	pre-exponential factor
k	rate constant
Sh	Sherwood number
Sc	Schmidt number
Re	Reynolds number
k_c	external mass transfer coefficient (m/s)
D_{AB}	molecular diffusivity (m^2/s)
d_p	particle diameter (m)

$c_{A,g}$	concentration of bio-compound A in gas phase (mol/m^3)
$c_{A,s}$	concentration of bio-compound A on solid surface (mol/m^3)
$W_{A,r}$	theoretical molar flux of bio-compound A vapour ($\text{mol m}^{-2} \text{s}^{-1}$)
r_A	consumption rate of bio-compound A experimentally observed ($\text{mol m}^{-2} \text{s}^{-1}$)

Chapter 1

Introduction: background, scope and objectives of the research

1.1 Research background

We are currently living in a ‘fossil fuel economy’ as the world energy consumption is predominantly supplied by fossil fuels. Coal, petroleum and natural gas are widely used as primary energy sources in residential and commercial buildings, industrial and transportation sectors. However, the reserves of fossil fuels on earth are limited and a series of environmental problems (e.g. acid rain, global warming, and air pollution) are caused by the combustion of fossil fuels. In order to achieve sustainable development, some strategies have been proposed which typically involve three aspects: reducing energy consumption, increasing the energy utilization efficiency and using renewable energy sources to replace fossil fuels [1]. Common renewable energy sources include solar, wind, biomass, hydro-electric, and geothermal energy. According to the International Energy Agency, renewable energy technologies can be distinguished as three temporal generations: (1) hydropower, biomass combustion, and geothermal energy, as the first generation technologies, have reached maturity; (2) solar energy, wind power, and modern forms of bio-energy as the second generation technologies are undergoing rapid development; (3) the third generation technologies including concentrating solar power (CSP), ocean energy, improved geothermal, and integrated bio-energy systems are currently in early development stages.

The utilization of renewable energy sources increases continuously but remains limited. By the end of 2011, an estimated 19% of global final energy consumption was supplied by renewable energy sources (**Figure 1.1**) [2]. Approximately 9.3% of the total energy came from traditional biomass combustion used for heating or cooking in rural areas of developing countries. Modern utilization of renewable energy sources made up 9.7% of the global final energy consumption. It has been noted that biomass is a versatile energy source that can be used to generate heat, power or bio-fuels.

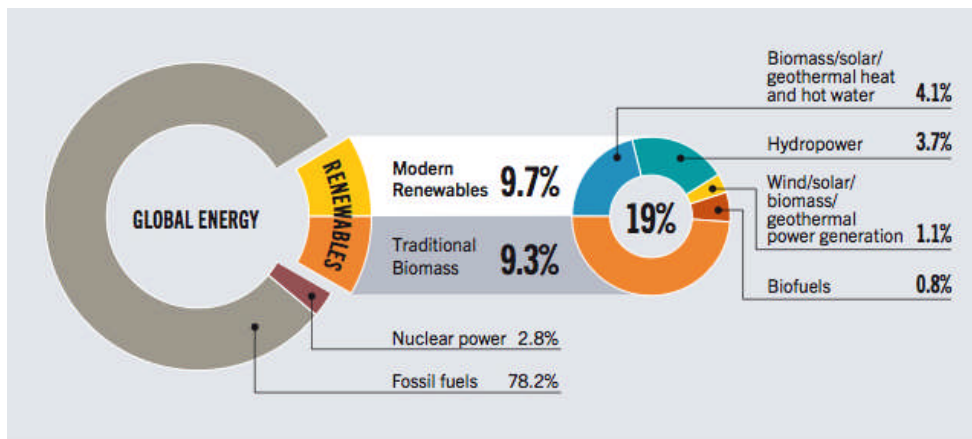


Figure 1.1 Renewable energy share of global final energy consumption in 2011 (source: renewables 2013 global status report from REN 21)

In 2007, the European Council proposed the so-called ‘20-20-20’ targets: to reduce the emission of greenhouse gases by 20%, to increase energy efficiency by 20% and to raise the share of European Union (EU) energy consumption produced from renewable resources to 20% by 2020. According to Eurostat newsrelease (37/2014-10 March 2014), renewable energy was estimated to contribute 14.1% of the gross final energy consumption in EU in 2012. The target for different states varies because of their different starting points, renewable energy potential and economic performance. The distance from the level in 2012 to their specific target in 2020 for EU 28 nations is shown in **Figure 1.2**. The highest shares of renewable energy in final energy consumption in 2012 were found in Sweden (51.0%), Latvia (35.8%) and Finland (34.3 %). For UK, the share of renewable energy in final energy consumption in 2012 was only 4.2%, far below its target for 2020 (15%).

The UK government has introduced a number of regulations to increase the use of renewable energy sources as reported in the ‘UK Renewable Energy Roadmap Update 2013’. The Renewables Obligation (RO) and Feed in Tariffs (FITs) scheme carries on playing an important role in supporting the development of renewable electricity capacity. The Renewable Heat Incentive (RHI) continues to help stimulate growth in the deployment of renewable heat, with around 16.4 TWh (1 TWh=10¹² Watt hours) of energy generated from all renewable heat sources in 2012.

The 2012 Bioenergy Strategy focuses on achieving more efficient uses of biomass resources.

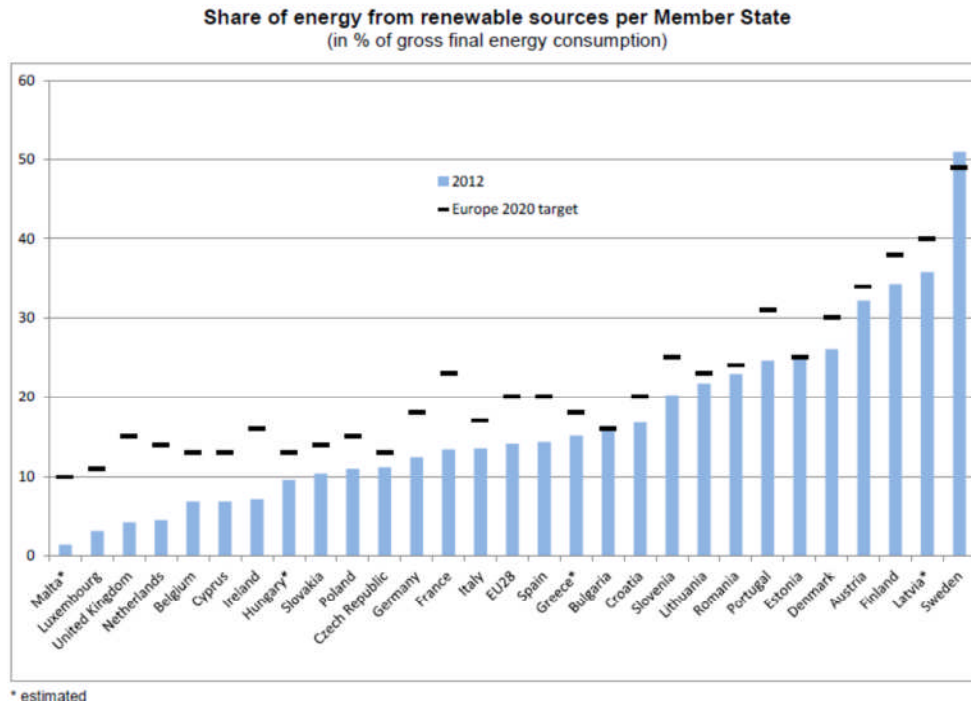


Figure 1.2 Share of renewable energy in gross final energy consumption per member state of EU in 2012 (Source: Eurostat newsrelease, 37/2014-10 March 2014)

The ‘Hydrogen economy’ is a sustainable energy vision of our future in which H₂ is produced from renewable energy sources, and utilized in transportation and distributed heat and power generation system by fuel cells, internal combustion engines and other technologies. H₂ is considered as an ideal energy carrier because it has a high mass energy density (~142 MJ/kg) and the only by-product of its complete oxidation or combustion is water. At present, approximately 96% of the H₂ is produced from fossil fuels through various thermal processes [3]. As **Figure 1.3** [4] shows, about half of the H₂ is obtained from natural gas through reforming processes (catalytic steam reforming, partial oxidation and autothermal reforming). About 30 % of the H₂ is produced from heavy oils and naphtha mainly as a by-product of catalytic reforming of naphtha [5]. Coal gasification contributes 18% of

the H₂ production. Till date, the most commonly used process for industrial H₂ production is catalytic steam reforming of natural gas followed by water gas shift reaction. The efficiency of this process can go up to 85% [5-9]. These fossil fuel-based H₂ production processes are associated with greenhouse gas emission. Therefore, it is of great importance to develop technologies of producing H₂ from renewable resources [9].

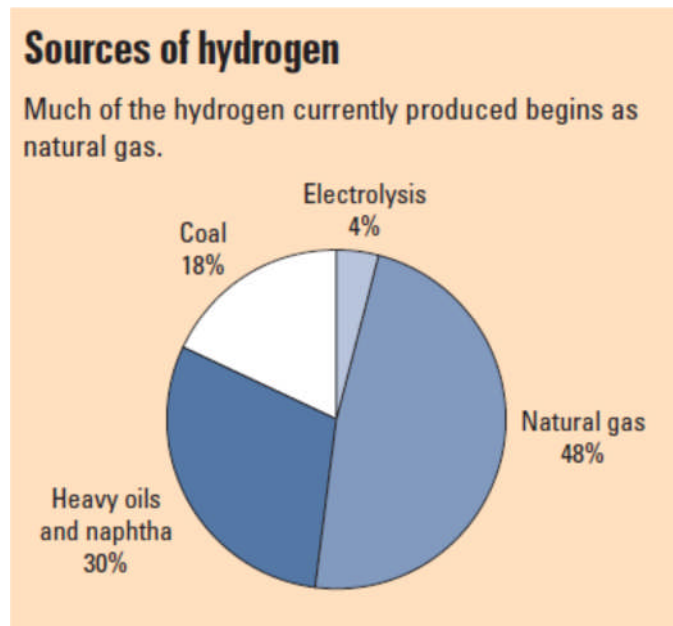


Figure 1.3 Global H₂ production share by sources [4]

There is still a long way to go for a complete substitution of fossil fuels with renewable energy sources. In the near term, fossil fuels remain being the dominant energy sources although their share in global energy consumption will decrease by 4% from 2010 to 2040 (International Energy Outlook 2013, U.S. Energy Information Administration, DOE/EIA-0484(2013) [10]). The IPCC's Fifth Assessment Report (AR5), on which 803 scientists worked, concludes with 95% certainty that human activity is the dominant cause of observed global warming since the mid-20th century. The combustion of fossil fuels makes a major contribution to the rise in atmospheric concentration of CO₂ (from a pre-industrial level of 280 to 390 ppm), which is the primary reason for the global warming [11]. In this background, a

transition economy ‘low carbon economy’ is being established aiming at reducing the negative impact of fossil fuel utilization on the environment. CO₂ capture seems to be a feasible approach to reduce CO₂ emission from fossil fuel combustion. In order to capture CO₂, a number of techniques are available currently, such as (1) oxy-fuel combustion, which uses pure oxygen obtained from cryogenic nitrogen separation from air and (2) post-combustion separation, which separate CO₂ from the flue gases using adsorption, absorption or membranes, etc. However, these processes are energy intensive, resulting in a significant decrease of the overall energy efficiency. In contrast, chemical looping combustion (CLC) appears to a promising green combustion technology as it features easy CO₂ capture and no combustion pollutants like NO_x [12, 13]. If biomass is used in a CLC process, the CO₂ captured can be considered as a negative emission.

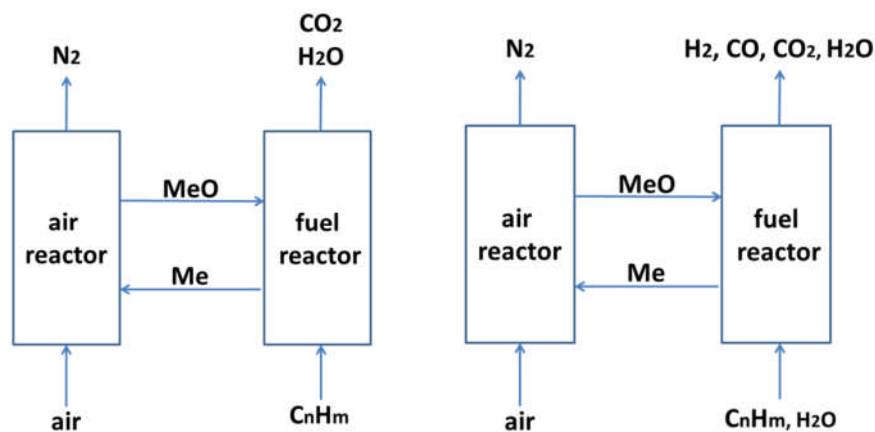


Figure 1.4 Schematic diagrams of chemical looping combustion (left) and chemical looping reforming (right) (MeO: oxidized oxygen carrier, Me: reduced oxygen carrier, C_nH_m: fuel)

A basic CLC system consists of two reactors, for air feed and fuel feed, respectively, as illustrated in **Figure 1.4** (left). Direct contact between the fuel (C_nH_m) and air is avoided. Instead, an oxygen carrier, usually a supported metal oxide, performs the task of bringing oxygen from the air to the fuel by circulating between the two reactors. In the air reactor, the oxygen carrier is oxidized. In the fuel reactor, it is

reduced by the fuel. In turn, the fuel is combusted with the lattice oxygen of oxygen carrier to produce CO_2 and H_2O , without dilution by N_2 . Thus, CO_2 can be readily captured by condensing water vapour.

As an extension of CLC, chemical looping reforming (CLR) has a similar configuration (**Figure 1.4** (right)) and a similar working principle. The CLR is essentially considered as an autothermal reforming process for syngas production. The process occurring in the fuel reactor includes first the combustion of fuel (meanwhile the oxygen carrier is reduced), and then the steam reforming of fuel. The heat required for the steam reforming reaction is supplied by the internal combustion of the fuel. In a CLR process, the reduced oxygen carrier is supposed to have a catalytic activity for subsequent steam reforming reaction. Among various oxygen carrier candidates, supported NiO is generally believed to be the most promising oxygen carrier for the CLR of CH_4 due to its good redox reactivity and catalytic activity [14]. If high-purity H_2 is required, a water gas shift reactor needs to be added following the fuel reactor. Compared with conventional autothermal reforming, the CLR eliminates the need for oxygen separation from air [15]. The coked catalyst can be regenerated in the air reactor through carbon combustion. In addition, it is easy to incorporate in situ CO_2 adsorption into a CLR process by mixing solid CO_2 sorbent (e.g. CaO) with oxygen carrier (sorption enhanced CLR) [16-18]. In the fuel reactor, the CO_2 removal from gas products could enhance H_2 purity and H_2 yield because of the shifted chemical equilibrium [19, 20]. In the air reactor, the saturated sorbent can be regenerated by thermal decomposition reaction since the oxidation of reduced oxygen carrier is exothermic.

Biomass is an important primary energy source and renewable energy source. The utilization of biomass is a near- CO_2 neutral process as the CO_2 released could be absorbed by newly grown plants through photosynthesis. Following petroleum, coal and natural gas, biomass is the fourth largest energy source, which provides about 14% of the global primary energy consumption [21]. However, the energy is obtained mainly by traditional biomass combustion with low energy efficiency. In China, biomass is widely used for cooking and heating through burning with a thermal efficiency only between 10% and 30% [22]. Modern biomass utilization with enhanced energy efficiencies is desired.

Recently, biomass finds its application in H₂ production, green combustion and sustainable metallurgical operation as substitute of fossil fuels. Processes involved include catalytic steam reforming of bio-fuels [6, 23-26], CLR of bio-fuels [17, 18, 27, 28], CLC of biomass [29, 30], and direct reduction of iron ore with biomass or biomass char [31, 32]. Such a substitution of fossil fuels with biomass or biomass derivatives in these processes exploits opportunities of utilizing biomass. Meanwhile some challenges may arise since the difference between biomass-based fuels and fossil fuels is evident (e.g. biomass contains more moisture and oxygen) [6]. For example, bio-oil (a liquid product of biomass fast pyrolysis) contains a variety of oxygenated hydrocarbons, which are easily decomposed to form solid carbonaceous deposits on the catalyst during the steam reforming process. As a result, the catalyst deactivation is much more severe in the steam reforming of bio-oil than in the steam reforming of natural gas or naphtha. In addition, the steam reforming of bio-oil goes through much more complex reaction channels with various intermediates being produced because bio-oil consists of numerous compounds [33]. In order to get a better understanding of the steam reforming process of the whole bio-oil, a commonly used method is to investigate the performance of individual compound present in bio-oil (model compound of bio-oil, or bio-compound) [34-38].

In contrast with conventional steam reforming of bio-oil, the CLR of bio-oil has several advantages. (1) The heat required by the steam reforming of bio-oil is supplied by the internal combustion of bio-oil rather than the external heat supply from fossil fuel combustion. Thus, the CLR process is completely based on biomass resource. (2) The characteristics of CLR that the catalyst is cyclically regenerated through carbon combustion may be a solution to the severe carbon deposition during bio-oil steam reforming. (3) It is easy to achieve the regeneration of a CO₂ sorbent if in situ CO₂ capture is considered.

In the CLR process, whether the bio-oil is able to perform the reduction of oxygen carrier is critical to the subsequent steam reforming reaction as the reduced oxygen carrier plays the role of reforming catalyst. Furthermore, different components of bio-oil may exhibit diverse reducing abilities and their influence on the catalyst activity may also be dissimilar.

In addition to the CLR process, other biomass utilizations such as CLC of biomass and sustainable metallurgical operation also involve the reduction of metal oxide with biomass or its derivatives. Hence, the study on this reaction is of great significance in exploiting biomass resources. However, few studies have been conducted on this subject although the reduction with H₂ [39, 40], CO [41], carbon [42-45] and light hydrocarbons [46] has been extensively investigated.

1.2 Research scope

In this project, 18 wt% NiO/Al₂O₃ is selected as a model compound of supported NiO materials which are commonly used as a steam reforming catalyst [8, 33, 47] and also considered as a potential oxygen carrier for CLR [48-50]. Five compounds with different functional groups are selected to represent five common chemical families of bio-oil, respectively. They are acetic acid (carboxylic acids), ethanol (alcohols), acetone (ketones), furfural (furans) and glucose (sugars). The compound that exists in biomass or biomass derivatives (e.g. bio-oil) is termed 'bio-compound' in this project. The process investigated here is the reduction of nickel oxide with these bio-compounds and the subsequent steam reforming of these bio-compounds, which represents the half cycle occurring in the fuel reactor of a CLR system. For comparison, CH₄ as a common non-oxygenated hydrocarbon is also studied in this integrated reduction and steam reforming process. The oxidation of metal in the air reactor and the cyclic performance of the oxygen carrier are not in our research scope. The reduction and steam reforming process is performed in a packed bed reactor at different temperature (500-750 °C) with different S/C (4.5-9 for glucose and 0-5 for the other bio-compounds). In addition, thermodynamics equilibrium calculation of related reactions (metal oxide reduction, bio-compound pyrolysis and bio-compound steam reforming) are carried out based on minimisation of Gibbs free energy using NASA Lewis Research Centre's computer program CEA (Chemical Equilibrium with Applications).

Apart from the reduction with bio-compounds in vapour phase, the temperature programmed reduction (TPR) of metal oxide with solid bio-compounds (glucose and citric acid) is also investigated using a TGA-FTIR instrument.

1.3 Research objectives

1. Thermodynamic study of NiO reduction with bio-compounds: (a) to check reduction feasibility, (b) to calculate the energy demand, (c) to find out the influence of temperature, the presence of steam and the availability of NiO, and (d) to obtain the thermodynamic domain for avoidance of carbon formation. (Chapter 4)
2. Thermodynamic study of steam reforming of bio-compounds: (a) effects of temperature, S/C and molecular formula of bio-compounds on equilibrium yields, (b) thermodynamic evaluation for carbon free region, (c) energy balances. (Chapter 5)
3. Experimental investigation on isothermal reduction of nickel catalyst (NiO/Al₂O₃) with bio-compounds in a steam reforming environment (termed 'auto-reduction'): (a) reduction process analysis, (b) kinetic modelling and apparent activation energy calculation, (c) effects of steam content on reduction kinetics, (d) comparing the reducing abilities and reduction kinetics of different bio-compounds. (Chapter 6 and 7)
4. Experimental investigation on steam reforming of bio-compounds following the auto-reduction: (a) the influence of auto-reduction on the steam reforming performance compared with H₂ reduction, (b) effects of temperature and S/C on the steam reforming performance, (c) catalytic pyrolysis of bio-compounds (S/C=0), (d) to find out the main barrier for steam reforming of each bio-compound. (Chapter 6 and Chapter 8)
5. Experimental investigation on non-isothermal reduction of nickel catalyst with solid bio-compounds (glucose and citric acid): (a) to examine reaction feasibility and reduction extent, (b) to analyse the nature of actual reductant (carbonaceous material from bio-compound pyrolysis), (c) to propose a reduction mechanism, (d) to study reduction kinetics. (Chapter 9)

Chapter 2

Literature review

2.1 Introduction

As introduced in Chapter 1, this project will demonstrate the reduction of reforming catalyst with oxygenated bio-compounds derived from bio-oil as well as the subsequent steam reforming performance of these bio-compounds. Such a study aims at exploiting the potential of liquid bio-fuels for sustainable H₂ production through a CLR process. Accordingly, basic concepts and recent research progress of the following subjects are summarised in this chapter. (1) Bio-oil production and bio-oil properties; (2) H₂ production via fossil fuel-based processes and steam reforming of bio-oil; (3) critical issues of a CLR process and (4) reaction mechanism and kinetic models of metal oxide reduction with various reducing agents.

2.2 Thermochemical conversion of biomass

Biomass is an important renewable energy source. In general, biomass resources include (a) energy crops, (b) agricultural residues and wastes, (c) forestry residues and wastes, and (d) industrial and municipal wastes [22]. The conversion of biomass to energy or an energy carrier (secondary energy source) is usually carried out through biochemical processes (e.g. anaerobic digestion to produce biogas, alcoholic fermentation to produce bio-ethanol) or thermochemical processes (e.g. combustion, gasification, pyrolysis, etc.). As a traditional biomass utilization route, biomass combustion has the disadvantage of low energy efficiency and significant emission of pollutants. In order to exploit biomass resources, other thermochemical conversion technologies have been developed in recent decades.

2.2.1 Pyrolysis

Pyrolysis is a thermal decomposition process that converts biomass to liquid (termed 'bio-oil', or 'pyrolysis oil'), charcoal and non-condensable gases in the absence of air in the temperature range of 300-1000 °C [51]. Conventional pyrolysis which is

mainly for charcoal production is performed at a low heating rate (0.1-1°C/s). If the purpose is to maximize the yield of bio-oil, a high heating rate and short gas residence time would be required. This process is termed 'fast pyrolysis'. At present, fast pyrolysis is considered as a promising route for the production of liquid bio-fuels. Liquid bio-fuels have advantages in transport and storage over either unprocessed biomass (a lower energy density) or flammable gas products from biomass gasification.

The essential features of a fast pyrolysis process are [52]:

- (a) High heating rate and high heat transfer rate, hence a finely ground biomass feed is required
- (b) Carefully controlled pyrolysis temperature (around 450-550 °C)
- (c) Short vapour residence time (1-5s)
- (d) Rapid quenching at the end of pyrolysis

Recent laboratory research and commercial developments in fast pyrolysis techniques can be found in ref. [53, 54]. As the development of fast pyrolysis techniques, the yield of bio-oil can reach 70-75% on the basis of dry biomass (anhydrous biomass). Various types of biomass have been screened, aiming at finding the correlation between biomass characteristics and properties of resulting bio-oil. Generally, the woody feedstock produces the oil with the best quality in terms of carbon and hydrogen content and water content. Aquatic biomass has also been widely used in the fast pyrolysis process due to its fast growing rate and the feature of not using land. A commonly recommended scheme of converting biomass to bio-oil is (1) decentralized bio-oil production from the biomass gathered from a certain area and (2) transportation of the bio-oil to central destination (e.g. bio-oil refinery plant) [55].

2.2.2 Gasification

Biomass gasification is the thermochemical conversion of biomass at elevated temperatures (>700 °C) under an oxygen-starved condition into a flammable gas mixture of CO, H₂, CH₄, CO₂ and small quantities of hydrocarbons [56]. Air, oxygen, steam as well as mixtures of these can be used as a gasifying agent. The

choice of which depends on the desired product gas composition and energy considerations [57]. In general, a typical biomass gasification process consists of the following four stages.

- (1) Drying: water vapour is driven off the biomass.
- (2) Pyrolysis: as the temperature increases the dry biomass decomposes into gases, vapours, carbon (char) and tar.
- (3) Combustion: the pyrolysis products are partially oxidized with oxygen to form CO, CO₂ and H₂O.
- (4) Reduction: the H₂O and CO₂ previously formed react with carbon to produce CO, H₂ and CH₄.

Biomass gasification is considered as one of the most promising technologies for exploitation of biomass resources due to its high energy conversion efficiency and its flexibility on product application (**Figure 2.1**). The resulting gas mixture comprised mainly of CO and H₂ (termed as ‘syngas’) can be burned to provide heat. Clean syngas can be used in either a compression-ignition engine (diesel engine) or a spark-ignition engine (gasoline engine). H₂ can be produced through steam reforming of gasification products followed by water gas shift reaction. Synthesis of fuels and chemicals (such as ammonia, methanol) is another important application of the gasification products. Biomass integrated gasification-Fischer-Tropsch (BIG-FT) technology is being developed for the production of synthetic hydrocarbons from biomass, which may offer a carbon neutral alternative to conventional diesel, kerosene and gasoline in transportation sector [58].

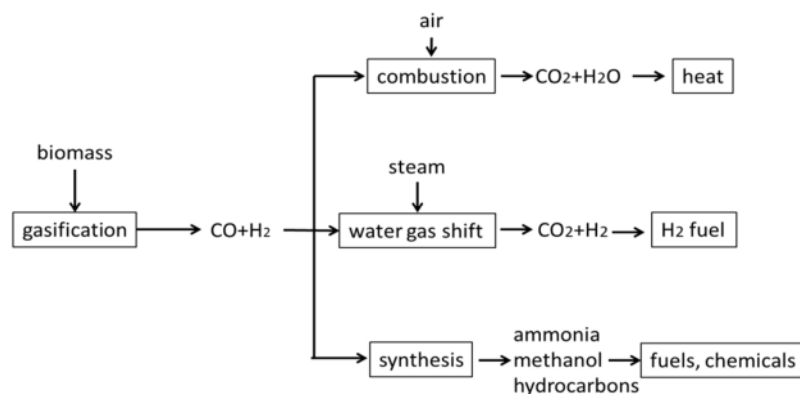


Figure 2.1 Various applications of syngas produced from biomass gasification

One problem of biomass gasification is the tar formation which may contaminate the resulting gas and block filters and pipelines. The tar production could be minimized by reactor design, process control or using catalysts. Common catalysts for tar elimination in biomass gasification process include: (1) natural catalysts such as dolomite and olivine, (2) alkali metal-based catalysts such as K_2CO_3 and (3) transition metal-based catalysts such as Ni catalysts [59]. In addition, char, a by-product of biomass gasification can be used for tar removal in two ways. The char itself exhibits some activity for tar reforming. The char also acts as a good support to disperse active clusters at nanoscale (e.g. char-supported Fe catalyst, char-supported Ni catalyst) [60].

2.2.3 Hydrothermal processing

Hydrothermal processing of biomass is to convert biomass to desired products in an aqueous medium at elevated temperature and pressure [56]. Under critical conditions of water (around 374 °C and 218 bars), the water can serve as a solvent, a reactant, and even a catalyst. Hence, those biomass components (e.g. lignin, cellulose) which are not water soluble at ambient conditions, are readily dissolved in water under hydrothermal conditions and then be subject to hydrolytic attack and fragmentation of bio-macromolecules. As a result, higher-value fuels are produced.

Depending on the experimental conditions, different types of products could be obtained. Under mild conditions (250-350 °C, 40-165 bar), biomass is converted to viscous bio-oil. This process is hydrothermal liquefaction. At higher temperatures (350-500 °C), with suitable catalysts present, it is possible to convert primary fragments to gases (mainly CH_4). The process is catalytic hydrothermal gasification. When the temperature is further increased (500-800 °C), primary fragments further decompose to produce a H_2 -rich gas [61]. This process is termed as supercritical water gasification (SCWG).

Compared with pyrolysis and gasification, the advantage of hydrothermal process is that wet biomass can be directly used without drying operation. However, conditions of hydrothermal process are much more severe than pyrolysis and gasification, and it is a challenge to achieve large-scale production at present.

2.2.4 Bio-oil properties and applications

2.2.4.1 Physical properties of bio-oil

Table 2.1 Typical properties of wood pyrolysis bio-oil and heavy fuel oil [62]

Physical property	Bio-oil	Heavy fuel oil
moisture content, wt%	15-30	0.1
pH	2.5	-
specific gravity	1.2	0.94
elemental composition, wt%		
C	54-58	85
H	5.5-7.0	11
O	35-40	1.0
N	0-0.2	0.3
ash	0-0.2	0.1
HHV, MJ/kg	16-19	40
viscosity (at 50 °C), cP	40-100	180
solid, wt%	0.2-1	1
distillation residue, wt%	up to 50	1

Bio-oil is a dark brown, free-flowing liquid and has a distinctive smoky odour. It is comprised of numerous organic compounds which are derived primarily via dehydration and fragmentation reactions of biomass building blocks (cellulose, hemicellulose, and lignin). Therefore, the elemental composition of bio-oil resembles that of biomass rather than that of petroleum oil. The physical properties of bio-oil and heavy fuel oil are compared in **Table 2.1** [62].

(1) High oxygen content

As shown in **Table 2.1**, the oxygen content of bio-oil is 35-40 wt%, much higher than that of heavy fuel oil. The presence of a large amount of oxygen element in bio-oil is considered as the main reason for the different properties between bio-oil and fossil fuel oil. High oxygen content results in a low energy density (less than 50% of

the energy density of heavy fuel oil) and immiscibility with hydrocarbon fuels. High oxygen content also leads to thermal instability of bio-oil. Oxygenated compounds in bio-oil can readily decompose and form solid carbonaceous deposits (coking). Recently, a novel fast pyrolysis processor was designed in order to produce bio-oil with low oxygen content [63]. In this processor, calcined limestone was used to provide process heat by carbonation reaction and to lower acidity and oxygen content of the bio-oil produced.

(2) High water content

The water content of bio-oil is 15-30 wt%, much higher than that of heavy fuel oil. The water present in bio-oil originates from the moisture of biomass feedstock and the dehydration reaction during pyrolysis. Therefore, the water content varies over a wide range depending on the feedstock and process conditions used. It is not easy to remove the water because many components of bio-oil are soluble in water. The presence of water in bio-oil lowers the heating value and increases the ignition delay. On the other hand, high moisture content reduces the oil viscosity, which is beneficial for the pumping and atomization of bio-oil during a combustion process. Recently, Yang et al. [64] investigated the performance of diesel engine with bio-oil being added to diesel. They found that the incorporation of bio-oil in diesel decreased the combustion efficiency although certain aspects of combustion were enhanced (e.g. NO_x emission was reduced).

(3) Wide volatility distribution

Bio-oil contains both volatile compounds (water and volatile organics) and non-volatile compounds (sugars and lignin-derived oligomers). As a result, a wide boiling point distribution was observed [65]. Moreover, the polymerization of some compounds present in bio-oil (e.g. aldehydes and phenols) during their vaporisation may decrease the overall volatility of bio-oil.

(4) Viscosity and aging

The viscosity of bio-oil covers a wide range which is determined by the feedstock and the process conditions (especially the cooling rate at the end of pyrolysis). The decrease in the viscosity could be achieved by adding a polar solvent such as methanol or acetone. The viscosity of bio-oil will increase with time especially

when it is stored at a high temperature. This ‘aging’ phenomenon is likely caused by chemical reactions between reactive compounds, such as etherification and esterification [66]. Another possible reason is some bio-oil components are oxidized by air.

(5) Corrosiveness

The presence of organic acids (e.g. acetic acid and formic acid) in bio-oil leads to a pH value of 2-3. Because of the acidity, bio-oil is corrosive to certain materials, such as carbon steel and aluminium. Elevated temperatures and high water contents make the corrosiveness more severe.

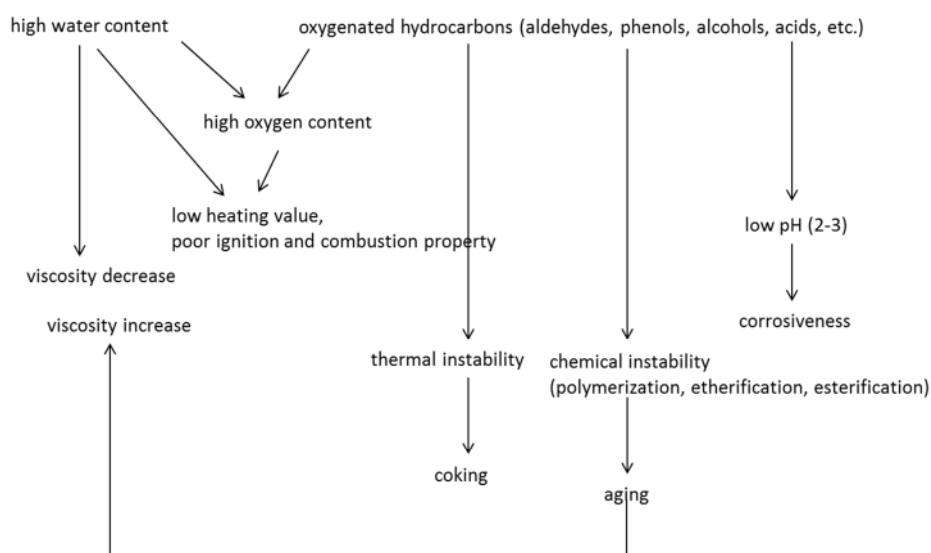


Figure 2.2 Properties of bio-oil and their correlations

2.2.4.2 Chemical composition of bio-oil

As shown in **Table 2.2**, bio-oil has a complicated chemical composition, which greatly depends on biomass feedstock and pyrolysis conditions.

Table 2.2 Chemical composition of bio-oil from different feedstock and different processes (yield in wt% of dry biomass) [26]

Products	Fluidized bed (University of Waterloo)			Vortex (NREL)
	poplar (504 °C)	maple (508 °C)	spruce (500 °C)	oak (~500 °C)
	acetic acid	5.4	5.8	3.9
formic acid	3.1	6.4	7.2	3.3
hydroxyacetaldehyde	10.0	7.6	7.7	4.3
glyoxal	2.2	1.8	2.5	3.0
methylglyoxal	n/a	0.65	n/a	n/a
formaldehyde	n/a	1.2	n/a	2.2
acetol	1.4	1.2	1.2	1.8
ethylene glycol	1.1	0.6	0.9	n/a
levoglucosan	3.0	2.8	4.0	3.8
anhydroglucofuranose	2.4	n/a	n/a	n/a
fructose	1.3	1.5	2.3	n/a
xylose	n/a	n/a	n/a	0.9
glucose	0.4	0.6	1.0	n/a
cellobiosan	1.3	1.6	2.5	n/a
oligosaccharides	0.7	n/a	n/a	n/a
pyrolytic lignin	16.2	20.9	20.6	24.9
unidentified	11.9	17.1	12.9	5.8
oil	65.8	67.9	66.5	55.3
water	12.2	9.8	11.6	10.4
char	7.7	13.7	12.2	12.4
gas	10.8	9.8	7.8	12.2

The compounds present in bio-oil (termed as ‘bio-compounds’) generally fall into seven chemical families: carboxylic acids, aldehydes, alcohols, ketones, sugars, furans and phenols [26, 65, 67, 68]. The compounds in the first six groups are mainly derived from carbohydrates of biomass (cellulose and hemicellulose). The

group of phenols is mainly derived from lignin and hence also termed as ‘pyrolytic lignin’. Most compounds in this group are present as oligomers and have a molecular weight ranging from 900 to 2500. By adding water, bio-oil can be separated into two immiscible phases: a monomer-rich aqueous phase and an oligomer-rich hydrophobic phase.

2.2.4.3 Applications of bio-oil

(1) Combustion for heat or power

Bio-oil can substitute for fossil fuel oil in some static applications such as boilers, furnaces, engines and turbines [69, 70]. In recent bio-oil combustion tests at industrial scale, bio-oil has been found to be technically suitable for district heating instead of heavy fuel oils [69]. Compared with fossil fuel oils, bio-oil is essentially CO₂ neutral and has low sulphur content.

(2) Chemicals production

There are a range of chemicals that can be extracted or produced from the whole bio-oil or its fractions. The most successful example of chemicals production from whole bio-oil may be the production of BioLime [71]. The carboxylic acids and phenols present in bio-oil can easily react with lime to form calcium salts and phenates, two main components of BioLime. The BioLime material shows a good performance in capturing SO_x emitted from coal combustion. The products derived from the aqueous fraction of bio-oil include food flavourings and calcium salts of carboxylic acids (used as de-icers). The products derived from water-insoluble fraction include resins and adhesives [62].

(3) Upgrading bio-oil to transport fuels

Bio-oil can be upgraded through hydro-treatment [72]. In petroleum industry, hydro-treatment is usually designed to remove sulphur, nitrogen, oxygen and other contaminants, as well as cracking heavy compounds to lighter fractions. For bio-oil, the main contaminant that needs to be removed is oxygen [73]. Hydrodeoxygenation of bio-oil is carried out at high temperature, high H₂ pressure and in the presence of catalysts (typically sulfided CoMo or NiMo supported on Al₂O₃).

However, upgrading bio-oil to transport fuels is still a big challenge in the short term. At present, the simplest approach to use bio-oil in transportation is to make blends with fossil diesel [64] or bio-diesel [65] with the aid of surfactants (e.g. Span 80 and Tween 80). Bio-diesel is usually produced via trans-esterification of vegetable oils (soybean, rapeseed, sunflower and palm oil) or animal fats with alcohols using acidic catalyst (e.g. H_2SO_4) or basic catalyst (e.g. NaOH) [74]. Compared with petroleum-derived diesel, bio-diesel tends to have low oxidation stability and poor cold flow property. The addition of bio-oil to bio-diesel has the advantage of improving the oxidation stability because phenolic compounds present in bio-oil are excellent antioxidants [65].

(4) Steam reforming of bio-oil for H_2 production

Another important application of bio-oil is for H_2 production by catalytic steam reforming and the subsequent water gas shift reactions. This part will be presented in detail in Section 2.3.2.

2.3 Hydrogen production via thermal processes

The world production of H_2 was 53 Mtons in 2010 and is predicted to grow at a rate of 10% per year. The H_2 is currently used (a) 54% for fertiliser production (e.g. ammonia synthesis via the Haber process), (b) 35% for chemical industry and refineries, and (c) the remainder for metallurgy, electronic industry and food industry, etc. [9]. H_2 is considered as a promising alternative fuel in the future because it has several advantages over other fuels. Firstly, H_2 offers the highest energy density (energy-to-weight ratio) as shown in **Table 2.3**. Secondly, H_2 is an absolutely clean energy source. When the energy stored in H_2 is released by combustion, fuel cells or other routes, the only by-product is water, without any pollutant emission at the point of use.

Table 2.3 Energy density of selected fuels (data from Wikipedia)

Fuel	Specific energy (MJ/kg)
H ₂	142
LPG	46.4
gasoline/diesel/fuel oil	46
Jet fuel	43
crude oil	41.9
bituminous coal	24
natural gas	38-50
fat (animal/vegetable)	37
wood	16.2
bio-diesel	37.8

H₂ is rarely found in pure form on the earth. It must be produced from compounds that contain it, such as natural gas, biomass, alcohols and water. For this reason, H₂ is actually an energy carrier rather than a primary energy source. At present, the H₂ is predominantly produced from fossil fuels via catalytic steam reforming, partial oxidation, autothermal reforming, and gasification processes [75]. In addition, a large part of H₂ is produced as a by-product of catalytic naphtha reforming (not to be confused with catalytic steam reforming) [5, 76]. Sustainable H₂ production using renewable energy sources is at a developmental stage mainly by the following routes [9].

- (1) Thermal routes based on renewable hydrocarbons (e.g. biomass gasification, steam reforming of bio-fuels or wastes)
- (2) Water electrolysis powered by wind turbines, photovoltaic or photoelectrochemical cells
- (3) Solar water thermolysis via direct water splitting at high temperature (around 2000 °C, the efficiency is about 4%) or thermochemical cycles (e.g. iron oxide-based redox cycle) [77-79]
- (4) Biological routes (e.g. photobiological H₂ production from microalgae [80])

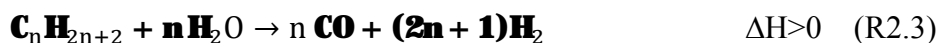
2.3.1 Hydrogen production from fossil fuels

2.3.1.1 Steam reforming (SR) of natural gas or naphtha

Catalytic steam reforming of natural gas is the main industrial process for commercial H₂ production. Its efficiency can go up to 85% and it meets up to 50% of the total H₂ consumption worldwide [75]. Natural gas is a gas mixture primarily containing CH₄. The steam reforming of CH₄ is an endothermic reaction (R2.1). Hence, this reaction is favoured by high temperature and low pressure. However, to maximize the economics of scale of H₂ production, the steam reforming is performed at pressure around 30 bars and temperature of 750-800 °C with S/C of 3.0-3.5 in industry, despite the high pressure being adverse to the reaction. Normally, the steam reforming reactor is followed by a shift reactor so that the H₂ yield can be further increased by water gas shift (WGS) (R2.2).



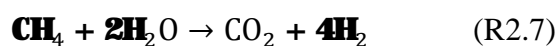
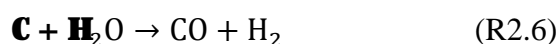
Although naphtha is not widely used in steam reforming process at a large scale, it is often used as a standby feed. Naphtha is a flammable liquid mixture of hydrocarbons (e.g. natural gas condensate or a distillation product of petroleum). The main components of naphtha are paraffins, olefins, naphthenes and aromatics. Naphtha fractions with a final boiling point less than 220 °C are generally considered as suitable for catalytic steam reforming. The steam reforming reaction of saturated hydrocarbons with a general formula C_nH_{2n+2} can be expressed as R2.3. As with natural gas, the naphtha steam reforming is favoured by high temperature and low pressure. The steam reforming of naphtha has a larger tendency towards carbon formation on catalysts than natural gas steam reforming. Therefore, the S/C ratio of 3.5-4.5 is commonly used in practice, slightly higher than the value used in natural gas steam reforming.



To overcome kinetic limitations in a steam reforming reaction, reforming catalysts are normally required. Despite noble metal catalysts (Pt, Ir, Rh, etc.) exhibiting the best catalytic activity, the commonly used catalyst in industry is Ni catalyst because

of its low cost and adequate catalytic activity in both steam reforming and water gas shift. To enhance the surface area of active phase and the mechanical strength of a catalyst, Ni is deposited on refractory materials such as Al_2O_3 and CaAl_2O_4 by precipitation or impregnation methods. The catalytic activity is affected by Ni content (there is an optimal content 15-20%), Ni surface area, Ni crystallite size, and the nature of the support [8]. The challenges faced by Ni reforming catalysts (catalytic activity, sulphur poisoning, carbon formation and sintering) were reviewed by Sehested [81].

For natural gas steam reforming, CH_4 cracking (R2.4) and the Boudouard reaction (R2.5) are two main reasons for carbon deposition. If reaction conditions are carefully controlled, the carbon deposition could be reduced or even eliminated. Heavy hydrocarbons have a greater tendency to deposit carbon than CH_4 because the intermediates from hydrocarbon pyrolysis tend to polymerize and then form carbon deposits. The cracking and polymerization are even more severe when using acidic support. This problem can be solved by introducing alkali metal (e.g. K, Na) and alkaline earth metal (e.g. Mg, Ca, Ba) materials to the catalyst [8]. These additives facilitate the steam gasification of carbon (R2.6) and at the same time retard cracking and polymerization by neutralizing the acidity of the support. The most effective alkali is found to be K_2O due to its mobility on the catalyst surface.



Sorption enhanced steam reforming (SESR) and membrane reactor are two recent developments of natural gas steam reforming [9]. In a SESR process, the incorporation of a CO_2 sorbent to the catalyst bed makes CO_2 removal occur in the reformer. The capital cost is reduced because of process intensification. Meanwhile, the H_2 yield is enhanced as the equilibrium of R2.7 (overall reaction of SR and WGS) is shifted to the product side. Typical sorbents include CaO and K-promoted double layered hydrotalcite [82]. The challenge faced by SESR is to match sorbent properties with the catalytic system used. Similar to the SESR process, in a

membrane reactor, steam reforming, WGS and H₂ purification take place almost simultaneously. An inorganic membrane (e.g. Pd membrane) which is selectively permeable to H₂ is used to separate H₂ and CO₂ in the reformer (**Figure 2.3**). As the steam reforming reaction proceeds, the H₂ produced is driven by the pressure difference across the membrane to the permeate side, leaving CO₂ and other by-products in the retentate side. If the reaction conditions is carefully controlled, a complete CH₄ conversion and a high-purity H₂ can be achieved [83].

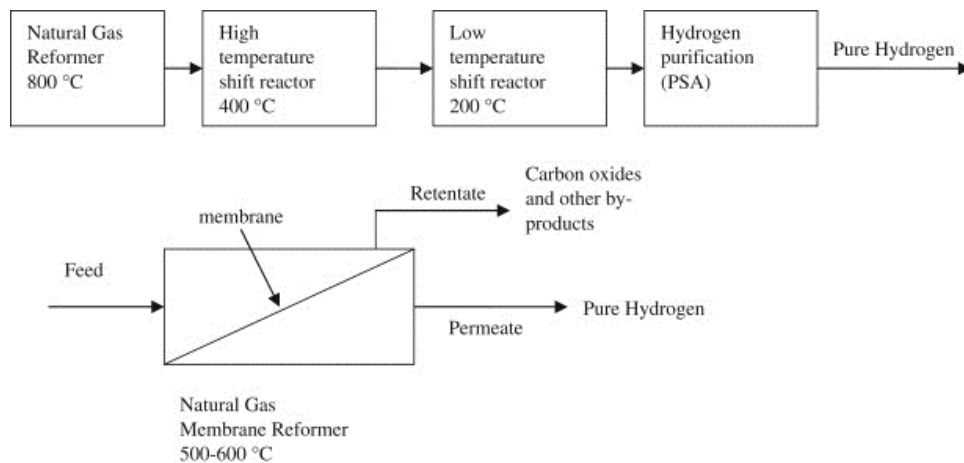


Figure 2.3 Scheme of pure H₂ production by steam reforming of natural gas in a conventional system (up) and in a membrane reactor (down) [83]

2.3.1.2 Partial oxidation (POX) of natural gas or heavy oil

The partial oxidation is a process in which hydrocarbons react with an appropriate amount of oxygen to produce CO and H₂ (R2.8, taking CH₄ as an example) rather than full combustion (R2.9). In industry, the partial oxidation process is mainly applied to natural gas and heavy oils. To a much lower extent, solid biomass is used as the feedstock of partial oxidation, which is termed as ‘biomass gasification’ (see Section 2.2.2).



Compared with steam reforming (R2.1), the partial oxidation of natural gas produces syngas with a lower H₂/CO ratio. The oxygen used in the partial oxidation reaction is usually obtained by an air separation unit which increases the capital and operating costs. However, in contrast with endothermic steam reforming reaction, the exothermic partial oxidation process does not need external heat supply. Another advantage is that a wide range of hydrocarbons including heavy oils, which is rarely used in the steam reforming process, is suitable for partial oxidation.

The partial oxidation could be carried out either with catalyst or without catalyst [9, 84]. Non-catalytic partial oxidation is usually performed at high temperatures (1150-1315 °C) in order to achieve a considerable conversion of hydrocarbons to syngas. In contrast, the temperature of catalytic partial oxidation is relatively low (around 800 °C) because the reaction kinetics is greatly enhanced by the catalyst.

2.3.1.3 Autothermal reforming (ATR)

In practice, a considerable amount of steam is introduced into a catalytic partial oxidation system to suppress carbon deposition. As a result, the steam reforming reaction takes place inevitably. The heat released from partial oxidation or complete oxidation drives the steam reforming reaction so that the overall heat demand is almost zero. This process is known as autothermal reforming (ATR). It is also known as oxidative steam reforming. In an ATR process, the relative feed rates of hydrocarbon, oxygen and steam need to be carefully designed so that a general autothermal effect can be achieved.

The ATR process has some drawbacks such as (1) the formation of hot spots in the initial part of the reactor, (2) low activity of the catalyst due to the oxidation of the active metal phase, and (3) coke formation in the final part of the reactor due to the lack of oxygen. These problems can be partially overcome if the catalyst and the reactor configuration are designed properly. It has been reported that Rh and Pd catalysts are more effective for the suppression of hot spot formation than Ni catalysts [85]. Tomishige et al. [86] found the addition of Pd to Ni catalysts could inhibit the oxidation of metallic Ni and reduce the carbon deposition during the ATR of CH₄. Herguido et al. [87] demonstrated the applicability of two zone fluidized bed reactor (TZFBR) in the ATR process of CH₄. The TZFBR was proposed [88] to

substitute two different reactors or a single reactor with periodic operation which are commonly used in chemical looping technology. As **Figure 2.4** shows, the oxygen-steam mixture is fed through the lower part of the TZFBR, while CH_4 is introduced at a middle point of the bed. In this way, two zones are provided in one reactor. In the lower part (regeneration zone), Ni is oxidized and coke on the catalyst is combusted (both reactions are exothermic). In the upper part (the reaction zone), the CH_4 steam reforming takes place once the oxidized catalyst is reduced by CH_4 (both reactions are endothermic). The heat is circulated between the two zones as the solid materials are circulated. Compared to two reactors or a single reactor with periodic operation, the TZFBR configuration has the advantage of process intensification. However, pure oxygen is required to obtain exit gases undiluted by N_2 .

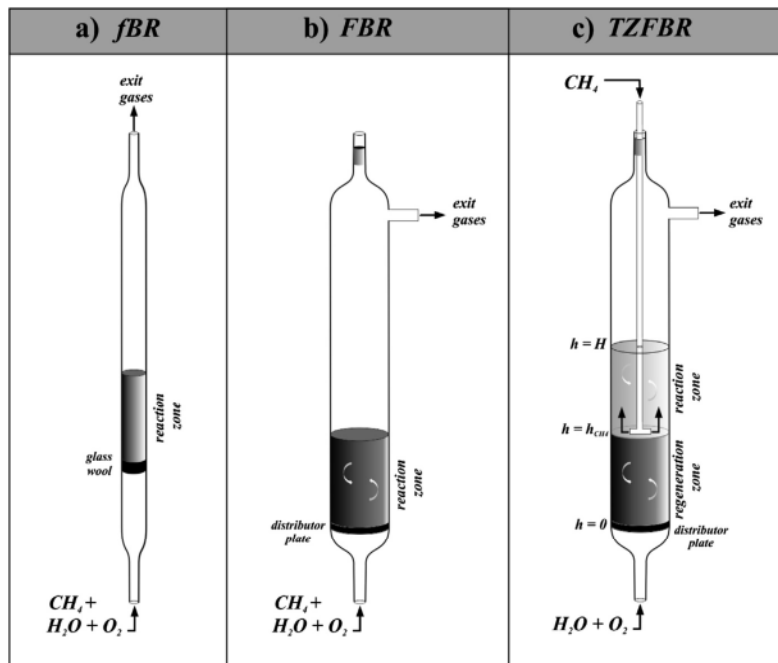


Figure 2.4 Three types of reactor configuration for ATR process a) fixed bed reactor, b) fluidized bed reactor and c) two zone fluidized bed reactor [87]

2.3.2 Hydrogen production from biomass

Two promising routes for H_2 production from biomass are (1) fast pyrolysis and then steam reforming of the pyrolysis oil (bio-oil) or (2) biomass gasification.

The general knowledge of biomass gasification has been introduced in Section 2.2.2. Here, H₂ production from biomass gasification is focused on. In gasification reactions, the gasifying agent used has a significant influence on the composition of the product gas. Compared with biomass air gasification or biomass oxygen gasification, biomass steam gasification is more favourable for H₂-rich gas production (30-60 vol% on dry and N₂ free basis) [57, 89, 90]. The main problem of biomass steam gasification is the formation of undesirable CO₂ and tar. The use of CaO in biomass steam gasification has been acknowledged as a feasible method to eliminate CO₂ and tar production within the process. Nonetheless, the deactivation of CaO after capturing CO₂ is a challenge for continuous H₂ production. To overcome this problem, the concept of CaO-based chemical looping gasification was proposed and gained attention in recent years [57].

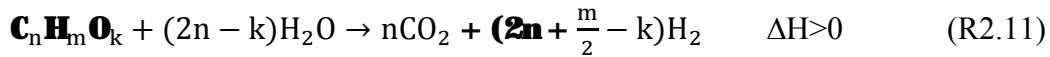
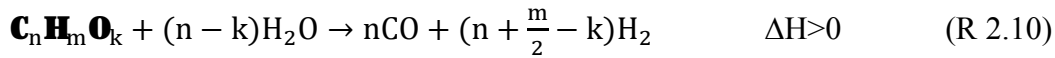
Biomass gasification is most appropriate for large-scale, centralized H₂ production due to the nature of handling large amounts of biomass and the required economy of scale for this type of process. In contrast, the process of biomass pyrolysis and then steam reforming of bio-oil has a great potential for distributed H₂ production. The H₂ yield via the pyrolysis-steam reforming process is similar to that of biomass gasification (12 wt% of biomass, the theoretical maximum is 17 wt%) [26]. However, the pyrolysis-steam reforming process is less severe than the gasification process. If the bio-oil is first refined to yield valuable oxygenates and the residual fraction is used for steam reforming, this route will be more attractive.

2.3.2.1 Steam reforming of bio-oil or its aqueous fraction

(1) Steam reforming of bio-oil

The steam reforming of bio-oil or its model compound has been reviewed in [33, 91]. Apart from steam reforming, there are other approaches for H₂ production from bio-oil, such as partial oxidation, aqueous-phase reforming, supercritical water reforming [91]. The steam reforming of bio-oil is very similar to the steam reforming of natural gas. The bio-oil is reacted with steam at high temperatures in the presence of a catalyst to produce a reformat gas composed mostly of H₂ and CO. Additional H₂ and CO₂ are produced by reacting the CO formed with steam (WGS reaction).

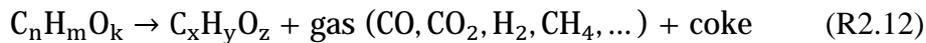
The chemical reaction for steam reforming of bio-oil is given in R2.10 ($C_nH_mO_k$ represents a general molecular composition of bio-oil). The overall reaction of steam reforming and WGS is presented in R2.11 [26].



The stoichiometric H_2 yield is $2+(m/2n)-(k/n)$ moles per mole of carbon feed. According to this, the lignin-derived phenols would theoretically have a higher H_2 yield than the carbohydrate-derived compounds such as acid, ethanol and acetone because the term of k/n is much less than 1 for phenols whereas the k/n is close to 1 for most carbohydrate-derived compounds [26].

Some common side reactions are listed below. Other side reactions specific to major constituents of bio-oil will be presented later.

Thermal decomposition:



Methanation:



Boudouard reaction:



Compared with steam reforming of natural gas or naphtha, the steam reforming of bio-oil shows at least three features. First, higher operation temperature is necessary for an efficient conversion due to the presence of compounds with lower reforming activity (e.g. phenolic oligomers). Second, catalyst deactivation during bio-oil reforming is much more severe. The bio-oil contains a variety of oxygenates, which are easily decomposed and form solid carbonaceous deposits on the catalyst, resulting in catalyst deactivation. Third, the bio-oil steam reforming goes through

much more complicated reaction channels with various intermediates being produced due to the complex chemical composition of bio-oil [33].

(2) Steam reforming of aqueous fraction of bio-oil

As presented in Section 2.2.4, the bio-oil can be easily separated into an aqueous fraction and a hydrophobic fraction by adding water. The presence of the hydrophobic fraction in bio-oil lowers its steam reforming performance from the following aspects. The hydrophobic fraction, which is mainly made up of phenolic oligomers, cannot be easily vaporized without significant coke formation. Experiments also showed that the carbon deposition in steam reforming of the hydrophobic fraction was more severe than that of the aqueous fraction [92]. In addition, a higher temperature is required for the steam reforming of the hydrophobic fraction (800°C) than that for the aqueous fraction (650 °C). Moreover, delivering the feedstock and the water separately into a reformer is required for the steam reforming of bio-oil whereas the aqueous fraction can be mixed with water to make a solution before being fed to the reformer. To conclude, the aqueous fraction is more favourable to be steam reformed than the whole bio-oil. The isolated hydrophobic phase can be used as phenol replacement for adhesive resin production or upgraded to transport fuel by catalytic hydro-treatment.

Similar to the whole bio-oil, the steam reforming of aqueous fraction also involves a complex reaction network due to its heterogeneous composition. A thorough understanding of both thermally induced cracking and catalytic steam reforming reactions of bio-oil model compounds can guide the selection of catalysts and operating conditions for the steam reforming of bio-oil or its aqueous fraction.

2.3.2.2 Steam reforming of acetic acid

Acetic acid has been extensively tested in a catalytic steam reforming process as a model compound of bio-oil. This is because the presence of acetic acid in bio-oil is common and its content is high.

(1) Reaction mechanism of acetic acid steam reforming

Wang et al. [93] have proposed a reaction mechanism for acetic acid steam reforming (**Figure 2.5**, R2.15). The acetic acid molecule is dissociatively adsorbed on metal sites of a catalyst. The adsorbed acetate species $(\text{CH}_3\text{COO})_{\text{ads}}$ then

decarboxylate to form an adsorbed methyl radical species $(\text{CH}_3)_{\text{ads}}$. The $(\text{CH}_3)_{\text{ads}}$ species undergo the same reaction pathway as for CH_4 steam reforming, being gasified by adsorbed steam to produce CO and H_2 .

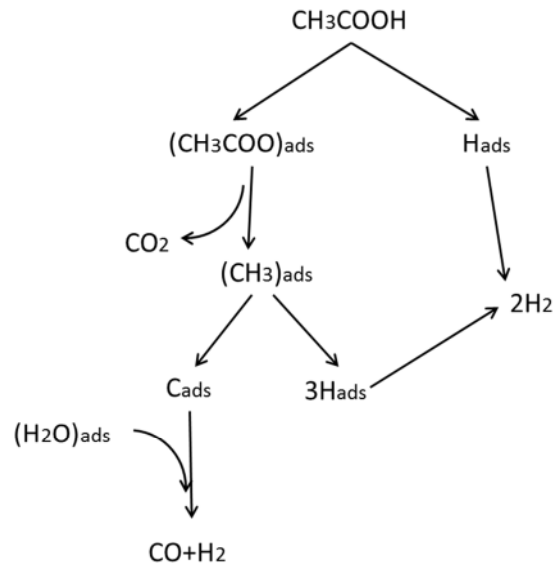
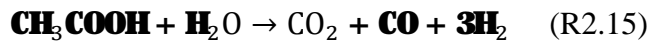


Figure 2.5 Schematic diagram of acetic acid steam reforming reaction [93]

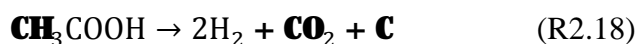


The overall reaction of acetic acid steam reforming and WGS reactions:



(2) Possible side reactions

The $(\text{CH}_3)_{\text{ads}}$ species may combine with H_{ads} to form CH_4 or accumulate to form coke. Hence, two common side reactions are as below.



Apart from the catalytic steam reforming route, the thermal decomposition of acetic acid and subsequent secondary reactions are also common. Hence, a complex reaction network is formed (**Figure 2.6**, the steam reforming reactions of intermediates are not shown).

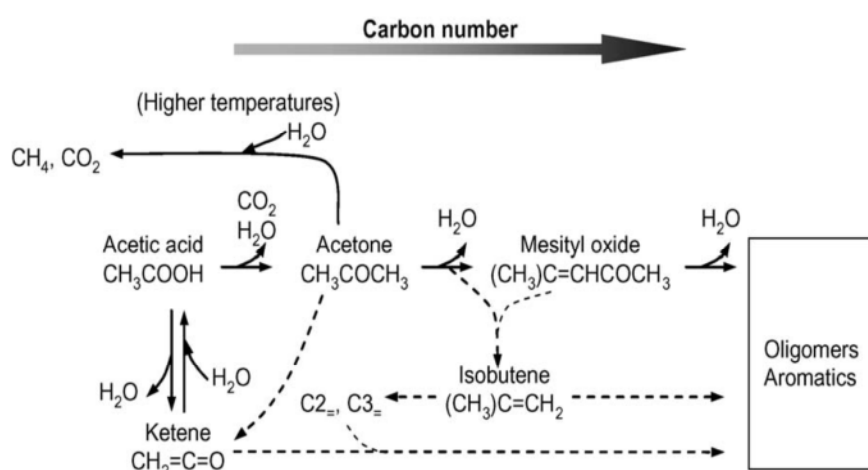
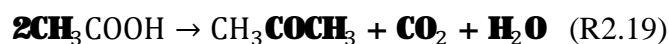
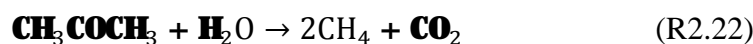
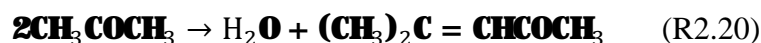


Figure 2.6 Thermal decomposition of acetic acid and subsequent secondary reactions [94]

Route one: ketonization



The ketonization reaction is known to take place on polycrystalline oxides, and numerous metal oxides (e.g. Al_2O_3 , ZrO_2) have been found to promote it [93]. The presence of Ni on metal oxide surface can suppress this reaction [95]. The acetone formed undergoes aldol condensation to form mesityl oxide (MO) (R2.20), which is an important coke precursor (via polymerization). The acetone may also undergo decomposition reactions (R2.21 and R 2.22).



Route two: dehydration to form ketene



R2.23 and R2.17 are two competing reactions for homogeneous decomposition of acetic acid [96]. The presence of steam suppresses acetic acid dehydration due to its

reversible nature [96]. The ketene formed undergoes R2.24 to form ethylene. Coke can be produced from ethylene by polymerization or cracking.



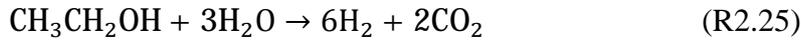
(3) Catalysts for acetic acid steam reforming

The complete conversion of acetic acid was reported to occur at temperatures between 400-800 °C, depending on catalysts and operating conditions used. Rapid coking was observed at temperature below 650 °C when using commercial Ni catalysts which are originally designed for naphtha steam reforming [25]. Various catalysts were investigated for the steam reforming of acetic acid. Results showed that Ni catalysts exhibited a high activity and a good selectivity to H₂, even better than noble metal catalysts in some cases. The order of activity was 17%Ni/Al₂O₃ > 0.5%Rh/Al₂O₃ > 1%Ru/Al₂O₃ > 1%Pd/Al₂O₃ > 1%Pt/Al₂O₃ [97]. Nevertheless, the noble metals are less prone to carbon formation. For Al₂O₃ supported base metals, the order of decreasing activity was Ni>Co>Fe>Cu [98]. Ni and Co catalysts showed catalytic activity for acetic acid steam reforming while Fe and Cu catalysts presented negligible activity. The difference was attributed to their different cracking abilities towards C-C and C-H bonds. Ni catalysts exhibited a better resistance to carbon deposition and metal oxidation than Co catalysts. The effects of a series of promoters (Li, Na, K, Mg, Fe, Co, Zn, Zr, La) on the performance of a Ni/Al₂O₃ catalyst was evaluated in acetic acid steam reforming reaction [99]. It was found that the addition of K reduced the CH₄ formation by inhibiting methanation reactions, increased the number of metallic Ni sites by promoting the reduction of NiO and enhanced the catalyst stability by suppressing coke formation [100]. In the aspect of catalyst support, Ce_{1-x}Zr_xO₂ was investigated widely as a promising candidate because it had high oxygen vacancy and oxygen mobility which inhibited carbon formation [101].

2.3.2.3 Steam reforming of ethanol

Steam reforming of ethanol has been extensively studied in the context of producing high-purity H₂ from bio-ethanol for fuel cell applications [102-104]. Bio-ethanol is a mixture of ethanol and water, which is obtained from the fermentation of biomass, such as sugarcane, corn or cellulosic feedstock. Compared with steam reforming of

CH₄ or acetic acid, the steam reforming of ethanol can be performed at relatively low temperatures (around 450 °C). This feature favours the decrease in CO product caused by favourable water gas shift, leading to the production of a H₂-rich gas.



In addition to the ethanol steam reforming and WGS reactions (R2.25), there are some other side reactions [33, 103, 105-107] as shown in **Figure 2.7**. The common by-products include acetaldehyde, ethylene, methane, and acetone.

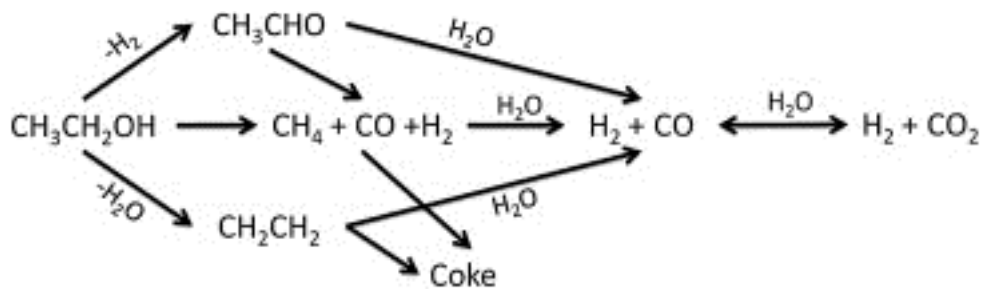
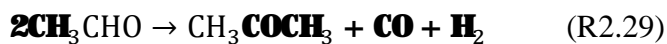
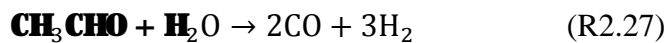
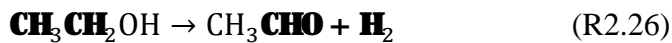


Figure 2.7 Reaction network during ethanol steam reforming proposed by ref. [106] and adapted from ref. [33]

(1) Dehydrogenation to acetaldehyde



Sahoo et al. [105] and Song et al. [102] suggested that both the steam reforming and the decomposition of ethanol occur through acetaldehyde intermediates which are produced by R2.26. The acetaldehyde subsequently undergoes decomposition (R2.28) or steam reforming (R2.27). Frusteri et al. [108] proposed a reaction mechanism in which the ethanol steam reforming is actually a combination of

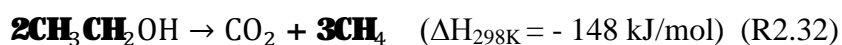
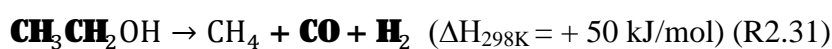
ethanol decomposition (R2.31) and steam reforming of the decomposition product CH₄. Acetone is produced via the recombination of acetaldehyde (R2.29) [33].

(2) Dehydration to ethylene



Ethylene can be formed through R2.30 over both acidic and basic supports. In general, the acidic support (e.g. Al₂O₃) has a higher selectivity to ethylene than the basic support (e.g. MgAl₂O₄) [109].

(3) Decomposition



(4) Catalysts for ethanol steam reforming

Major concerns of ethanol steam reforming are the fast coke formation and the formation of by-products such as CH₄ and acetaldehyde. Ni, Co, Ni/Cu and noble metal (Rh, Pt, Pd) catalysts have shown good catalytic activity for ethanol steam reforming. The Co/Al₂O₃ catalyst exhibited a high selectivity to H₂ by suppressing methanation and decomposition reactions [110]. Rh catalyst was found to be resistant to coke formation [108]. Rh catalyst was also found to be twice as active as Ni catalyst in terms of C-C bond cleavage [102], which could be attributed to the formation of an oxametallacycle intermediate on the Rh metal surface [111]. The catalytic activity of Ni catalyst was found to be comparable with noble metal catalysts while the resistance to carbon formation was not as good as noble metal catalysts, similar to the steam reforming of natural gas or acetic acid [112]. Since Ni catalyst is less active for WGS while Cu catalyst is a commonly used low-temperature shift catalyst, the combination of Ni and Cu catalysts exhibited a good performance (the production of CO and coke was decreased) [113, 114]. Al₂O₃ is a widely used support material of the catalyst for ethanol steam reforming. However, coke is easily formed as Al₂O₃ induces ethanol dehydration (R2.30). The addition of basic metal oxides (MgO, CaO) to the Al₂O₃ support can partially reduce the coke formation. Textural modification of catalysts has also been attempted to achieve high catalytic performance in ethanol steam reforming. Xerogel-based nickel

catalyst exhibited a strong resistance to coke deposition and nickel sintering due to their mesoporous structure [115, 116]. Low diffusion restrictions and high dispersion of the active phases on the support was achieved by using the mesoporous structure [117].

2.3.2.4 Steam reforming of other oxygenates

In addition to acetic acid and ethanol, other oxygenates which are commonly found in bio-oil have also been tested in steam reforming process as a signal model compound of bio-oil. They include hydroxyacetaldehyde [93], ethylene glycol [118], acetone [118], acetol [119], ethyl acetate [118], glucose [25, 118], xylose [25], sucrose [25], m-cresol [25, 120], m-xylene [118], di-benzyl ether [25], methanol [121] etc. Molecular structures of these model compounds are shown in **Figure 2.8**.

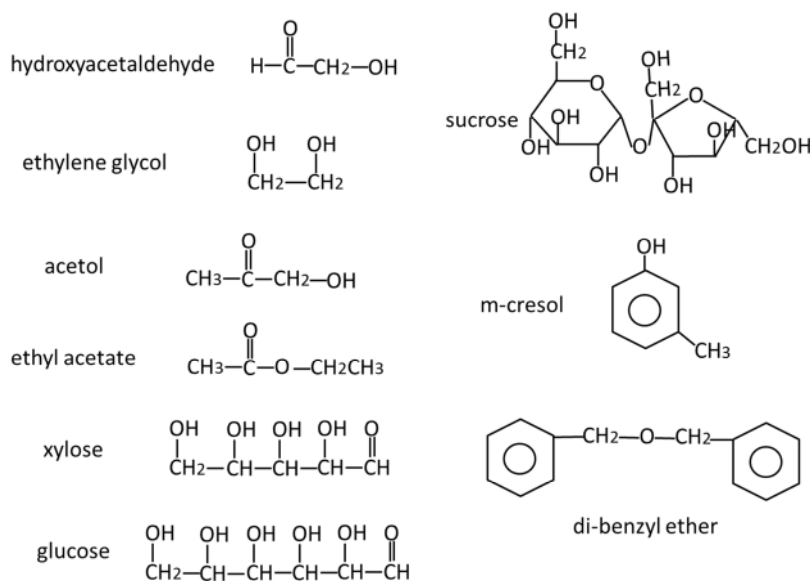


Figure 2.8 Molecular structures of bio-oil model compounds that were investigated in steam reforming processes in the literature

The effects of temperature and S/C ratio on the steam reforming performance of a series of model compounds were investigated in detail by Xu and Lu [118]. In general, elevated temperature and S/C ratio facilitate the conversion of the feedstock and the removal of by-products. Light oxygenates can reach high conversion at

relatively low temperature (400-500 °C). In contrast, higher temperature and more water feeding are required to reform heavy oxygenates such as ethyl acetate (720 °C) and m-xylene (650 °C). The carbon deposition from aromatic molecules (e.g. m-cresol) and long chain molecules (e.g. glucose) is more severe than small molecules. For both alcohols and ketones, the tendency of coke formation increases with the chain length. The reaction pathway for coke formation may vary with the feedstock. Decomposition or polymerization of the feedstock is the main route of coke formation during the steam reforming of glucose, m-xylene, and acetone. For the steam reforming of ethyl acetate, ethylene glycol, and acetic acid, carbon deposits are formed by reactions of by-products including ethylene, CO, or acetone.

The decomposition of sugars is the major barrier for the steam reforming of sugars. Because of the non-volatility of sugars, a nozzle is usually used to spray sugar solution into a reactor in laboratory experiments. After the solution is fed into the reactor, the water is vaporized and mixed with carrier gas flow while the sugar molecules quickly decompose to form char before contacting the catalyst bed [25]. High S/C ratios (e.g. above 10 for glucose and xylose) are required to gasify the char that has been deposited on the catalyst. However, the increase in the S/C ratio has no effect on changing the chemistry of char formation by homogeneous pyrolysis. In order to decrease sugar carbonization and improve the contact between the sugar and the catalyst, fluidized bed reactors are recommended [25].

For heavy organic compounds in bio-oil (e.g. aromatics, m-cresol), the formation of liquid pollutant (condensate) is another problem in addition to the carbon deposition [122]. It is difficult to convert the heavy compounds to gas completely even at high temperature and high S/C ratio. Some unreacted feedstock and intermediates may evolve from the reactor and become condensate. An operation of liquid condensate recycling was proposed by Wu and Liu [122] aiming at eliminating liquid pollutant and reducing carbon deposition.

2.4 Chemical looping technology

The working principle and basic configuration of chemical looping combustion (CLC) and chemical looping reforming (CLR) has been introduced in Chapter 1.

Both processes are based on the transfer of the oxygen from air to the fuel by means of a solid oxygen carrier.

The CLC is an innovative combustion technology for heat production which can feature subsequent easy CO₂ capture. The oxidation of reduced oxygen carrier occurring in an air reactor is always strongly exothermic. In most cases, the reduction of oxygen carrier with fuel occurring in a fuel reactor is endothermic except for CuO [13]. The net energy released from the whole reaction system is the same as that from the combustion of the fuel. Compared with conventional combustion, the CLC has two main advantages. First, the exhaust from the air reactor mainly consists of N₂ and unreacted O₂. NO_x is rarely formed since the oxidation of oxygen carriers takes place without flame and at a moderate temperature. Second, the gas from the fuel reactor consists of CO₂ and H₂O, without dilution with N₂. Thus, the CO₂ could be readily captured by condensing water vapour.

The CLR was proposed by Mattisson and Lyngfelt in 2001 [123] as an extension of the CLC concept. Actually, Lyon and Cole proposed a similar concept in 2000 using unmixed combustion to uniformly supply heat for steam reforming reaction [19]. The desired product of a CLR process is H₂ and CO (syngas) rather than heat. In some studies [124-126], the CLR was described as a partial oxidation process where oxygen carriers are used as a source of undiluted oxygen. The oxygen to fuel ratio should be kept low to prevent the complete oxidation of fuel to H₂O and CO₂. The oxygen carrier should be capable of converting fuel to CO and H₂ rather than CO₂, H₂O and unreacted fuel. In some other research [16, 19, 27, 50, 127], the CLR is essentially considered as an autothermal reforming process, which is also termed as 'unmixed steam reforming'. The process occurring in the fuel reactor includes first the combustion of fuel (meanwhile the oxygen carrier is reduced), and then the steam reforming of fuel catalysed by the reduced oxygen carrier. The heat required for the steam reforming reaction is supplied by the internal CLC of fuel. The advantages of a CLR process have been presented in Chapter 1 in comparison with conventional autothermal reforming. In this project, a CLR process refers to the advanced autothermal reforming process. Compared with the partial oxidation-based CLR, it makes full use of the heat from fuel combustion, produces syngas with a

higher H₂/CO ratio, and use moderate operation temperature (700 °C [16, 19, 27] vs. 950 °C [124-126])

Both CLC and CLR processes involve two critical issues which are the reduction reactivity of metal oxide with fuel and the carbon deposition on oxygen carrier.

2.4.1 Reduction reactivity of oxygen carrier with fuel

A key aspect of chemical looping technology is the selection of adequate oxygen carriers. A suitable oxygen carrier should exhibit good redox reactivity, thermal stability, sufficient oxygen transport capacity and high mechanical strength [13]. For a CLR process, it helps for the reduced oxygen carrier to have catalytic activity for the subsequent steam reforming reaction as well. The reactivity data and kinetic parameters of redox reactions of an oxygen carrier are important to the design of a chemical looping system, such as the solid inventory (how many kilograms of oxygen carrier is used per MW of power output) and the solid circulation rate between the air reactor and the fuel reactor [128-131].

The thermodynamic feasibility of using various metal oxides as oxygen carriers in a CLC system has been investigated by Mattisson and Lyngfelt [12]. It was concluded that metal oxides NiO, CoO, Fe₂O₃, Mn₃O₄ and Cu₂O are potential oxygen carriers. To increase their reactivity (specific surface area) and mechanical strength, oxygen carriers are usually prepared by depositing active metal oxides on refractory materials such as Al₂O₃, SiO₂, ZrO₂, TiO₂ or YSZ (yttria-stabilized zirconia) [13, 132].

The reduction reactivity of oxygen carriers based on NiO, CuO, Fe₂O₃ and Mn₃O₄ has been examined using CH₄, H₂, CO or syngas as reducing agents in a thermogravimetric analyzer [12, 48, 128-130]. It is generally believed that NiO is a promising oxygen carrier for both CLC and CLR processes using CH₄ as fuel due to its high reduction reactivity and good catalytic activity for steam methane reforming and reasonable activity for water gas shift. Cho et al. [133] found that Ni-, Cu-, and Fe-based oxygen carriers exhibited enough reactivity for their application in CLC system. However, Cu- and Fe-based oxygen carriers showed signs of agglomeration. NiAl₂O₄-supported NiO displayed the highest reduction rate but limited mechanical strength. Zafar et al. [14] tested the redox reactivity of a series of metal oxides

supported on SiO₂ using CH₄ as fuel in a CLR process. In general, the reduction reactivity was in the order NiO > CuO > Mn₂O₃ > Fe₂O₃. It was concluded that NiO seemed to be the most feasible oxygen carrier for a CLR process due to its high reduction reactivity and its selectivity to H₂, although temperatures exceeding 800 °C should be avoided. Apart from the active metal oxide, the support material used may also affect the reactivity of oxygen carriers [48, 133]. Refractory Al₂O₃ material has been widely used as the support of oxygen carriers [15]. However, the interaction between the active metal oxide and the support at high temperature leads to the partial transformation of NiO to spinel compound NiAl₂O₄, which impairs the reducibility of this oxygen carrier. The addition of MgO or CaO to the oxygen carrier can improve the reduction activity by forming MgAl₂O₄ and CaAl₂O₄ [49, 131]. Recently, the use of bimetallic oxygen carriers in chemical looping system has achieved promising results due to synergistic effects between the two metal oxides [134, 135]. Siriwardane et al. [136] have demonstrated that bimetallic oxygen carrier Fe-Cu/support exhibited a better stability and a higher reduction rate than Fe/support in the CLC process of syngas. Hossain and Lasa [135] suggested that the incorporation of a second metal Co to the Ni/Al₂O₃ could enhance its reducibility by influencing the metal-support interaction. Meanwhile, the addition of Co also improved its stability by minimizing the formation of NiAl₂O₄ and inhibiting metal particle agglomeration.

As the chemical looping technology is developed, the fuel applied to the chemical looping system is not just restricted to gaseous fuels (e.g. natural gas, or syngas from coal gasification). Some volatile liquid fuels derived from renewable resources (e.g. bio-oil [28], wasted cooking oil [17, 27], pyrolysis oil of scrap tyre [127], glycerol [18], sunflower oil [137]) have been tested in a CLR process. The CLC of solid fuels (e.g. coal, biomass, solid wastes) has also attracted great interest [29, 30, 138-140]. The use of coal in CLC is very promising in the near future, since coal remains a main energy source in many parts of the world that have little natural gas or crude oil reserves. In the case of using biomass as fuel, the CO₂ captured can result in negative emission. The selection of oxygen carriers depends on the fuel used. Supported NiO is a promising oxygen carrier for the CLC of CH₄ while CuO shows the best properties in the CLC process of coal [140].

Since the reaction between the oxygen carrier and the fuel is a crucial step in a chemical looping process, the study on the reduction of metal oxides with various reductants is of great importance. However, the literature in this field is quite scarce, which is summarized in Section 2.5.

2.4.2 Carbon deposition

Carbon deposition is another concern of chemical looping technology. It is desirable that an oxygen carrier shows resistance to net carbon formation. It was found that a Fe-based oxygen carrier is less prone to carbon deposition than Mn-, Cu-, and Ni-based oxygen carriers [13, 50, 141]. During CLR and CLC with CH₄ as fuel, solid carbon can be formed by either Boudouard reaction or hydrocarbon decomposition. Both can be catalysed by the reduced oxygen carrier (e.g. metallic Ni and Fe). In a CLC system, the carbon deposited on oxygen carrier is oxidized in the air reactor, resulting in a subsequent lower CO₂ capture efficiency. In a CLR system, the carbon deposited on the reduced oxygen carrier may impair its catalytic activity for steam reforming reaction and water gas shift. The carbon deposition behaviour is affected by reaction conditions. Thermodynamics calculations [123] revealed that low temperature, high pressure and low oxygen ratio (the actual amount of oxygen added in the form of metal oxide over the stoichiometric amount needed for the full conversion) are favourable for carbon formation during the CLC of CH₄. Experimental results also suggested that carbon deposits could be reduced by increasing the reaction temperature or adding steam or CO₂ to the fuel [48, 132, 142]. Cho et al. [141] investigated the carbon deposition on Ni- and Fe-based oxygen carriers to assess whether it had adverse effects on the CLC process. The strong dependence of carbon formation on the availability of oxygen was found on the Ni-based oxygen carrier. At the early stage, only minor amounts of carbon were formed. When more than 80% of the NiO was reduced to Ni, significant carbon formation started.

2.5 Reduction of metal oxides

2.5.1 Application fields

In Section 2.4, the importance of metal oxide reduction to a chemical looping system has been discussed. In addition to that, the reduction of metal oxides is also an important reaction in areas of metallurgy and heterogeneous catalysis.

(1) Metallurgy

In a process of extracting metal from its ore, metal oxide is first obtained through a series of treatments on its ore (e.g. concentration, roasting and smelting). Subsequently, the metal oxide is converted to metal via a reduction reaction. One of the most famous reduction processes for Ni production is the 'Mond Process', which has three steps. (i) NiO reacts with syngas to remove oxygen and leave impure Ni, (ii) impure Ni reacts with CO to form volatile nickel tetracarbonyl ($\text{Ni}(\text{CO})_4$), and (iii) $\text{Ni}(\text{CO})_4$ is decomposed at higher temperature to high purity Ni dust. In addition to using syngas as reductant, the use of CH_4 in Ni ore reduction has also been proposed as an economical and feasible route for countries with abundant natural gas resources [143]. Like Ni, Fe production also involves a reduction process. Traditional iron ore reduction is carried out in blast furnace using CO from partial combustion of coke. This method requires separate coke making (from coal) and sintering plants, which are considered as costly and polluting. Considering these drawbacks, direct reduction of iron ore (DRI) was proposed for using lower grade of coals in steel and iron manufacturing industry [144]. In the DRI process, iron oxide is reduced by volatiles released from coal volatilisation as well as CO generated from char gasification. The DRI technology finds a utilization opportunity for high volatile coals, which are otherwise useless in the steel industry. However, all these reduction processes mentioned above rely on the availability of fossil fuels and produce greenhouse gases. To meet these challenges, the concept of sustainable metallurgical operation was proposed [145], in which biomass is used as a substitution of fossil fuel-based reductants for mineral processing. The reduction of iron ore with biomass (sawdust [145], palm kernel shell [146]) or biomass char [32] has been reported. In contrast, few studies have been devoted on nickel ore reduction with biomass or compounds derived from biomass.

(2) Heterogeneous catalysis

A number of refining processes involve heterogeneous catalysis and rely on various catalysts. These catalysts are generally supplied in an inert form so that they can remain stable at atmospheric conditions and therefore safer during transport, storage and loading in the reactors. They require to be activated just prior to being used in the relevant catalytic processes, after reactor loading and isolation from undesirable potential oxidation sources. This activation procedure usually involves the reduction of metal oxide to metallic state or lower oxidised state. For example, nickel reforming catalysts are supplied as supported NiO and need to be reduced to metallic Ni (R2.33). High-temperature shift catalysts are supplied in the form of $\text{Fe}_2\text{O}_3/\text{Cr}_2\text{O}_3$ and need to be converted to Fe_3O_4 (R2.34). Low-temperature shift catalysts are supplied as supported CuO and need to be reduced to Cu (R2.35). Ammonia synthesis catalysts are supplied in the form of Fe_3O_4 and need to be reduced to metallic Fe (R2.36). These reduction processes require careful control to give the maximum activity of catalysts [147]. This is because reduction conditions such as reducing agent, temperature, duration, and the presence of steam may affect the properties of the active phase for the desired reaction. For the Ni reforming catalysts [8], the highest initial Ni surface area is obtained when the reduction is done using pure H_2 at the temperature of 600 °C. Below this temperature, reduction could be slow and incomplete. Above this temperature, some sintering may take place, which lowers the Ni surface area. The presence of steam lowers the Ni surface area as Ni sintering is enhanced by steam [8]. Excessive reduction period may also make Ni sintering more severe. In industry, natural gas, ammonia or methanol are also used for the reduction of reforming catalysts [147]. It is generally believed that the actual reductant species is H_2 , which can be formed via in situ cracking of these compounds. Hence, it is an advantage to ensure there is some H_2 present in the inlet feed gas together with these compounds. Otherwise, the top portion of catalyst bed may not be reduced properly and subsequently the effective catalyst volume is decreased. In the case of using CH_4 , a careful protocol of starting conditions with large excess of steam (steam carbon ratio is 7:1) is recommended in industry to avoid carbon deposits from CH_4 decomposition.



2.5.2 Kinetic models of metal oxide reduction

Kinetics of many solid state reactions can be expressed by Eq. 2.1 or its integral form Eq. 2.2, where α is the conversion fraction of solid reactant in time t , $d\alpha/dt$ is the rate of conversion with time, k is the reaction rate constant, and $f(\alpha)$ or $g(\alpha)$ represents the reaction mechanism. The commonly used kinetic models fall into three groups: (1) diffusion models, (2) geometrical contraction models and (3) nucleation and nuclei growth models (**Table 2.4**).

$$\frac{d\alpha}{dt} = k \times f(\alpha) \quad (\text{Eq. 2.1})$$

$$g(\alpha) = \int \frac{d\alpha}{f(\alpha)} = k \times t \quad (\text{Eq. 2.2})$$

Two common kinetic models for the reduction of metal oxides are nucleation model (or called nucleation and nuclei growth model, Avrami-Erofeyev model) and shrinking core model (or called contracting volume model, phase-boundary controlled model, one of the geometrical contraction models) [148]. These words ‘pellet’, ‘particle’, ‘grain’ and ‘crystallite’ are usually used to describe a solid reactant. To avoid confusion, the definition of these words in this thesis is as follows. The ‘grain’ or ‘primary particles’ refers to an aggregate of crystallites. The ‘pellet’ or ‘particle’ refers to an aggregate of grains and the ‘pellet’ could be made into different shapes such as slab, cylinder or sphere.

Table 2.4 Common kinetic models for solid state reaction [149-151]

model (symbol)	differential form $f(\alpha)=1/k \times d\alpha/dt$	integral form $g(\alpha)=kt$
nucleation model		
random nucleation (or first-order) (F1)	$1-\alpha$	$-\ln(1-\alpha)$
two-dimensional nuclei growth (A2)	$2(1-\alpha)[- \ln(1-\alpha)]^{1/2}$	$[- \ln(1-\alpha)]^{1/2}$
three-dimensional nuclei growth (A3)	$3(1-\alpha)[- \ln(1-\alpha)]^{2/3}$	$[- \ln(1-\alpha)]^{1/3}$
geometrical contraction model		
zero order (R1)	1	α
contracting area (R2)	$2(1-\alpha)^{1/2}$	$1-(1-\alpha)^{1/2}$
contracting volume (R3)	$3(1-\alpha)^{2/3}$	$1-(1-\alpha)^{1/3}$
diffusion model		
one-dimensional diffusion (D1)	$1/(2\alpha)$	α^2
two-dimensional diffusion (D2)	$-[1/\ln(1-\alpha)]$	$((1-\alpha)\ln(1-\alpha))+\alpha$
three-dimensional diffusion (D3)	$[3(1-\alpha)^{2/3}]/[2(1-(1-\alpha)^{1/3})]$	$(1-(1-\alpha)^{1/3})^2$
Ginstling-Brounshtein (D4)	$3/[2((1-\alpha)^{-1/3}-1)]$	$1-(2/3)\alpha-(1-\alpha)^{2/3}$

2.5.2.1 Nucleation model

The activation of gas reductant on the metal oxide surface is the first step of a reduction reaction mechanism. Subsequently, surface oxygen ions are removed from the lattice of the metal oxide by reduction, leaving behind anion vacancies. When the concentration of vacancies reaches a critical value, small clusters (or aggregates) of the reduced oxide (usually metal) are formed by rearrangement of the lattice. This process is called nucleation or nuclei formation. The small clusters of reduced oxide grow by the inward diffusion of the reduced metal ions and/or outward diffusion of the oxygen ions. This process is called nuclei growth. The reduced metal oxide with coordinatively unsaturated metal cations can activate gaseous reductant more readily

than the fully oxidized oxide. The increase in the size of the reduced oxide clusters (nuclei growth) leads to an increase in the supply rate of activated reductant to the oxide and hence an increase in the reduction rate. Upon the clusters of reduced oxide starting to coalesce, the reduction rate decreases with time. Eventually, an oxide core with a shell of reduced oxide is formed, from which the reduction follows a shrinking core model [148]. Correspondingly, the plot of reduction fraction (α) with respect to time has a sigmoidal shape, starting slowly, rising rapidly, and then levelling off again. The presence of an induction period (nucleation process) and the possibility of autocatalysis are two characteristics of this reduction kinetics.

The overall chemical reduction rate is determined by the rate of nucleation and nuclei growth as well as the concentration of potential nuclei-forming sites (also called germ nuclei). Either nucleation or nuclei growth or their combination is the rate-determining step. Among mathematical models derived from nucleation and nuclei growth mechanism, the Avrami-Erofeyev model [149, 152, 153] has achieved a wide application. This model was originally developed for phase transformations of steel, and then crystallization, precipitation and decomposition reactions. Recently, this model was used to study reduction kinetics of bulk or supported metal oxides [40, 151, 154].

The mathematical expression of Avrami-Erofeyev model is shown as follows

$$\text{Conversion-time function: } \alpha = 1 - \exp[-(kt)^n] \quad (\text{Eq. 2.3})$$

$$\text{Differential form: } f(\alpha) = n(1 - \alpha)[- \ln(1 - \alpha)]^{n-1/n} \quad (\text{Eq. 2.4})$$

$$\text{Integral form: } g(\alpha) = [- \ln(1 - \alpha)]^{1/n} \quad (\text{Eq. 2.5})$$

where n is the Avrami exponent. The value of n may relate to the reaction mechanism and nuclei growth dimensionality. The value of 1, 2 and 3 taken for n corresponds to random nucleation, two-dimensional nuclei growth and three-dimensional nuclei growth mechanisms, respectively [135].

The reduction kinetics of NiO with H_2 was described by the nucleation model properly. An induction period and the autocatalytic effect was first observed by Benton and Emmet in 1924 [155], who measured water formation as an indication of the reduction extent. They also concluded that the addition of water decreased the

reduction rate and increases the induction period. The presence of defects or alternative ions in the outer surface of NiO grains also influences the induction period. It is generally believed that the induction period is the generation of Ni nuclei. Following nucleation, Ni clusters grow two-dimensionally across the surface until they are large enough to initiate H₂ dissociation, at which point the reduction process accelerates autocatalytically [40].

Compared with the shrinking core model, the nucleation model was found to better fit the reduction kinetics of a bimetallic Co-Ni/Al₂O₃ oxygen carrier with H₂ (random nucleation mechanism) [135, 154] and of a CrO_x/Al₂O₃ catalyst with H₂ (instantaneous nucleation and two-dimensional nuclei growth mechanism) [151]. Considering the general applicability of nucleation model to reduction kinetics, the three-dimensional nuclei growth model (A3 model) is likely feasible for the reduction of certain bulk oxides. The applicability of two-dimensional nuclei growth (A2 model) is probably restricted to the reduction of supported oxides. This is because the supported oxide has a tendency to form large monolayer clusters. The amount of the oxide on the support may be an important parameter to determine which nuclei growth model is suitable [151].

2.5.2.2 Shrinking core model

Different from the nucleation model, this shrinking core model incorporates structural parameters, such as grain size and porosity. The shrinking core model assumes that the nucleation and nuclei growth processes are so quick that a uniform layer of reduced oxide is formed immediately. The oxide core shrinks with time as **Figure 2.9** shows.

The reduction rate is controlled by either chemical reaction at the phase boundary or the diffusion through the product layer. Szekely et al. [150] defined a parameter which could be used to distinguish which resistance plays a major role in the reaction system. If chemical reaction is the controlling process, a sharp boundary between the reacted and unreacted zones is assumed and hence the reduction rate is proportional to the surface area of the core. The reaction interface moves towards the core at a constant rate. In contrast with the nucleation model, an obvious characteristic of the shrinking core model is the absence of an induction period.

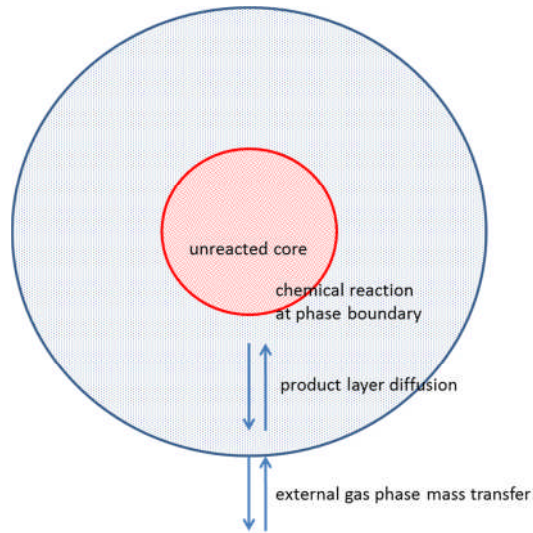


Figure 2.9 Schematic diagram of shrinking core model

Depending on the morphology and the porosity of the particles studied, the macroscopic shrinking core model and the microscopic shrinking core model are available. The macroscopic shrinking core model treats a whole particle as the study object [156, 157] while the microscopic shrinking core model focuses on individual metal oxide grains [41, 128, 130].

There are several assumptions for the use of the microscopic shrinking core model. (1) The internal diffusion (gas diffusion in pores of the particle) is not significant and the reducing gas can reach all the grains at the same time with the same probability. (2) The particle can be considered as isothermal during the reduction. (3) Individual grains are assumed to be non-porous. To make the experimental condition approach these assumptions, the particles studied should have large porosity and small size and are composed of large individual grains. The effect of particle size on the reaction rate can be used to check if the internal diffusion resistance limits the reduction rate [130]. Conversely, the macroscopic shrinking core model is applicable to the particles with small porosity and large size. In this case, the reaction rate is greatly affected by the particle size.

Shrinking core model has been successfully used to study the reduction of supported metal oxide with CH_4 , H_2 , or CO in fields of chemical looping combustion [128, 130, 156] and reforming catalyst activation [39].

2.5.3 Reduction mechanism with H₂, CO or syngas

The reduction mechanism of metal oxide with H₂ and CO has been clarified [148]. The first step is the activation of the reducing agent. If CO is used, it is most likely adsorbed onto a coordinatively unsaturated surface metal ion. This is followed by its reaction with the lattice oxygen to form a surface carbonate which decomposes to CO₂. Meanwhile the metal cation is reduced. If H₂ is used, it is dissociatively adsorbed on metal oxide surface to form a surface hydroxyl group. The hydroxyl group reacts with a hydride to produce water. In this way, the lattice oxygen of metal oxide is removed. According to this mechanism, the reduction of NiO prefers to occur at those sites that constitute defects and dislocations of a crystal [43].

The prevailing mechanism for bulk NiO reduction with H₂ was summarized [40]: (1) dissociation of H₂ (initially by NiO during the induction period, then by previously formed Ni), (2) surface diffusion of hydrogen atoms to a reduction centre, (3) rupture of Ni–O bonds to produce Ni atoms, (4) nucleation of Ni atoms into metallic Ni clusters, and (5) growth of Ni clusters into metal crystallites. Any one or combination of these steps, together with removal of water, may control the overall reaction rate.

Some differences may arise if NiO grains are deposited on support materials. Richardson et al. [39] proposed a mechanism in which Ni atoms are liberated through the reduction of NiO and then migrate across Al₂O₃ support until they reach a nucleation site. At the nucleation site, Ni atoms nucleate to Ni clusters and then the Ni clusters grow into crystallites. The migration of Ni atoms away from the reduction centre was verified by TEM observations which showed Ni crystallites cover a much larger fraction of Al₂O₃ surface than NiO [158]. The adsorbed water on the material surface inhibits the chemical reduction and the diffusion-controlled nucleation but does not affect the nuclei growth process. When the surface water retention was enhanced by adding promoters (CaO or MgO), the nucleation process was retarded more severely [159, 160].

2.5.4 Reduction mechanism with CH₄ and other light hydrocarbons

A radical formation and desorption mechanism was widely used to model the reduction of metal oxide with light hydrocarbons. Hydrocarbon molecules are

activated on the solid surface by the steps of adsorption, dissociation and the formation of radicals [161, 162]. These surface radicals either participate in a reduction reaction or leave the solid surface. The desorbed radicals may combine with each other or other gaseous species and then lose activity. A re-adsorption of radicals onto the solid surface was also observed in a porous supported catalyst [163-165]. Desorption and re-adsorption behaviour of radicals, which depends on the nature of the radicals and the solid surface, influences the overall reduction rate and relates to carbon deposition.

The influence brought about by the presence of porous support on the NiO reduction was investigated [166]. It was found that, in addition to chemical reaction and mass transfer, the fate and activity of radical species play a role in determining the reduction kinetics. Desorption of hydrocarbon radicals from solid surface significantly slows down the reduction rate of bulk NiO. In contrast, the presence of a rigid porous silica support hinders the radical desorption. Therefore, the ease with which a radical migrates from its generation site on a metallic island to the Ni-NiO boundary is an important rate-determining factor for the reduction of supported NiO.

2.5.5 Reduction mechanism with solid carbonaceous materials

2.5.5.1 Pure carbon

A number of theories have been proposed to explain the reduction mechanism of metal oxide with pure carbon (e.g. graphite, carbon black). There are some conflicting views, regarding product layer diffusion and reduction products.

(1) Diffusion direction

Siriwardane et al. [138] suggested that metal oxide first dissociates into metal and oxygen and consequently the oxygen reacts with carbon. However, Sharma et al. [44] thought that the reduction proceeds as carbon atoms diffuse through the product layer previously formed.

(2) Reduction products

Previous studies indicated that metal oxide is reduced by carbon to form CO which then reacts with metal oxide to produce CO₂. CO is an important intermediate for

CO₂ formation. However, Sharma et al. [44] suggested that both CO₂ and CO are primary products of NiO-carbon reaction.

(3) Carbon gasification reaction (reverse Boudouard reaction)

Carbon gasification reaction (R2.37) is an important reaction during metal oxide reduction with carbon. Through this reaction, CO with higher reducing ability than solid carbon is produced. Once this reaction is initiated, the reduction mechanism changes from solid-solid reaction to gas-solid reaction. The reduction product CO₂ (R2.38) reacts with carbon to produce more CO. A cycle (the regeneration of CO and CO₂) is built by these two reactions. Two examples involving this reduction mechanism are shown below.



The reduction of synthetic ilmenite with graphite was studied by TGA [45]. The reduction was initiated near 860 °C at the contact points between the reactants. The main reduction mechanism is the solid-solid reaction in the range of 860 to 1020 °C ($E_a=359$ kJ/mol). When the temperature was above 1020 °C, an increase in the reduction rate was observed, which was attributed to the change of reducing agent from carbon to CO ($E_a=268$ kJ/mol).

The mechanism of CuO reduction with coal char was investigated using TGA-MS technique [30]. The direct reduction of CuO by coal char occurred with onset temperatures as low as 500 °C. As the temperature increased, the reactivity of carbon gasification was improved and the gasification product CO became the main reducing agent for CuO reduction.

2.5.5.2 Coal, biomass and other solids

The reduction of metal oxides by solid fuels especially coal has attracted attention recently for its application in the direct CLC technology of solid fuels and the DRI technology.

A two-step mechanism is common for the reduction of metal oxides with solid carbonaceous materials. In the first step, the reducing gases (H₂ and/or CO)

produced from direct metal oxide reduction with carbon [30, 32], coal devolatilization [30, 167] or biomass pyrolysis [31] initiate the reduction reaction. In the second step, the regeneration of reducing gases via carbon gasification with products CO_2 and H_2O (R2.37 and 2.39) sustains the reduction. Therefore, solid carbonaceous materials containing high volatile matters would be favourable for the reduction [30].

The mechanism mentioned above involves gaseous intermediates (H_2 and/or CO). However, Siriwardane et al. [138] suggested that volatiles are not necessary for the CuO -coal reduction system. A ‘fuel-induced oxygen release’ mechanism was reported by them. In this mechanism, oxygen is released from CuO decomposition and then reacts with carbon. The carbon in close contact with CuO can induce Cu-O bond breaking, resulting in a lower reduction temperature. Surface melting of Cu and wetting of carbon contribute to the solid-solid contacts.

2.6 Conclusions

Biomass, as an important renewable resource, has been widely exploited for the production of chemicals, fuels and power, especially through thermochemical conversion technologies such as pyrolysis and gasification. Fast pyrolysis is a promising route for the production of liquid bio-fuels as a high yield of bio-oil (70-75% of the dry biomass) can be obtained and related techniques have reached maturity. However, the characteristics of bio-oil such as high oxygen content, high water content, wide volatility distribution and acidity restrict its direct use as transport fuel. At present, the utilization of bio-oil in transportation can be implemented by adding bio-oil to fossil diesel or bio-diesel. Another important application of bio-oil is for H_2 production by catalytic steam reforming and the subsequent water gas shift reactions.

H_2 production is important not only for the production of fertilizer at present but also for the establishment of hydrogen economy in the future. Currently, H_2 is mainly produced from fossil fuels using various thermal processes. Catalytic steam reforming of natural gas is the most used industrial process for H_2 production. Recent research of natural gas steam reforming mainly focuses on sorption enhanced

steam reforming (SESR) and membrane reactor. Both techniques are for in situ CO₂ separation and then the direct production of a H₂-rich gas by taking the advantage of process intensification.

Biomass pyrolysis and then steam reforming of the pyrolysis oil (bio-oil) seems to be a potential approach for sustainable H₂ production. However, the steam reforming of bio-oil undergoes complicated reaction channels and has a large tendency to form carbon deposits due to the complex chemical composition. The bio-oil is a complex mixture of water and various oxygenated hydrocarbons (carboxylic acids, alcohols, aldehydes, ketones, furans, sugars, phenols, etc.). In order to understand the steam reforming performance of the whole bio-oil, the performance of bio-oil model compounds (acetic acid, ethanol, glucose, acetone, acetol, m-cresol, m-xylene, di-benzyl ether, hydroxyl-acetaldehyde, ethylene glycol, ethyl acetate, xylose, sucrose, etc.) has been investigated with emphasis on the reaction network and process features (such as the tendency of coke formation, the reaction pathway for coke formation, suitable operation conditions).

Recently, some renewable liquid fuels (bio-oil, glycerol, vegetable oil, pyrolysis oil of scrap tyre) have been tested in a CLR process as the CLR configuration has advantages of internal heat supply, cyclic catalyst regeneration and easy integration with in situ CO₂ adsorption. Whether the reforming fuel employed is able to reduce the oxygen carrier (supported metal oxide) at the beginning of fuel feed is critical to the subsequent steam reforming reaction. Previous studies in this area mainly focused on screening suitable metal oxides based on their reduction reactivity with CH₄. It was found that supported NiO is a promising oxygen carrier due to its good reduction reactivity and catalytic activity towards steam reforming reaction. The reducibility of NiO/Al₂O₃ could be enhanced by adding alkali earth metal oxides to stabilize the support or incorporating a second metal (e.g. Co) to form bimetallic oxygen carrier. The carbon deposition occurring in the fuel reactor is another concern of a CLR process. It was found that the carbon deposition depends on the nature of active metal oxide (Fe-based oxygen carrier has a less tendency to form carbon) and the availability of oxygen in the lattice of metal oxide or the surrounding atmosphere. To the author's knowledge, few studies have been devoted to the performance of individual bio-compound derived from bio-oil in a CLR

process. The investigation on the reducing ability of bio-compounds as well as their influence on the catalytic activity of reduced metal oxide is rare in the literature, but quite significant to the potential application of bio-oil in a CLR process.

For the reduction of metal oxide, which is also important reaction in fields of heterogeneous catalysis and metallurgy, the commonly used reducing agents include H₂, CO, CH₄ and carbon. Related reduction mechanisms have been investigated, which normally involve surface adsorption, activation and radical formation. The reduction kinetics are usually described using nucleation models or shrinking core model. With the development of DRI technology and the use of solid fuels in CLC, some solid carbonaceous materials such as coal, biomass and solid wastes have emerged as reducing agents. The understanding of the reduction mechanism is carrying on but still far from completion. A two-step mechanism which involves the formation of reducing gases from solid carbonaceous materials and the regeneration of reducing gases by carbon gasification is usually suggested. The reduction process of supported NiO with solid bio-compounds (e.g. glucose and citric acid) has not been investigated. Such a study will help to understand the complicated reaction process when using biomass as reducing agent.

Chapter 3

Experimental materials, reactor set-up and methodology

3.1 Experimental materials

3.1.1 Steam reforming catalyst

The catalyst used in this project is 18 wt% NiO supported on α -Al₂O₃ (NiO/ α -Al₂O₃), which was supplied in pellet form by Johnson Matthey Plc as shown in **Figure 3.1**. It has a bulk density of 1100 kg/m³, and average crush strength of 735 N. The NiO/ α -Al₂O₃ catalyst pellets were crushed and sieved to particle size of 1.0-1.4 mm prior to being used in packed bed reactor experiments. These catalyst particles have a density of 3946 kg/m³ and a surface area of 2.5 m²/g [168].

Blank α -Al₂O₃ pellets, which were also provided by Johnson Matthey Plc., were crushed into the same particle size for the use in control experiments.



Figure 3.1 Images of catalyst pellet (left) and catalyst particles (right) used in this project

3.1.2 Bio-compounds

The bio-compounds used in packed bed reactor experiments include acetic acid, ethanol, acetone, glucose and furfural, which represent five common chemical

families of bio-oil (acids, alcohols, ketones, sugars and furans). In addition, glucose and citric acid were chosen as representatives of solid bio-compounds and used in TPR experiments of the NiO/ α -Al₂O₃ catalyst. This is because glucose is the basic building block of cellulose (a major biomass component) and citric acid naturally exists in a variety of fruits and vegetables. All the bio-compounds used had a purity of > 99%. Related physical properties of these bio-compounds are shown in **Table 3.1** and **Table 3.2**. Their molecular structures are shown in **Figure 3.2**.

Table 3.1 Basic physical properties and suppliers of the liquid bio-compounds used in this work

Bio-compound	molecular formula	Boiling point (°C)	Density (g/cm³)	Water solubility	Supplier
acetic acid	C ₂ H ₄ O ₂	118	1.049	miscible	Sigma-Aldrich
ethanol	C ₂ H ₆ O	78.37	0.789	miscible	Sigma-Aldrich
acetone	C ₃ H ₆ O	56	0.791	miscible	Fisher Scientific
furfural	C ₅ H ₄ O ₂	162	1.16	8.3g/100mL	Sigma-Aldrich

Table 3.2 Basic physical properties and suppliers of the solid bio-compounds used in this work

Bio-compound	Molecular formula	Meting points (°C)	Density (g/cm³)	Water solubility (g/100 mL)	Supplier
D-glucose, anhydrous	C ₆ H ₁₂ O ₆	146-150	1.54	90.9	Fisher Scientific
citric acid	C ₆ H ₈ O ₇	153	1.66	147.76	Fisher Scientific

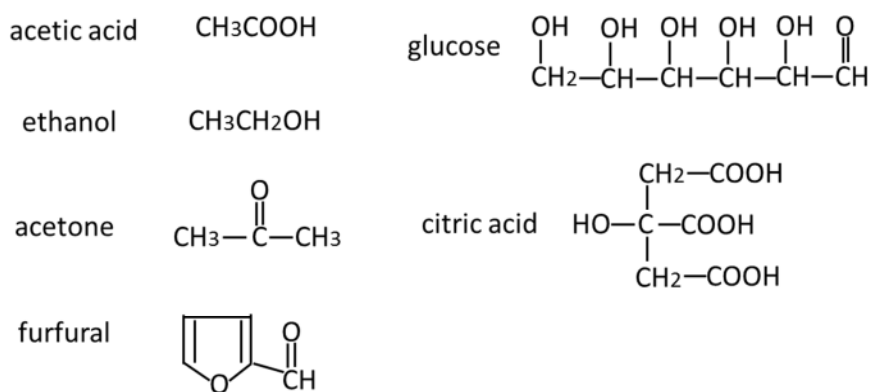


Figure 3.2 Molecular structures of the bio-compounds investigated in this project

3.2 Packed bed reactor set-up and operation procedure

The packed bed reactor set-up used in this project (**Figure 3.3**) was composed of six functional modules: reactor, liquid feeding, gas feeding, temperature control, cooling system, outlet gas analysis. (1) The reactor was made of quartz with an inner diameter of 12 mm and the length of 49.5 cm. It was manufactured by Yorlab Company. (2) During experiments, the reactor was held inside a tube furnace (Elite Thermal Systems Ltd. TSV12/50/300). The temperature of the furnace was regulated by a Eurotherm 2416 temperature controller. The temperature of the reactor, which may be slightly different from that of the furnace, was monitored in real-time by a K-type thermocouple as shown in **Figure 3.3**. The reaction temperature mentioned hereafter refers to the reactor temperature. (3) The liquid feeding (the injection of bio-compounds and water into the reactor) was performed by programmable syringe pumps (New Era Pump Systems). (4) The gas feeding to the reactor was controlled by MKS mass flow rate controllers. (5) The gaseous products from the reactor were cooled down by a condenser. A coolant (ethylene glycol and water in volume ratio of 1:1) at $-5\text{ }^\circ\text{C}$ was circulated between the condenser and a chiller (Fisher Scientific 3016S) to maintain the condenser at a low temperature. Condensable gas products and unreacted water were trapped in a condensate collector, with residual moisture later removed by silica gel. (6) The composition of the dry outlet gas was measured by Advanced Optima gas analyser

from ABB and recorded online at 5 second intervals. The ABB gas analyser consisted of three analyser modules: Uras 14, Caldos 15 and Magnos 106. The Uras 14 was capable of detecting CH₄, CO₂ and CO based on infrared absorption principle. The Caldos 15 was used for H₂ measurement by thermal conductivity. When required, the concentration of O₂ was measured by a Magnos 106 paramagnetic analyser module. A micro gas chromatograph (GC, equipped with MS5 and PPQ columns purchased from Agilent) was used following the ABB gas analyser to detect other possible hydrocarbon gases C₂ (C₂H₄, C₂H₆) and C₃ (C₃H₆, C₃H₈). Both MS5 and PPQ columns were equipped with thermal conductivity detectors (TCD).

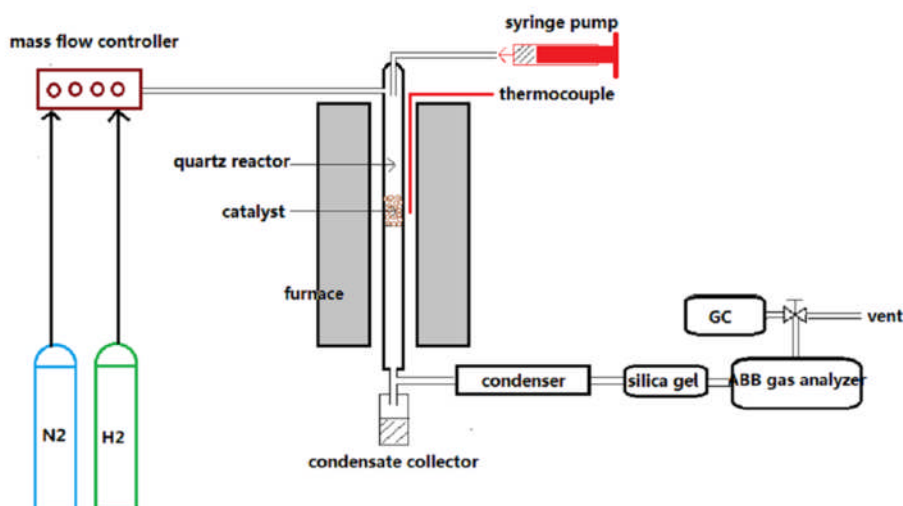


Figure 3.3 Schematic diagram of a packed bed reactor set-up

For each run of experiment, 2 g of fresh catalyst was placed in the middle of the quartz reactor. The 2 g of catalyst typically occupied 2 mL volume in the reactor. Around 1.7 g of α -Al₂O₃ balls (3 mm in diameter) was added on the top of the catalyst bed as pre-heater when using furfural as feedstock. For the other bio-compounds, no precautions were taken below or above the catalyst bed. The experimental process was carried out at atmospheric pressure under a continuous N₂ flow of 200 sccm and in the absence of air. When the reactor was heated to a set

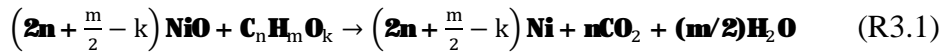
temperature, the liquid feedstock was fed into the reactor at a certain flow rate (**Table 3.3**). For water-soluble bio-compounds (acetic acid, ethanol, acetone and glucose), an aqueous solution of bio-compound was made first and then injected into the reactor by one syringe pump. Different molar steam to carbon ratios (S/C) were achieved by changing the molar ratio of water to bio-compound in the solution. The insoluble bio-compound furfural and water were fed into the reactor separately by two syringe pumps. Different S/C ratios were achieved by setting the flow rates of furfural and water. The flow rate of carbon equivalent (the flow rate of bio-compound multiplied by the number of carbon atoms in the bio-compound molecule) was kept at around 1.174 mmol/min for all the bio-compounds except for glucose. Previous studies [25, 118] reported that the steam reforming of glucose had a larger tendency to form coke and required higher S/C ratios than other bio-compounds. Therefore, the carbon equivalent input of glucose in this project was 0.6061 mmol/min and the S/C ratio (4.5-9) investigated was larger than that for the other bio-compounds (1-5).

Table 3.3 Flow rates of liquid feedstock into the packed bed reactor

Bio-compound	carbon equivalent (mmol/min)	Fuel (ml/min)	Solution or Water (ml/min)			
			S/C1	S/C2	S/C3	S/C5
acetic acid	1.1749	n/a	0.0552	0.0768	0.0984	0.1416
ethanol	1.1732	n/a	0.0558	0.0774	0.0990	0.1422
acetone	1.1755	n/a	0.0503	0.0719	0.0935	0.1367
furfural	1.1740	0.0194	n/a	0.0424	0.0637	0.1061
			S/C4.5	S/C6	S/C7.5	S/C9
glucose	0.6061	n/a	0.0636	0.0750	0.0966	0.1100

3.3 Elemental balance and definition of process outputs

In a typical packed bed experiment, the reduction of NiO (R3.1) and the steam reforming of bio-compound (R2.11) are two main reactions. Here, $C_nH_mO_k$ represents a generic formula of bio-compound. The reaction (R3.1) merely shows the global mechanism of production of Ni, CO₂, and H₂O observed in experiments (see Chapter 6 and 7) and in thermodynamics calculation (see Chapter 4). The actual reduction may involve a more complex mechanism such as the formation of intermediates CO and H₂.



The initial data include:

- (1) The molar fraction of CO₂, CO, CH₄, and H₂ in the dry outlet gas measured by ABB gas analyser
- (2) The molar fraction of C₂ (C₂H₄, C₂H₆) and C₃ (C₃H₆, C₃H₈) hydrocarbons in the dry outlet gas measured by GC
- (3) The flow rate of water, carrier gas N₂, and bio-compound
- (4) The mass of the catalyst used in each run and the NiO loading in the catalyst

Process outputs that are desired include:

- (1) The reduction rate of NiO to Ni
- (2) The conversion fraction of water or bio-compound
- (3) Gas yields

These data could be obtained through elemental balance calculation and some reasonable assumptions [169]. Related parameter symbols are defined as follows.

Nomenclature:

n_i : flow rate of species i in mol/s

y_i : molar fraction of species i in the dry outlet gas

X_i : conversion fraction of species i

$$y_{C_2} = y_{C_2H_4} + y_{C_2H_6}$$

$$y_{C_3} = y_{C_3H_6} + y_{C_3H_8}$$

n : the number of carbon atoms in bio-compound molecule

m : the number of hydrogen atoms in bio-compound molecule

k : the number of oxygen atoms in bio-compound molecule

M_{bio} : the molecular weight of bio-compound $C_nH_mO_k$

M_{H_2} : the molecular weight of H_2

The subscript ‘dry’, ‘in’, and ‘out’ refer to conditions following water removal, at reactor inlet and outlet, respectively.

The molar flow rate of total dry outlet gas ($n_{out,dry}$) was estimated based on nitrogen balance (Eq. 3.1). The molar flow rate of N_2 (n_{N_2}) was maintained at 1.386×10^{-4} mol/s, equivalent to a volume flow rate of 200 sccm (sccm or standard cubic centimetre per minute = cm^3/min at 293 K and 1 atm) during the experimental process.

$$n_{out,dry} = \frac{n_{N_2}}{1 - y_{CH_4} - y_{CO} - y_{CO_2} - y_{H_2} - y_{C_2} - y_{C_3}} \quad (\text{Eq. 3.1})$$

The conversion fraction of bio-compound (X_{bio}) to gases was calculated based on a carbon balance, dividing the total molar flow of carbon in the gaseous products by the molar flow of carbon in feed, as described in Eq. 3.2.

$$X_{bio} = \frac{n_{out,dry} \times (y_{CO} + y_{CO_2} + y_{CH_4} + 2y_{C_2} + 3y_{C_3})}{n \times n_{bio,in}} \quad (\text{Eq. 3.2})$$

The H_2O conversion fraction (X_{H_2O}) and the yield of H_2O (in mol/mol carbon feed) during reduction are calculated on a basis of hydrogen balance (Eq. 3.3 and Eq. 3.4).

$$X_{H_2O} = \frac{n_{out,dry} \times (4y_{CH_4} + 2y_{H_2} + 4y_{C_2H_4} + 6y_{C_2H_6} + 6y_{C_3H_6} + 8y_{C_3H_8}) - m \times n_{bio,in} \times X_{bio}}{2 n_{H_2O,in}} \quad (\text{Eq. 3.3})$$

$$H_2O \text{ yield} = \frac{m \times n_{bio,in} \times X_{bio} - n_{out,dry} \times (4y_{CH_4} + 2y_{H_2} + 4y_{C_2H_4} + 6y_{C_2H_6} + 6y_{C_3H_6} + 8y_{C_3H_8})}{2 \times n \times n_{bio,in}} \quad (\text{Eq. 3.4})$$

The yield of gas i is defined as the moles of gas i produced per mole of carbon feed (Eq. 3.5).

$$\text{gas yield (mol/mol carbon feed)} = \frac{n_{out,dry} \times y_i}{n \times n_{bio,in}} \quad (\text{Eq. 3.5})$$

Gas concentration of species i is defined as the molar fraction of i in dry outlet gas divided by the sum of molar fractions of all the product gases (excluding N_2).

The mass yield of H_2 is defined as the mass of H_2 produced with respect to the mass of bio-compound input (Eq. 3.6).

$$H_2 \text{ yield (wt\%)} = 100 \times \frac{M_{H_2} \times n_{out,dry} \times y_{H_2}}{M_{bio} \times n_{bio,in}} \quad (\text{Eq. 3.6})$$

On the basis of an oxygen balance, Eq. 3.7 was used to estimate the rate of NiO reduction to Ni.

$$\text{reduction rate} = n_{out,dry} \times (y_{CO} + 2y_{CO_2}) - n_{H_2O,in} \times X_{H_2O} - k \times n_{bio,in} \times X_{bio} \quad (\text{Eq. 3.7})$$

The total moles of NiO reduced to Ni over a given duration were obtained from the time integration of the above rate equation. The conversion extent of NiO to Ni (or ‘extent of reduction’) was then shown as a fraction of the initial moles of Ni present in catalyst.

When required, after the fuel feed, air was switched on to combust carbon deposits in the reactor. The total amount of carbon (on the catalyst and the reactor wall) was then calculated based on a carbon balance and the time integration of the carbon removal rate (Eq. 3.8).

$$\text{carbon removal rate} = n_{out,dry} \times (y_{CO} + y_{CO_2}) \quad (\text{Eq. 3.8})$$

3.4 Characterisation and analysis methods

3.4.1 TGA-FTIR

Thermal gravimetric analysis (TGA) provides quantitative information on the mass change of a sample as a function of time or temperature as the sample is subjected to a programmed heating (defined by heating ramps and plateaus of set temperatures) under a specific gas atmosphere. Fourier transform infrared spectroscopy (FTIR) is a technique that is used to obtain an infrared absorption spectrum of a sample (solid, liquid, or gas). The infrared absorption of a substance is caused by its molecular vibration such as stretching and bending. From a FTIR spectrum, substances present in a sample can either be identified or, if not specific enough, valuable information on the nature of its chemical bonds can be inferred according to their characteristic infrared absorption bands. The combination of TGA with FTIR is capable of real-time FTIR analysis of most of the principal gaseous products evolved from a TGA process (evolved gas analysis).

The TGA apparatus used in this project was Stanton Redcroft TGH1000 and the FTIR spectrometer was Thermo Scientific Nicolet iS10. The gases formed in a TGA process was transferred through a heated transfer line (at 170 °C) into a heated gas cell (at 200 °C) of the FTIR spectrometer. In a typical TGA-FTIR experiment, FTIR spectral scanning from 4000 to 400 cm^{-1} on the gaseous product was repeated every 60 seconds. Thus, a series of IR spectra (IR absorbance vs. wavenumber) were recorded with respect to time. The evolution profile of a specific substance (IR signal intensity vs. time or temperature) was obtained by integrating its characteristic absorption band for each IR spectrum. Hence, the evolution profile of a substance (also termed chemigrams) was specified with a spectral region. The analysis of IR spectra and the creation of chemigrams were performed by the Thermo Scientific OMNIC software.

In this project, the TGA-FTIR technique was also used to perform temperature programmed oxidation (TPO) of the reacted catalyst in order to find information about the carbon deposits. In addition, the temperature programmed reduction (TPR) of the fresh catalyst with glucose or citric acid was also carried out on the TGA-

FTIR instrument. Detailed experimental conditions can be found in corresponding chapters.

3.4.2 XRD and Rietveld Refinement

Crystal planes cause an incident beam of X-rays to constructively interfere with one another as they leave the crystal. Consequently, a diffracted beam is detected. This phenomenon is called X-ray diffraction (XRD). The X-ray diffraction at a certain crystal plane only occurs at certain angles of incidence according to Bragg's Law ($n\lambda=2d\sin\theta$), in which n is an integer, λ is the wavelength of incident X-ray beam, d is the interplanar distance, and θ is the angle defined by the X-ray and the plane. For a crystal, different crystal planes have different spacing d . Hence, the diffraction angle (2θ) varies with the crystal plane. If a sample consists of numerous crystals (as in a powdered sample), the random orientation of these crystals in the sample enables that each crystal plane is present at the sample surface with the same probability. Hence, all the possible diffraction directions could be detected by scanning the sample with varying angles of incidence. The diffraction angle and the diffraction intensity of different crystal planes contain important information of crystalline structure.

In this project, XRD tests were performed on an X-ray diffractometer (D8 from Bruker). A voltage of 40 kV and a current of 40 mA were applied to the X-ray generator. In this generator, a stream of electrons were directed from cathode to anode and collided with anode material Cu to produce Cu $K\alpha_1$ radiation (1.54060Å) and Cu $K\alpha_2$ radiation (1.54443Å), which were the x-rays used. The scanning range (2θ) of X-rays was from 20 ° to 80 ° with an increment of 0.0332 °/step and a speed of 0.7 second/step. The sample was crushed to fine powder prior to XRD tests.

The XRD patterns obtained were used for phase analysis and composition analysis. Both analysis were conducted using the X'Pert HighScore Plus software from PANalytical. The phase analysis was performed by searching the best matched reference patterns in International Centre for Diffraction Data (ICDD) database for the XRD pattern obtained experimentally. The composition of a sample as well as the crystallite size of each substance in the sample was calculated using Rietveld refinement method. The basic idea behind Rietveld refinement is to calculate the

entire XRD pattern using a variety of refinable parameters and to improve a selection of these parameters by minimizing the differences between the measured data and the calculated data using least squares methods. Rietveld refinement is a full-pattern fit method and able to deal reliably with strongly overlapping reflections. Its result determines the mass percentage of each substance in the sample. The fit of the calculated pattern to the observed data is evaluated by weighted residual value (R_{wp}), and goodness of fit (GOF) [170]. Ideally, the R_{wp} should approach the statistically expected residual value (R_{exp}), which reflects the quality of the observed data. The GOF is defined as the square of the ratio between R_{wp} and R_{exp} . Normally, a fit with a GOF less than 4 and a R_{wp} less than 10 could be considered as satisfactory [171].

The analysis of crystallite size by the Rietveld method is based on the change of the profile parameters, compared to a standard sample. Hence, The XRD pattern of a standard material (corundum, with no micro strain and no size broadening) was measured first and then refined. The refined profile parameters were taken as size-strain standard for the following sample refinement.

3.4.3 CHN elemental analysis

CHN elemental analysis is a commonly used technique for the determination of mass fractions of carbon, hydrogen and nitrogen in a sample. In this project, a CHN elemental analyser (Flash EA 2000 by CE Instruments) was employed to determine the amount of carbon (and hydrogen, if any) in a catalyst sample [115]. A powered sample of around 15 mg was weighted into a tin capsule. The tin capsule containing the sample was folded properly to remove any trapped air and then placed inside an auto-sampler. The sample was dropped into a combustion reactor and was burned with excess oxygen gas at a high temperature (1000-1800 °C). Helium, a carrier gas, brought the combustion product CO_2 (and H_2O if have) to a chromatography column, in which the gases were separated. The amount of each gas was measured using a highly sensitive thermal conductivity detector (TCD). The CHN elemental analysis yielded mass fractions of carbon and hydrogen in a sample. Duplicate determination was made to ensure the result was reliable and precise. The mean values were reported.

3.4.4 SEM-EDX

In the scanning electron microscopy (SEM) technique, a sample is scanned with a focused beam of high-energy electrons and various signals are produced at the sample surface due to electron-sample interactions. The types of signals produced include secondary electrons, back-scattered electrons, characteristic X-rays, etc. The detection of secondary electrons is commonly used for displaying the morphology and topography of the sample (secondary electron imaging). X-rays are emitted from the sample when the electron beam removes an inner shell electron from the sample and a higher-energy electron fills the shell. The wavelength of X-rays produced is related to the difference in energy levels of electrons in different shells for a given element. Hence, the detection of these characteristic X-rays can be used for elemental analysis, which is achieved by the energy dispersive X-ray spectroscopy (EDX) technique.

In this project, the sample imaging (the fresh catalyst and reacted catalysts) and semi-quantity analysis of elements at sample surfaces were performed on a scanning electron microscope (LEO Gemini 1530) equipped with an EDX system (Oxford Instruments AztecEnergy). The sample particles were mounted on a sticky pad of a SEM stem and then coated with a platinum or gold layer of 10 nm prior to SEM-EDX tests.

3.4.5 Adsorption/Desorption Isotherm

The adsorption/desorption isotherm analysis is a physical gas adsorption technique to measure the specific surface area and the pore size of a solid material. A Quantachrome Nova 2200e instrument was used in this work to carry out this analysis. Catalyst samples were degassed at 200 °C for 3 hours to remove moisture and contaminants adsorbed on the sample surface prior to analysis. The isothermal adsorption of N₂ (at 77.35 K) on the catalyst sample was conducted at different pressures (increase pressure and then decrease pressure). Meanwhile the amount of adsorbed gas was measured as a function of relative pressure. Multiple-point BET method was employed for surface area calculation based on the Brunauer–Emmett–Teller (BET) theory which is an extension of the Langmuir theory (monolayer molecular adsorption) to multilayer adsorption. Barrett-Joyner-Halenda (BJH)

method was used to determine the pore size. Each sample was tested twice to ensure the result was reliable and precise (see Appendix A).

3.4.6 TOC

The Total Organic Carbon (TOC) of a water sample can be measured by two methods, differential method and non-purgeable organic carbon (NPOC) method. In the NPOC method, the sample is acidified (e.g. using hydrofluoric acid 'HF') and then purged with a carbon-free gas to remove inorganic carbon (carbonate). Then the sample is combusted in an oxygen-rich atmosphere to completely convert the organic carbon to CO₂. The resulting CO₂ is then measured with a non-dispersive infrared absorption detector. In the differential method, both the Total Carbon (TC) and the Inorganic Carbon (IC) are measured separately. The TOC is obtained by subtracting the IC from the TC.

In this project, a TOC analyser (Hach-Lange IL550) was used to analyse the condensate sample collected from packed bed experiments based on the NPOC method. Prior to the TOC measurement, the condensate sample was centrifuged to remove any solid particles and then diluted with deionized water by 100 times.

3.4.7 ICP-MS

The inductively coupled plasma-mass spectrometry (ICP-MS) is an analytical technique used for elemental determinations. The high-temperature ICP source converts the atoms of a sample to ions. These ions are then separated and detected by the mass spectrometer. Mass spectrometry measures the mass-to-charge ratio (m/z) and abundance of gas-phase ions. The resulting mass spectrum is a plot of the ion signal intensity as a function of the mass-to-charge ratio, which can be used to determine the elemental or isotopic signature of a sample and to elucidate the chemical structures of molecules.

In this project, an ICP-MS analyser (SCIEX Elan 900 by Perkin Elmer) was used to determine the Ni ion concentration in condensate samples collected from the packed bed reactor experiments. Prior to the ICP-MS analysis, the condensate sample was centrifuged to remove suspended particles in the condensate and then diluted with deionized water by 100 times.

3.5 Thermodynamic equilibrium calculation

3.5.1 Principles of thermodynamic equilibrium calculation

For a chemical system, the global Gibbs free energy (G) is determined by temperature, pressure and molar quantities of components in the system. At a specific temperature and pressure, the system has a tendency to decrease the total Gibbs free energy by changing the chemical composition of the system (e.g. chemical reaction). When the Gibbs free energy is at a minimum, the system reaches an equilibrium state. The discrepancy between the present Gibbs free energy of a system and the minimum Gibbs free energy is a driving force for the system to approach a chemical equilibrium and thus for related chemical reactions to take place. A chemical reaction takes place spontaneously only when the Gibbs free energy change (ΔG) is negative. Thermodynamic equilibrium calculation is based on the minimization of Gibbs free energy and used for determining the chemical composition of a given system at equilibrium. The pathway and kinetics of a chemical reaction are not involved in the thermodynamic calculation. Knowing the equilibrium composition of a system permits one to calculate theoretical thermodynamic properties (e.g. enthalpy, entropy, Gibbs free energy) for the system.

3.5.2 Calculation software (CEA from NASA)

The computer program CEA (Chemical Equilibrium with Application) developed by NASA Lewis Research Centre was used to calculate chemical equilibrium compositions at assigned temperatures and pressures [172, 173]. The calculation was performed on a Java graphical-user-interface (gui) of the CEA program. The program required the input of temperature, pressure and amounts of reactants. Reactants were input in the form of molar fractions and the total amount of reactants was 1 mol. After executing the CEA program, molar fractions of equilibrium products were generated in the output. In order to calculate total moles of equilibrium products per mole of initial reactant mixture, a small amount of argon (0.01 mol) was added to the initial reactant mix as an interior label. It was assumed that the absolute amount of argon does not change during the equilibrium calculation. The total moles of equilibrium products were then used for the calculation of product yields, as well as the enthalpy balance (see Chapter 5).

3.5.3 Thermodynamic data

Thermodynamic data of reactants and potential products are essential to the thermodynamic calculation. Thermodynamic data of numerous species are provided with the CEA program on a separate file (thermo.inp). Names of species contained in thermo.inp can be found in ref. [172]. For those reactants or products which are not included in thermo.inp, it was necessary to find out their thermodynamic data from the literature and write them into the thermo.inp according to a given format [172]. For each species, the seven coefficients (a_1 - a_7) for C_p°/R in Eq. 3.9 and the two enthalpy and entropy integration constants (b_1 , b_2) in Eq. 3.10 and Eq. 3.11 were the main thermodynamic data required by the CEA program (nine constant functional form). In Eqs. 3.9-3.11, R is the gas constant 8.314 J/mol·K, C_p° , H° and S° are the specific heat capacity, enthalpy and entropy of a species at a standard state, respectively. The standard state for a gas is ideal gas at 1 atm. The standard state for liquids and solids is the state of the pure substance subjected to the pressure of 1 atm. The thermodynamic data used for furfural was from ref. [174]. The nine constants of glucose and NiO(cr), which are not available in the literature, were derived from their thermal properties (heat capacity, enthalpy, entropy) at different temperatures [170, 175, 176], as demonstrated in Appendix B. The formatted thermodynamic data of furfural, glucose and NiO(cr) were also shown in Appendix B.

$$\frac{C_p^\circ}{R} = a_1 T^{-2} + a_2 T^{-1} + a_3 + a_4 T + a_5 T^2 + a_6 T^3 + a_7 T^4 \quad (\text{Eq. 3.9})$$

$$\frac{H^\circ(T)}{RT} = -a_1 T^{-2} + a_2 T^{-1} \ln T + a_3 + a_4 \frac{T}{2} + a_5 \frac{T^2}{3} + a_6 \frac{T^3}{4} + a_7 \frac{T^4}{5} + \frac{b_1}{T} \quad (\text{Eq. 3.10})$$

$$\frac{S^\circ(T)}{R} = -a_1 \frac{T^{-2}}{2} - a_2 T^{-1} + a_3 \ln T + a_4 T + a_5 \frac{T^2}{2} + a_6 \frac{T^3}{3} + a_7 \frac{T^4}{4} + b_2 \quad (\text{Eq. 3.11})$$

Conversely, the thermodynamic properties (H° and S°) of a species at a given temperature can be calculated according to Eqs. 3.10-3.11 if related coefficients (a_1 - a_7 , b_1 , b_2) are available. The standard Gibbs free energy (G°) is obtained according to Eq. 3.12. The change in Gibbs free energy (ΔG) of a reaction can be expressed as

Eq. 3.13, where v_i is the stoichiometric number of species i (reactant or product of this reaction), and G_i is the Gibbs free energy of species i .

$$G^\circ = H^\circ - TS^\circ \quad (\text{Eq.3.12})$$

$$\Delta G = \sum v_i G_i \quad (\text{Eq. 3.13})$$

For a complete reaction, the change in enthalpy (ΔH) is calculated using Eq. 3.14, where H_i is the enthalpy of species i . Otherwise, the enthalpy change is evaluated based on the equilibrium composition using Eq. 3.15 [177].

$$\Delta H = \sum v_i H_i \quad (\text{Eq. 3.14})$$

$$\Delta H = H \text{ of products} - H \text{ of reactants} \quad (\text{Eq. 3.15})$$

Chapter 4

Thermodynamics of NiO reduction with bio-compounds

4.1 Introduction

The reduction of metal oxides is an important chemical process in the fields of metallurgy [31, 32, 45, 167, 178], heterogeneous catalysis [46, 147] and chemical looping technologies [12, 29, 30, 138] (see Section 2.4 and 2.5 in Chapter 2). Common reducing agents include H₂, CO, solid carbon and CH₄. With a growing interest in exploiting biomass resources, some biomass derivatives (biomass char [32, 179], bio-liquids [27, 28, 180]) and even biomass [30, 31, 145] were used for the reduction of metal oxides in various fields. Previous studies on this subject either treat biomass-based reductants as a whole with attention only on the reduction feasibility [27, 28] or assume that the syngas produced from feedstock pyrolysis acts as the reductant [31]. Few studies have been concerned with the reducing ability of individual bio-compound (normally oxygenated hydrocarbons). Kale et al. [180] carried out a systematic thermodynamic analysis on the reaction between a series of metal oxides and ethanol for the production of syngas.

This chapter performs a thermodynamic analysis on the NiO reduction with selected bio-compounds (acetic acid, ethanol, acetone, furfural, and glucose) as well as CH₄. The aim of this work together with Chapter 5, is to theoretically explore the potential of bio-oil in chemical looping reforming (CLR) process for sustainable H₂ production. The issues needing to be addressed here include (1) the feasibility of NiO reduction with bio-compounds, (2) the energy demand for the reduction, and (3) the thermodynamic domain for avoidance of carbon formation.

4.2 Thermodynamic feasibility of NiO reduction with bio-compounds

The Gibbs free energy change (ΔG°) of a reaction indicates the feasibility of the reaction. The equilibrium constant K for any reaction that approaches a complete conversion (e.g. 99.99%) can be expressed as:

$$K = \frac{99.99}{0.01} = 9999 \approx 10000$$

Since $K = \exp\left(\frac{-\Delta G^\circ}{RT}\right)$

for $K=10000$ at 298 K, the ΔG° is -22.8 kJ/mol. Thus, a reaction with ΔG° less than -22.8 kJ/mol has the potential to reach completion. Conversely, a reaction with ΔG° more positive than +22.8 kJ/mol will not occur to any noticeable extent [181]. In a system, a reactant may be involved in several feasible reactions. The priority of reactions can be evaluated through comparing their ΔG° . The reaction with more negative ΔG° is more thermodynamically favourable.

4.2.1 Competition of reduction, pyrolysis and steam reforming reactions

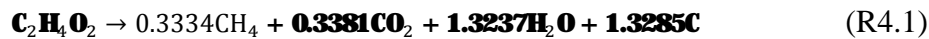
The system investigated here consists of solid NiO, steam and bio-compound vapour, which is similar to the case in the fuel reactor of a chemical looping reforming (CLR) process. In this system, the reduction of NiO with bio-compounds, the pyrolysis of bio-compound and the steam reforming of bio-compounds are three possible reactions of bio-compound conversion. The ΔG° for reduction and steam reforming reactions was calculated according to related reaction equations as shown below. It is difficult to give a generic equation for the bio-compound pyrolysis as there are multiple pyrolysis pathways and the composition of pyrolysis product varies with the temperature. Hence, the ΔG° for pyrolysis reaction was calculated based on the equilibrium composition which was obtained by thermodynamic equilibrium calculation using CEA program. For example, $(0.3334\text{CH}_4 + 0.3381\text{CO}_2 + 1.3237\text{H}_2\text{O} + 1.3285\text{C})$ are produced when 1 mol acetic acid is input at 200 °C. Correspondingly, the reaction equation of pyrolysis at this temperature is compiled as R4.1.

Reduction:

Acetic acid	$C_2H_4O_2 + 4NiO \rightarrow 2CO_2 + 2H_2O + 4Ni$	$\Delta H_{298K}^\circ = 121 \text{ kJ/mol}$
Ethanol	$C_2H_6O + 6NiO \rightarrow 2CO_2 + 3H_2O + 6Ni$	$\Delta H_{298K}^\circ = 161 \text{ kJ/mol}$
Acetone	$C_3H_6O + 8NiO \rightarrow 3CO_2 + 3H_2O + 8Ni$	$\Delta H_{298K}^\circ = 229 \text{ kJ/mol}$
Furfural	$C_5H_4O_2 + 10NiO \rightarrow 5CO_2 + 2H_2O + 10Ni$	$\Delta H_{298K}^\circ = 112 \text{ kJ/mol}$
Glucose	$C_6H_{12}O_6 + 12NiO \rightarrow 6CO_2 + 6H_2O + 12Ni$	$\Delta H_{298K}^\circ = 199 \text{ kJ/mol}$
CH ₄	$CH_4 + 4NiO \rightarrow CO_2 + 2H_2O + 4Ni$	$\Delta H_{298K}^\circ = 156 \text{ kJ/mol}$
H ₂	$H_2 + NiO \rightarrow Ni + H_2O$	$\Delta H_{298K}^\circ = -2 \text{ kJ/mol}$
CO	$CO + NiO \rightarrow Ni + CO_2$	$\Delta H_{298K}^\circ = -43.2 \text{ kJ/mol}$
Graphite carbon (C _{gr})	$C + 2NiO \rightarrow CO_2 + 2Ni$	$\Delta H_{298K}^\circ = 86 \text{ kJ/mol}$

Complete steam reforming (steam reforming + water gas shift):

Acetic acid	$C_2H_4O_2 + 2H_2O \rightarrow 2CO_2 + 4H_2$	$\Delta H_{298K}^\circ = 128.9 \text{ kJ/mol}$
Ethanol	$C_2H_6O + 3H_2O \rightarrow 2CO_2 + 6H_2$	$\Delta H_{298K}^\circ = 173.4 \text{ kJ/mol}$
Acetone	$C_3H_6O + 5H_2O \rightarrow 3CO_2 + 8H_2$	$\Delta H_{298K}^\circ = 245.7 \text{ kJ/mol}$
Furfural	$C_5H_4O_2 + 8H_2O \rightarrow 5CO_2 + 10H_2$	$\Delta H_{298K}^\circ = 132.7 \text{ kJ/mol}$
Glucose	$C_6H_{12}O_6 + 6H_2O \rightarrow 6CO_2 + 12H_2$	$\Delta H_{298K}^\circ = 223.9 \text{ kJ/mol}$
CH ₄	$CH_4 + 2H_2O \rightarrow CO_2 + 4H_2$	$\Delta H_{298K}^\circ = 164.7 \text{ kJ/mol}$

Pyrolysis (taking acetic acid at 200 °C as example):

For each bio-compound as well as CH₄, the ΔG° curves of these three competing reactions over the temperature range of 0-850 °C are presented as an Ellingham-type diagram in **Figure 4.1**. Temperatures higher than 850 °C were not considered in this work because in practice a high reduction temperature could lead to the sintering of

metallic Ni and then a decrease in its catalytic activity for the subsequent steam reforming [8, 81].

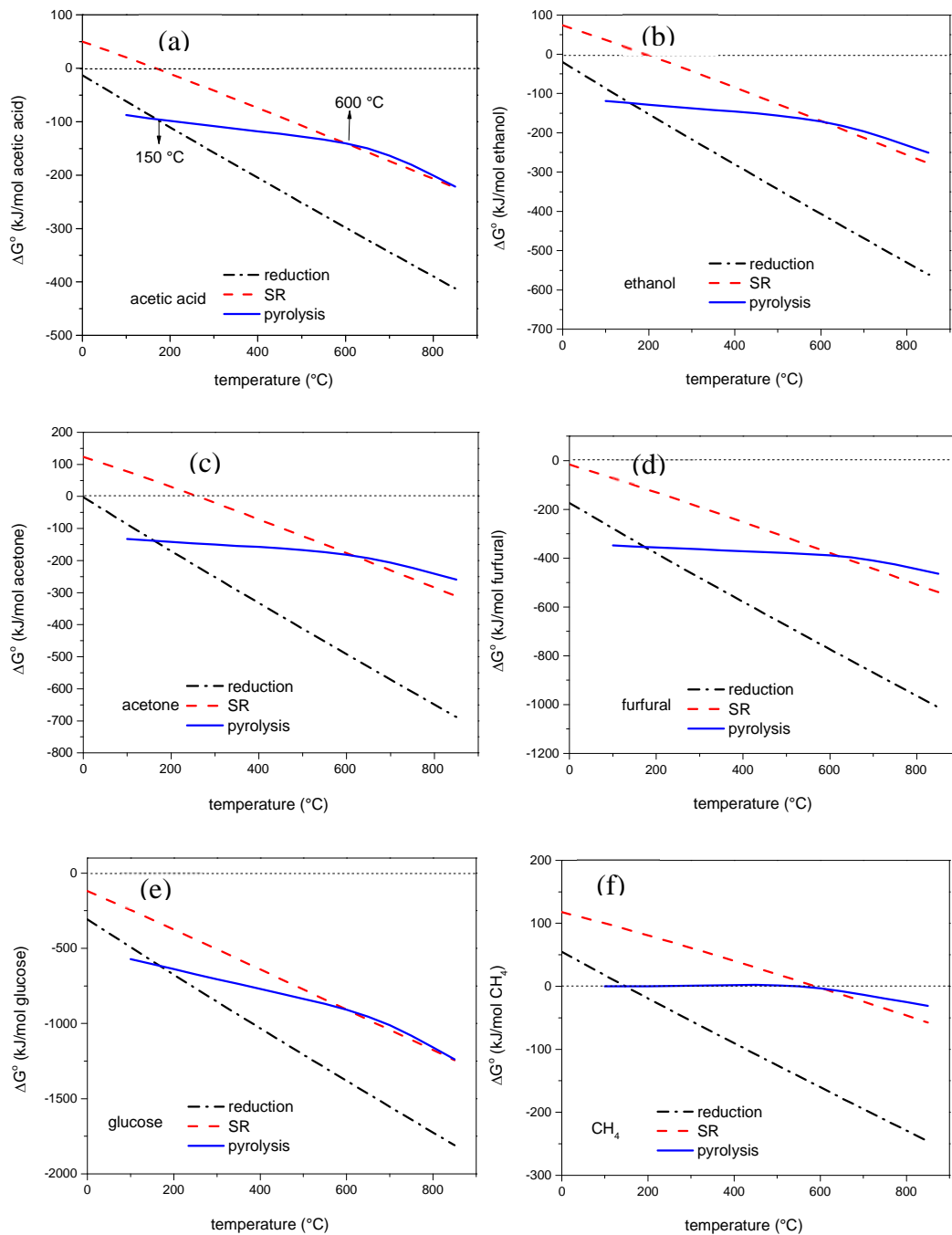


Figure 4.1 Comparison of Gibbs free energy changes for the reduction, steam reforming and pyrolysis reactions: (a) acetic acid, (b) ethanol, (c) acetone, (d) furfural, (e) glucose and (f) CH_4

The NiO reduction with these bio-compounds is thermodynamically feasible at temperatures as low as room temperature (**Figure 4.1a-e**), in contrast with the case of CH₄, with which the reduction is enabled at temperature above 150 °C (**Figure 4.1f**). Comparing the three reactions, all the bio-compounds as well as CH₄ exhibit the general trend that reduction is more favourable than the pyrolysis and the steam reforming reaction at temperatures above 150 °C, as the ΔG° for the reduction is the most negative. When the temperature is below 150 °C, pyrolysis becomes dominant. In a common temperature range (450-850 °C) and for a system consisting of NiO catalyst, steam and bio-compounds, the bio-compounds would preferably reduce NiO rather than react with steam or decompose, so as to minimize the total Gibbs free energy of the system. It should be noted that the argument above is based on chemical equilibrium. In practice, the priority of reactions is determined first by kinetics and ultimately by chemical equilibrium. Experimental results suggest that the steam reforming of bio-compounds can occur as soon as the NiO reduction is initiated (see Chapter 6 and 7). Metallic Ni produced from NiO reduction acts as a catalyst for the steam reforming reaction which in principle allows it to proceed in parallel with NiO reduction.

4.2.2 Ease of NiO reduction with different reducing agents

The ΔG° curves of NiO reduction with different reducing agents (bio-compounds and traditional reducing agents) are compared in **Figure 4.2**. The ΔG° lines of bio-compounds are below those of traditional reducing agents when the temperature is above 450 °C, indicating that the bio-compounds have a larger potential to reduce NiO than traditional reducing agents. At 650 °C, the ease of NiO reduction decreases in this order: glucose > furfural \approx acetic acid > ethanol > acetone > CH₄ \approx C_{gr} \approx H₂ \approx CO. This result indicates that NiO would preferably react with glucose and then with the other bio-compounds if all these reducing agents were simultaneously available to NiO.

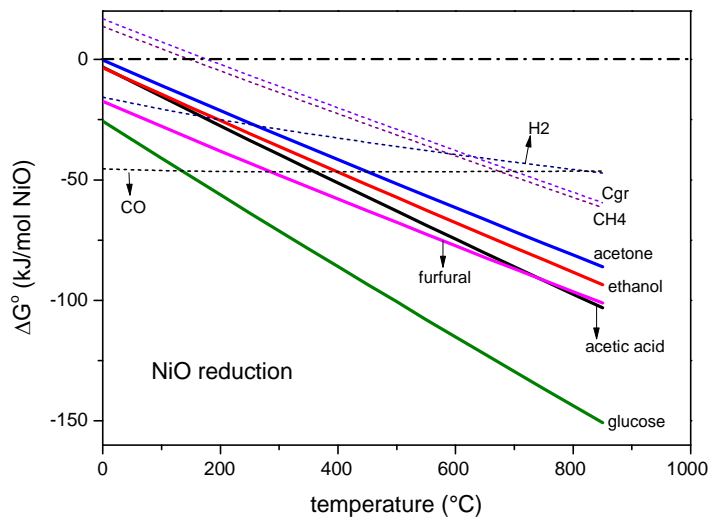


Figure 4.2 Comparison of Gibbs free energy change for NiO reduction with different agents (bio-compounds in solid line, traditional reducing agents in dash line)

For a reaction at temperature T: $\Delta G = \Delta H - T\Delta S$ (Eq. 4.1)

At a specific temperature, the value of ΔG° is determined by the enthalpy change (ΔH°) and the entropy change (ΔS°) (Eq. 4.1). As shown in **Table 4.1**, for all the reducing agents used except H_2 and CO, the NiO reduction is an endothermic process ($\Delta H^\circ > 0$) that is not favourable for the spontaneity of a reaction. The negative ΔG° values obtained are entirely contributed by the increase in the entropy (more gases are produced). The largest increase in the amount of gases is observed for the NiO reduction with glucose, resulting in the most negative ΔG° . In contrast, the exothermicity is the main driving force for the reduction of NiO with CO.

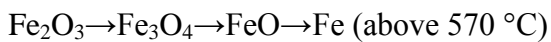
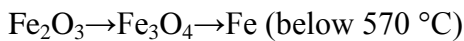
Table 4.1 The Gibbs free energy change, the enthalpy change and the entropy change per mol of NiO reduced with different reducing agents at 650 °C

Compound	ΔG° (kJ/mol NiO)	ΔH° (kJ/mol NiO)	ΔS° (kJ/K mol NiO)	Δn *
glucose	-122.3	10.33	0.143	0.917
furfural	-82.1	6.32	0.096	0.6
acetic acid	-80.3	25.65	0.115	0.75
ethanol	-72.9	22.7	0.104	0.667
acetone	-66.5	24.5	0.099	0.625
CH ₄	-44.4	35.25	0.086	0.5
carbon	-42.1	38.3	0.087	0.5
H ₂	-41.1	-11.8	0.032	0
CO	-46.5	-47.3	-0.001	0

* Δn is the change in the moles of gas in the reaction system for per mol NiO reduction.

4.2.3 Other metal oxide reduction

In addition to the NiO reduction, the reduction of Fe₂O₃ and CuO has also been extensively studied as they are important reactions in catalysis, metallurgy and chemical looping combustion [12, 30, 167, 180, 182]. Experimental studies found that Fe₂O₃ undergoes stepwise reduction [32, 167, 182]. The reduction of Fe₂O₃ to Fe occurs in three steps when temperatures are above 570 °C and two steps below 570 °C as shown below [178, 182].



It was also found that non-stoichiometric FeO is the intermediate product of the reduction of Fe₃O₄ to Fe when the temperature is above 570 °C [183]. For this reason, non-stoichiometric iron oxide Fe_{0.947}O is used instead of FeO for the thermodynamic analysis in this work. Iron oxide reduction systems (Fe₂O₃/Fe₃O₄, Fe₃O₄/Fe_{0.947}O, Fe_{0.947}O/Fe) and CuO/Cu are considered, in comparison with NiO reduction.

As shown in **Figure 4.3**, for each reducing agent, the ease of metal oxide reduction is in the order of $\text{CuO/Cu} > \text{Fe}_2\text{O}_3/\text{Fe}_3\text{O}_4 > \text{NiO/Ni} > (\text{Fe}_3\text{O}_4/\text{Fe}_{0.947}\text{O}, \text{Fe}_{0.947}\text{O/Fe})$. The ΔG° values for the former three systems are below zero in the temperature range of 200-1200 °C. Thermodynamic equilibrium calculation (stoichiometric ratio of metal oxide and reducing agent are input) shows that the three reductions can reach completion in this temperature range. Compared with the other reduction systems, the CuO reduction shows a significantly larger thermodynamic driving force, even at low temperature. This may explain that the reduction of CuO can be operated at temperatures below 230 °C [147].

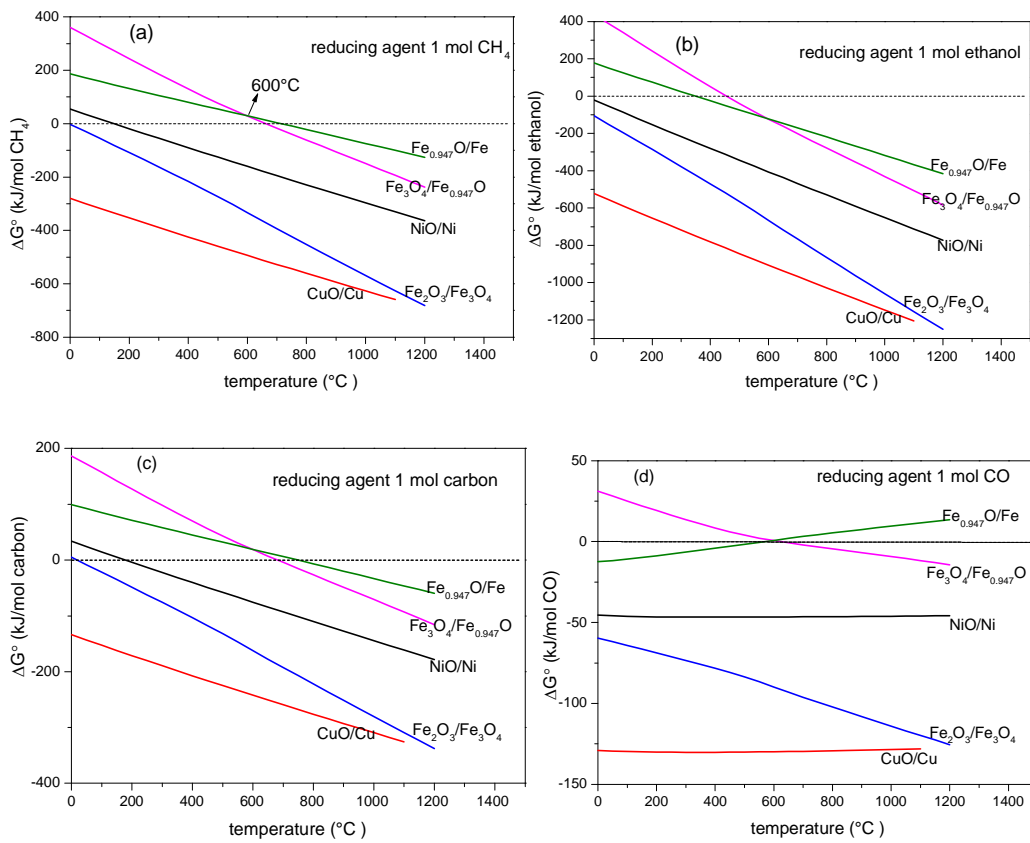


Figure 4.3 Gibbs free energy change for the reduction of different metal oxides with 1 mol reducing agents (a) CH_4 , (b) ethanol, (c) solid carbon and (d) CO

When the temperature is below 600 °C, the ΔG° line of $\text{Fe}_{0.947}\text{O}/\text{Fe}$ is below that of $\text{Fe}_3\text{O}_4/\text{Fe}_{0.947}\text{O}$ (**Figure 4.3**), indicating that the reduction of Fe_3O_4 to FeO without further reduction is not thermodynamically favourable. This result is consistent with the fact that Fe_3O_4 is reduced directly to metallic Fe without FeO being formed below 570 °C [178, 182]. Above 600 °C, the $\text{Fe}_3\text{O}_4/\text{Fe}_{0.947}\text{O}$ is more thermodynamically favourable than the $\text{Fe}_{0.947}\text{O}/\text{Fe}$. The stepwise reduction of Fe_2O_3 to Fe experimentally observed may be controlled by the thermodynamics of each reduction system.

For the $\text{Fe}_2\text{O}_3/\text{Fe}$ system (assuming that metallic Fe , CO_2 and H_2O are products), if stoichiometric amounts of Fe_2O_3 and reducing agent are input, thermodynamic equilibrium calculation shows that the Fe_2O_3 could be completely converted to Fe_3O_4 between 200-600 °C. Above 600 °C, no Fe_3O_4 is found in the product as the reduction of Fe_3O_4 to $\text{Fe}_{0.947}\text{O}$ is thermodynamically favourable and complete. The transformation of $\text{Fe}_{0.947}\text{O}$ to Fe occurs above 650 °C. However, the reduction of $\text{Fe}_{0.947}\text{O}$ to Fe which has a less negative ΔG° cannot reach completion. As a result, both $\text{Fe}_{0.947}\text{O}$ and Fe exist in the final product even the temperature goes up to 1200 °C. It has to be noted that a complete reduction of Fe_2O_3 to Fe by CO can be achieved at 870-1200 °C in experiments [167] as practical reactions take place at non-standard state.

4.3 Enthalpy changes (energy demand for NiO reduction)

The total energy demand for the reduction of one mol of NiO with stoichiometric amounts of bio-compounds is comprised of three parts [177]: (1) the energy consumption for heating the bio-compound from normal state at 25 °C to gas phase at reaction temperature T ; (2) the energy consumption for heating solid NiO from 25 °C to T , and this term is the same for all the bio-compounds since the energy calculation is based on one mol of NiO being reduced; and (3) the energy demand for converting reactants to equilibrium products at T . Each part can be calculated on the basis of enthalpy change from the initial state to the final state as illustrated in **Figure 4.4** and denoted as ΔH_{bio} , ΔH_{NiO} and $\Delta H_{\text{reaction}}$, respectively. Combining them gives the total enthalpy change ΔH_{total} (Eq. 4.2).

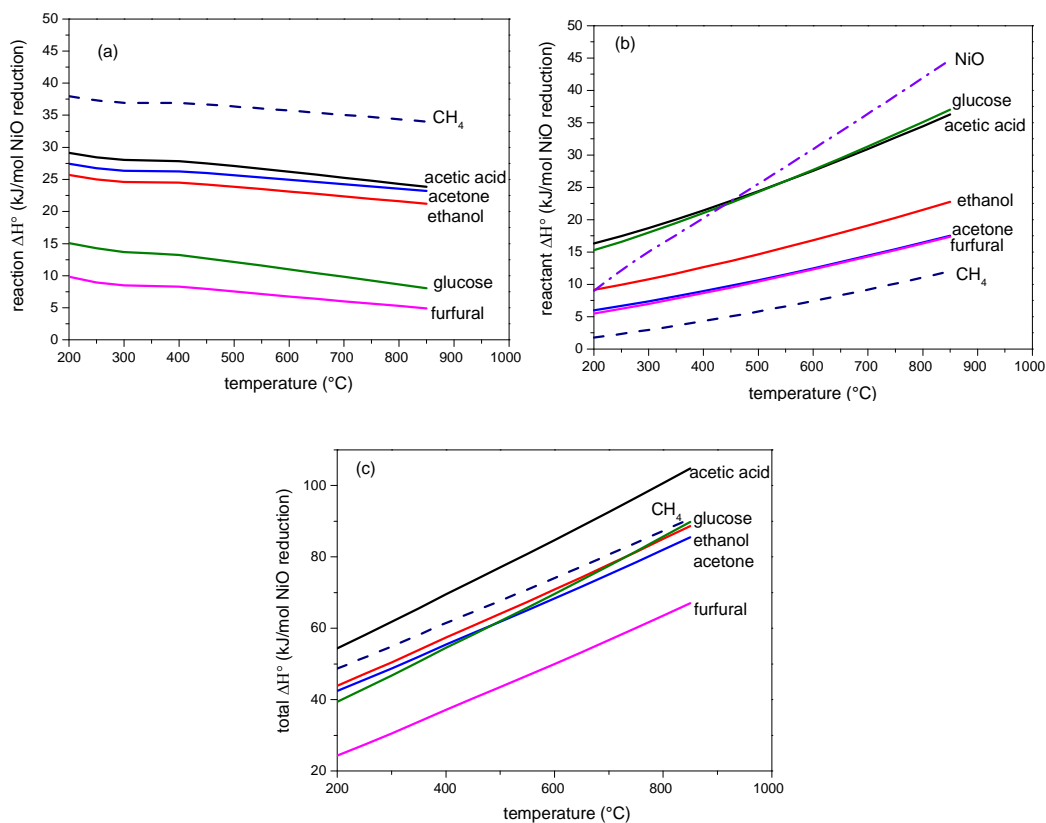


Figure 4.5 Enthalpy terms vs. temperature for the system of 1 mol NiO and stoichiometric amounts of reductant: (a) the enthalpy change of the reduction reaction, (b) the enthalpy change of heating each reactant to reaction temperature, and (c) the total enthalpy balance for 1 mol NiO reduced.

Determined by the three enthalpy terms, the total enthalpy change per mol of NiO reduced decreases in this order: acetic acid > (CH_4 , ethanol, acetone, glucose) > furfural (**Figure 4.5c**). The NiO reduction with acetic acid requires the largest energy input (89 kJ/mol at 650 °C) while furfural shows the most attractive energy feature (53 kJ/mol at 650 °C). For the other bio-compounds, the total energy demands per mol of NiO reduced are quite close to each other and approximate that with CH_4 .

4.4 Influencing factors of equilibrium products

The influence of temperature, pressure, the presence of steam and the NiO/C ratio on the product distribution was studied by thermodynamic equilibrium calculation using CEA program. Bio-compound (g. i.e. ‘gas phase’) and NiO(cr. i.e. ‘crystalline phase’) at a certain ratio were input and the reaction temperature and pressure were specified. The species considered in this calculation include Ni(cr), CO₂(g), H₂O(g), CO(g), H₂(g), CH₄(g), NiO(cr), acetic acid(g), ethanol(g), acetone(g), furfural(g), glucose(g) and C(gr, ‘graphite’). Other related species were also considered in the calculation but normally their molar fractions in equilibrium product were less than 5×10^{-6} , therefore they were regarded as negligible. The yield of product *i* is defined as the moles of product *i* over the moles of bio-compound or carbon feed. The molar NiO/C ratio was defined as the moles of NiO input over the initial moles of carbon in the bio-compound used (Eq.4.3).

$$\frac{\text{NiO}}{\text{C}} = \frac{\text{initial moles of NiO}}{\text{initial moles of biocompound} \times \text{carbon number in biocompound molecule}} \quad (\text{Eq. 4.3})$$

4.4.1 Temperature and pressure

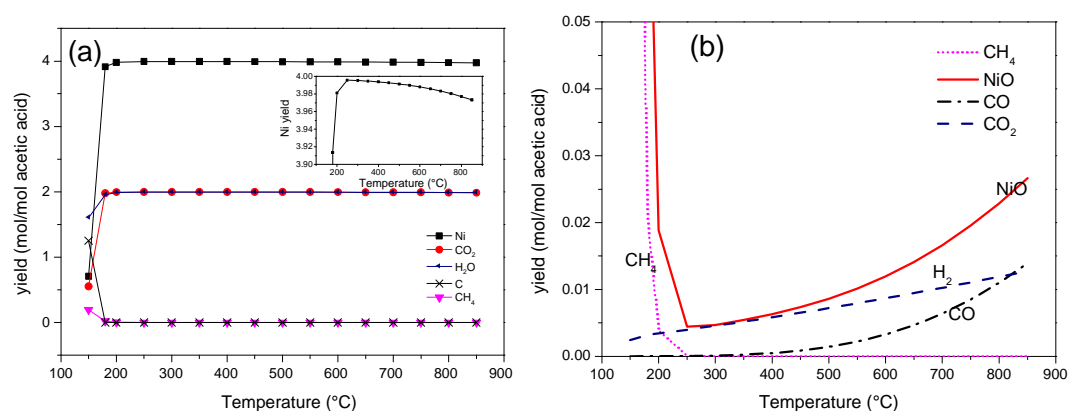


Figure 4.6 Yields of equilibrium products when 1 mol acetic acid reacts with the stoichiometric amount of NiO at different temperatures and 1 atm: (a) major products with the yield of Ni being zoomed in, (b) minor products

To study the influence of temperature on the reduction, the initial amounts of NiO and bio-compound were kept at stoichiometric ratio and the pressure was fixed at 1 atm while the temperature was varying from 150 to 850 °C. It was found that stoichiometric quantities of Ni, H₂O and CO₂ were produced at temperatures above 200 °C for all the bio-compounds as well as CH₄. The influence of temperature on the product yields was negligible (**Figure 4.6a**). Hence, the NiO reduction could be considered as a complete (irreversible) reaction. Below 200 °C, the NiO conversion decreased dramatically. Taking acetic acid as an example, the conversion of NiO to Ni was only 17.7% at 150 °C. The main products at this temperature included Ni, CH₄, solid carbon, CO₂, and H₂O. Thus, the general reaction could be considered as a combination of NiO reduction and acetic acid pyrolysis. Above 250 °C, the extent of NiO reduction decreased marginally with temperature (**Figure 4.6a** inset) with trace amounts of CO and H₂ being produced (**Figure 4.6b**).

In addition, the influence of pressure on the reduction was checked by changing system pressure from 1 atm to 20 atm and fixing the temperature at 650 °C. It was found that the change in the pressure had no influence on the NiO reduction.

4.4.2 The presence of steam

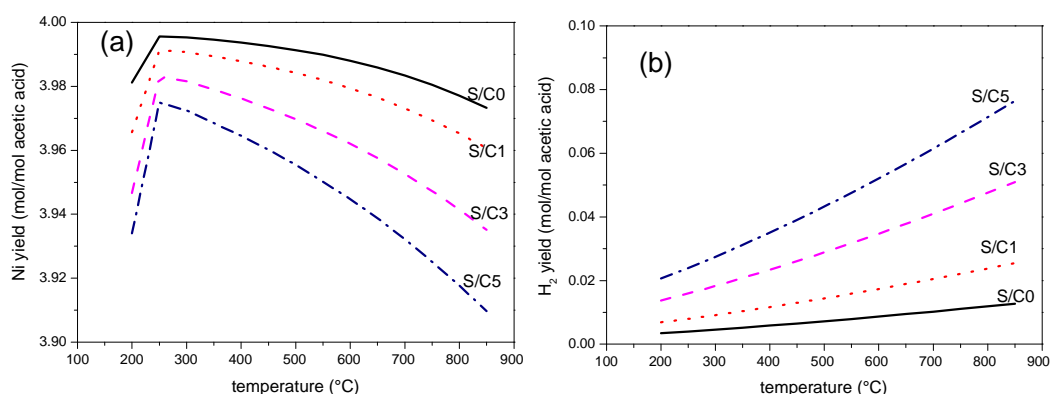


Figure 4.7 Changes in (a) the Ni yield and (b) the H₂ yield when different amounts of steam are added to the system of acetic acid and NiO in a stoichiometric ratio at 1 atm

In industry, the reduction of reforming catalysts (supported NiO) with natural gas is operated with co-feed of steam. It is recommended that the molar steam/carbon ratio (S/C) is maintained at or above 7:1 to avoid the carbon formation [147]. In this work, the influence of steam on NiO reduction was checked from the aspect of thermodynamics. The reactants input to the CEA program included NiO and bio-compound (in a stoichiometric ratio) as well as steam (the amount of steam used is defined as S/C ratio). It was found that the influence of steam on the NiO reduction was negligible. Ni, CO₂, and H₂O were still the major products and approximated their stoichiometric quantities. With the increase in the amount of steam, the reduction extent of NiO decreased slightly (**Figure 4.7a**), as predicted by Le Chatelier's principle. The yield of H₂ was quite low although it showed an increasing trend as the S/C ratio rose (**Figure 4.7b**).

4.4.3 NiO/C ratio

As discussed above, approximately stoichiometric amounts of Ni, CO₂ and H₂O could be produced when stoichiometric amounts of NiO and bio-compound for CO₂ and H₂O final products were input at temperatures above 200 °C. If the amount of NiO is insufficient, a complete reduction of NiO can still be achieved but the product composition deviates from the intended CO₂ and H₂O final products. **Figure 4.8** shows the moles of equilibrium products as a function of the amount of NiO added to 1 mol bio-compound at 650 °C and 1 atm. As the amount of NiO used increased from zero to the stoichiometric quantity, the yields of carbon, CH₄ and H₂ decreased while the yields of CO₂ and H₂O increased. The CO yield rose first and then declined to zero, peaking at the point where the carbon deposition disappeared.

The formation of carbon is thermodynamically favoured by decreasing the amount of NiO used below stoichiometry of the reduction reaction to CO₂ and H₂O final products. The dependence of carbon formation on the availability of oxygen in a reduction process is similar to that in a steam reforming process where the oxygen element is added as steam. It has been experimentally observed that rapid carbon formation did not occur until more than 80% of the oxygen in the NiO crystal lattice was consumed while carbon formation was rare when the NiO existed in its fully oxidized state [141]. In chemical looping combustion, extensive carbon formation could be avoided by keeping the degree of reduction below a certain value (e.g. 40%

[142]). However, this method is not applicable to the chemical looping reforming process as the residual NiO would be reduced anyway in the subsequent steam reforming process.

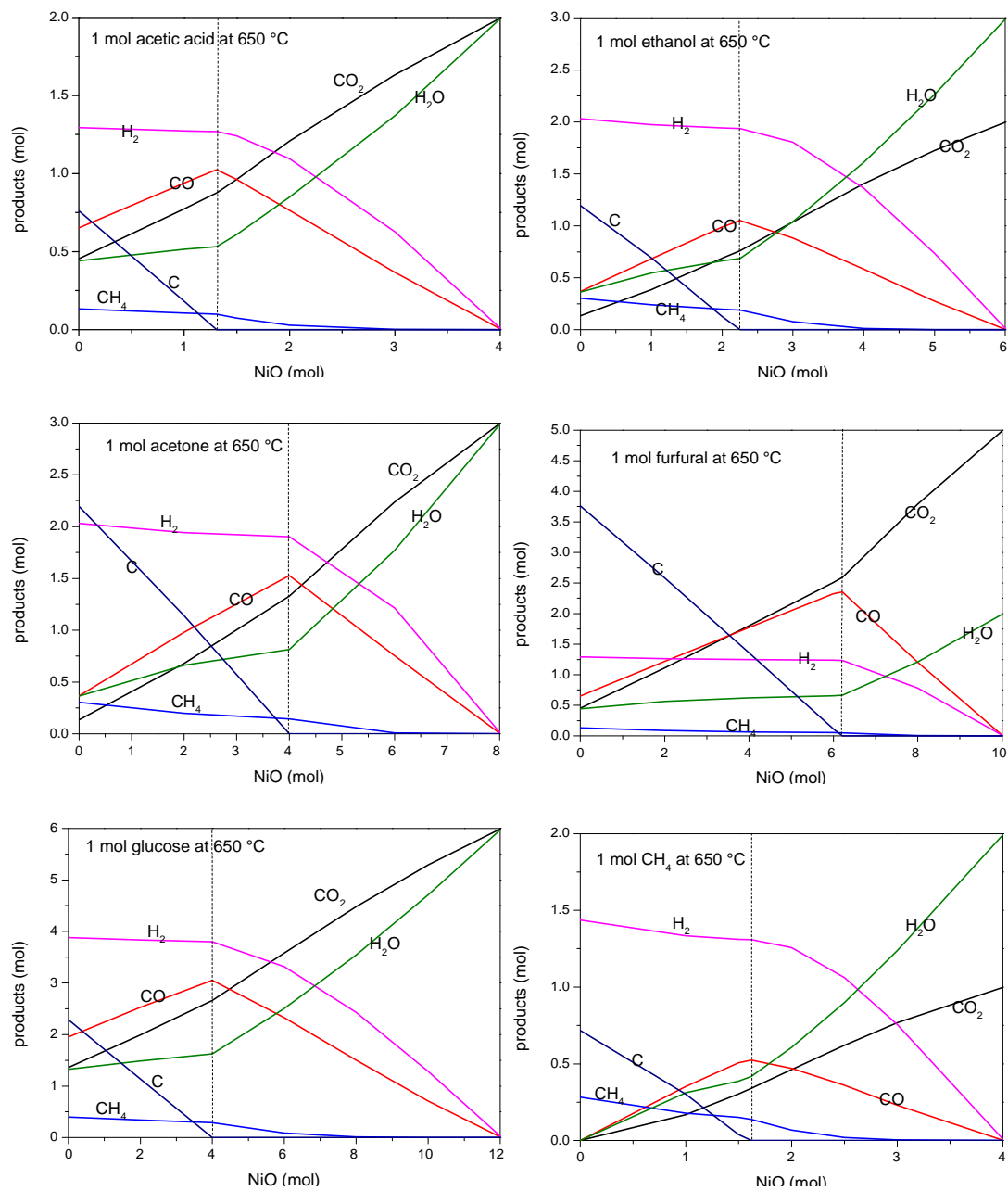


Figure 4.8 Equilibrium yields of products when 1 mol bio-compound reacts with different amounts of NiO at 650 °C and 1 atm

In practice, the case that NiO is in short supply may take place under two conditions: (1) in a packed bed reactor, a quite large flow rate of bio-compound vapour is used or the reduction comes close to the end, (2) in a fluidized bed reactor, the relative flow rate of NiO against that of bio-compound is low. To prevent the carbon formation, the bio-compound feed to the packed bed reactor for NiO reduction should be at a low flow rate. As the reduction proceeds, a decrease in the flow rate of bio-compound is recommended.

For different bio-compounds, the smallest amount of NiO for avoidance of carbon formation is different, which was summarized in **Table 4.2**. The minimum NiO/C ratio is defined as the smallest amount (moles) of NiO for avoidance of carbon formation divided by the number of carbon atoms in the bio-compound molecule, which can be used to indicate the resistance of bio-compound to carbon formation during the NiO reduction process. Based on the minimum NiO/C ratio, the bio-compounds as well as CH₄ are ranked in this order: acetic acid \approx glucose < ethanol < furfural < acetone < CH₄ at 650 °C (**Table 4.2**). This order is found to be related with the O/C ratio in the bio-compound molecule. In general, more oxygen in the bio-compound molecule introduces more resistance to carbon formation.

Table 4.2 The lower limit of the amount of NiO for no carbon formation at 650 °C and 1 atm, as well as the syngas yield (CO+H₂) and H₂/CO ratio at this point

Compounds	NiO/compound ratio	minimum NiO/C ratio	O/C ratio in molecules	syngas yield (mol/mol carbon feed)	H ₂ /CO ratio
acetic acid	1.31	0.66	1.00	1.15	1.24
ethanol	2.26	1.13	0.50	1.49	1.84
acetone	4.00	1.33	0.33	1.14	1.25
furfural	6.21	1.24	0.40	0.72	0.52
glucose	4.00	0.67	1.00	1.14	1.25
CH ₄	1.62	1.62	0	1.83	2.50

It is also of great interest to produce syngas through partial oxidation of bio-liquids using metal oxide as oxygen carrier [180]. As shown in **Figure 4.8**, the maximum

syngas yield is achieved at the minimum NiO/C ratio rather than at the stoichiometric ratio for partial oxidation (Eq. 4.4, taking ethanol as example). When the actual NiO/C ratio is lower than the minimum NiO/C ratio, a negligible change is found to the H₂ yield but the CO yield is considerably decreased. Correspondingly, undesirable carbon and CH₄ emerge in products. If the NiO/C ratio is higher than the minimum NiO/C ratio, the syngas yield declines as the syngas is oxidized to CO₂ and H₂O. At the minimum NiO/C ratio, the use of CH₄ produces more syngas with a higher H₂/CO ratio than the use of bio-compounds. Among the bio-compounds, the syngas yield from ethanol is highest (1.49 mol/mol carbon feed) while the syngas yield from furfural is lowest (0.72 mol/mol carbon feed).

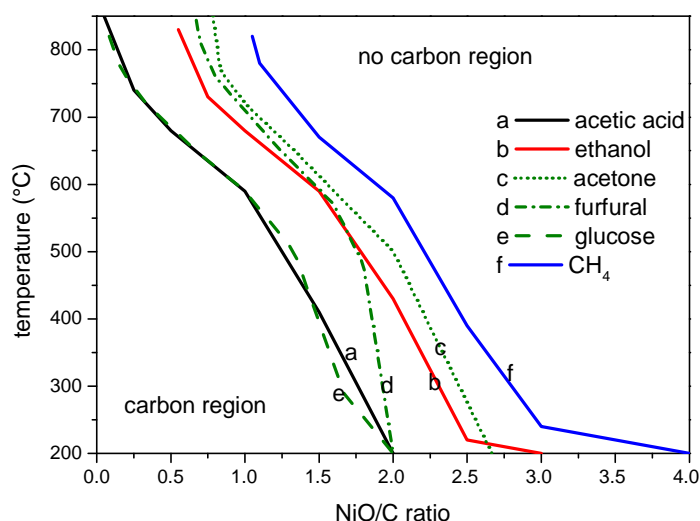


Figure 4.9 Thermodynamic domains (temperature and NiO/C ratio) for avoidance of carbon formation at the pressure of 1 atm

In addition to the NiO/C ratio, the reaction temperature is another important factor to affect the formation of carbon. **Figure 4.9** depicts the thermodynamic domain (temperature and NiO/C ratio) for carbon formation. Low temperatures and low NiO/C ratios favour the formation of carbon. When a mixture consisting of various

bio-compounds is used to reduce NiO and the NiO/C ratio is known, **Figure 4.9** can be employed to estimate which bio-compound is the likely reason for carbon formation. At a given NiO/C ratio and given temperature, glucose and acetic acid show the best resistance to carbon formation while CH₄ has a larger tendency to produce carbon. Therefore, during the NiO reduction with bio-compounds, the side reactions leading to the formation of CH₄ (e.g. methanation, decomposition) should be suppressed by using suitable catalysts or controlling reaction temperature or pressure.

4.5 Conclusions

Compared with the reduction systems of CuO/Cu and Fe₂O₃/Fe₃O₄, the NiO/Ni has a lower affinity to react with bio-compounds. Nonetheless, it is thermodynamically feasible to reduce NiO with the five bio-compounds considered in this project as well as CH₄ at temperatures above 200 °C (including 200 °C). Moreover, the NiO reduction is more thermodynamically favourable than the pyrolysis of bio-compounds and the steam reforming of bio-compounds. Thermodynamic equilibrium calculations show that NiO reduction with the bio-compounds approaches completion above 200 °C. When NiO and the bio-compound are input in a stoichiometric ratio, the amounts of Ni, H₂O and CO₂ produced approximate their stoichiometric quantities. The influences of temperature, pressure, and the presence of steam are negligible. If the amount of NiO is insufficient to completely oxidize the bio-compound to the CO₂ and H₂O final products, other products (carbon, CH₄, CO, and H₂) are generated in addition to Ni, H₂O and CO₂. The carbon formation depends on the temperature and the availability of NiO. For each bio-compound as well as CH₄, the thermodynamic region (temperature and NiO/C ratio) for avoidance of carbon formation was obtained.

The thermodynamic driving force for NiO reduction with each bio-compound considered in this work is larger than that with the traditional reducing agents at temperatures above 450 °C. When all the bio-compounds are available at the same time, the NiO reacts preferably with glucose as it has the most negative ΔG° . Considering the total enthalpy change, the NiO reduction with furfural requires less energy input (53 kJ per mol NiO reduced at 650 °C), while a large amount of energy

(89 kJ at 650 °C) is needed to reduce the same amount of NiO with acetic acid. The energy demand for NiO reduction with the other bio-compounds (glucose, ethanol, and acetone) is close to that with CH₄ (77 kJ per mol of NiO reduced at 650 °C). All the bio-compounds, especially acetic acid and glucose, show a better resistance to carbon formation than CH₄ when the NiO/C is low.

Chapter 5

Thermodynamics of hydrogen production from steam reforming of bio-compounds

5.1 Introduction

Steam reforming of bio-oil obtained from the condensates of biomass fast pyrolysis, is considered as a promising route for sustainable H₂ production. Bio-oil is a complex mixture, consisting of various oxygenated hydrocarbons, such as acids, alcohols, ketones, aldehydes, sugars, furans and phenols. To have an insight into the chemistry of bio-oil steam reforming, many efforts have been made on the performance of individual bio-compounds based on experimental investigations [25, 26, 93, 107, 118, 119, 184] or thermodynamic analysis [181, 185-187]. Bio-compounds that have been subjected to thermodynamic equilibrium analysis include acetic acid [168, 186], ethylene glycol [186], acetone [186], glycerol [188] and especially ethanol [181, 185, 187, 189-191]. To the author's knowledge, few studies have been carried out on the thermodynamics of steam reforming of furfural and glucose. Moreover, the dependence of equilibrium compositions on the molecular formula of feedstock has not been reported.

In this chapter, the thermodynamics of H₂ production from five bio-compounds (acetic acid, ethanol, acetone, furfural and glucose) as well as CH₄ by steam reforming process was studied. Four aspects were covered (1) the thermodynamic driving force (ΔG°) for a complete steam reforming reaction, (2) effects on the steam reforming equilibrium yields of the following parameters: temperature, molar steam to carbon ratio (S/C), molecular formula of bio-compounds and presence of NiO in the initial mixture, (3) thermodynamic evaluation for the carbon free region, and (4) energy balances.

5.2 Method and definition of outputs

The bio-compound/steam systems were studied here to simulate the case of steam reforming. The calculation of equilibrium composition was based on the Gibbs free

energy minimization and implemented using the CEA program from NASA. The species considered in this calculation included acetic acid (g, i.e. ‘gas phase’), ethanol (g), acetone (g), furfural (g), glucose (g), H₂O (g), H₂ (g), CO₂ (g), CO (g), CH₄ (g), and C (gr, ‘graphite’). Other possible products such as ethylene (g), acetaldehyde (g) were also considered, but their molar fractions at equilibrium were found to be negligible (less than 5×10⁻⁶). The temperature range covered in the calculations was 200-850 °C and the pressure was fixed at 1 atm. The total amount of reactants (bio-compound and steam) input was set as 1 mol, and a small amount of argon (0.01 mol) was added in order to facilitate the calculation of the total moles of equilibrium products by argon balance (see Chapter 3). The outputs involved in the discussion of this chapter were defined as follows [177].

(1) The total moles of equilibrium products:
$$n_{eq} = \frac{y_{Ar,in}}{y_{Ar,eq}}$$

(2) Yield of species ‘i’:
$$i \text{ yield} = \frac{n_{eq} \times y_{i,eq}}{n \times 1 \times y_{bio,in}} \quad \text{in mol/mol carbon feed}$$

(3) The weight yield of H₂:
$$H_2 \text{ yield (wt\%)} = 100 \times \frac{2 \times n_{eq} \times y_{H_2,eq}}{M_{bio} \times y_{bio,in}}$$

Where $y_{i,eq}$ was the molar fraction of species i in equilibrium products, $y_{Ar,in}$ and $y_{bio,in}$ were the molar fractions of Ar and bio-compound input, n was number of carbon atoms in the bio-compound molecule, and M_{bio} was the molar mass of bio-compound in gram.

(4) ΔH_{bio} was defined as the enthalpy of bio-compound in gaseous phase at reaction temperature T minus the enthalpy of bio-compound in its natural phase at 298 K and 1 atm, in kJ/mol carbon feed.

(5) ΔH_{H_2O} was defined as the enthalpy of H₂O vapour at reaction temperature T minus the enthalpy of liquid H₂O at 298 K and 1 atm, in kJ/mol carbon feed. The amount of H₂O input could be determined by the amount of carbon feed and S/C ratio.

(6) $\Delta H_{reaction}$ was defined as the total enthalpy of equilibrium products at T minus the total enthalpy of reactants at T in kJ/mol carbon feed.

(7) The total energy demand in kJ/mol carbon feed:

$$\Delta H_{total} = \Delta H_{bio} + \Delta H_{H_2O} + \Delta H_{reaction} \quad (\text{Eq. 5.1})$$

(8) ΔH ratio was defined as the total energy input for producing one mole of H_2 via steam reforming process divided by the energy input for producing 1 mole of H_2 via water splitting ($H_2O \rightarrow H_2 + 0.5O_2$). The reactant water is liquid at 298 K and 1 atm and the gas products H_2 and O_2 are at the same reaction temperature T as that used for steam reforming. A process with ΔH ratio <1 is considered efficient and favourable from an energy viewpoint. Conversely, ΔH ratio >1 represents a non-viable process [177].

In a bio-compound/steam system, common reactions include thermal decomposition of bio-compounds (R5.1, taking ethanol as example [107]), steam reforming of bio-compounds to produce H_2 and CO (R5.2), and subsequently water gas shift reaction (WGS, R5.3), Boudouard reaction (R5.4), methanation (R5.5, R5.6), carbon gasification (R5.7), etc.



5.3 Gibbs free energy changes for complete steam reforming

Complete steam reforming (CSR) refers to the overall reaction of steam reforming and WGS. It is the ideal output of a steam reforming process as all the carbon atoms in the feedstock convert to CO_2 and all the hydrogen atoms to H_2 . The reaction equations for CSR of the five bio-compounds as well as CH_4 can be found in Chapter 4. The Gibbs free energy change (ΔG°) of a reaction depends on the

expression of the reaction equation. Here, the ΔG° for the CSR reaction was calculated on the basis of 1 mole of carbon feed.

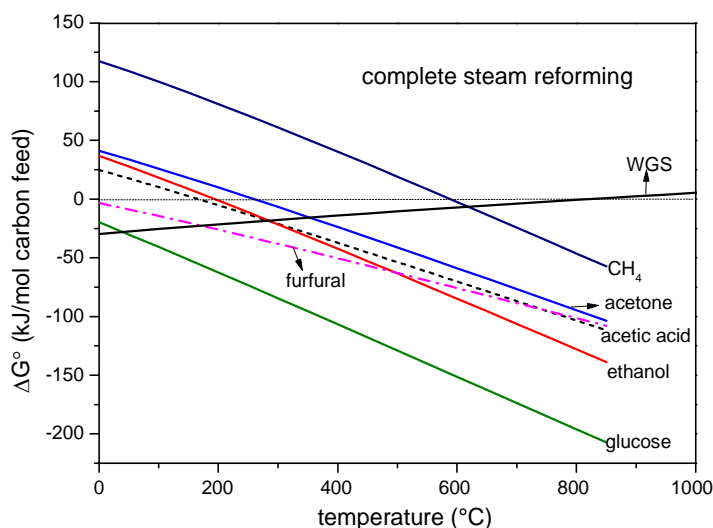


Figure 5.1 Gibbs free energy changes for the complete steam reforming reactions of the bio-compounds and CH_4 as well as the water gas shift reaction

As shown in **Figure 5.1**, CSR of the bio-compounds is theoretically feasible at temperatures as low as 250 °C while a temperature above 600 °C is required for CSR of CH_4 . With increasing temperature, the ΔG° for all the bio-compounds and CH_4 become more negative, implying their CSR reactions are more favourable at elevated temperatures. For the same amount of carbon feed and at 650 °C, the ease of the CSR reaction decreases in this order: glucose > ethanol > (furfural \approx acetic acid) > acetone > CH_4 .

Both experimental study and thermodynamic simulation [25, 181] indicated that CH_4 is a minor but common product from the steam reforming of bio-compounds, and can become significant at low temperature. The CH_4 formed by the decomposition of bio-compounds or by methanation (R5.5 and R5.6) [95, 99, 107] is undesirable as it impairs the H_2 yield. To reduce the concentration of CH_4 in the product, the operating temperature of a steam reforming process is recommended to be above 600 °C so that the CH_4 produced could be steam reformed (reverse R5.5). If a mild operating temperature is necessary (e.g. for the production of H_2 -rich gas

with low CO concentration), the decrease in the CH₄ yield could be accomplished by suppressing the kinetics of CH₄ formation. Hu and Lu [99] found that alkali metal modified Ni catalyst could effectively inhibit CH₄ formation during the steam reforming of acetic acid. They also found that methanation reactions were remarkably suppressed by acidifying neutral reforming feedstock (e.g. alcohols).

In addition to CH₄, CO is a common by-product in steam reforming process. As indicated in **Figure 5.1**, the WGS reaction (shifting the CO formed to CO₂) is favourable at low temperatures and cannot reach completion at temperatures above 150 °C ($\Delta G^\circ = -23.5$ kJ/mol at 150 °C). In the typical temperature range (600-850 °C) for a steam reforming process, the WGS reaction approaches equilibrium ($\Delta G^\circ \approx 0$). As a result, a sizeable amount of CO remains in the product. When high-purity H₂ is desired, for example for its use in proton exchange membrane fuel cells (PEMFC), downstream processes such as WGS reformer, preferential oxidation or methanation reactions, membrane/pressure swing adsorption [181] are usually employed for CO clean-up.

5.4 Influencing factors of equilibrium yields

In the temperature range of 200-850 °C and the molar steam to carbon ratio (S/C) range of 0-9, the equilibrium products from the bio-compound/steam system included H₂, CO, CO₂, H₂O, CH₄ and sometimes solid carbon. The bio-compounds input were completely converted to other species as they were not found in the product.

5.4.1 Temperature

The effect of temperature on the H₂ production was investigated for the bio-compound/steam system with S/C=3 (**Figure 5.2**), which represented an excess of steam for all the systems. The H₂ production from different bio-compounds exhibited a similar change trend with temperature. As the temperature was raised, the H₂ yield increased rapidly and reached a maximum at around 650 °C for all the bio-compounds (ca. 700 °C for CH₄ steam reforming). This significant increase in the H₂ yield below 650 °C could be explained as the steam reforming reaction (endothermic) which contributed to the H₂ production was promoted by a rise in temperature. Above 650 °C, the H₂ yield underwent a slight decline because high

temperatures resulted in a strong suppression of the WGS reaction (exothermic) or in favour of the H₂-consuming reverse WGS. Therefore, a further increase in the reaction temperature from 650 °C would not lead to an increase in the H₂ yield from the aspect of thermodynamics. The calculation for different S/C ratios (figures are not displayed here) showed that the temperature for the maximum H₂ yield was shifted to lower temperature as the S/C ratio increased [168, 185]. Under conditions of 650 °C and S/C=3, the H₂ yield from ethanol and acetone was the largest (22 wt%), which was twice that from acetic acid and glucose (11 wt%), although it was lower than that from CH₄ (39 wt%) as shown in **Figure 5.2b**. Compared with the CH₄ steam reforming, the steam reforming of these bio-compounds required a lower temperature to obtain the maximum H₂ yield (650 °C vs 700 °C).

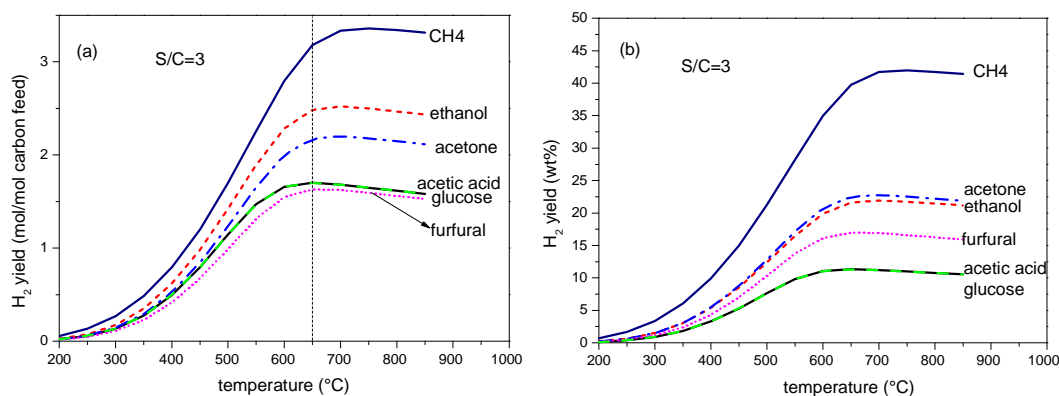


Figure 5.2 H₂ yield versus reaction temperature for the bio-compound/steam system at S/C=3 (a) in mol/mol carbon feed, (b) in wt% of the bio-compound input

Apart from H₂, gases CO₂, CO and CH₄ also existed in the equilibrium product and their yields are shown in **Figure 5.3**. The production of CO started to become significant above 500 °C. Increasing temperature favoured the production of CO (**Figure 5.3b**) probably through enhancing steam reforming reaction while inhibiting the WGS and methanation. The reactions producing CO₂ (R5.3 and R5.4) were facilitated by the increased CO concentration (as reactant) but suppressed by the elevated temperature due to their exothermic nature. The competition between these two factors led to CO₂ yield peaking at around 550 °C (**Figure 5.3a**).

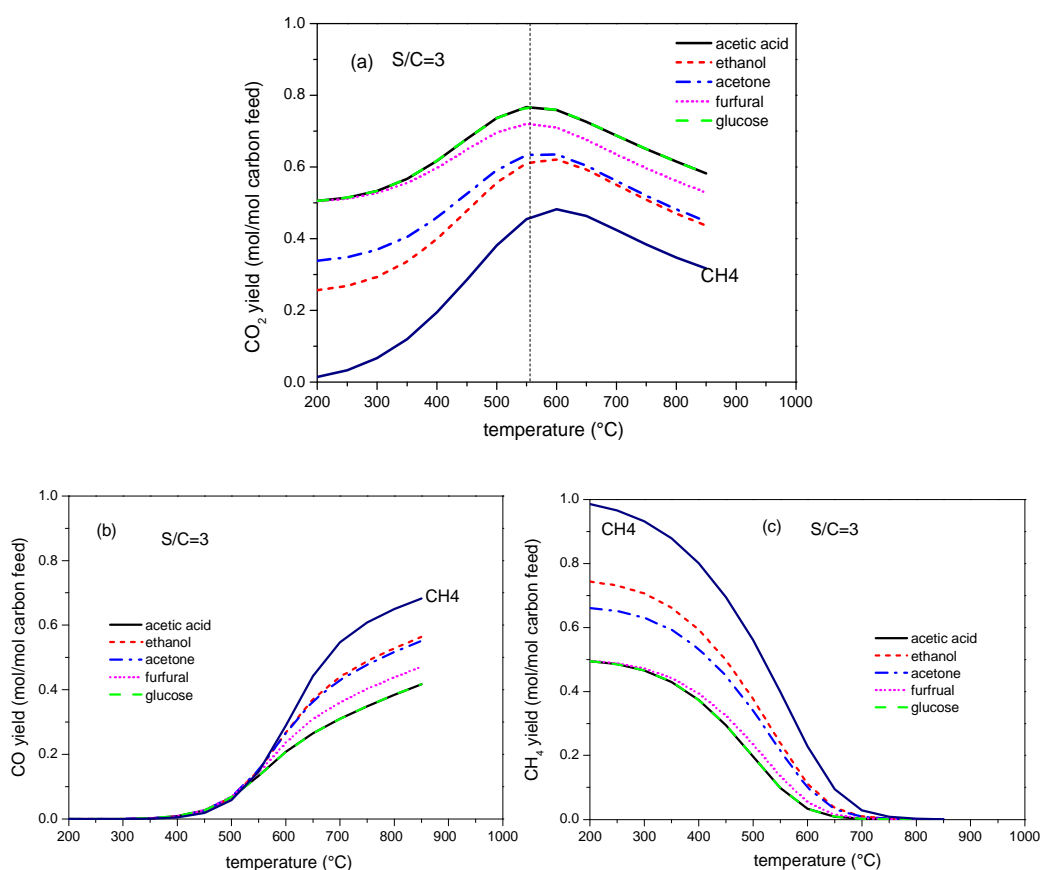


Figure 5.3 Carbon-containing product yields versus the reaction temperature for the bio-compound/steam system at S/C=3: (a) CO₂, (b) CO and (c) CH₄

CH₄ was the only product that competed with H₂ for hydrogen atoms. Thus, their yields were expected to show a converse trend. The CH₄ yield kept decreasing as the temperature rose (**Figure 5.3c**). CH₄ together with CO₂ were predominant products at low temperatures (200-350 °C). A sharp decrease in the CH₄ yield was observed between 350 and 600 °C, probably because methanation reactions R5.5 and R5.6 were strongly inhibited. Above 650 °C, the CH₄ steam reforming reaction took over methanation. As a result, the CH₄ yield became negligible.

5.4.2 Molar steam to carbon ratio (S/C)

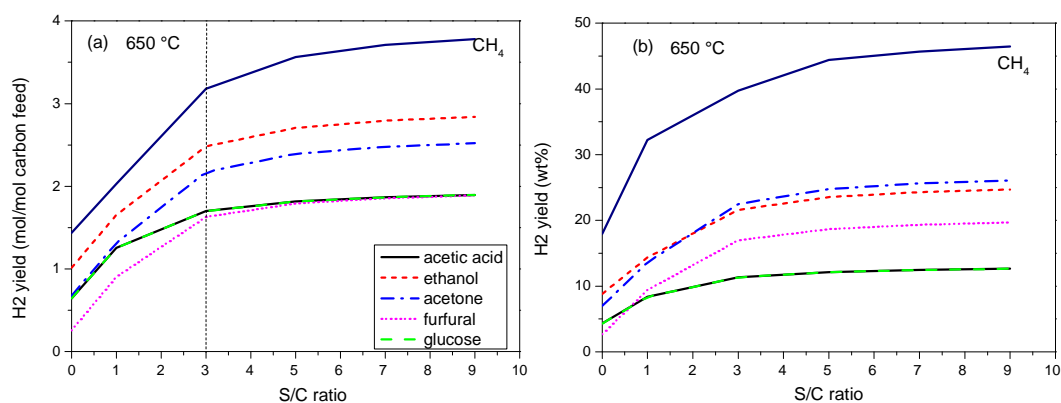


Figure 5.4 H₂ yield versus the S/C ratio for the bio-compound/steam system at 650 °C: (a) in mol/mol carbon feed, (b) in wt% of the bio-compound input

The variation of H₂ yield at 650 °C with S/C is shown in **Figure 5.4**. According to Le Chatelier's principle, a rise in steam content in the bio-compound/steam system would shift steam reforming and WGS in the direction of H₂ production. As a result, the equilibrium yield of H₂ would increase, as found in **Figure 5.4**. However, the enhancement in the H₂ yield by further increasing S/C beyond 3 was not as pronounced as that raising the S/C from 0 to 3. Moreover, a higher S/C represents escalating energy costs through energy intensive steam generation and larger infrastructure associated with operating with and recycling large volumes of vapour. Therefore, the optimum S/C of 3 for the steam reforming of bio-compounds was chosen.

Similar to the H₂ production, the production of CO₂ was also promoted by increasing S/C (**Figure 5.5a**). With S/C rising from 1 to 9, the CO yield decreased gradually as more CO was consumed by the enhanced WGS reaction (**Figure 5.5b**). But small amounts of CO still existed in the equilibrium product even at S/C=9, corroborating that the reverse WGS was significant at 650 °C (see **Figure 5.1**). The CO yield from bio-compound pyrolysis (expressed in the case S/C=0) was much lower than that for S/C=1 as the production of CO from pyrolysis was restricted by the availability of oxygen atoms in bio-compound molecules and by the fact that

some solid carbon was predicted in the equilibrium products (**Figure 5.9**). The sharp increase in the CO yield when raising the S/C ratio from 0 to 1 could be interpreted as the solid carbon formed being gasified by the H₂O added to the system (R5.7).

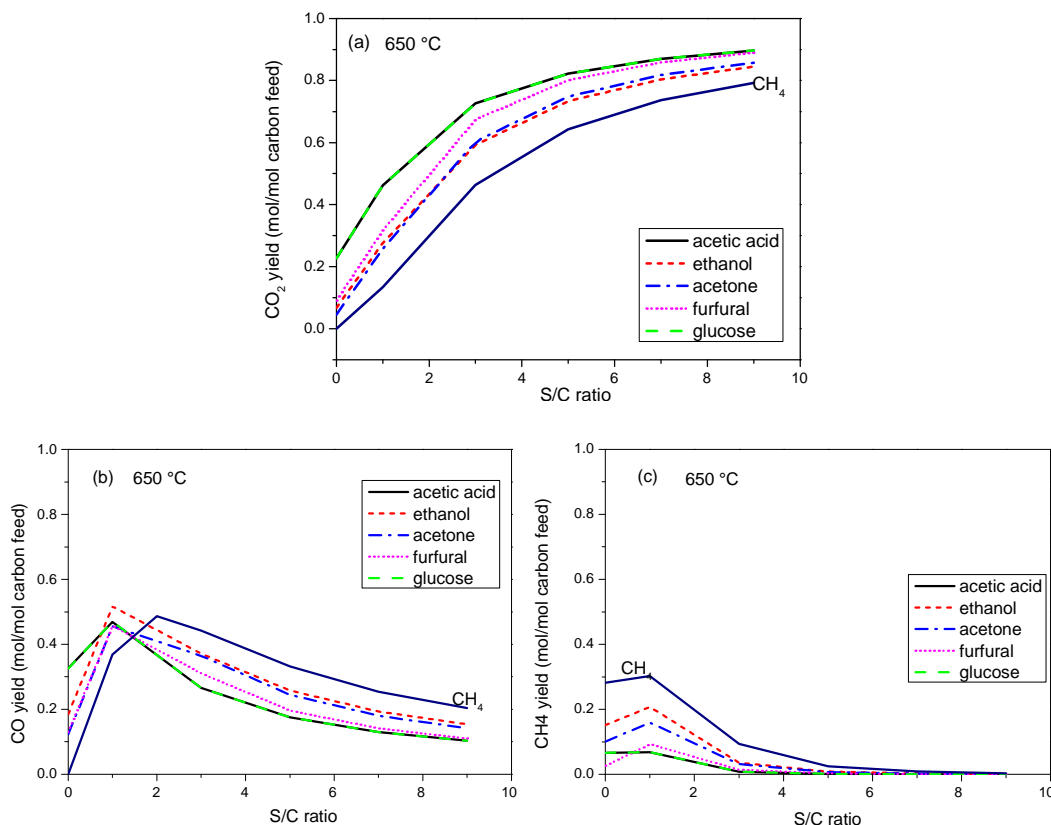


Figure 5.5 Carbon-containing product yields versus the S/C ratio for the bio-compound/steam system at 650 °C: (a) CO₂, (b) CO and (c) CH₄

The profile of CH₄ yield with respect to S/C (**Figure 5.5c**) was similar to that of the CO yield. A slight increase in the CH₄ yield was found when raising S/C from 0 to 1. With S/C further increasing, CH₄ production underwent a remarkable decline, probably resulting from the promoted CH₄ steam reforming reaction. At S/C= 4, the amount of CH₄ produced was negligible.

5.4.3 Molecular formulas of feedstock

5.4.3.1 Hydrogen-containing products (H₂ and CH₄)

Comparing the five bio-compounds and CH₄ as reforming feedstock, the H₂ yield (mol/mol C feed) under the same condition (e.g. 650 °C and S/C=3) declined in this order: CH₄ > ethanol > acetone > (acetic acid, glucose and furfural) (**Figure 5.2**). The production of CH₄ also decreased in the same order (**Figure 5.3c**). For different reforming feedstock, the difference in their H₂ or CH₄ yield may be related to the H/C ratio and O/C ratio in their molecules, which are listed in **Table 5.1**.

Table 5.1 Molecular composition of feedstock as well as equilibrium yields of H₂, CH₄, CO and CO₂

feedstock	molecular formula	O/C ratio	H/C ratio	^a CH ₄	^b H ₂	^b CO	^b CO ₂
furfural	C ₅ H ₄ O ₂	0.4	0.8	0.2339	1.6308	0.3103	0.6750
glucose	C ₆ H ₁₂ O ₆	1	2	0.1969	1.7009	0.2654	0.7262
acetic acid	C ₂ H ₄ O ₂	1	2	0.1968	1.7010	0.2654	0.7262
acetone	C ₃ H ₆ O	0.33	2	0.3404	2.1743	0.3650	0.6032
ethanol	C ₂ H ₆ O	0.5	3	0.3771	2.4839	0.3713	0.5925
methane	CH ₄	0	4	0.5606	3.1805	0.4428	0.4630

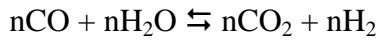
^aThe equilibrium yield of CH₄ (in mol/mol C feed) was calculated at 500°C and S/C=3

^bThe equilibrium yields of H₂, CO and CO₂ (in mol/mol C feed) were calculated at 650 °C and S/C=3

Among the five bio-compounds, the highest H₂ yield was obtained from the steam reforming of ethanol, which could be attributed to the high H/C ratio in ethanol molecule. When the bio-compounds had the same H/C ratio (e.g. acetone, acetic acid, and glucose), the bio-compound with a lower O/C ratio showed a higher H₂ yield (i.e. acetone). The H₂ yield from steam reforming of furfural was close to that

from the steam reforming of acetic acid and glucose probably because both the O/C and H/C ratios of furfural were relatively low. The general trend is that the H/C ratio makes a positive contribution to the H₂ and CH₄ yields while the O/C ratio has a negative impact on these two outputs.

Overall the trends reflected the stoichiometry of the steam reforming and WGS:



from which the maximum yield of H₂ per mol of carbon in the feed is therefore $(2+0.5 m/n - k/n)$, or using the O/C and H/C definitions, $(2 + 0.5 H/C - O/C)$.

The dependence of the H₂ and CH₄ yields (in mol/mol carbon feed) on the H/C and O/C ratios in the feedstock molecule was fitted into equations. The H₂ yield predicted at 650 °C and S/C=3 was used in the fitting while the CH₄ yield obtained at 500 °C and S/C=3 was selected as the variation of the CH₄ yield arising from using different feedstock was not obvious at a higher temperature (almost zero at 650 °C as shown in **Figure 5.3c**). The H/C and O/C ratios were incorporated in one parameter, namely molecular factor. It was found that the H₂ yield $Y(H_2)$ and the CH₄ yield $Y(CH_4)$ can be linearly fitted against molecular factors X_1 and X_2 , respectively as shown in **Figure 5.6** and Eq. 5.2-5.5.

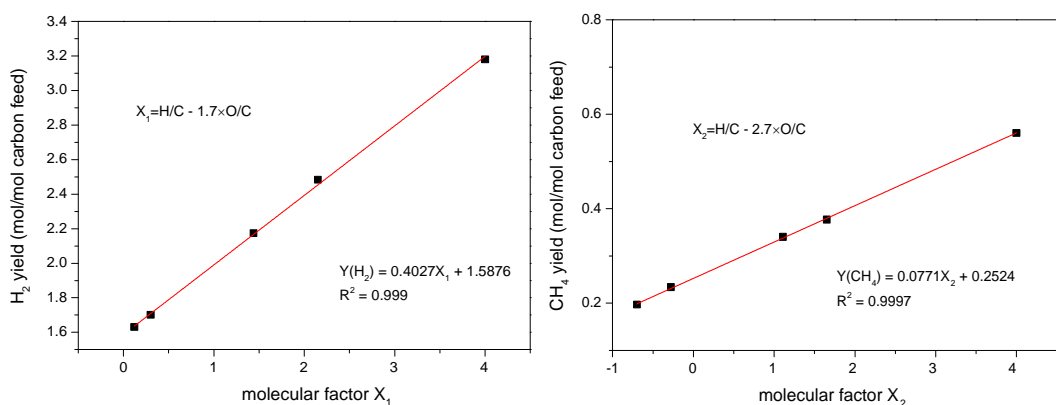


Figure 5.6 Dependence of (a) H₂ yield and (b) CH₄ yield on the molecular formula of feedstock used for steam reforming process (the H₂ yield was calculated at 650 °C and S/C=3, the CH₄ yield was at 500 °C and S/C=3)

$$X_1 = H/C - 1.7 \times O/C \quad (\text{Eq. 5.2})$$

$$Y(H_2) = 0.4027X_1 + 1.5876 \quad \text{with } R^2 = 0.9990 \quad (\text{Eq. 5.3})$$

$$X_2 = H/C - 2.7 \times O/C \quad (\text{Eq. 5.4})$$

$$Y(CH_4) = 0.0771X_2 + 0.2524 \quad \text{with } R^2 = 0.9997 \quad (\text{Eq. 5.5})$$

5.4.3.2 Oxygen-containing products (CO₂ and CO)

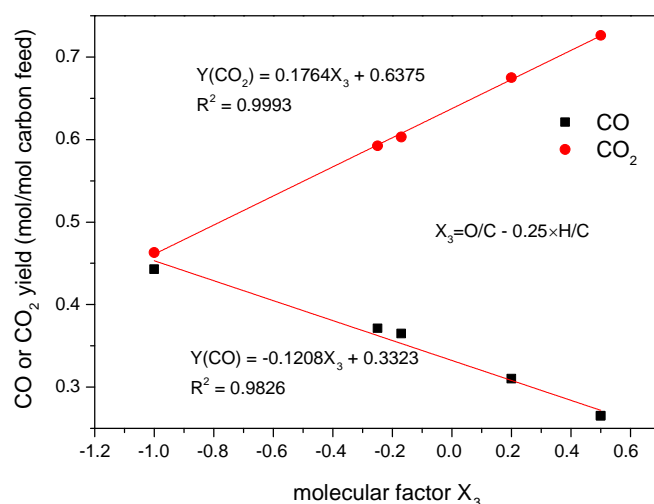


Figure 5.7 Dependence of the CO and CO₂ yields at 650 °C and S/C=3 on the molecular formula of feedstock used for steam reforming process

The ranking of bio-compounds as well as CH₄ according to their CO₂ yield (mol/mol of C feed) was as follows: (acetic acid, glucose) > furfural > (ethanol, acetone) > CH₄, which was just opposite to that based on their CO yield. It was found that the bio-compound with a high O/C ratio in its molecule tended to produce more CO₂ and less CO (e.g. acetic acid and glucose), compared to those with a low O/C ratio (e.g. furfural, acetone and ethanol). When the O/C ratio was similar (e.g. furfural, acetone and ethanol), the lower H/C ratio in furfural molecule was likely responsible for its higher CO₂ yield. The dependence of CO₂ yield $Y(\text{CO}_2)$ and the CO yield $Y(\text{CO})$ on the H/C and O/C ratios was also successfully fitted into equations (Eq. 5.7-5.8) as did to the H₂ yield and the CH₄ yield (**Figure 5.7**). Here, the molecular factor was defined as X_3 (Eq. 5.6) and the CO₂ and CO yields used in

the fitting were obtained at 650 °C and S/C=3.

$$X_3 = O/C - 0.25 \times H/C \quad (\text{Eq. 5.6})$$

$$Y(\text{CO}_2) = 0.1764X_3 + 0.6375 \quad \text{with } R^2 = 0.9994 \quad (\text{Eq. 5.7})$$

$$Y(\text{CO}) = -0.1208X_3 + 0.3323 \quad \text{with } R^2 = 0.9826 \quad (\text{Eq. 5.8})$$

Table 5.2 Comparison of the equilibrium yields obtained using the fitted equations (in black colour) and through CEA calculation (in red colour)

Compounds	formulas	^a CH ₄	^b CO	^b CO ₂	^b H ₂
methanol	CH ₄ O	0.3400	0.3368	0.6387	2.5652
		0.3526	0.3323	0.6375	2.5138
ketene	C ₂ H ₂ O	0.2273	0.3020	0.6847	1.6446
		0.2254	0.3021	0.6816	1.6480
acetaldehyde	C ₂ H ₄ O	0.3030	0.3409	0.6355	2.0648
		0.3025	0.3323	0.6375	2.0507
hydroxyacetic acid	C ₂ H ₄ O ₃	0.1040	0.1909	0.8069	1.3001
		0.0943	0.2115	0.8139	1.3661
propanol	C ₃ H ₈ O	0.3901	0.3837	0.5748	2.4504
		0.3886	0.3726	0.5787	2.4333
propanoic acid	C ₃ H ₆ O ₂	0.2665	0.3160	0.6669	1.9488
		0.2678	0.3122	0.6669	1.9366
1-hydroxy-2-butanone	C ₄ H ₈ O ₂	0.3030	0.3409	0.6355	2.0647
		0.3025	0.3323	0.6375	2.0507
phenol	C ₆ H ₆ O	0.3018	0.3573	0.6156	1.8675
		0.2948	0.3424	0.6228	1.8762
m-cresol	C ₇ H ₈ O	0.3184	0.3659	0.6036	1.9407
		0.3108	0.3496	0.6123	1.9500
2-methoxyphenol	C ₇ H ₈ O ₂	0.2858	0.3433	0.6337	1.8502
		0.2810	0.3323	0.6375	1.8522
2,6-dimethoxyphenol	C ₈ H ₁₀ O ₃	0.2740	0.3329	0.6467	1.8355
		0.2707	0.3248	0.6485	1.8343

^aThe equilibrium yield of CH₄ (in mol/mol C feed) at 500 °C and S/C=3,

^bThe equilibrium yields of CO, CO₂ or H₂ (in mol/mol C feed) at 650 °C and S/C=3.

The suitability of these fitted equations for other oxygenated hydrocarbons was checked. As shown in **Table 5.2**, the equilibrium yields of H₂, CH₄, CO and CO₂ calculated using these fitted equations were in good agreement with that obtained through CEA thermodynamic simulation. These fitted models are also applicable to a mixture of numerous hydrocarbons (e.g. bio-oil) as reforming feedstock provided that the generic molecular formula is given. It has to be noted that the calculation of equilibrium yields based on these fitted equations is restricted to the specific conditions (S/C=3, 650 °C for H₂, CO, and CO₂ yields while 500°C for CH₄ yield). Nonetheless, these fitted equations have a wide application in predicting the potential of various feedstocks for H₂ production without doing the repeated simulation work.

5.4.4 Equilibrium system with Ni/NiO: SR with NiO reduction

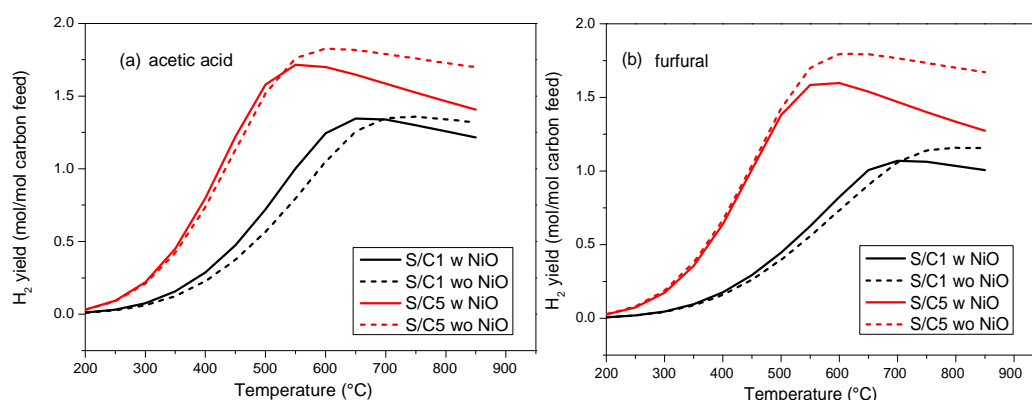


Figure 5.8 Effects of incorporating NiO reduction into the steam reforming system on the H₂ yield using (a) acetic acid and (b) furfural as feedstock ('w' represents 'with NiO reduction' in solid line and 'wo' represents 'without NiO reduction' in dash line)

At the onset of fuel feed in a chemical looping reforming process in packed bed configuration, the reduction of oxygen carrier (e.g. supported NiO) with fuel may take place simultaneously with the steam reforming of the fuel. Reduction of NiO with bio-compounds is more thermodynamically favourable than steam reforming of

bio-compounds (see Section 4.2 in Chapter 4). However, metallic Ni produced from NiO reduction acts as a catalyst for the steam reforming reaction, which significantly enhances the kinetics of this reaction. As a result, in practice, the steam reforming of bio-compounds may occur as soon as the NiO reduction is initiated (see Chapter 6 and 7). To simulate the co-existence of NiO reduction and steam reforming, the amount of the bio-compound input was designed to be the sum of two parts. One was to reduce NiO and the other was to take part in steam reforming. In the CEA simulation, an additional 1 mol of mixture of NiO and bio-compound (in stoichiometric ratio for CO₂ and H₂O final products) was added to the original reactant mix (the bio-compound/steam system). Here, the H₂ yield was calculated by dividing the moles of H₂ produced with the moles of carbon left for steam reforming after all the NiO was reduced.

As discussed in Chapter 4, the NiO reduction is a complete reaction with stoichiometric amounts of Ni, CO₂ and H₂O being produced. Hence, the influence of incorporating NiO reduction can be considered as the effect of additional CO₂ and H₂O on the equilibrium of bio-compound/steam system. The addition of H₂O would shift the system's equilibrium to producing more H₂ whereas the extra CO₂ would suppress the H₂ production. Which effect was dominant depended on the temperature and the S/C used, as predicted by equilibrium calculation (**Figure 5.8**). For S/C=1, the H₂ yield was enhanced at temperatures below 700 °C but inhibited above 700 °C, compared to that without containing NiO reduction. This result suggested that the positive effect on H₂ yield caused by additional H₂O was dominant at low temperature while the negative effect of extra CO₂ became overwhelming at high temperature. For S/C=5, the promotion of H₂ production due to H₂O addition (from NiO reduction) was negligible as abundant H₂O was available in the system. This effect was similar to that no significant increase in the H₂ yield was observed when further increasing the S/C from 3 to 9 (**Figure 5.4**). At high temperature, the suppression of H₂ production caused by the extra CO₂ became more remarkable since the reverse effect of H₂O was mitigated. To conclude, the incorporation of NiO reduction did not affect the H₂ yield at low temperatures but severely decreased the H₂ yield at temperatures higher than 550 °C for S/C=5.

5.5 Thermodynamic evaluation for carbon free region

One of the problems arising from the steam reforming of bio-oil is the thermal decomposition of oxygenated bio-compounds present in the bio-oil, which leads to severe carbon deposition. This is a main cause for the catalyst deactivation as the active sites are blocked by carbon deposits. Moreover, the carbon deposition may cause a pressure drop in the reactor.

5.5.1 Pyrolysis of bio-compounds

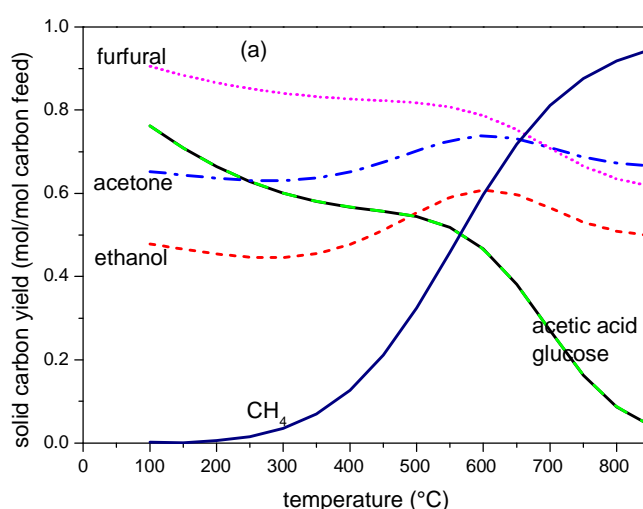


Figure 5.9 Yields of solid carbon from bio-compound pyrolysis over temperature range of 100-850 °C at 1 atm

The equilibrium decomposition products of bio-compounds were predicted by using the bio-compounds as the sole reactant in the CEA calculation. The variation of carbon formation with respect to temperature is shown in **Figure 5.9**. In contrast to CH₄, the oxygenated bio-compounds decomposed readily and produced carbon at temperatures as low as 100 °C. As the temperature rose, the carbon yield from a given bio-compound pyrolysis decreased or levelled off whereas the carbon yield from CH₄ pyrolysis went up steadily. The carbon yield from the pyrolysis of acetic acid and glucose underwent a sharp decline above 550 °C and approached zero at 850 °C. For the remaining three compounds, the influence of temperature on the

carbon yield was not significant. At 650 °C, the carbon yield decreased in the order of (furfural, acetone, CH₄) > ethanol > (acetic acid, glucose).

5.5.2 Dependence of carbon formation on temperature and S/C

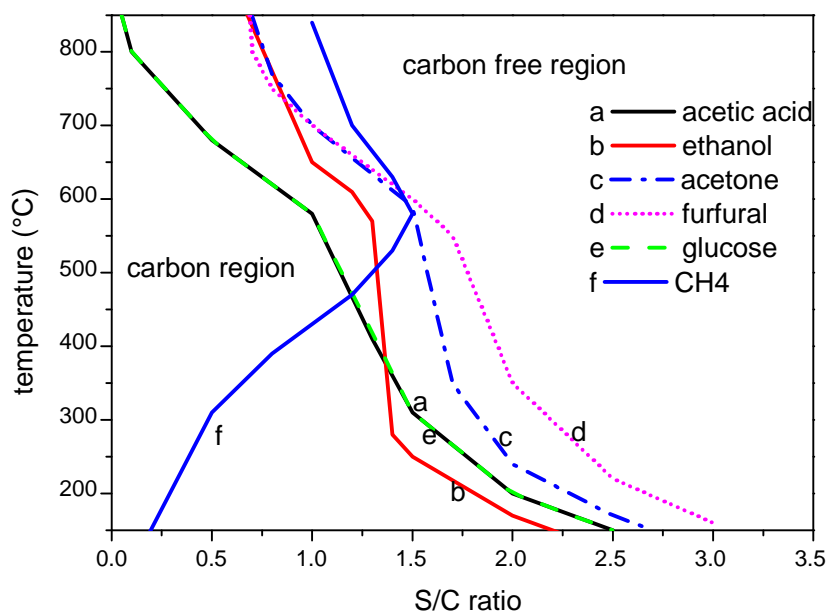


Figure 5.10 Thermodynamic domains (temperature and S/C ratio) for the avoidance of carbon formation at atmospheric pressure predicted by thermodynamic equilibrium calculation using CEA

In a steam reforming process, the carbon formation can be prevented by ensuring the S/C exceeds a certain minimum from the thermodynamic viewpoint. For different bio-compounds at a specific temperature, the smaller the minimum S/C ratio is, the more resistance to carbon formation the bio-compound exhibits.

Figure 5.10 depicts the thermodynamic domain (temperature and S/C) for the avoidance of equilibrium carbon at atmospheric pressure. The general trend found for all the five bio-compounds was that increasing the reaction temperature and increasing S/C favoured the suppression of equilibrium carbon. This trend could be interpreted as the endothermic reaction of carbon removal R5.7 was enhanced by high temperature and high S/C. At temperatures above 600 °C, the carbon product could be theoretically eliminated by using S/C beyond 1.5 for all the bio-compounds.

At 650 °C, the minimum S/C increased in this order: (acetic acid, glucose) < ethanol < (acetone, furfural) < CH₄. Below 600 °C, the carbon region for furfural steam reforming was considerably larger than that for the other bio-compounds, indicating furfural had a large tendency to form carbon at low temperatures. In contrast, ethanol became the most resistant to carbon formation at low temperature (below 400 °C).

For the CH₄/steam system, the dependence of carbon product on the temperature and S/C ratio was different from that for the bio-compounds, which is also illustrated in **Figure 5.11**. The trend it presented was that at a given S/C ratio, the carbon was formed in a temperature range. Out of this temperature range, equilibrium carbon was avoided. With the S/C increasing, the temperature range for carbon formation became narrow (**Figure 5.10**). The avoidance of equilibrium carbon at low temperature for the CH₄/steam system was attributable to the fact that the carbon formation from CH₄ pyrolysis was suppressed at low temperature (**Figure 5.9**).

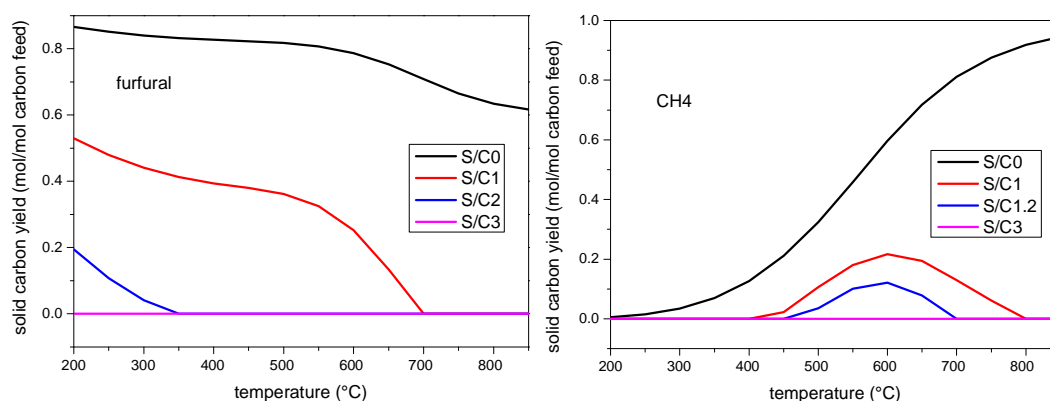


Figure 5.11 Dependence of equilibrium carbon on the temperature and the S/C: (a) furfural and (b) CH₄

5.6 Energy calculation

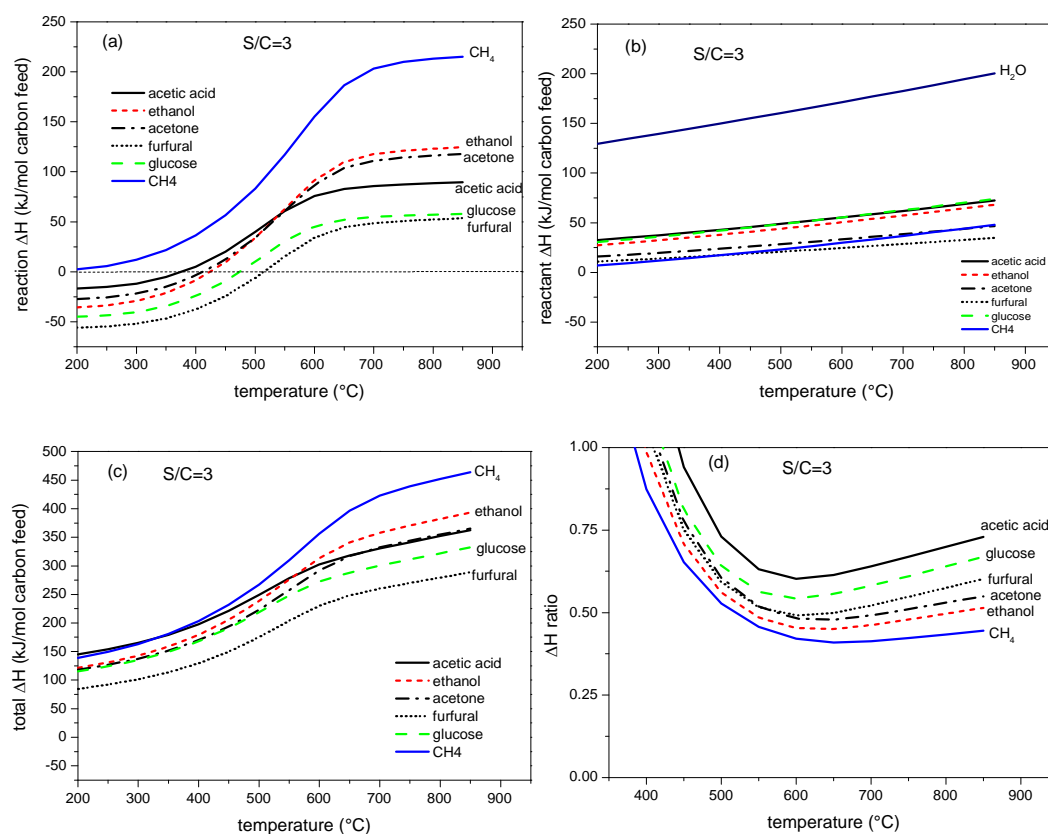


Figure 5.12 Energy balance for the system of bio-compound and water at S/C = 3: (a) energy demand for related reactions in steam reforming process, (b) energy demand for heating reactants (water and bio-compound) from room temperature to reaction temperature T, (c) the total energy demand ΔH_{total} , and (d) ΔH ratio

The system of bio-compound/water with S/C = 3 in the absence of NiO was selected for the energy calculation. The enthalpy change for the global reaction occurring for the bio-compound/steam system ($\Delta H_{\text{reaction}}$) increased with temperature (**Figure 5.12a**). At low temperature, the global reaction was exothermic, as indicated by negative $\Delta H_{\text{reaction}}$. In contrast, the global reaction for the CH₄/steam system was always endothermic and required a considerably higher energy for the same amount of carbon feed. The increase in the $\Delta H_{\text{reaction}}$ with temperature was slowed down above 650 °C.

Before the steam reforming takes place in the reformer, the reactant (bio-compound and water) need to be heated from the natural state at room temperature to vapour phase at reaction temperature T . From **Figure 5.12b**, it is found that the ΔH_{bio} of different bio-compounds are similar to each other and close to that for CH_4 . The energy for generating steam ($\Delta H_{\text{H}_2\text{O}}$) was much larger than ΔH_{bio} , indicating steam generation was the most energy intensive process. The total enthalpy change (ΔH_{total}) consisted of the three terms (Eq. 5.1). The $\Delta H_{\text{H}_2\text{O}}$ made the largest contribution to the total enthalpy change, followed by the $\Delta H_{\text{reaction}}$. At 650 °C, the total energy requirement for the same amount of carbon feed decreased in this order: $\text{CH}_4 > \text{ethanol} > (\text{acetone, acetic acid}) > \text{glucose} > \text{furfural}$ (**Figure 5.12c**).

The temperature range for ΔH ratio < 1 (considered as a viable process) is shown in **Figure 5.12d**. It was found that H_2 production from the bio-compounds by steam reforming process was viable at temperature above 450 °C. The smallest ΔH ratio (most energy efficient) was obtained between 600 and 650 °C. A further increase in the reaction temperature marginally raised the ΔH ratio, which was not favourable. Depending on the ΔH_{total} and the H_2 yield (see **Figure 5.2a**), the ΔH ratio at 650 °C increased in the order of $\text{CH}_4 < \text{ethanol} < \text{acetone} < \text{furfural} < \text{glucose} < \text{acetic acid}$. This result suggested, among the H_2 productions from the different bio-compounds tested, that from ethanol was the most viable while that from acetic acid was the least from an energy viewpoint.

In a CLR process, the energy required by the steam reforming process is supplied by the unmixed combustion of bio-compounds, in which the oxygen is transferred from the air to the reformer by means of an oxygen carrier (**Figure 5.13**, also see the concept of chemical looping reforming in Chapter 1). The energy gain from the bio-compound combustion and the energy consumption for the steam reforming of bio-compounds are shown **Table 5.3**. The former was calculated using the same method as the latter. It was the balance of the energy generated from the complete combustion (for CO_2 and H_2O final products) and the energy required for heating the reactants (O_2 and bio-compound) from natural phase at 25 °C to reaction temperature 650 °C. For an autothermal CLR process, the amount of NiO (in mol) taking part in the redox cycling for one mole of H_2 produced was defined as **NiO inventory**, which is also shown in **Table 5.3**. Low NiO inventory is desired in a

moving bed CLR configuration as less energy is required to circulate NiO between the air reactor and the fuel reactor. Among the five bio-compounds, furfural and ethanol need the lowest NiO inventory (0.74), which is slightly higher than that of CH₄. The largest NiO inventory (1.097) was observed when using acetic acid as feedstock for the chemical looping reforming process.

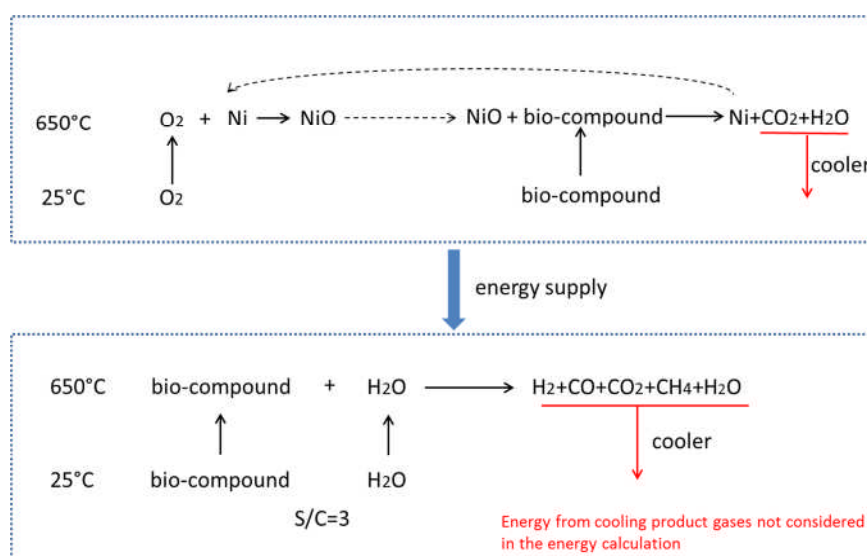


Figure 5.13 Schematic diagram of energy calculation for a chemical looping reforming system at 650 °C and S/C=3

Table 5.3 The energy balance for the combustion of bio-compounds and the steam reforming of bio-compounds as well as NiO inventory for 1 mol of H₂ produced in an autothermal CLR process at 650 °C and S/C=3

compound	ΔH for combustion (kJ/mol C feed)	ΔH_{total} for steam reforming (kJ/mol C feed)	H ₂ yield (mol/mol C feed)	NiO inventory
acetic acid	-341.2	318.4	1.701	1.097
ethanol	-554.6	340.8	2.484	0.742
acetone	-500.0	316.9	2.174	0.777
furfural	-411.8	248.3	1.631	0.739
glucose	-371.3	288.3	1.701	0.913
CH ₄	-727.5	396.9	3.181	0.686

5.7 Conclusions

The complete steam reforming (steam reforming followed by WGS) of all the bio-compounds were thermodynamically feasible at temperatures as low as 250 °C. However, a reaction temperature higher than 600 °C was recommended for the steam reforming of bio-compounds in order to reduce the concentration of CH₄ in products. A maximum H₂ yield was observed at around 650 °C if S/C=3 was used, above which the H₂ yield underwent a negligible decrease. The H₂ yield could also be improved by increasing the S/C ratio, but the improvement beyond S/C =3 was not as significant as that raising the S/C from 0 to 3. Under conditions of 650 °C and S/C=3, the H₂ yields from steam reforming of ethanol and acetone were the largest (22 wt% of the fuel), twice that from acetic acid and glucose (11 wt%), although it was lower than that from CH₄ (39 wt%), which is currently the main feedstock for industrial hydrogen production.

The equilibrium yields of H₂, CH₄, CO and CO₂ were successfully fitted as a linear function of the H/C and O/C ratios in the feedstock molecule at S/C of 3 and 650 °C, (CH₄ yield was fitted at 500 °C). Moreover, the suitability of these fitted equations for other oxygenated hydrocarbons was checked. To conclude, the equilibrium yields depend on the molecular formula of feedstock rather than the molecular structure if the feedstock input is thermally unstable. The numerical determination of the relationship between the equilibrium yields and the feedstock's molecular composition is useful for predicting the potential of various feedstocks in H₂ production, without doing repeated simulation work.

The region of temperature and S/C ratio for avoidance of carbon product was thermodynamically evaluated. The general trend found for all the bio-compounds was that high temperature and high S/C ratio favoured the suppression of carbon. Above 600 °C, the carbon product could be theoretically eliminated by using S/C beyond 1.5 for all the bio-compounds. At 650 °C, the tendency to carbon product decreased in this order: CH₄ > (acetone, furfural) > ethanol > (acetic acid, glucose).

H₂ production from the bio-compound/steam system with S/C=3 became energy efficient (ΔH ratio < 1) above 450 °C. The most energy efficient (smallest ΔH ratio) occurred between 600-650 °C. At 650 °C, the ranking of feedstock according to

their energy efficiency was $\text{CH}_4 > \text{ethanol} > \text{acetone} > \text{furfural} > \text{glucose} > \text{acetic acid}$. If the energy required by the steam reforming process was supplied by the unmixed combustion of bio-compounds (autothermal CLR), the amount of oxygen carrier NiO for one mole of H_2 produced was also calculated (defined as NiO inventory). Furfural and ethanol required the lowest NiO inventory, which was slightly higher than that for CH_4 .

Chapter 6

Nickel catalyst auto-reduction during steam reforming of bio-compound acetic acid

6.1 Introduction

This chapter demonstrates experimentally the reduction of reforming catalyst with acetic acid and the subsequent steam reforming performance. This process represents the half cycle of fuel feed in a chemical looping reforming process (see Chapter 1). In contrast to conventional steam reforming, in which catalysts are normally activated by H₂ or CH₄ just prior to catalysing the reforming reaction, the process studied here carries out the catalyst reduction using the reforming fuel directly (termed ‘integrated process’ and ‘auto-reduction’, respectively). Acetic acid (HAc) is selected as a model compound of bio-oil [25, 93, 94] as it is one of the major constituents present in bio-oil, with content that may be up to 30 wt% [26, 168, 192].

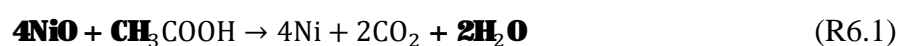
In this chapter, the feasibility of a nickel catalyst reduction with HAc was examined first. Secondly, the influence of reaction temperature and molar steam to carbon ratio (S/C) in the feed mixture on the reduction kinetics as well as the subsequent steam reforming of HAc was investigated. Moreover, the integrated process and conventional steam reforming process (initiated by H₂ reduction) were compared from aspects of reforming activity, loss of active Ni, carbon element distribution, and morphology of carbon deposits.

6.2 Experimental

6.2.1 Integrated catalyst reduction and steam reforming process

The integrated process was conducted in a down-flow packed bed reactor and using 18 wt% NiO/ α -Al₂O₃ catalyst, which were described in Chapter 3. The definition of process outputs as well as their calculation equations based on elemental balance can also be found in Chapter 3.

The integrated process was carried out at atmospheric pressure under a continuous N₂ flow of 200 sccm (as carrier gas) and in the absence of air. After the reactor was heated to a set temperature (550-750 °C), the pre-prepared HAc-water solution was fed into the reactor at a certain flow rate. Each experiment proceeded for about 45 min. The feed of liquid HAc into the reactor was constant at 1.174 mmol/min for all the experimental runs. Different S/C were achieved by changing the water content in the HAc solution. NiO reduction with HAc (R6.1), HAc steam reforming (R6.2) (according to the mechanism proposed by Wang et al. [38]) and water gas shift reaction (R6.3) are presented as follows. The overall stoichiometric reaction (R6.4) of steam reforming and water gas shift is also given.



Reactions R6.1 to R6.4 merely show the global mechanisms of production of the main species CO, CO₂ and H₂ and reduced Ni but do not represent the actual, more complex mechanism involving adsorption of reactants, dissociation and formation of intermediates on the catalyst surface, recombination reactions, and desorption of products from the catalyst. In particular, reaction R6.2 is chosen here with co-production of CO₂ and CO as opposed to the more logical decomposition of HAc into 2CO and 2H₂, to underline the observed early formation of CO₂ from steam reforming of HAc [38]. Once CO and H₂ appear in the products, they act in turn as reductants of NiO, but CO can also potentially methanate and disproportionate depending on prevalent local conditions. These result in formation of undesirable by-products CH₄ and solid carbon, which have slower kinetics of reaction with steam in the production of hydrogen.

6.2.2 Conventional steam reforming process (using H₂ to reduce catalyst)

After the reactor was heated to a certain temperature, the fresh catalyst was reduced by 5 % H₂/N₂ gas at a flow rate of 200 sccm (R6.5). The completion of reduction was evidenced by H₂ concentration returning to 5%. After that, steam reforming of HAc was carried out in the same procedure as described in Section 6.2.1.



6.2.3 Characterization

The characterization methods used in this chapter as well as corresponding instrument information have been described in Chapter 3.

The fresh and reacted catalysts were characterized by XRD. Based on the XRD data obtained, composition analysis and crystallites size analysis were carried out using the method of Rietveld refinement [193]. The surface morphology of reacted catalysts was scanned by SEM technique. Temperature-programmed oxidation (TPO) of reacted catalysts was conducted on a TGA-FTIR instrument. The samples were heated from ambient temperature to 900 °C with 10 °C/min under an air flow of 50 ml/min. The evolution of CO₂ from TPO process with respect to temperature was obtained by creating CO₂ chemigrams at 2250-2400 cm⁻¹. The amount of carbon deposited on the reacted catalyst was measured by CHN Elemental Analyser. Catalysts needed to be crushed into fine powder for XRD, TGA-FTIR and CHN tests whereas catalyst particles coated with a platinum layer of 10 nm were used directly for SEM imaging.

In addition to the aforementioned catalyst characterisation, the total carbon content of the condensate liquid collected from the packed bed reactor setup was analysed by TOC technique. Ni ion concentration in the condensate was detected using ICP-MS.

6.2.4 Thermodynamic equilibrium calculations

Thermodynamic equilibrium calculations based on minimisation of Gibbs free energy were implemented using the CEA program from NASA (See Chapter 3). In Chapter 5, the effects of temperature and S/C on the equilibrium of HAc/steam

system have been checked. In contrast to the work presented in Chapter 5, carrier gas N_2 was included in the reactant mixture in this work to simulate the actual conditions of the reactor. Equilibrium concentrations of H_2 , CO , CO_2 and CH_4 from the HAc/steam system at atmospheric pressure in the temperature range of 550-750 °C for different S/C were compared with the experimental data.

6.3 Results and discussion

6.3.1 Auto-reduction of NiO by HAc

6.3.1.1 Process analysis

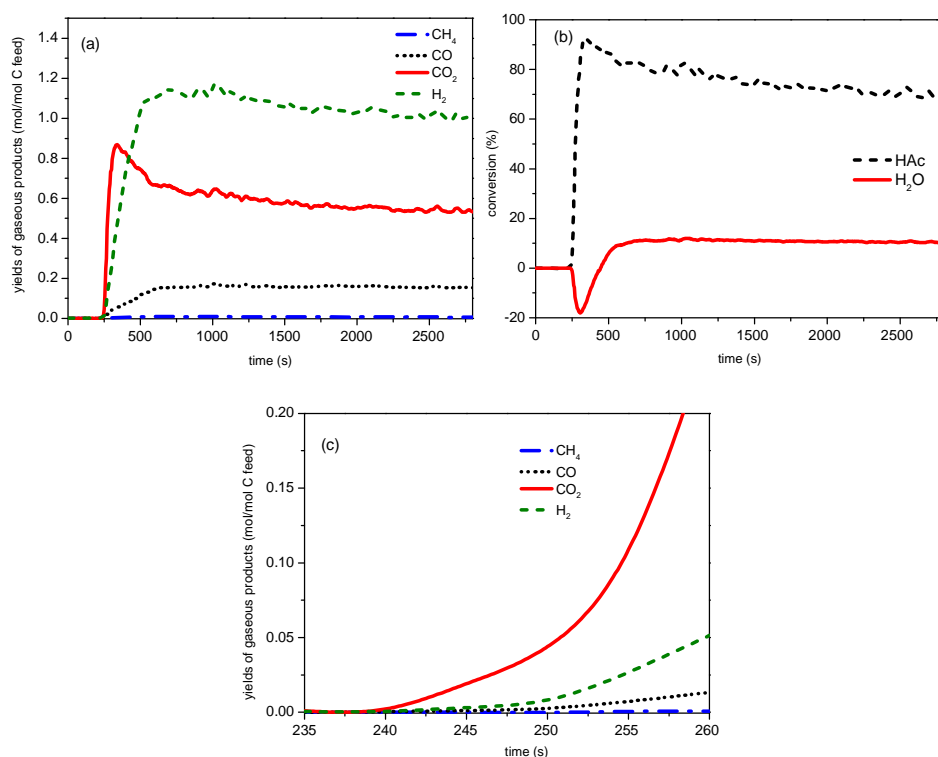


Figure 6.1 An integrated catalyst reduction and steam reforming experiment at 650 °C with S/C=3 (a) yields of gaseous products; (b) feedstock conversion and (c) zoom in the onset of reactions

An integrated catalyst reduction and steam reforming experiment at 650 °C with S/C=3 was chosen as representative of all the other conditions to analyse the auto-

reduction process. Yields of gaseous products as well as feedstock conversions with respect to time are shown in **Figure 6.1**. The occurrence of NiO reduction (R6.1) at the onset of the experiment was evidenced by H₂O formation (a negative H₂O conversion in **Figure 6.1b**), and by a large amount of CO₂ production (a significant CO₂ yield in **Figure 6.1a**). In previous studies [28, 194], NiO auto-reduction with reforming fuel (e.g. scrap tyre oil or bio-oil) was featured with clearly identified plateaus of CO₂ and H₂O, which indicated the reduction stage was almost separated from the subsequent reforming stage. However, an intermediate regime where reduction and reforming coexisted was shown in the present study as the production of CO and H₂ (indicator of steam reforming reaction) only lagged behind the CO₂ production (indicator of NiO reduction) by around 10 seconds (**Figure 6.1c**). The yields of H₂ and CO increased linearly, probably due to the continuous generation of metallic Ni which acted as catalyst of steam reforming reaction. After about 360 seconds, the yields of all the gaseous products as well as the feedstock conversions levelled off, suggesting the NiO reduction had ended and the steam reforming of HAC together with water gas shift became dominant and stable.

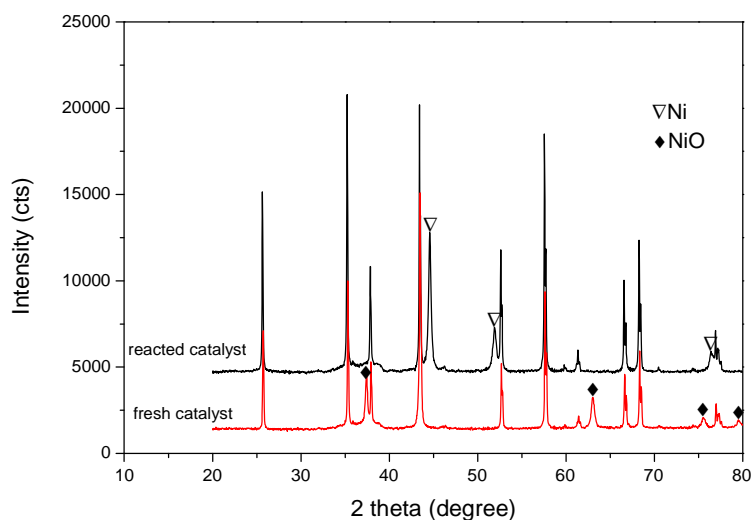


Figure 6.2 XRD patterns of the catalyst reacting for 360 seconds and the fresh catalyst: (▽) Ni characteristic peaks, (◆) NiO characteristic peaks, the other unmarked peaks are attributed to α -Al₂O₃

The complete conversion of NiO to metallic Ni was further supported by the fact that characteristic diffraction peaks of NiO disappeared whereas diffraction peaks of metallic Ni appeared in the XRD pattern of the catalyst after reacting for 360 seconds (**Figure 6.2**). Although the reduction was completed according to the XRD data, the reduction rate calculated using Eq. 3.7 did not return to zero (**Figure 6.3a**) and consequently the calculated conversion was larger than 100% (**Figure 6.3b**). The possible reason for this error will be discussed in Chapter 7. In this work, kinetics modelling was performed only on the conversion range of 0-50%.

When the reaction temperature fell to 500 °C, the reduction process could not proceed smoothly. Catalyst composition analysis based on the XRD data showed that only 38.6% of NiO was reduced to Ni in the first 1200 s of the experiment. For the other reaction temperatures (550 °C, 600 °C, 700 °C and 750 °C), 100% reduction could be achieved within hundreds of seconds depending on the temperature used. Therefore, 550 °C is considered as the lowest auto-reduction temperature of this catalyst when using HAc aqueous solution (S/C=3).

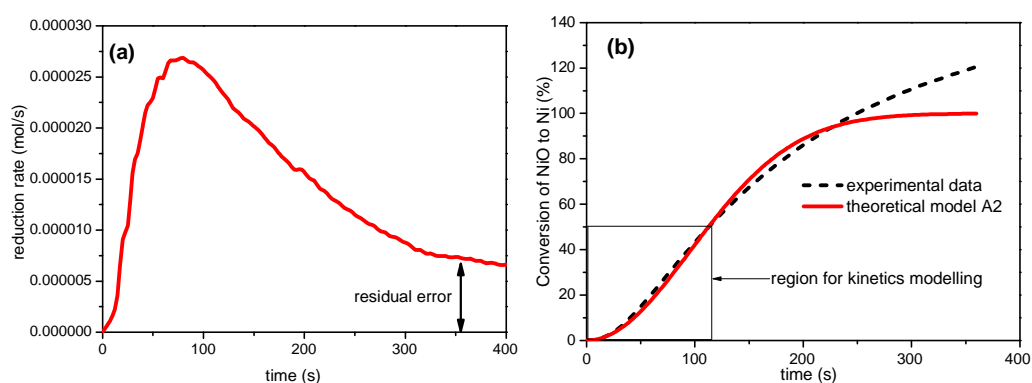


Figure 6.3 NiO reduction with HAc during an integrated process at 650 °C with S/C=3 (a) the reduction rate of NiO vs. time and (b) the conversion of NiO to Ni vs. time

6.3.1.2 Kinetics modelling

Kinetics of solid state reaction can be expressed as Eq. 6.1 or its integral form Eq. 6.2, where α is the conversion fraction of reactant in time t , k is the reaction rate constant, and $f(\alpha)$ or $g(\alpha)$ represent the reaction mechanism. The kinetic models

generally used fall into three groups [195-197]: (1) diffusion models, (2) geometrical contraction models and (3) nucleation and nuclei growth models. Related equations of these models are listed in **Table 6.1**.

$$\frac{d\alpha}{dt} = k \times f(\alpha) \quad (\text{Eq. 6.1})$$

$$g(\alpha) = \int \frac{d\alpha}{f(\alpha)} = k \times t \quad (\text{Eq. 6.2})$$

$$\alpha = 1 - \exp(-\beta \times t^m) \quad (\text{Eq. 6.3})$$

$$\ln(-\ln(1-\alpha)) = \ln(\beta) + m \times \ln(t) \quad (\text{Eq. 6.4})$$

Table 6.1 Kinetic models of solid state reactions [149, 197, 198]

Models	$g(\alpha)$	m
One-dimensional diffusion (D1)	α^2	0.62
Two-dimensional diffusion (D2)	$(1-\alpha)\ln(1-\alpha) + \alpha$	0.57
Three-dimensional diffusion by Jander (D3)	$[1-(1-\alpha)^{1/3}]^2$	0.54
Three-dimensional diffusion by Ginstling-Brounshtein (D4)	$1-2\alpha/3-(1-\alpha)^{2/3}$	0.57
first-order (F1)	$-\ln(1-\alpha)$	1.00
geometrical contraction (cylinder) (R2)	$1-(1-\alpha)^{1/2}$	1.11
geometrical contraction (sphere) (R3)	$1-(1-\alpha)^{1/3}$	1.07
Two-dimensional nucleation and nuclei growth (A2)	$[-\ln(1-\alpha)]^{1/2}$	2.00
Three-dimensional nucleation and nuclei growth (A3)	$[-\ln(1-\alpha)]^{1/3}$	3.00

Hancock and Sharp [196] developed a convenient method for kinetic model-fitting of isothermal solid state reactions based on the Avrami-Erofeyev equation (Eq. 6.3) and its transformation (Eq. 6.4), where β is a constant, m depends on the geometry of reactant particles and reaction mechanism. It was pointed out that experimental data obeying any one of the kinetic models in **Table 6.1** gives rise to approximately linear plots of $\ln[-\ln(1-\alpha)]$ vs. $\ln(t)$ if the range of α is limited to 0.15-0.5. The gradient m of such plots could be used to help select the most suitable kinetic model. Theoretically, the m value is located around 0.5 for diffusion controlled reactions,

around 1.0 for geometrical contraction controlled and first-order reactions, and 2.00 or 3.00 for nucleation and nuclei growth controlled reactions.

In the present study, the Hancock-Sharp method was employed. The m values varied with reaction temperatures and S/C used but were located between 1 and 2. It was difficult to distinguish among geometrical contraction models (R2, R3) and two-dimensional nucleation and nuclei growth model (A2) solely depending on m values. Hence, $g(\alpha)$ against t based on R2, R3 and A2 models were plotted. Such plots should have been straight lines if the corresponding theoretical model was fitting. For this reason, the coefficient of determination (R^2) for linear fit was used as a criterion of agreement with theoretical models. The A2 and R3 models were found to have R^2 much closer to 1 compared with the R2 model, representing better fits. The change trends of m values and R^2 values with respect to temperature or S/C ratio are shown in **Figure 6.4**. With temperature increasing from 550 to 650 °C or S/C ratio decreasing, the m value exhibited a rising trend, suggesting a progressive mechanism change from R3 to A2. That was why the R^2 for the A2 model increased whereas the R^2 for the R3 model decreased, as shown in **Figure 6.4**. After 650 °C, the m value was stable at about 1.75 and a satisfactory goodness of fit (with R^2 larger than 0.996) was attained for the A2 model. This indicated that the reduction reaction was isokinetic for the temperature range of 650-750 °C with S/C=3.

Normally, chemical reaction is the rate determining step of reactions which follow geometrical contraction models (or known as phase-boundary controlled models, shrinking core model) [39, 157, 199, 200]. Geometrical contraction models assume that nucleation occurs rapidly on the surface of the solid reactant. A reaction interface moves from the edge of a cylinder (R2) or the surface of a sphere (R3) toward the centre of the solid reactant with a constant rate.

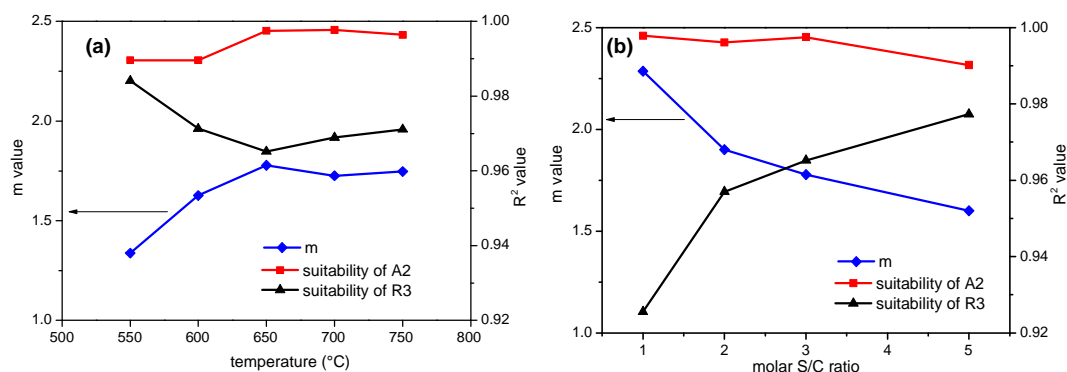


Figure 6.4 Change trend of m values and R^2 values of kinetic models (A2 or R3) with (a) temperature, and (b) S/C (A2: two-dimensional nucleation model, R3: geometrical contraction model of sphere, R^2 : R-squared value of linear fit)

Nucleation and nuclei growth models (also known as nucleation model, Avrami-Erofeyev models) [151, 195, 201] give a typical S-shape for conversion α against time t , starting slowly, rising rapidly, and then levelling off again. The macroscopic conversion-time behaviour is determined by the relative rate of nucleation, nuclei growth and the concentration of potential germ nuclei. As for the dimensionality of nuclei growth, Kanervo et al.[202] pointed out that three-dimensional nucleation and nuclei growth model (A3) was likely feasible only for reduction of bulk metal oxides while the A2 model was probably confined to reduction of supported oxide systems. In the present work, the A2 model is more acceptable than A3 probably because Ni crystallites have a tendency to form a two-dimensional overlayer on the α -Al₂O₃ support.

Although many studies suggested that reduction kinetics of NiO, either bulk or supported, obeyed geometrical contraction models [130, 157, 162, 200, 203], nucleation and nuclei growth models also found applications in kinetic analysis of NiO reduction [13, 158, 201, 204]. Hossain et al. [201] compared the nucleation model with the geometrical contraction model when studying reduction kinetics of a Co-Ni/Al₂O₃ catalyst. It was concluded that the adequacy of the nucleation model was superior to that of the geometrical contraction model for the system they studied. Hardiman et al. [204] directly applied the nucleation and nuclei growth model ($m=3$) to fit their experimental data because the profile of conversion vs. time they obtained

showed a characteristic S-shape. In these two studies, however, the interpretation of kinetic model in terms of reaction mechanism was not clarified.

In the present study, the A2 model is considered as the best-fit kinetic model as the R^2 values of fitting with A2 model was higher (>0.99) than that with R3 model. The presence of water in the reaction system may account for the fitness of A2 model. The influence of water on the reduction of NiO/ α -Al₂O₃ catalyst has been investigated by Richardson and Twigg [158] and a reduction mechanism was also proposed. The Ni atoms liberated from NiO crystallites through reduction migrated across the Al₂O₃ surface and reached a nucleation site where nuclei were formed and grew into crystallites. The water adsorbed on catalyst surface retarded the nucleation and nuclei growth by limiting the diffusion of Ni atoms across the Al₂O₃ surface. The textural factors of the catalyst also affected the role of water in retarding NiO reduction [162]. When hydrophilic additives, such as Ca and Mg, were present in the catalyst, the suppression of nucleation by adsorbed water was enhanced [159, 160]. In this work, the considerable amount of water present in reaction system may slow down the nucleation of Ni atoms and nuclei growth. Therefore, nucleation and nuclei growth became the rate determining step.

6.3.1.3 Apparent activation energy of NiO reduction

The relation of reduction rate constant k with temperature is represented by the Arrhenius equation (Eq. 6.5), where A is pre-exponential factor, E_a is the apparent activation energy and T is the absolute temperature. The rate constant k was obtained from the slope of $A2(\alpha)$ against t ($A2(\alpha)=[-\ln(1-\alpha)]^{1/2}$).

$$k = A \exp\left(-\frac{E_a}{RT}\right) \quad (\text{Eq. 6.5})$$

Two types of errors for the k values could be identified. One is the standard error produced when deriving k from α and t . The other is the standard deviation of two measurements which were carried out under the same condition. It was found the standard error is considerably smaller than the standard derivation. Hence, the error bar shown in the Arrhenius plot (**Figure 6.5**) was based on the standard deviation. It has to be noted that the feed of HAc solution, the flow rate of N₂, and the measurement of gas concentrations may also introduce some errors to k values as the

k values were derived from these quantities through several steps of calculations (see Eq. 3.1-3.7).

Inspection of these data points in **Figure 6.5** indicates that two kinetic regimes may exist with a transition temperature at about 650 °C as shown in dash lines. The linear fit of the data points below 650 °C (line 1, $R^2=0.970$) is not as satisfactory as that for higher temperatures (line 2, $R^2=0.998$). The small number of data points (3 data points) in each regime makes these two fits less justified. An adequate correlation coefficient ($R^2=0.973$) is obtained when fitting these five points into one line (line 3). Moreover, the activation energies obtained from the three lines are close to each other (30 ± 2 kJ/mol, 40 ± 4 kJ/mol, 38 ± 4 kJ/mol, respectively). Considering these facts, one line fit was used tentatively. A similar treatment can be found in ref [130]. This decision does not affect the main conclusion that at the same temperature the reduction rate constant of HAc is smaller than those of acetone and ethanol but larger than those of furfural and glucose (see Section 7.6). To determine which assumption (a single line or two lines) is more suitable, more data points are required in the future.

Derived from the slope of line 3 (**Figure 6.5**), the E_a of NiO reduction with HAc was 38 ± 4 kJ per mol of NiO, within the breadth of 14-114 kJ/mol found in the literature when using H_2 , CO or CH_4 as reducing agents [130, 157, 162, 200, 201, 203].

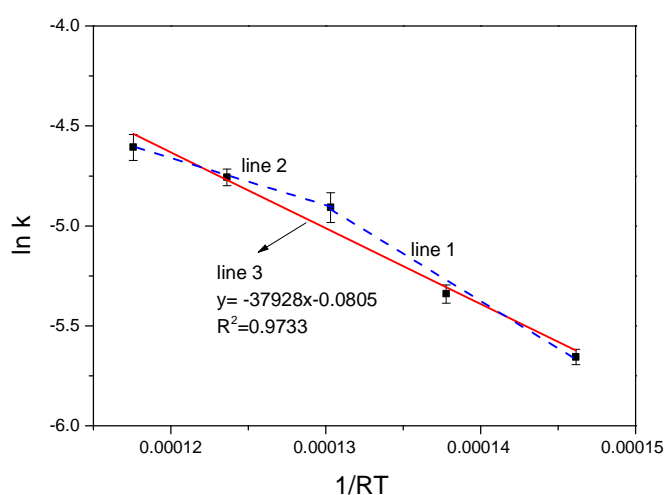


Figure 6.5 Arrhenius plot of NiO reduction by HAc solution with S/C=3 for the NiO to Ni conversion range of 0-50%

6.3.1.4 Effects of water content on NiO reduction

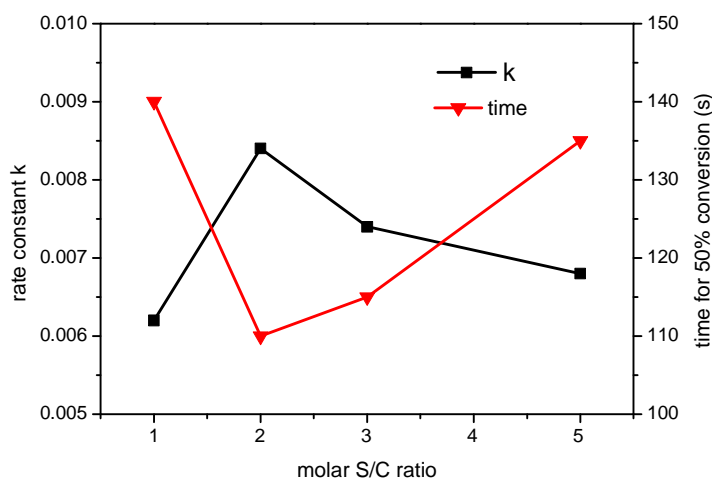


Figure 6.6 Influence of water content on the reduction rate constant and reduction time at 650 °C

As **Figure 6.6** shows, the rate constant of NiO reduction exhibited a correlation to water content in the feed stream, which supported the argument that water has an important role in the reduction mechanism. The largest reduction rate constant was obtained at $S/C=2$. It is understandable that the reduction rate constant decreased as the S/C increased from 2 to 5 because water retained on the catalyst surface impeded the nucleation of Ni atoms and nuclei growth. To explain why the reduction rate constant for $S/C=1$ was smaller than that for $S/C=2$, a set of comparative experiments were carried out and their experimental conditions are listed in **Table 6.2**. After steam reforming experiments, the reacted catalysts were collected for TGA-FTIR tests under the same TPO condition. Corresponding CO_2 chemigrams (Intensity of CO_2 IR signal vs. temperature) are compared in **Figure 6.7**.

Two CO_2 emission peaks were shown for the run 1 sample (**Figure 6.7a**), indicating two different carbonaceous materials were deposited on the catalyst surface. They accounted for one CO_2 peak at 330 °C and the other at 530 °C, respectively. For convenience, they are denoted as 330 CD ('carbon deposits') and 530 CD hereafter. The existence of two CO_2 peaks during the TPO of used catalyst has been reported in the literature [205-207]. It was generally believed that the lower temperature peak

(around 300 °C) was due to the coke deposited on active metal, while the higher temperature peak (around 550 °C, the most significant one) was attributed to the coke formed on the support. In addition to different deposition sites, the structures of the two types of coke were considered different. The former consisted of polyaromatic compounds whereas the latter had a pseudo-graphitic structure.

Table 6.2 Reaction conditions for a set of comparative experiments

Run no.	Solid material	Reduced by	S/C
1	NiO/Al ₂ O ₃	HAc	1
2	NiO/Al ₂ O ₃	H ₂	1
3	NiO/Al ₂ O ₃	HAc	2
4	bare Al ₂ O ₃	---	1

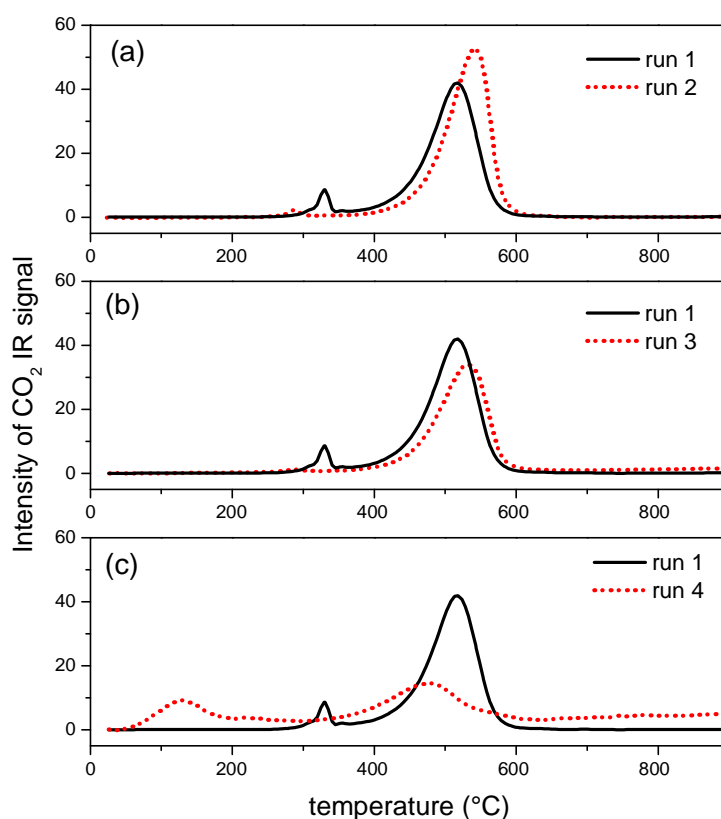
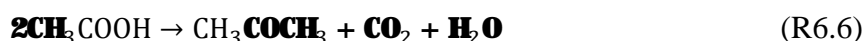


Figure 6.7 CO₂ chemigrams (2250-2400 cm⁻¹) during the TPO of reacted catalysts (a) different reducing agents (b) different S/C ratios (c) NiO/ α -Al₂O₃ catalyst and bare α -Al₂O₃

In this study, the comparison of run 1 with run 2 (**Figure 6.7a**) implied that 330 CD was only formed during NiO reduction with HAc. The comparison of run 1 with run 3 (**Figure 6.7b**) indicated that the formation of 330 CD only occurred at low S/C. In contrast, the 530 CD was common to samples of run1, run 2 and run 3 as well as the the bare α -Al₂O₃ sample (**Figure 6.7c**). This result indicated that the 530 CD was produced, at least partially, due to reactions occurring on the Al₂O₃ surface. Ketonization of HAc (R6.6) is a common reaction when support materials are used without active phase [207, 208]. The acetone produced could further undergo oligomerization reactions via intermediate mesityl oxide to form coke [209]. This type of coke may contribute to the CO₂ peak locating at 530 °C. The reason for the 330 CD will be discussed below.



As has been described in the literature [161, 162, 166], the first step of NiO reduction is the dissociation of the reducing agent to form adsorbed radical species, initially by NiO, then by metallic Ni as it becomes available. In the case of using HAc as reductant, a series of dissociation reactions (R6.7-6.9) may take place and result in the production of adsorbed radicals H_{ads} and (CH₁₋₃)_{ads} [38]. Desorption and re-adsorption of these radicals could also occur on the catalyst surface [164, 166]. The H_{ads} radicals formed on Ni sites either play the role of reducing species when re-adsorbed onto NiO surface or produce H₂ when combining with each other. (CH₁₋₃)_{ads} may also desorb from the Ni surface, diffuse and then adsorb on the NiO surface, causing NiO reduction. The desorption of radicals from Ni and re-adsorption onto NiO are essential to the occurrence of reduction reaction [166]. For those (CH₁₋₃)_{ads} still adsorbed on the Ni surface, there are two possible reaction pathways. One is to be gasified by steam to produce CO and H₂ (steam reforming, R6.10), both of which have strong reducing ability. The other is to accumulate to form coke on Ni sites (R6.11). In the present work, (CH₁₋₃)_{ads} on Ni sites could not be gasified sufficiently due to the low steam content (S/C=1), and hence formed coke which contributed to the CO₂ emission peak at 330 °C. This type of coke would have adversely affected the dissociation of HAc on Ni sites and subsequently the formation of reducing species (e.g. (CH₁₋₃)_{ads}, H_{ads}). To conclude, the lack of reducing species as well as the suppression of HAc dissociation resulting from low

steam content may be responsible for the smallest reduction rate constant observed at $S/C=1$. The presence of water in the feedstock does not always have a negative impact on the NiO reduction. The S/C of 2 was found to be optimal for the NiO reduction in this study. According to the discussion above, the reduction reaction mechanism is illustrated in **Figure 6.8**.

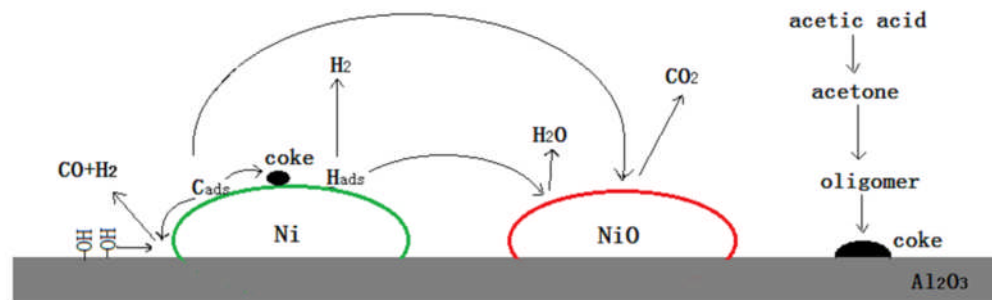
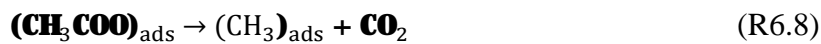


Figure 6.8 Mechanism diagram of NiO/ α -Al₂O₃ catalyst reduction with HAc solution

6.3.2 Steam reforming performance in the integrated process

The integrated process of catalyst reduction and steam reforming has been examined at a series of temperatures or with different S/C ratios. Only H₂, CO₂, CO and small quantities of CH₄ were detected in the reformat. Average values of feedstock conversions, H₂ yield and gas concentrations over the test period were used to demonstrate the effects of temperature and S/C on the steam reforming performance. Previous studies [207, 208] have shown that there was a complex reaction network

during steam reforming of HAc on Ni based catalysts. Apart from the steam reforming reaction (R6.2) and water gas shift (R6.3), several side reactions like thermal decomposition ($\text{CH}_3\text{COOH} \rightarrow \text{CH}_4 + \text{CO}_2$), ketonization (R6.6), and CO disproportionation ‘Boudouard reaction’ ($2\text{CO} \rightleftharpoons \text{CO}_2 + \text{C}$) may take place as well.

6.3.2.1 Effects of temperature

Figure 6.9 shows the influence of reaction temperature on the steam reforming performance of HAc (in solid line). As **Figure 6.9a** reveals, the H_2 yield and the HAc conversion experimentally obtained kept increasing as the temperature rose while the H_2O conversion remained almost stable. An increase in the reaction temperature favoured the endothermic steam reforming reaction (R6.2, $\Delta H_{298\text{K}}=170.8 \text{ kJ/mol HAc}$) thermodynamically and kinetically and hence led to an increase in the HAc conversion. The constant H_2O conversion resulted from a balance between the promoted steam reforming reaction and the restrained water gas shift (both reactions consumed H_2O) as the temperature increased.

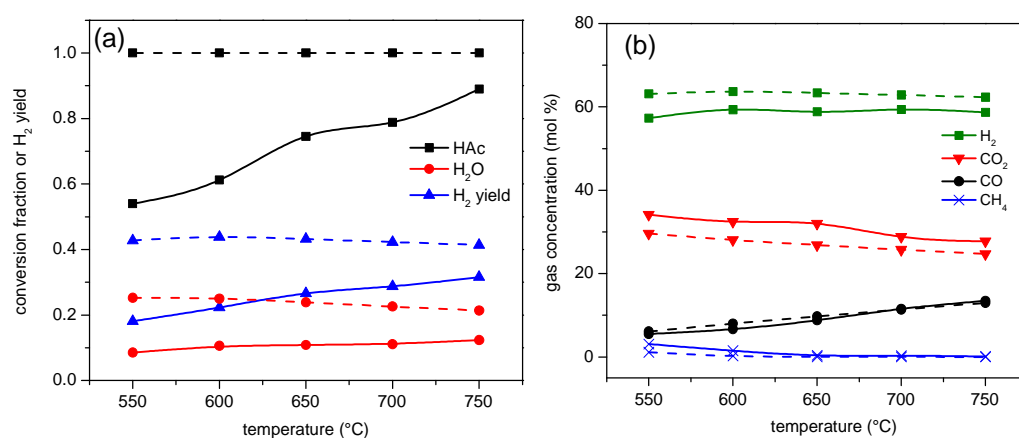


Figure 6.9 Effects of temperature on steam reforming performance at S/C=3 (a) conversion fractions of HAc and water as well as H_2 yield in mol/mol C feed, (b) gaseous product concentration in dry outlet gas excluding N_2 (solid line: experimental data, dash line: thermodynamic equilibrium data)

As for the composition of the reformat (Figure 6.9b), the H_2 concentration seemed unaffected by temperature in the range studied, but concentrations of the other three

gases changed with temperature. CH₄ concentration dropped to approximately zero as the temperature increased to 650 °C probably because the endothermic steam reforming of CH₄ was enhanced by an increased temperature to the detriment of methanation. The contribution of CH₄ steam reforming to H₂ production compensated the decrease in the H₂ production caused by the inhibition of water gas shift. As a result, the H₂ concentration levelled off in the temperature range of 550-750 °C. Meanwhile, the suppression of both water gas shift and Boudouard reactions (exothermic) by elevated temperatures led to an increase in the CO concentration and a decrease in the CO₂ concentration as shown in **Figure 6.9b**.

When the reaction temperature was below 650 °C, a large amount of carbon was deposited on the reactor wall probably through Boudouard reaction. When the temperature was raised to 650 °C or above, the carbon deposition on the reactor wall could be eliminated. The thermodynamic equilibrium calculation in Chapter 5 has shown that the carbon formation could be avoided at temperatures above 600 °C and S/C beyond 1.5. However, the experimental condition for avoidance of carbon product is more severe than that thermodynamically predicted, indicating that the carbon removal reactions are controlled by kinetics.

6.3.2.2 Effects of S/C

The effect of S/C ratio on the performance of HAc steam reforming is illustrated in **Figure 6.10**. As shown in **Figure 6.10a**, the HAc conversion and the H₂ yield were increased by using a higher S/C. This was because increased steam content promoted both steam reforming and water gas shift reactions to produce more H₂. The enhancement of water gas shift reaction also led to the decrease in the CO concentration and the increase in the CO₂ concentration as shown in **Figure 6.10b**. The decrease in H₂O conversion could be ascribed to the increased feed of water. Apart from steam reforming and water gas shift reactions, the CH₄ steam reforming reaction was also favoured at a high S/C. At S/C=3, the amount of CH₄ in the reformat was negligible.

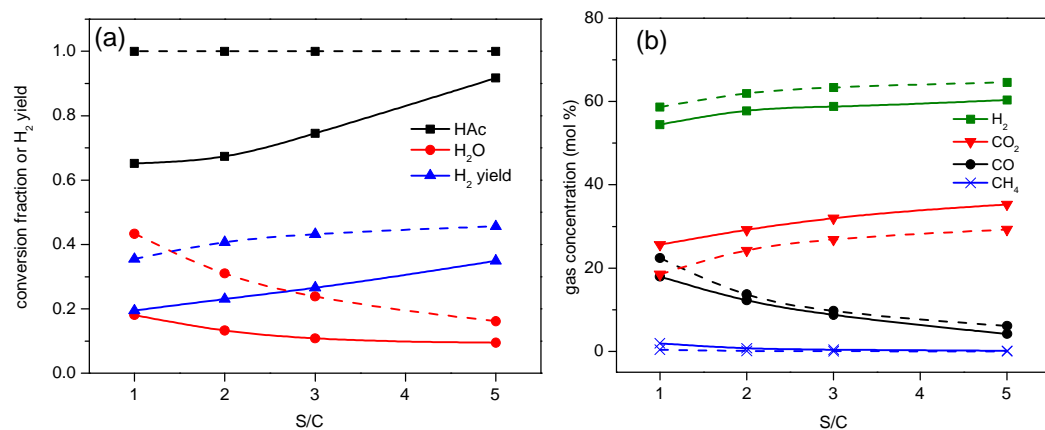


Figure 6.10 Effects of S/C ratio on steam reforming performance at 650 °C (a) conversion fractions of HAC and water as well as H₂ yield in mol/mol C feed, (b) gaseous product concentration in dry outlet gas excluding N₂, (solid lines: experimental data, dash lines: thermodynamic equilibrium data)

The steam reforming performance of HAC observed in the integrated process was comparable with results obtained via a conventional steam reforming process [98, 101, 210-212] (summarised in **Table 6.3**).

Table 6.3 H₂ yield from steam reforming of HAC in the literature

Catalysts	Temperature (°C)	S/C	HAc conversion fraction	H ₂ yield (mol/mol C feed)	Reference
15%Ni/Al ₂ O ₃	600	2	0.45	0.14	[211]
17%Ni/Al ₂ O ₃	750	1.5	0.80	0.50	[210]
20%Ni/Al ₂ O ₃	400	2.5	0.80	0.26	[98]
30%Ni/Al ₂ O ₃	400	7.5	0.68	0.33	[212]
15%Ni/Al ₂ O ₃	650	3	0.75	0.33	[101]
		6	0.95	0.46	
18%NiO/Al ₂ O ₃	750	3	0.89	0.32	present work
	650	3	0.75	0.27	

6.3.2.3 Comparison of experimental data with thermodynamic equilibrium data

The results of thermodynamic equilibrium calculation for HAc/steam system are also shown in **Figure 6.9** and **Figure 6.10** (in dash line). The HAc conversion reached 100% at equilibrium for the conditions studied in this work. Compared to the equilibrium data, a lower H₂ yield (around 25% lower than its counterpart at equilibrium at 750 °C for S/C=3) was obtained experimentally, along with lower conversions of HAc and water. The main reason for the discrepancy between the equilibrium data and the experimental data was the kinetic limitation on steam reforming reaction. Some of HAc molecules and intermediate products did not have enough time to react with water over the catalyst before being flushed out of the reactor.

With temperature increasing (**Figure 6.9a**), this gap decreased suggesting that steam reforming reaction was accelerated at high temperature and got closer to equilibrium. The increase in the steam content also improved the conversions of HAc and water as well as the H₂ yield to approach their equilibrium data as shown in **Figure 6.10a**. This was probably because the kinetics of steam reforming reaction was enhanced by increasing the concentration of reactant (i.e. steam). Although the feedstock conversion and H₂ yield experimentally obtained were below equilibrium, the gaseous product composition was in a good agreement with the equilibrium values except for a slightly higher CO₂ concentration and lower H₂ concentration (**Figure 6.9b** and **Figure 6.10b**). In summary, the improvement of kinetics by elevating temperature, increasing the contact time of HAc with catalyst (decrease the weight hourly space velocity), or using catalysts with high activity will bring the steam reforming performance closer to its thermodynamic equilibrium.

6.3.2.4 HAc auto-reduced and H₂-reduced catalyst activities in steam reforming

In contrast to conventional steam reforming, here the NiO catalyst is auto-reduced by the reforming fuel in an integrated process. It is well known that reduction conditions, such as reducing agent, temperature, duration and the presence of steam, affect catalyst activity in subsequent steam reforming [147]. To find out the difference between the auto-reduced catalyst and the H₂-reduced catalyst, a set of comparative experiments were conducted. For convenience, the samples collected

from the integrated and the conventional steam reforming processes are denoted as ‘HAc sample’ and ‘H₂ sample’, respectively. Experimental conditions and test results are listed in **Table 6.4**.

As shown, the steam reforming activity of the catalyst reduced with HAc was slightly inferior to that of the H₂-reduced catalyst. The influence on Ni crystallite size of using different reducing agents was not evident as the Ni crystallite sizes of both HAc and H₂ samples were located in the range of 33-34 nm. With respect to carbon element distribution, there was a remarkable difference between the integrated process and the conventional process. Compared to the conventional process, less carbon was deposited on the used catalyst and a slightly lower carbon conversion to gases was obtained in the integrated process. However, the carbon content detected in the liquid condensate from the integrated process was higher than that from the conventional process. This indicated that more intermediates such as acetone were formed in the integrated process.

Table 6.4 Comparison of the integrated process (using HAc as reductant) and conventional steam reforming process (using H₂ as reductant)

Run no.	Conditions		Reforming activity		Characterization results			
	Reductant	S/C	HAc conversion fraction	H ₂ yield (mol/mol C feed)	C _s content (wt%)	C _l content (g/L)	Ni content (mg/L)	Ni crystallite size (nm)
5	HAc	2	0.67	0.23	1.9	88	90	34
6	H ₂	2	0.73	0.25	2.2	77	65	33
7	HAc	1	0.65	0.195	2.6	133	333	34
8	H ₂	1	0.72	0.22	3.1	128	247	34

Note: all experiments were performed at 650 °C with the same HAc feed rate

C_s: carbon on catalyst

C_l: carbon in condensate

ICP results revealed that some Ni atoms broke away from the catalyst and flowed into the condensate during steam reforming. HAc reacts with neither NiO nor Ni at room temperature. However, during steam reforming, the high temperature as well as the presence of steam makes the corrosion of NiO or Ni by HAc possible.

Moreover, it was found that the Ni loss from the HAc sample was more considerable than that from the H₂ sample, which probably accounted for the small drop in the steam reforming activity [36].

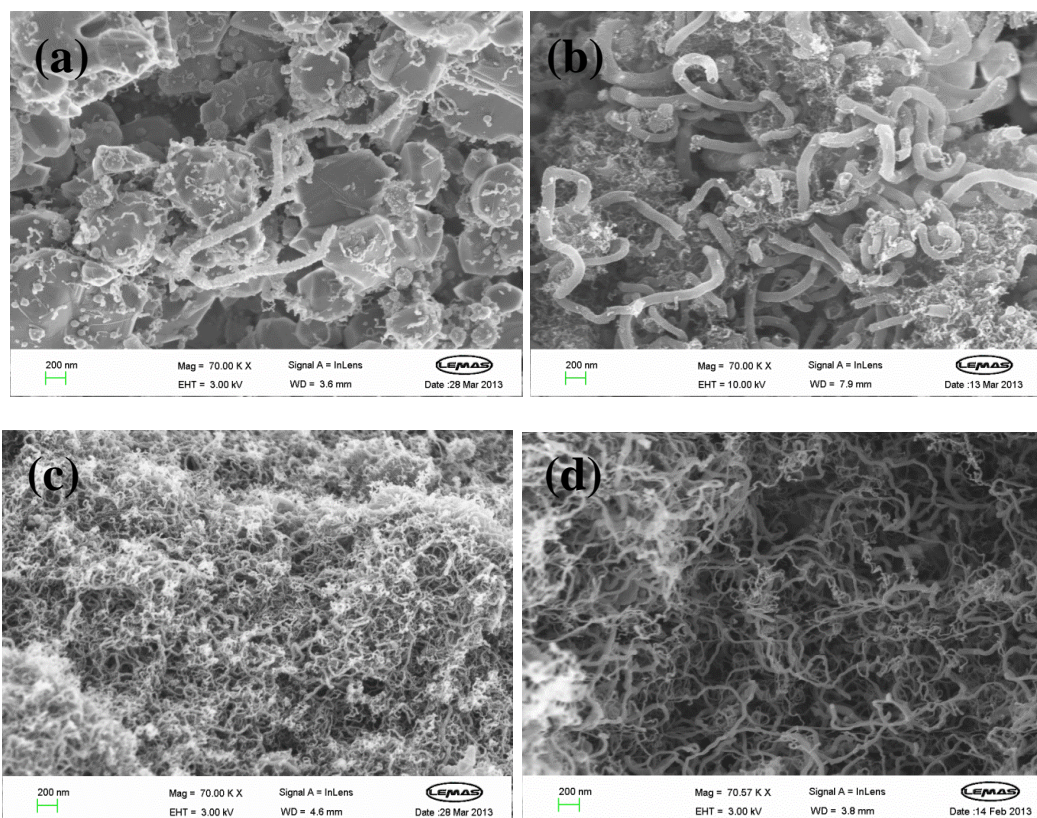


Figure 6.11 SEM images of used catalyst (a-c) different sites of catalyst reduced by HAc (d) catalyst reduced by H₂ (under the same steam reforming condition S/C=1, 650 °C and for 45 min)

SEM images of the reacted catalyst samples are shown in **Figure 6.11**. It was found that carbon deposits formed in the integrated process were not evenly distributed on the catalyst surface. Some parts of the catalyst surface were almost free of carbon deposits (**Figure 6.11a**) whereas others were covered by dense carbon filaments (**Figure 6.11b** and **c**). It was also noted that the carbon deposits on HAc sample was comprised of thick carbon filaments (300 nm in diameter) and thin carbon filaments (10 nm in diameter) (**Figure 6.11b**). In contrast, only medium sized filaments (50 nm in diameter) were found on the H₂ sample (**Figure 6.11d**). The comparison of

Figure 6.11c and **Figure 6.11d** revealed that carbon deposits on the HAc sample were denser than those on the H₂ sample, indicating a larger resistance for steam and fuel molecules to reach active sites in the integrated process. This could be another reason for the slight decrease in steam reforming activity in the integrated process.

6.4 Conclusions

An integrated process featuring auto-reduction of catalyst by reforming feedstock acetic acid (HAc) and subsequent steam reforming was proposed in this manuscript. This process was investigated at different temperatures with different molar steam to carbon ratios (S/C) over a NiO/ α -Al₂O₃ catalyst. At 650 °C and S/C=3, the steam reforming reaction took place instantly following NiO reduction with a lag time of only 10 seconds, and 100% reduction could be achieved in 360 seconds. The best fitting kinetic model for NiO reduction (0-50% conversion) was the two-dimensional nucleation and nuclei growth model (A2). Its corresponding apparent activation energy was 38 kJ/mol of NiO over 550-750 °C for S/C=3. In addition to temperature, steam content in the feed also affected reduction kinetics. S/C=2 was found to be optimal for achieving a quick reduction rate. When low steam content (e.g. S/C=1) was applied, CH₁₋₃ radicals adsorbed on Ni sites could not be gasified sufficiently by steam. As a result, the carbon deposited on Ni sites impaired HAc dissociation and hence lowered the reduction rate. Accordingly, a mechanism of NiO auto-reduction by HAc was proposed.

With respect to catalyst activity, a slight decrease was shown in the integrated process (auto-reduced), compared to a conventional HAc steam reforming process (H₂ pre-reduced). This is likely attributed to more Ni atoms lost into the condensate when using HAc to reduce the catalyst. Another possible reason is that the catalyst surface was covered by denser carbon filaments, which impeded the access of reactant molecules to the active sites. In spite of the small activity degradation, a H₂ purity of 58.68 vol%, a H₂ yield of 0.315 mol/mol C feed (i.e. 76.4% of the equilibrium value) and HAc conversion of 89% were achieved under reaction conditions of 750 °C and S/C=3.

In such an integrated process, the effect of temperature on the reduction rate was consistent with that on steam reforming activity. 650 °C was found to be the lowest temperature to afford fast reduction kinetics without CO disproportionation. However, the S/C ratio had opposite effects on the reduction rate and the steam reforming activity. A rise in S/C ratio increased steam reforming activity as expected, but led to a decrease in the reduction rate. Hence, a varying S/C regime may be required in an integrated process. Furthermore, the cyclic behaviour of catalyst in alternating fuel feed and air feed needs to be investigated for the potential application of bio-feedstock in chemical looping reforming.

Chapter 7

Auto-reduction of nickel catalyst with a series of bio-compounds

7.1 Introduction

The direct reduction of 18 wt% nickel catalyst supported on α -alumina by reforming fuel acetic acid during a steam reforming process has been investigated in Chapter 6 (termed 'auto-reduction'). As discussed, steam reforming of acetic acid took place as soon as metallic Ni was produced from NiO reduction. Hence, the auto-reduction is a complicated process as many species (e.g. bio-compound itself, decomposition intermediates, reforming products H_2 and CO) are involved, in contrast to conventional reduction which is with individual reducing species (e.g. H_2 or CO). In addition to carboxylic acids, alcohols, ketones, furans and sugars are common chemical families present in bio-oil as well. In this chapter, the auto-reduction of the same nickel catalyst with ethanol, acetone, furfural and glucose is studied with emphasis on comparing the reducing ability and reduction kinetics of different bio-compounds. This study aims to demonstrate the dependence of reduction rate on the type of bio-compounds, temperature, and steam content present in the reduction system.

7.2 Experimental

The auto-reduction process was carried out in a packed bed reactor at an approximately constant temperature (isothermal reduction). 2 g of fresh catalyst (18 wt% NiO/ α -Al₂O₃) was placed in the middle of the reactor for reduction. Like acetic acid, ethanol, acetone, and glucose were individually dissolved in water to make solutions with a certain molar steam to carbon ratio (S/C) prior to being fed into the reactor. Furfural and water were injected to the reactor separately as furfural is insoluble. The details of reactor, catalyst material, and feed rate of bio-compounds as well as measurement of product gas composition were described in Section 3.2 of Chapter 3. The reduction of fresh catalyst by H_2 was also conducted in the packed

bed reactor using 5% H₂/N₂ gas at a flow rate of 300 sccm in the absence of steam. 10% CH₄/N₂ gas with a flow rate of 222 sccm was used to study the reduction of fresh catalyst by CH₄. Water was fed into the reactor by syringe pump before the feed of CH₄ started, similarly to the recommended start-up procedure when using natural gas to reduce reforming catalyst in a commercial operation [147].

Each run of experiment proceeded for 45 min. Molar fractions of gaseous products from the reactor were used to calculate reduction rate on the basis of oxygen balance (Eq. 3.7). The Hancock-Sharp method [198] was employed for kinetics modelling of reduction process as what had been done to the case of acetic acid (Section 6.3.1.2 of Chapter 6). After reduction, the catalysts were collected for XRD characterisation, and the composition of reacted catalysts was derived from the XRD data using Rietveld refinement [213]. ICDD reference patterns 04-005-4505, 04-010-6148, and 04-013-0890 were selected for phases of α -Al₂O₃, Ni and NiO, respectively, during Rietveld refinement, as they matched with the diffraction peaks experimentally observed. The quality of the refinements was gauged by weighted R profile (R_{wp}) and goodness of fit (GOF) (see 3.4.2 of Chapter 3), and also displayed by the comparison of the calculated pattern with the observed pattern. A refinement with R_{wp} less than 10 and GOF less than 4 could be considered as good [171, 213]. All the Rietveld refinements shown in this chapter satisfied this requirement.

7.3 Reduction extent

The reduction extent of a reforming catalyst is influenced by various factors including the chemical nature of the catalyst support, the reduction temperature and duration, and the composition of reducing gas [8, 214]. According to the literature [8], when the reduction was carried out with pure H₂, the optimal temperature was found to be around 600 °C. Below this temperature the reduction was slow and incomplete. Above this temperature, some sintering may take place, which lowered the nickel surface area. Therefore, when using bio-compounds to reduce the NiO catalyst, it is also important to find out such an optimal temperature which could lead to complete reduction but no sintering.

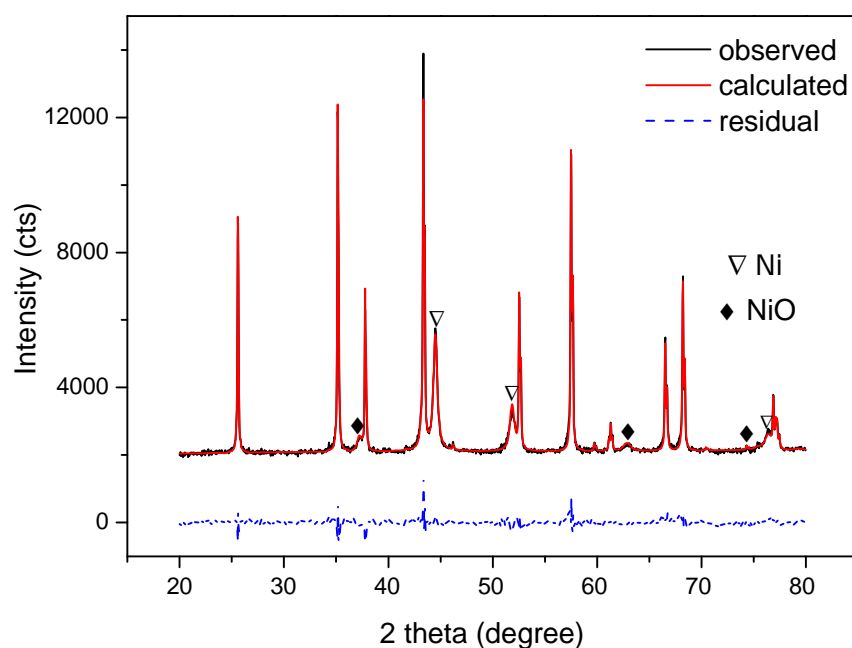


Figure 7.1 XRD pattern of the catalyst reacted with ethanol solution (S/C=3) at 550 °C and its model by Rietveld refinement (84.8 wt% α -Al₂O₃, 11.5 wt% Ni and 3.8 wt% NiO, R_{wp} = 2.86 and GOF=2.00)

Figure 7.1 shows the XRD profile of the catalyst reacted with ethanol solution (S/C=3) at 550 °C. The calculated pattern through Rietveld refinement and the residual (difference between the calculated and the observed data points) are also displayed in **Figure 7.1**. The fresh catalyst consisted of α -Al₂O₃ and NiO. When subjecting the catalyst to ethanol vapour at 550 °C, the reduction of NiO to Ni occurred, as evidenced by the appearance of Ni diffraction peaks. However, the reduction was not complete, as 3.8 wt% NiO was still present in the sample. When using the other reductants, similar XRD profiles were obtained. The difference among them was whether the NiO peaks persisted. Apart from the three phases α -Al₂O₃, NiO, and Ni, there was no evidence of other phases (e.g. graphite). To identify clearly the characteristic diffraction peak of NiO (at 2 theta ~62.9°), these XRD profiles were zoomed in the 2 theta range of 50°-65°, and shown in **Figure 7.2** and **Figure 7.3** along with corresponding calculated profiles.

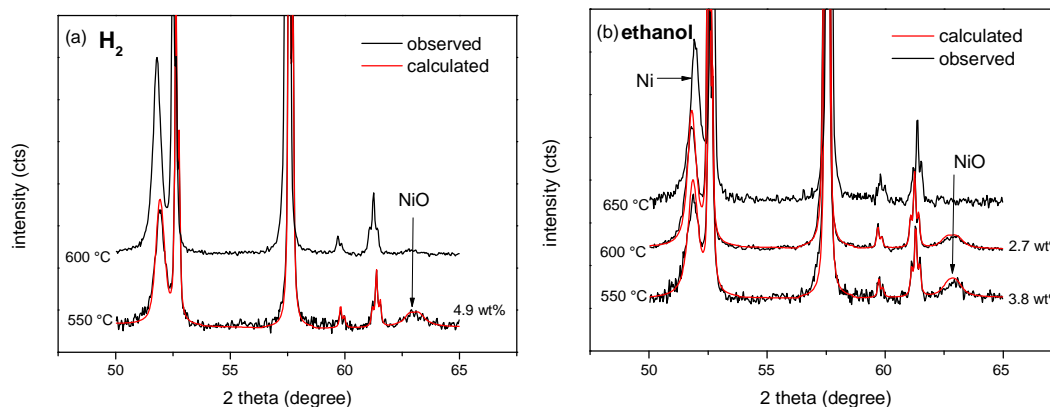


Figure 7.2 XRD patterns and Rietveld refinement results of catalysts after reduction with (a) H₂ and (b) ethanol solution (S/C=3)

A distinct NiO peak was observed in the XRD profile of the catalyst reduced with H₂ at 550 °C (**Figure 7.2a**), which accounted for 4.9 wt% of the catalyst. The NiO peak disappeared at 600 °C, indicating a complete conversion of NiO to Ni. When using ethanol as reductant, the intensity of the NiO peak at 62.9° decreased as the reduction temperature rose and the absence of this peak was observed at 650 °C (**Figure 7.2b**). This result corroborated that the reduction extent was affected by temperature. Compared to the reduction with H₂ or ethanol, the catalyst reduction with CH₄, acetone, furfural or glucose was easier as a nearly complete reduction could be achieved at a lower temperature (550 °C, **Figure 7.3**).

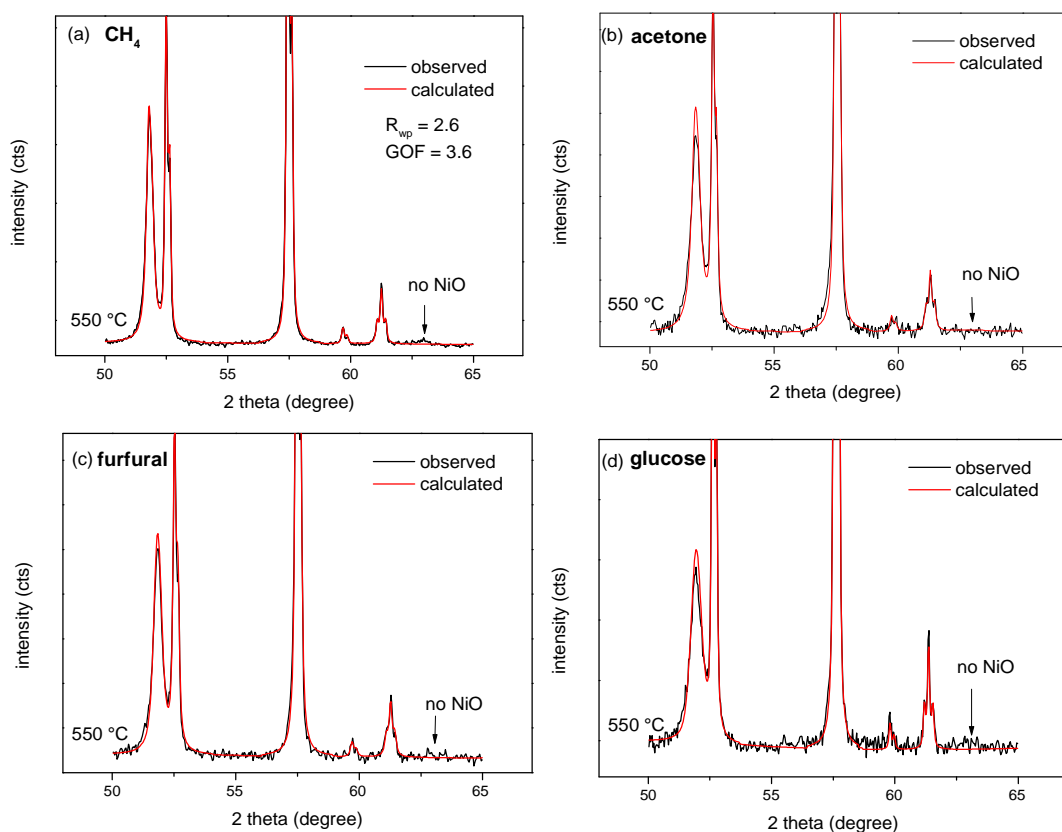


Figure 7.3 XRD patterns of catalysts after reduction with various reductants at 550 °C as well as Rietveld refinement results (a) CH₄, (b) acetone, (c) furfural, and (d) glucose. (S/C=3 for all these reductants except glucose, which is at S/C=6)

In summary, NiO catalyst could be completely reduced by ethanol at 650 °C and by acetic acid (see Chapter 6), acetone, furfural or glucose at 550 °C. To find out the influence of different reducing agents on Ni surface area (Ni dispersion), a further characterisation such as H₂ chemisorption [184] is required.

7.4 Reduction rate curves

7.4.1 Explanation for the residual error of reduction rate

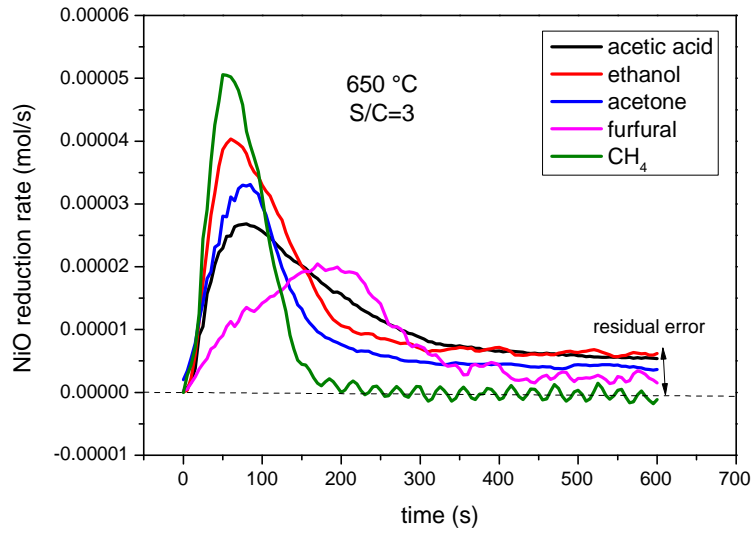


Figure 7.4 Plots of reduction rate vs. time at 650 °C and S/C=3

On the basis of oxygen balance (Eq. 3.7), the rate of NiO reduction with various reductants was estimated. Reduction rate profiles with respect to time are shown in **Figure 7.4**. As discussed in Chapter 6, when using acetic acid, the reduction was completed in the first 360 seconds of the experiment, evidenced by XRD characterization. However, a residual error of reduction rate was observed after 360 seconds in its reduction rate curve. The existence of residual error was also observed for the other bio-compounds (**Figure 7.4**). If a pre-reduced catalyst was used in the experimental process instead of the fresh catalyst, a similar residual error was also shown (**Figure 7.5**).

$$\text{reduction rate} = n_{\text{out,dry}} \times (y_{\text{CO}} + 2y_{\text{CO}_2}) - n_{\text{H}_2\text{O,in}} \times X_{\text{H}_2\text{O}} - k' \times n_{\text{bio,in}} \times X_{\text{bio}} \quad (\text{Eq. 3.7})$$

$n_{\text{out,dry}}$: flow rate of dry outlet gas in mol/s

$n_{\text{H}_2\text{O,in}}$: flow rate of water input in mol/s

$n_{\text{bio,in}}$: flow rate of bio-compound input in mol/s

y_i : molar fraction of specie i in the dry outlet gas

X_i : conversion fraction of specie i

k' : the number of oxygen atoms in bio-compound molecule

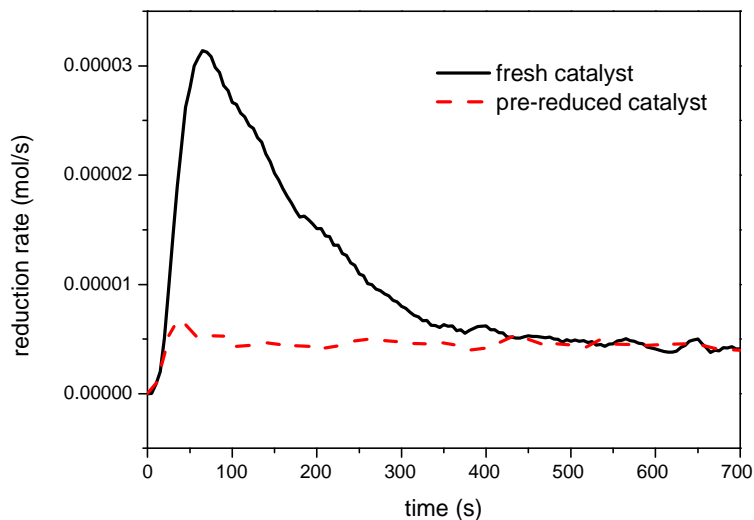


Figure 7.5 Reduction rate vs. time when subjecting fresh catalyst and pre-reduced catalyst to the atmosphere of acetic acid and steam with S/C=2 at 650 °C

In contrast to oxygenated hydrocarbons (bio-compounds), there was no evidence of residual error when using CH_4 as reductant (**Figure 7.4**). The wobbly line observed for the case of using CH_4 may be attributed to the pulsation of water feed. The stable CH_4 gas flow in the reactor was disturbed when a droplet of water fell on the catalyst bed. The residual error was probably caused by the underestimation of oxygen contribution from bio-compounds to oxygen-containing products. The calculation of reduction rate through Eq. 3.7 reproduced above, was based on oxygen balance and assumed that oxygen atoms in the outlet gases (CO and CO_2) were contributed by three terms. They were converted H_2O molecules, converted bio-compound molecules to CO , CO_2 , CH_4 , and reduced NiO molecules, respectively, as shown in **Figure 7.6**. Actually, oxygen atoms of the bio-compound molecules that were converted to carbon deposits may also be involved but not included in the oxygen balance, resulting in a larger reduction rate than the actual value. This is why a considerable residual error was observed in the reduction rate curve.

For CH_4 , the reduction rate was estimated by Eq. 7.1. The oxygen input only consisted of two terms. One was from reduced NiO molecules and the other was from converted H_2O molecules. The fuel term was omitted as no oxygen exists in

CH₄ molecule, which led to a more accurate estimation of reduction rate and thus the disappearance of residual error (**Figure 7.4**).

$$\text{reduction rate} = n_{out,dry} \times (y_{CO} + 2y_{CO_2}) - n_{H_2O,in} \times X_{H_2O} \quad (\text{Eq. 7.1})$$

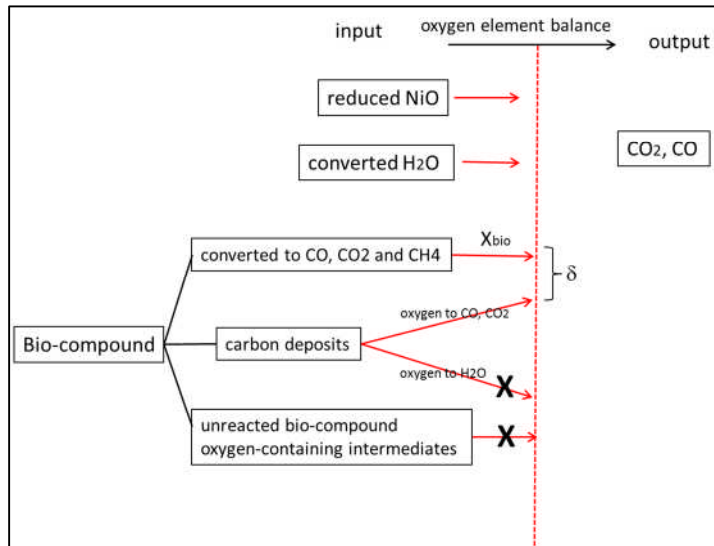


Figure 7.6 Illustration for oxygen element balance during the auto-reduction of NiO catalyst with bio-compounds

7.4.2 The conversion range selected for kinetic modelling

A negative residual error was observed if the reduction rate was calculated using Eq. 7.2, in which all the oxygen atoms in the bio-compound molecules were assumed to be engaged in the oxygen balance. This was because some oxygen atoms may be left over in condensate in the form of unreacted bio-compound molecules or oxygen-containing intermediates. Neither Eq. 3.7 nor Eq. 7.2 reflected the actual reduction rate. A more accurate equation is given as Eq. 7.3, in which $X_{bio} < \delta < 1$ and δ may change with time.

$$\text{reduction rate} = n_{out,dry} \times (y_{CO} + 2y_{CO_2}) - n_{H_2O,in} \times X_{H_2O} - k' \times n_{bio,in} \quad (\text{Eq. 7.2})$$

$$\text{reduction rate} = n_{out,dry} \times (y_{CO} + 2y_{CO_2}) - n_{H_2O,in} \times X_{H_2O} - k' \times n_{bio,in} \times \delta \quad (\text{Eq. 7.3})$$

It is difficult to quantify δ in the present study. Nonetheless, the gap between the X_{bio} and δ could be gauged by the amount of carbon deposits (**Figure 7.6**). The more

carbon was formed, the bigger the gap was. Thermodynamic calculations (**Figure 4.8** and **Figure 4.9** in Chapter 4) indicated that the carbon formation during NiO reduction with the bio-compounds depended on the availability of NiO in the reaction system. Chao et al. [141] experimentally observed that the carbon deposition was not significant until 80% NiO was reduced during chemical looping combustion of CH₄. Moreover, the fractional conversion curves based on Eq. 3.7 and Eq. 7.2 were found to overlap with each other in the segment of 0-0.5 (**Figure 7.7**), which supported the argument that the carbon deposition was negligible in the initial stage of reduction. Therefore, the data within the conversion fraction of 0-0.5 was reliable and valid as input for kinetics modelling. Kinetic analysis based on a selected conversion range is often used in the literature [197, 215] due to the difficulty in obtaining kinetic data in a full conversion range. For example, for the reduction of metal oxide with CH₄, kinetic data are normally obtained by recording the mass change of solid sample during reduction. However, the carbon deposition from CH₄ pyrolysis, which strongly depends on the oxygen availability, made it difficult to obtain valid kinetic data at high conversion level.

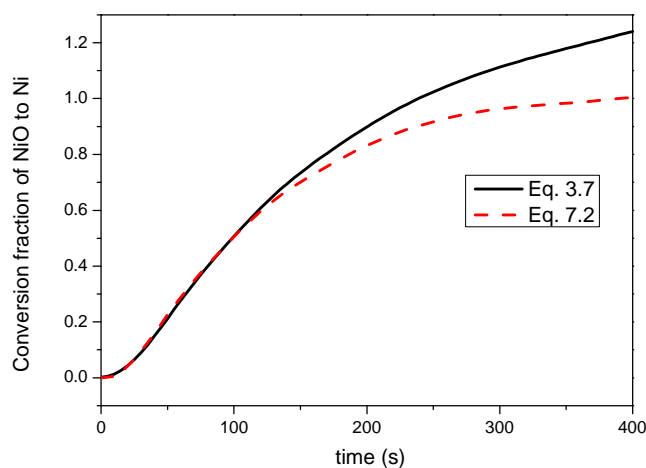


Figure 7.7 Plots of conversion fraction vs. time when reduction rate was calculated using Eq. 3.7 and Eq. 7.2 (NiO catalyst reduction with acetic acid solution at S/C=2 and 650 °C)

7.5 Kinetic modelling of NiO reduction

7.5.1 Mass transfer resistance

The reduction of NiO catalyst with bio-compound vapour is an example of gas-solid reactions. The global reduction kinetics is controlled by one of the following steps [130, 216]: diffusion of bio-compound vapour through gas phase to the exterior of particles (external mass transfer), diffusion into the porous particles (internal mass transfer), product-layer diffusion, or chemical reaction with NiO to produce Ni. Chemical reduction itself is a complex process, consisting of several steps. The reduction mechanism of supported NiO with H₂ was proposed as follows [216]: (1) dissociation of H₂ to form adsorbed H radicals (initially by NiO, then by newly formed Ni), (2) surface diffusion of H radicals to a reduction centre, (3) rupture of Ni–O bonds to produce Ni atoms, (4) nucleation of Ni atoms into metallic Ni clusters, and (5) growth of Ni clusters into crystallites. Any one or combination of these steps, together with the removal of water, may control the overall reaction rate. When using bio-compounds, the reduction process may become more complicated because of the availability of various reducing species (bio-compound, decomposition intermediates, H₂, CO, etc.), and the competition from steam reforming. Nonetheless, these basic steps including dissociative adsorption, surface diffusion of radicals, rupture of Ni–O bonds, nucleation and nuclei growth are believed to be common to different reductants.

In this section, the influences of external mass transfer and internal mass transfer on the global reduction rate were checked. Normally, the external diffusion resistance could be reduced as much as possible by using high gas flow and small mass of solid sample. In this work, a similar reduction rate was observed when decreasing the mass of NiO catalyst from 2 g to 1 g, indicating the external diffusion resistance was not significant. Additionally, the theoretical molar flux of bio-compound vapour ($W_{A,r}$) was calculated according to Eq. 7.4-7.6 [135, 217].

$$Sh = 2 + 0.6 Re^{1/2} Sc^{1/3} \quad (\text{Eq. 7.4})$$

$$k_c = \frac{D_{AB}}{d_p} Sh \quad (\text{Eq. 7.5})$$

$$W_{A,r} = k_c (c_{A,g} - c_{A,s}) \quad (\text{Eq. 7.6})$$

Sh, Sc and Re are the Sherwood number, the Schmidt number and the Reynolds number, respectively. Here, Re is assumed to be 0 and hence Sh is 2, which represents the worst case occurring in the external diffusion process. k_c is defined as the external mass transfer coefficient (m/s). D_{AB} is the molecular diffusivity and a typical value for gas-solid reaction is $10^{-5} \text{ m}^2/\text{s}$ [135, 217]. d_p is the particle diameter (0.0012 m). $c_{A,g}$ and $c_{A,s}$ are the concentration of bio-compound A in the gas phase and on the solid surface (mol/m^3), respectively. Here, $c_{A,s}$ is assumed to be zero, and $c_{A,g}$ is calculated using Eq. 7.7.

$$c_{A,g} = \frac{\text{moles of A input per second}}{\text{volume of (N}_2 + \text{A} + \text{H}_2\text{O) input per second}} \quad (\text{Eq. 7.7, A represents bio-compound})$$

The calculated value of $W_{A,r}$ for different bio-compounds are summarized in **Table 7.1**. The maximum consumption rate (r_A) of bio-compound experimentally observed at 650 °C and S/C=3 (S/C=6 for glucose) was calculated using Eq. 7. 8.

$$r_A = \frac{r_{NiO} \text{ at the peak of rate curve}}{\text{catalyst mass} \times \text{surface area} \times \mathcal{E}} \quad (\text{Eq. 7.8})$$

Where catalyst mass= 2 g, catalyst surface area= 2.5 m^2/g (BET characterisation), and \mathcal{E} refers to stoichiometric moles of NiO reduced by 1 mol of bio-compound. It was found that the value of $W_{A,r}$ was much greater than the observed consumption rate r_A . Therefore, the external diffusion limitation was considered as negligible for the five bio-compounds.

Table 7.1 Calculated molar flux of gas reactants ($W_{A,r}$) and observed consumption rate (r_A) in $\text{mol m}^{-2} \text{ s}^{-1}$

Gas reactants	$W_{A,r}$	r_A	$W_{A,r}/r_A$
acetic acid	7.95×10^{-4}	1.38×10^{-6}	578
ethanol	7.95×10^{-4}	1.33×10^{-6}	596
acetone	5.31×10^{-4}	8.25×10^{-7}	643
furfural	3.19×10^{-4}	4.00×10^{-7}	797
glucose	1.37×10^{-4}	2.00×10^{-7}	685

The internal diffusion resistance plays an important role in controlling global reaction rate when the gaseous reactant needs to go through the pores of solid material to reach the active sites. In the present study, BJH pore size analysis indicated that the catalyst material used had a quite small pore size (2.5 nm in diameter). XRD characterization suggested that the NiO crystallite size was around 45 nm, much larger than the pore size. Hence, it could be postulated that all the NiO crystallites were located on the surface of catalyst particles and the internal mass transfer was not present in the system. This conclusion agreed with the experimental result that the reduction rate was not affected by decreasing the particle size from 1.2 mm to 0.1 mm.

7.5.2 Model fitting

Some common kinetic models for solid-state reactions were shown in Table 6.1 (see Chapter 6). Handcock and Sharp [198] pointed out that kinetic data which follows any one of these models also obey Avrami-Erofeyev equation (Eq. 7.9) and its transformation (Eq. 7.10) if the fractional conversion α is limited to the range of 0.15-0.5. In Eq. 7.9 and Eq. 7.10, t is the reaction time, β is a constant, m is also a constant and varies with the reaction mechanism. Theoretical m values for each kinetic model are listed in Table 6.1.

$$\alpha = 1 - \exp(-\beta \times t^m) \quad (\text{Eq. 7.9})$$

$$\ln(-\ln(1-\alpha)) = \ln(\beta) + m \times \ln(t) \quad (\text{Eq. 7.10})$$

According to the Handcock and Sharp method [197, 198, 217, 218], for an isothermal solid-state reaction, the plot of $\ln[-\ln(1-\alpha)]$ vs. $\ln t$, in which the range of α is 0.15-0.5, should be approximately linear and its slope (i.e. m value) can be used as diagnostic of reaction mechanism. Generally, the reaction kinetics could be fitted by diffusion models if m is around 0.5. When m is around 1, the reaction may obey geometrical contraction models or a first-order model. Two-dimensional or three-dimensional nuclei growth models (A2 or A3) may fit the reaction that has an m value close to 2 or 3, respectively. Plots of $\ln[-\ln(1-\alpha)]$ vs. $\ln t$ for NiO reduction with furfural (S/C=3) at different temperatures are shown in **Figure 7.8** as an example.

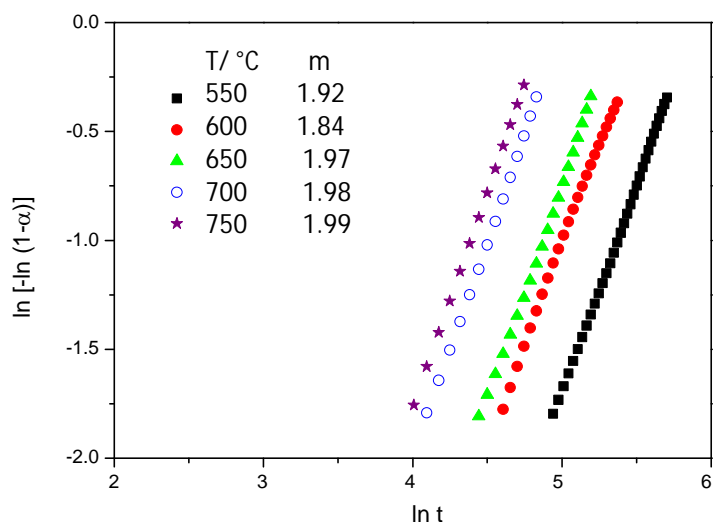


Figure 7.8 Plots of $\ln[-\ln(1-\alpha)]$ vs. $\ln t$ for the reduction of NiO catalyst with furfural (S/C=3) at different temperatures

When using the other bio-compounds to reduce NiO catalyst, similar linear plots were obtained and their m values were listed in **Table 7.2**. For the NiO reduction with furfural or CH_4 , the m values hardly changed with temperature, and were all close to 2.00, indicating a two-dimensional nuclei growth mechanism (A2 model). In contrast, the m values obtained from reduction using acetic acid, ethanol or acetone increased gradually as the temperature rose from 550 °C to 650 °C, suggesting a progressive mechanism change (from geometrical contraction model to A2 model). Within the temperature range of 650-750 °C, the reduction was an isokinetic process, indicated by a negligible variation in the m value [198]. For the three bio-compounds, the m values obtained at 550 °C were below 1.5, implying that the geometrical contraction model (e.g. R3) may be more suitable than the A2 model. It was found that only the initial stage of reduction at 550 °C obeyed the A2 model. Therefore, the following A2 model fit was performed in the conversion range of 0-0.20 for 550 °C whereas the conversion range of 0-0.5 was used for the other temperatures.

Table 7.2 The m values obtained at different reduction temperatures

reductants	m values				
	550 °C	600 °C	650 °C	700 °C	750 °C
acetic acid	1.34	1.63	1.78	1.73	1.75
ethanol	0.99	1.56	1.89	1.90	1.87
acetone	1.45	1.69	1.88	1.91	1.87
CH ₄	1.83	1.97	1.94	1.95	1.96
furfural	1.92	1.84	1.97	1.98	1.99
glucose	1.20	1.52	1.57	1.51	1.53

Glucose was the exception to all the bio-compounds studied, which had m values around 1.5. Neither the A2 model nor the R3 model could give a satisfactory fit to the experimental data. The use of Avrami-Erofeyev equation with non-integral m value ($m=1.34$) to fit the conversion curve observed from NiO reduction with H₂ has been reported in the literature [40, 219]. The physical meaning behind this model was not clear. It may be an intermediate regime where both nucleation and chemical reaction were rate-determining. In this study, Avrami-Erofeyev equation with $m=1.5$ (denoted as A1.5) was used to fit the kinetic data obtained from NiO reduction with glucose solution.

Once the kinetic model was determined, the rate constant k could be derived from experimental data (fractional conversion α vs. time) by two methods. One was to linearly fit the plot of $[-\ln(1-\alpha)]^{1/m}$ vs. t , and obtain k from the slope [218]. The other was to fit the plot of α vs. t with exponential function $\alpha = 1 - \exp[-(kt)^m]$. In both methods, m values of 1.5 and 2 were used for glucose and for the other reductants, respectively. The exponential fit method was employed in this work. A good agreement between the experimental data and theoretical model was achieved, as shown in **Figure 7.9** and through the correlation coefficient R^2 's closeness to 1 in **Table 7.3**.

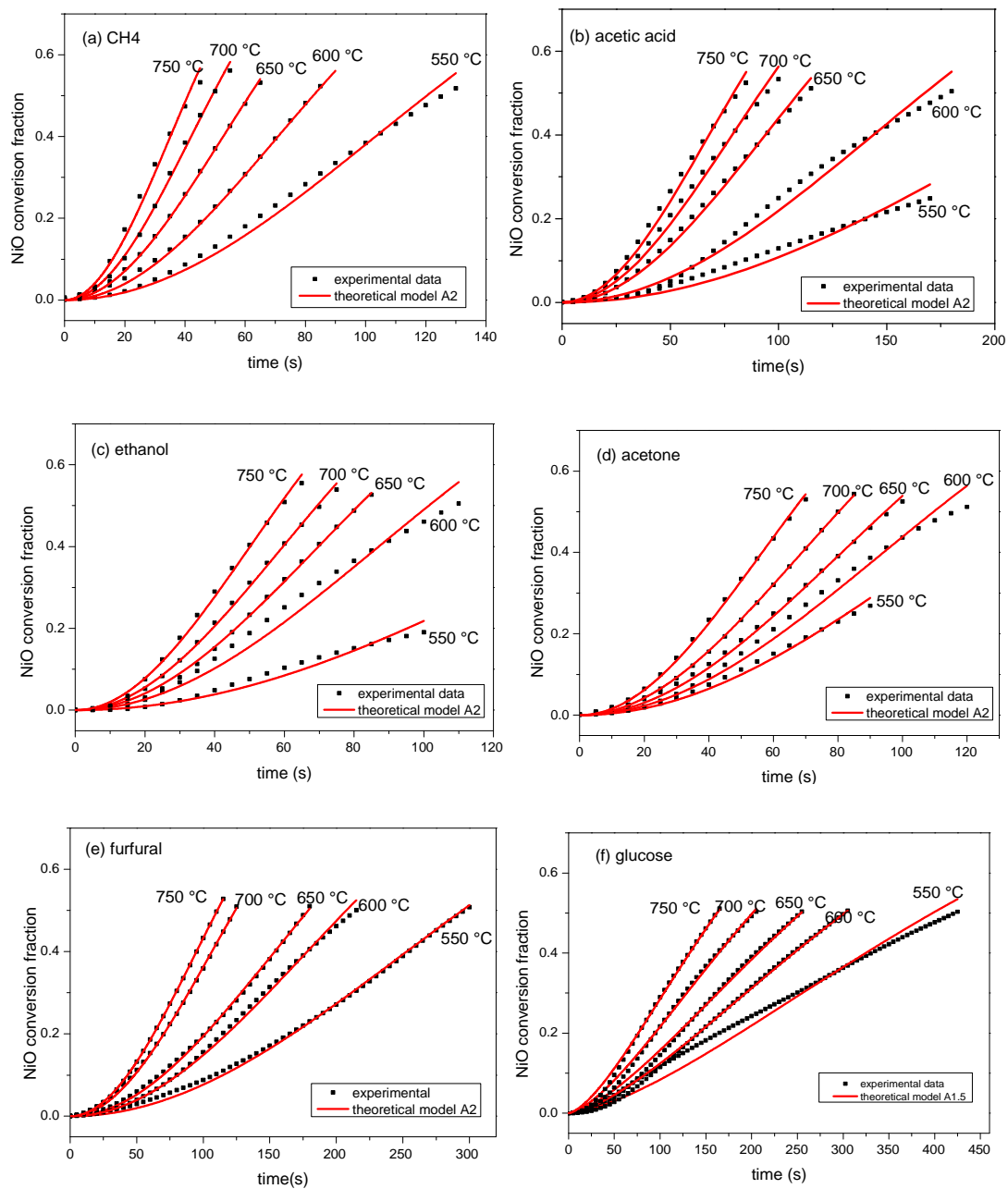


Figure 7.9 Comparison between the experimental data and A2 model for the reduction of NiO catalyst with (a) CH₄, (b) acetic acid, (c) ethanol, (d) acetone, (e) furfural and (f) A1.5 model with glucose (S/C=6 for glucose and S/C=3 for the other reductants)

Table 7.3 R-squared values for fitting reduction kinetic data with the A2 model

Reductants	R ² values for A2 model fitting				
	550 °C	600 °C	650 °C	700 °C	750 °C
acetic acid	0.961	0.987	0.996	0.993	0.992
ethanol	0.965	0.979	0.999	0.999	0.998
acetone	0.962	0.988	0.998	1.000	0.999
CH ₄	0.991	0.996	0.999	0.991	0.998
furfural	0.998	0.997	0.999	0.999	1.000
glucose*	0.980	0.998	0.996	0.997	0.996

* For glucose, A1.5 model was used.

7.6 Apparent activation energy and pre-exponential factor

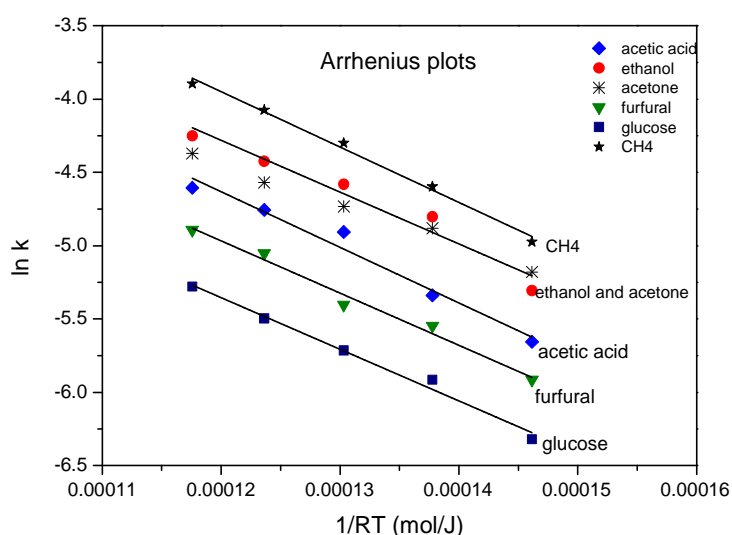


Figure 7.10 Arrhenius plots of NiO reduction with bio-compounds as well as CH₄ at S/C=3 (S/C=6 for glucose)

The reduction rate constants k obtained at different temperatures were plotted into Arrhenius plots (**Figure 7.10**). The apparent activation energies E_a , which were derived from the slope of the Arrhenius plots, were listed in **Table 7.4**. It was found that the values of E_a of NiO reduction with different reductants were close to each other and located at around 30-40 kJ/mol. This suggested that the influence of temperature on the reduction rate constant was the same for the different bio-

compounds. An approximate activation energy (53.5 kJ/mol) was observed for the reduction of NiO/ α -Al₂O₃ with CH₄ in the absence of steam using Avrami-Erofeyev model with m=1 by Hossain and Lasa [135].

$$\ln k = \ln A - \frac{E_a}{RT} \quad (\text{Eq. 7.11})$$

Table 7.4 Estimated kinetic parameters for NiO reduction with different reductants

Reductants	E_a (kJ/mol)	A
CH ₄	38±2	1.31
ethanol	35±4	0.96
acetone	30±2	0.89
acetic acid	38±4	0.67
furfural	36±3	0.48
glucose	35±2	0.34

Due to the similar E_a value, these Arrhenius plots could be considered as being parallel to each other. The order of pre-exponential factor A determined by the relative position of these Arrhenius plots was as follows: CH₄ > ethanol \approx acetone > acetic acid > furfural > glucose. If the pre-exponential factor of ethanol was set as 1, the relative pre-exponential factors of acetic acid, acetone, furfural, glucose and CH₄ would be 0.7, 0.93, 0.5, 0.35 and 1.36, respectively, obtained by averaging the ratios of rate constant k (**Table 7.5**). A large pre-exponential factor indicates that corresponding reducing species (carbon radicals and hydrogen radicals) could be excited with great ease and hence their chance to collide with NiO molecules was increased. A further characterization of the species adsorbed on the catalyst surface (e.g. X-ray photoelectron spectroscopy, XPS) is necessary in order to understand the difference arising from the different bio-compounds.

Table 7.5 Ratios of rate constant k with respect to ethanol

temperature (°C)	acetic acid k_1/k_2^*	ethanol k_2/k_2	acetone k_3/k_2	furfural k_4/k_2	glucose k_5/k_2	CH ₄ k_6/k_2
550	0.706	1	1.135	0.544	0.363	1.395
600	0.585	1	0.925	0.475	0.329	1.228
650	0.722	1	0.859	0.439	0.322	1.324
700	0.717	1	0.865	0.534	0.342	1.418
750	0.702	1	0.887	0.526	0.358	1.427
average	0.7	1	0.93	0.5	0.35	1.36

* The reduction rate constants of acetic acid, ethanol, acetone, furfural, glucose and CH₄ are denoted as k_1 , k_2 , k_3 , k_4 , k_5 and k_6 , respectively.

7.7 Effects of steam content on reduction rate

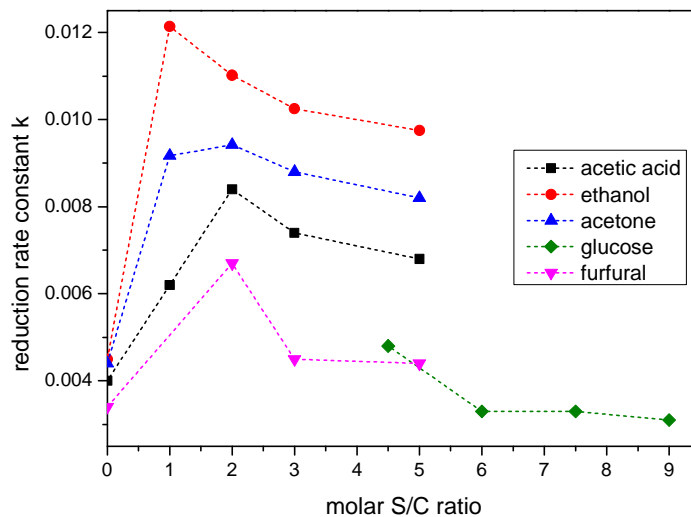


Figure 7.11 Influence of steam content on the reduction rate constant at 650 °C

The influence of water on oxide reduction has been investigated in the literature. Garden [218] observed that the presence of water vapour in the ambient gas considerably lowered the reduction rate of SiO₂ by H₂. He explained that surface activity of SiO₂ was decreased by the interaction between SiO₂ and water (formation of Si-OH) and hence fewer sites were available for the adsorption of H₂. Richardson et al. [39, 216] suggested that the adsorbed H₂O molecules decreased the reducibility

of NiO/Al₂O₃ catalyst by retarding the diffusion of metallic Ni atoms to appropriate nucleation sites. However, Abad and Garcia-Labiano [41, 128] found that the presence of H₂O or CO₂ had no effect on the reduction rate of supported metal oxide with CH₄, CO or H₂ as reductant.

In this study, the reduction rate constant k at 650 °C varied with the water content present in the reaction system as shown in **Figure 7.11**. When water was absent (S/C=0), a low rate constant was obtained. As the S/C rose, the rate constant increased first, and then decreased. This decrease became less pronounced at higher S/C. In general, the maximum reduction rate constants were obtained in the S/C range of 1-2. For glucose, the S/C studied in this work only covered from 4.5 to 9 due to the limitation on its solubility. Therefore, only the stages of decrease and levelling off were observed with increasing S/C.

According to the reduction mechanism proposed in Chapter 6 (**Figure 6.8**), the presence of water has two opposite effects on the reduction. On one hand, the adsorbed H₂O molecules retard the reduction by scavenging radicals (i.e. potential reducing species), and limiting the migration of Ni atoms to nucleation sites. On the other hand, an appropriate amount of H₂O could suppress the deposition of carbon by steam gasification. As a result, the dissociation of bio-compounds on Ni sites (the initial step of reduction) is not affected. Which effect is dominant depends on the reaction condition. **Figure 7.12** illustrates the effect of S/C on the adsorbed carbon radicals (C_{ads}), which explains the typical profile of rate constant vs. S/C observed in experiments at 650 °C.

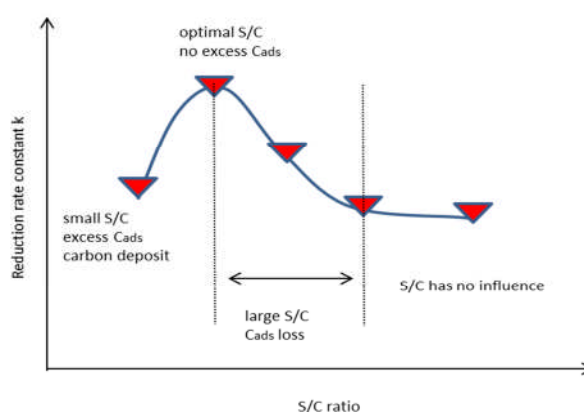


Figure 7.12 Illustration of the influence of S/C on reduction rate constant

The maximum reduction rate constant could be obtained when the amount of water (optimal S/C) is just enough to gasify the excess C_{ads} and not consume those which are supposed to reduce NiO. The optimal S/C varies with bio-compounds, which may be attributed to the different activities of carbon radicals produced from different sources as well as the consumption rate of carbon radicals (i.e. reduction rate). It should be noted that the optimal S/C range for reduction kinetics was below the S/C commonly used for steam reforming (e.g. S/C=2-3).

7.8 Conclusions

The auto-reduction of NiO/ α -Al₂O₃ catalyst with a series of bio-compounds as well as CH₄ was performed in a packed bed reactor. It was found that the NiO catalyst could be completely reduced by ethanol at 650 °C and by acetic acid, acetone, furfural, glucose and CH₄ at 550 °C. The model fit of reduction kinetics was carried out using Handcock and Sharp method after confirming that the external and internal diffusion resistances were not significant. The data within the conversion range of 0-50% were used for kinetic analysis as it was difficult to obtain valid data in the full conversion range. The reduction kinetics could be represented by a two-dimensional nuclei growth model (A2) very well except for glucose. The apparent activation energies of NiO reduction with the five bio-compounds were all located in the range of 30-40 kJ/mol. Their pre-exponential factors decreased in this order: CH₄ > ethanol \approx acetone > acetic acid > furfural > glucose, probably due to the different activities of reducing species (carbon radicals and hydrogen radicals) they produced. Apart from the type of reductants and temperature, the steam content present in reaction system also affected the reduction rate. With the S/C increasing, the rate constant increased first and then decreased tentatively. A maximum rate constant was observed in the S/C range of 1-2. Compared to the other bio-compounds, ethanol exhibited a larger reduction rate constant and a lower optimal S/C, probably because its carbon radicals had a higher activity. Further characterizations such as H₂ chemisorption to obtain the nickel surface area and XPS to detect the carbon species on the catalyst surface are desirable.

Chapter 8

Steam reforming of bio-compounds with auto-reduced nickel catalyst

8.1 Introduction

Chapter 7 demonstrated the feasibility of nickel catalyst auto-reduction with a series of bio-compounds. In this chapter, steam reforming (SR) of these bio-compounds following the auto-reduction was investigated. The effects of temperature and molar steam to carbon ratio (S/C) on the reforming performance were studied in detail. Experimental operations and output definitions were described in Chapter 3. For comparative purposes, the conventional SR process was also conducted with the catalyst pre-reduced by H₂. In addition to the SR reaction and water gas shift (WGS), common side reactions occurring in a SR process include fuel decomposition, Boudouard reaction, methanation, and carbon gasification. Related reaction equations can be found in Chapter 5.

8.2 Comparison between auto-reduction and H₂ reduction

The SR performances of ethanol, acetone and furfural with auto-reduced catalyst are presented in **Figure 8.1** in comparison with the case of using H₂-reduced catalyst. Similarly to what had been observed for acetic acid (Chapter 6), a CO₂ emission peak and a H₂O production peak were found at the initial stage of experiments as characteristics of auto-reduction. Following the auto-reduction, a stable SR performance (feedstock conversions and gas yields) over the reaction duration of 45-60 min was obtained, which was quite close to that observed for the H₂-reduced catalyst. In contrast, slight decreases in the H₂ yield and the fuel conversion were observed for SR of acetic acid when using the auto-reduced catalyst compared to the H₂-reduced catalyst (Chapter 6). This was tentatively ascribed to the corrosive action of acetic acid on NiO which led to the observed loss of active metal. Compared to acetic acid, ethanol, acetone and furfural were mild to NiO. ICP analysis of the

condensates also showed that the Ni concentrations collected from ethanol, acetone and furfural experiments were lower than that from the acetic acid experiment.

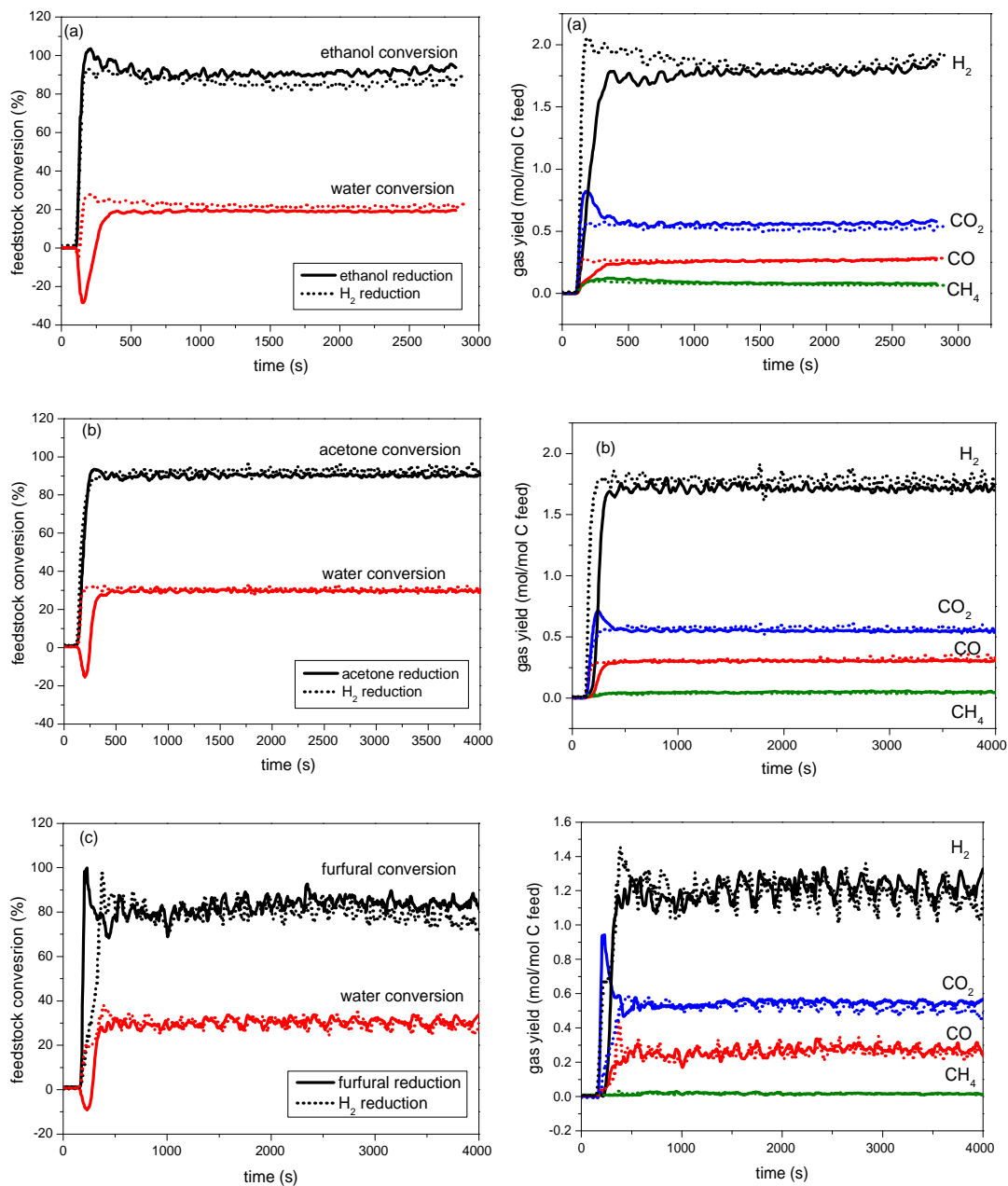


Figure 8.1 SR performance comparison between auto-reduction (solid line) and H₂ reduction (dotted line) at 650 °C, S/C=3: (a) ethanol, (b) acetone, and (c) furfural

Figure 8.1 also shows that as the auto-reduction progressed, the yields of CO and H₂ continuously increased until the auto-reduction came to an end (indicated by the termination of the CO₂ emission peak and of the H₂O production peak). This result suggests the amount of catalyst was the limiting factor for the SR process. In other words, the SR performance would be enhanced if more catalyst was used or the feed of bio-compounds was decreased. However, a large flow rate of bio-compounds and small mass of catalyst was necessary in order to reduce the external diffusion resistance in an auto-reduction process. To mediate between the auto-reduction and the SR, a varying feed rate of bio-compounds to the reactor is recommended.

8.3 Effects of temperature

8.3.1 Feedstock conversion

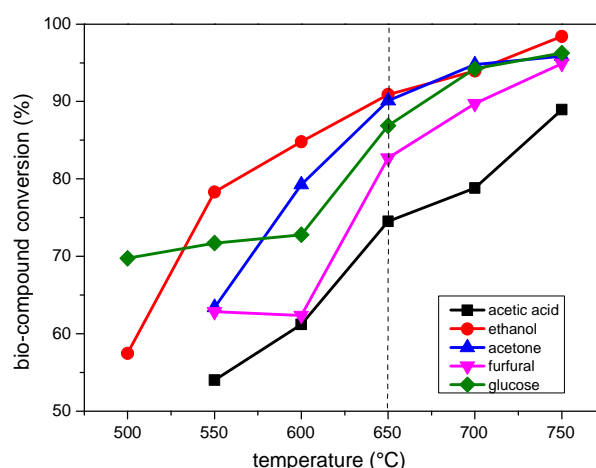


Figure 8.2 Effects of temperature on the bio-compound conversion (S/C=6 for glucose, and S/C=3 for the rest)

(1) Fuel conversion

According to the trends of fuel conversion with respect to temperature shown in **Figure 8.2**, the five bio-compounds could be categorized into two groups. For the light bio-compounds (acetic acid, ethanol and acetone), the fuel conversion increased gradually as the temperature rose. For the bio-compounds with large molecular structure (furfural and glucose), the fuel conversion hardly varied with

temperature until the temperature was raised to 600 °C. Above 600 °C, the fuel conversion exhibited an increasing trend with temperature, similar to that observed for the light bio-compounds. Xu and Lu [118] also observed that light bio-compounds (acetic acid, ethylene glycol, acetone) could be steam reformed with great ease while a higher temperature was required to convert the heavy bio-compounds (ethyl acetate, m-xylene). Giannakeas et al. [220] found that a high reaction temperature (750 °C) was required for an effective SR of scrap tyre pyrolysis oil which consisted of large molecular compounds (e.g. aromatics, aliphatics with carbon number greater than 6). It is understandable that the SR of heavy feedstocks require higher temperatures as more C-C bonds in the molecules need to be destroyed. In this work, the bottleneck temperature for effective dissociation of glucose and furfural molecules was 600 °C, above which a substantial fuel conversion was achieved. The fuel conversion at 650 °C decreased in this order: ethanol \approx acetone > glucose > furfural > acetic acid. The low fuel conversion observed for the SR of acetic acid may be ascribed to the loss of Ni element (Chapter 6).

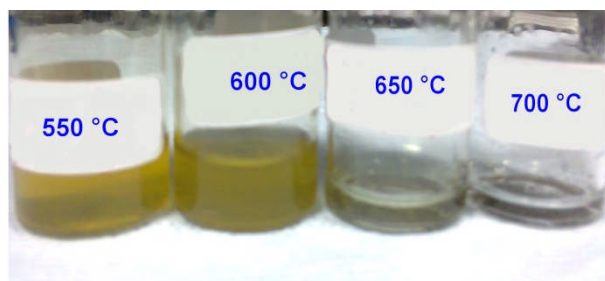


Figure 8.3 Photos of condensate samples collected from furfural experiments at different temperatures with S/C=3

The photos of condensate samples collected from furfural experiments are shown in **Figure 8.3**. A considerable volume of condensate with yellow colour was produced at 550 °C and 600 °C, indicating that there were some unreacted furfural molecules or its derivatives (e.g. furan) in the condensate. Kato [221, 222] found that furfural was fairly thermally stable and about 90% remained unchanged when heating furfural at 500 °C. When increasing the SR temperature from 600 °C to 650 °C in

this work, the amount of condensate dramatically decreased and the colour became transparent. This result was in good agreement with the considerable increase in the furfural conversion from 600 to 650 °C (**Figure 8.2**). It is common that unreacted fuel molecules or its liquid intermediates are found in the condensate when using heavy bio-oil compounds as SR fuel [122]. This not only represents a waste of resources (low fuel conversion) but also causes pollution if the condensate is not disposed of properly. Wu and Liu [122] proposed an operation of liquid condensate recycling for the SR of heavy bio-oil components, in which the condensate collected from the reactor was fed back to the running reactor.

The thermal stability of furfural molecules [221, 222] limited SR of furfural at low temperatures while the severe agglomeration of catalyst particles was the main problem for SR of glucose. As shown in **Figure 8.4**, the agglomeration extent decreased as the temperature increased, and was eliminated at temperatures above 650 °C.

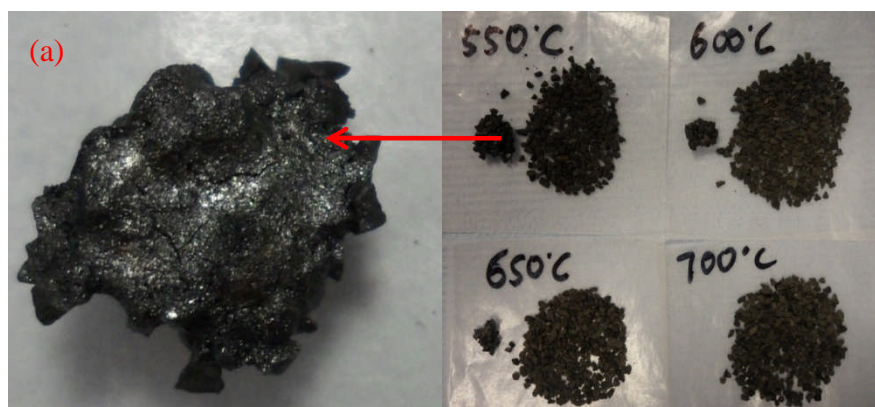


Figure 8.4 Photos of reacted catalysts collected from glucose experiments at different reaction temperatures with S/C=6

The image of catalyst agglomerate (**Figure 8.4a**) indicated that the agglomeration was caused by the coking of glucose. Extensive studies [221, 223, 224] on the thermal degradation of glucose suggested that this process was complex, consisting of fragmentation, polymerization, isomerisation and dehydration. Various oligo- and poly-saccharides as well as brown caramel matter formed in this process [224] may

act as glue to combine catalyst particles together. At low temperature (e.g. 550 °C), the ‘sugar glue’ decomposed slowly and thus coke was formed as illustrated in **Figure 8.5**. When the temperature was high (e.g. 700 °C), the ‘sugar glue’ was degraded rapidly and produced small molecules which could be easily dissociated to form radicals. CHN elemental analysis showed that the carbon content in the agglomerated catalyst particles was about 11 wt% while the carbon deposition on the non-agglomerated catalyst was negligible (0.5 wt% at 700 °C). This result suggested that SR of glucose was promising (high fuel conversion and low carbon deposition) once the catalyst agglomeration can be avoided by elevating temperature.

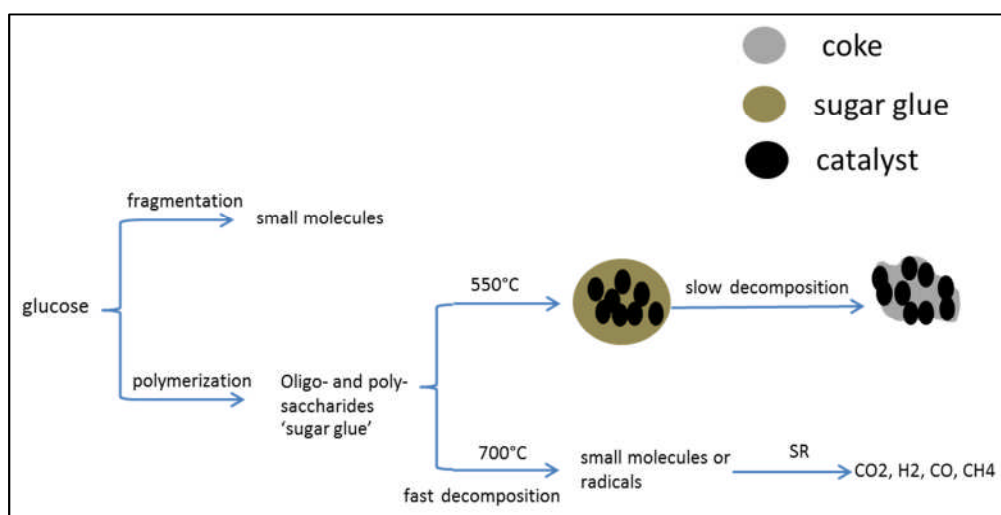


Figure 8.5 Schematic diagram of the agglomeration of catalyst particles due to glucose coking during steam reforming of glucose

(2) Water conversion

For light bio-compounds (acetic acid, ethanol and acetone), the water conversion almost levelled off over the temperature range studied (**Figure 8.6**), as a result of the balance between the promoted SR reaction (consuming more water) and the suppressed WGS reaction with increasing temperature. For furfural and glucose, the water conversion underwent a dramatic increase from 600 to 650 °C, which was consistent with the remarkable enhancement in the fuel conversion (**Figure 8.2**). The order of water conversion obtained from experiments was furfural≈

acetone>ethanol>acetic acid>glucose, in agreement with that from thermodynamic equilibrium calculation. The discrepancy between the experimental data and the equilibrium data was mainly attributed to the kinetic restriction on SR reaction (the fuel conversion was less than that achieved at equilibrium). The WGS reaction seemed to not suffer significantly from kinetic limitation since the composition of the dry product gas obtained in experiments was quite close to that at equilibrium (Appendix C).

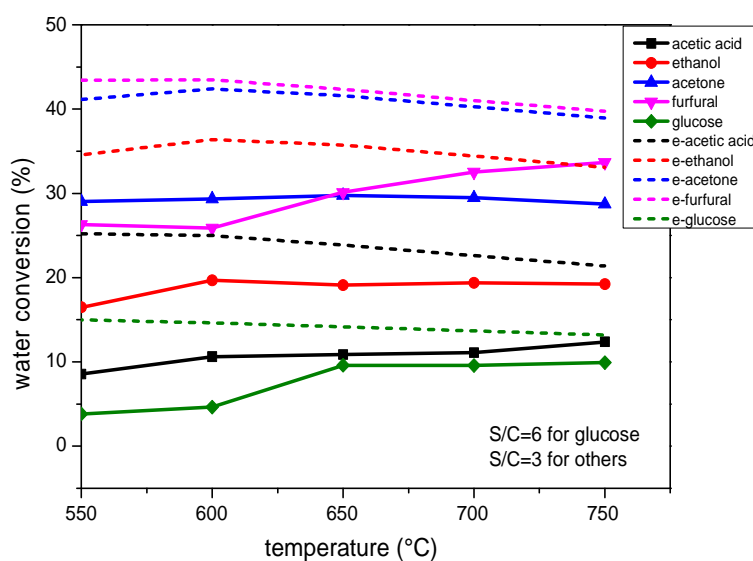


Figure 8.6 Effects of temperature on the water conversion obtained by experiments and thermodynamic equilibrium calculation (S/C=6 for glucose, S/C=3 for the rest, equilibrium data were indicated by ‘e’ in front of bio-compound name)

8.3.2 Gas product yields

(1) H₂ yield

As **Figure 8.7** shows, the H₂ yield increased with temperature. Above 650 °C, the H₂ yield in mol/mol C feed (**Figure 8.7a**) decreased in the order of ethanol > acetone > glucose > furfural > acetic acid. The H₂ yield depended on the bio-compound conversion as indicated by their similar variation trend with respect to temperature (**Figure 8.2**). Apart from this, the potential of bio-compound for H₂ production (stoichiometric H₂ yield and equilibrium H₂ yield shown in **Table 8.1**)

also played a role in determining H₂ yield. For instance, the H₂ yield decreased in this order: ethanol > acetone > glucose although the conversions of ethanol, acetone and glucose above 650 °C approximated to each other (**Figure 8.2**).

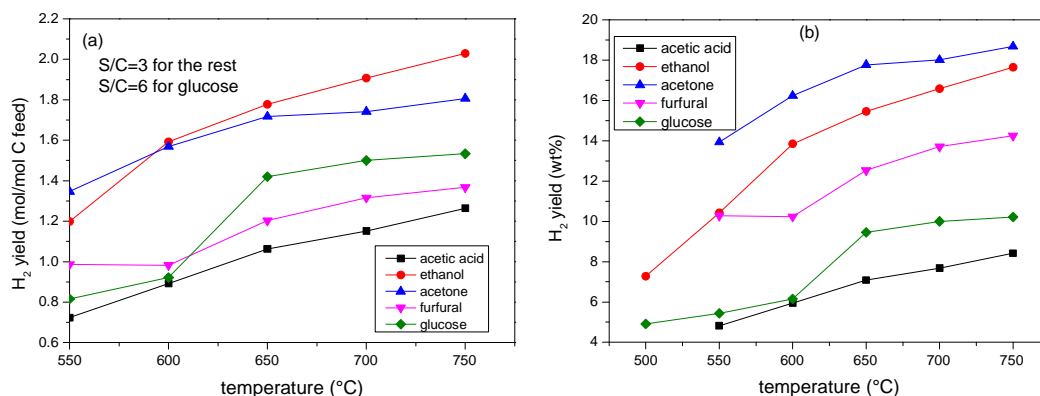


Figure 8.7 H₂ yield vs. temperature from steam reforming of bio-compounds (S/C=6 for glucose and S/C=3 for the rest): (a) in mol/mol carbon feed, (b) in wt% of the bio-compound input

The H₂ yield in weight percentage of the bio-compound used is also shown (**Figure 8.7b**). It decreased in the order of acetone > ethanol > furfural > glucose > acetic acid. This order was affected by the ratio of molar mass to carbon number in the bio-compound molecule (denoted as M_c). When the H₂ yield in mol/mol C feed is the same, the smaller the M_c value is, the larger the H₂ yield in wt% is. As listed in **Table 8.1**, the acetone and furfural have the smallest M_c while acetic acid and glucose have the largest M_c value due to the high O/C ratio in their molecules.

Table 8.1 H₂ yields (in mol/mol C feed) from different bio-compounds at 650 °C, S/C=6 for glucose and S/C=3 for the rest

bio-compound	^a stoichiometric	^b equilibrium	experiment	^c H ₂ yield efficiency (%)	^d M _c
ethanol	3	2.58	1.78	68.99	23
acetone	2.7	2.26	1.72	76.11	19.3
glucose	2	1.85	1.42	76.76	30
acetic acid	2	1.73	1.06	61.27	30
furfural	2	1.67	1.20	71.86	19.2

a: according to the complete steam reforming (see Chapter 4)

b: CEA thermodynamic equilibrium calculation including N₂ in the reactant mixture

c: H₂ yield efficiency was defined as the percentage of experimental H₂ yield with respect to the equilibrium values

d: M_c represents the ratio of molar mass to carbon number in the bio-compound molecule in gram.

(2) Yields of C-containing products

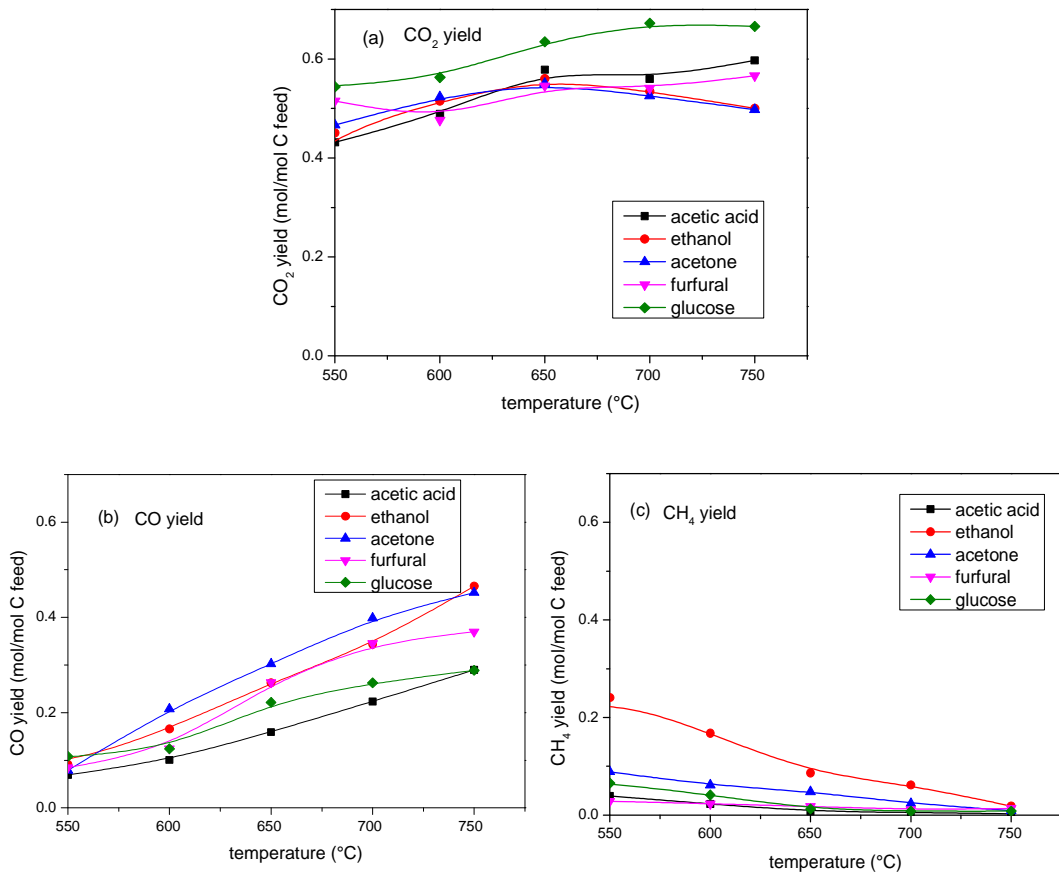


Figure 8.8 Yields of carbon-containing products vs. temperature from the steam reforming of bio-compounds (a) CO₂, (b) CO and (c) CH₄

The influence of temperature on the CO₂ yield was not significant (**Figure 8.8a**). With the temperature increasing between 550 and 750 °C, the CO₂ yield from SR of glucose and acetic acid grew marginally. For SR of ethanol and acetone, their CO₂ yields underwent a slight increase first and then decreased, peaking at 650 °C. The total amount of gaseous products increased with temperature as a result of the continuously increased bio-compound conversion (**Figure 8.2**) while the CO₂ concentration in the dry outlet gas decreased (Appendix C) as WGS was suppressed by elevated temperature. The balance between these two factors led to a negligible variation in the CO₂ yield with temperature. Comparing these bio-compounds, the CO₂ yield from SR of glucose (0.635 mol/mol C feed) at 650 °C was remarkably larger than the others (around 0.55), probably because of the large S/C used for SR of glucose (S/C=6).

In contrast to the CO₂ production, the dependence of CO production on temperature was more marked (**Figure 8.8b**). As the temperature rose, the CO yields of all the bio-compounds increased linearly. This increase in the CO yield resulted from two factors: (1) the increasing bio-compound conversion which produced more CO, (2) the suppressed WGS reaction which declined the conversion of CO to CO₂.

Conversely, the CH₄ yield showed a linear decreasing trend with temperature (**Figure 8.8c**) probably because the thermodynamic equilibrium of CH₄ steam reforming and its reaction kinetics were promoted. At 750 °C, the CH₄ yield was almost zero for all the bio-compounds. Below 750 °C, the ranking of bio-compounds in terms of CH₄ yield was as follows: ethanol > acetone > (furfural = glucose=acetic acid), in agreement with that observed at thermodynamic equilibrium (see Figure 5.3c in Chapter 5). The largest CH₄ yield was obtained from SR of ethanol, which may relate to the fact that a significant amount of CH₄ was formed during ethanol decomposition (**Table 8.3**). The CH₄ concentration in the experimentally obtained dry product gas was considerably larger than the value obtained from thermodynamic equilibrium calculation (see the dry gas composition in Appendix C), implying the consumption of CH₄ via SR and pyrolysis was kinetically restricted at the present condition. Lu and Hu [99] also found that the CH₄ selectivity was higher in SR of the pH neutral fuels (ethanol, 1-propanol) than

in SR of the acidic fuels (acetic acid, propanoic acid). They suggested that the acidification of neutral alcohols with nitric acid could suppress the CH₄ formation.

8.4 Catalytic pyrolysis of bio-compounds (S/C=0)

8.4.1 Product composition

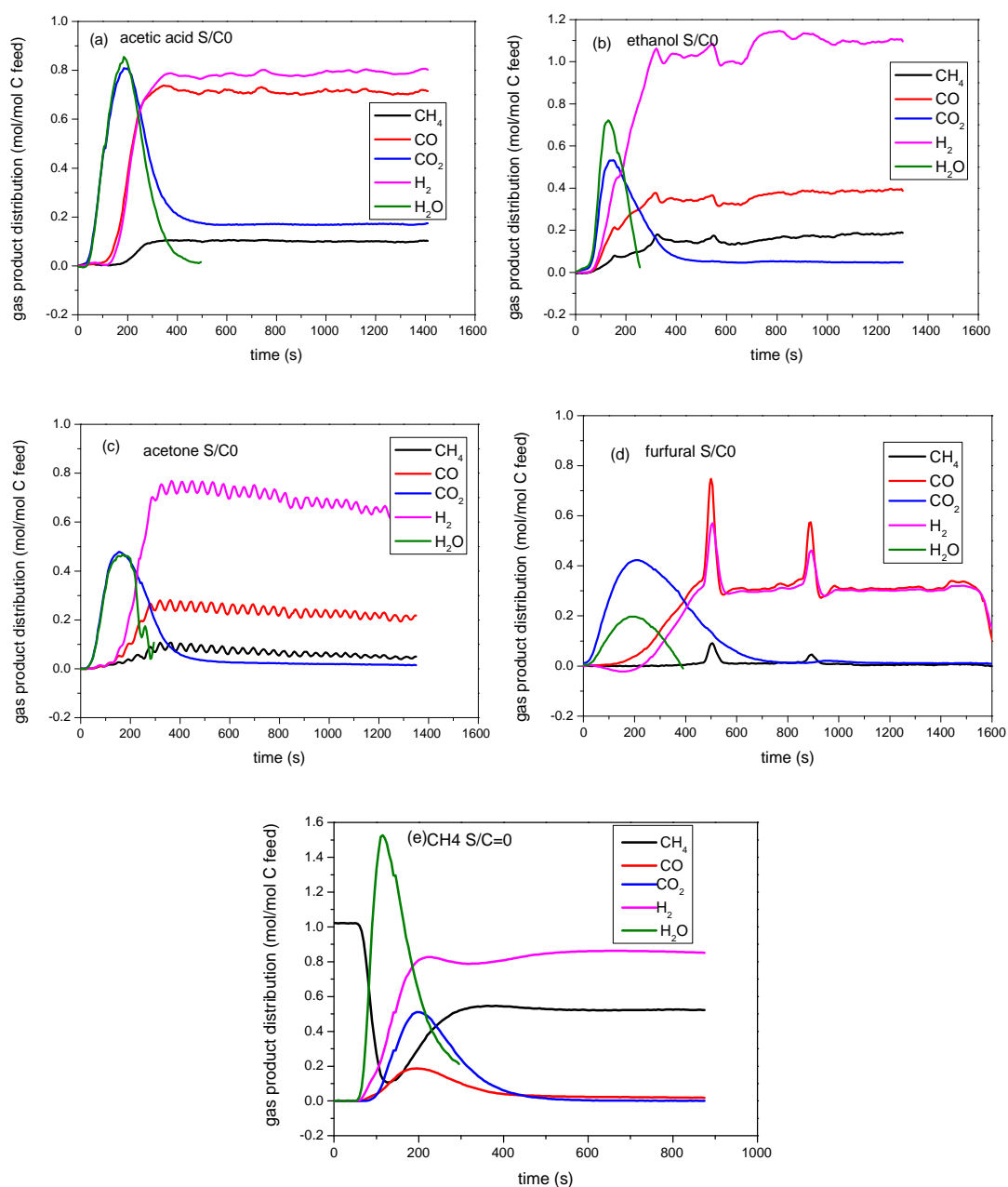


Figure 8.9 Pyrolysis of reforming fuel in the presence of fresh catalyst at 650 °C (a) acetic acid, (b) ethanol, (c) acetone, (d) furfural and (e) CH₄

Before studying the effect of S/C on SR performance, the special case S/C=0 was investigated at 650 °C. The presence of catalyst (catalytic pyrolysis) made this process different from the homogeneous pyrolysis. **Figure 8.9** displayed the gas evolution profile with respect to reaction time. The whole process could be considered as two stages: auto-reduction and catalytic pyrolysis. For furfural pyrolysis, two obvious spikes were noticed in the evolution profiles of H₂ and CO. The low volatility of furfural may be responsible for these spikes as a disturbance to the stable gas stream might occur when a droplet of furfural liquid fell on the catalyst bed.

(1) Auto-reduction stage

At the beginning of reaction, recognizable CO₂ formation peak and H₂O formation peak were shown, indicating the occurrence of catalyst auto-reduction. When using CH₄ as fuel, apart from the H₂O peak and the CO₂ peak, a small CO peak was shown indicating CO was also one of products. The height ratio of H₂O peak and CO₂ peak approximated to the stoichiometric ratio of H₂O to CO₂ according to reduction equations (**Table 8.2**), indicating the global reduction equations with CO₂ and H₂O as products shown in Chapter 4 were reasonable.

Table 8.2 Height ratio of H₂O peak to CO₂ peak

fuel	experimental	stoichiometric
acetic acid	1.05	1
ethanol	1.38	1.5
acetone	0.996	1
furfural	0.47	0.4

(2) Catalytic pyrolysis stage

The catalytic pyrolysis occurred following the auto-reduction. The composition of the product gas varied with the type of bio-compounds. The average of gas yield over the pyrolysis stage (not include the reduction stage) was summarized in **Table 8.3**. The yield of solid carbon was calculated on the basis of carbon balance and the

assumption that carbon element in product only existed in the form of CO, CO₂, CH₄ and solid carbon (Eq. 8.1). GC analysis suggested that there were no other hydrocarbons in addition to CH₄.

$$\text{solid carbon yield (mol/mol C feed)} = 1 - \text{CO}_2\text{yield} - \text{COyield} - \text{CH}_4\text{yield} \quad (\text{Eq. 8.1})$$

Table 8.3 Yields of CH₄, CO, CO₂ and H₂ (in mol/mol carbon feed) in the catalytic pyrolysis stage (yields below 0.05 were considered as measurement error)

Fuel	H ₂ yield	CO yield	CO ₂ yield	CH ₄ yield	solid carbon yield
acetic acid	0.79	0.71	0.17	0.1	0.02
ethanol	1.08	0.37	0.05	0.16	0.42
acetone	0.68	0.23	0.02	0.06	0.69
furfural	0.31	0.31	0.01	0.01	0.67
CH ₄	0.86	0.02	0.01	0.52	0.45

For the catalytic pyrolysis of bio-compounds, H₂ and CO were the main products. In addition, small amounts of CH₄ and CO₂ were also formed. The ratio of H₂ yield to CO yield was determined by the H/O ratio in bio-compound molecules. For acetic acid and furfural with a H/O ratio of 2, the H₂ yield and the CO yield were close to each other (**Figure 8.9a** and d). For ethanol and acetone with a H/O ratio of 6, the H₂ yield was approximately three times the CO yield (**Figure 8.9b** and c). The CH₄ yield from ethanol pyrolysis was the largest among all the bio-compounds studied. Except for the case of acetic acid pyrolysis, the CO₂ yield was almost zero.

8.4.2 Comparison with equilibrium composition

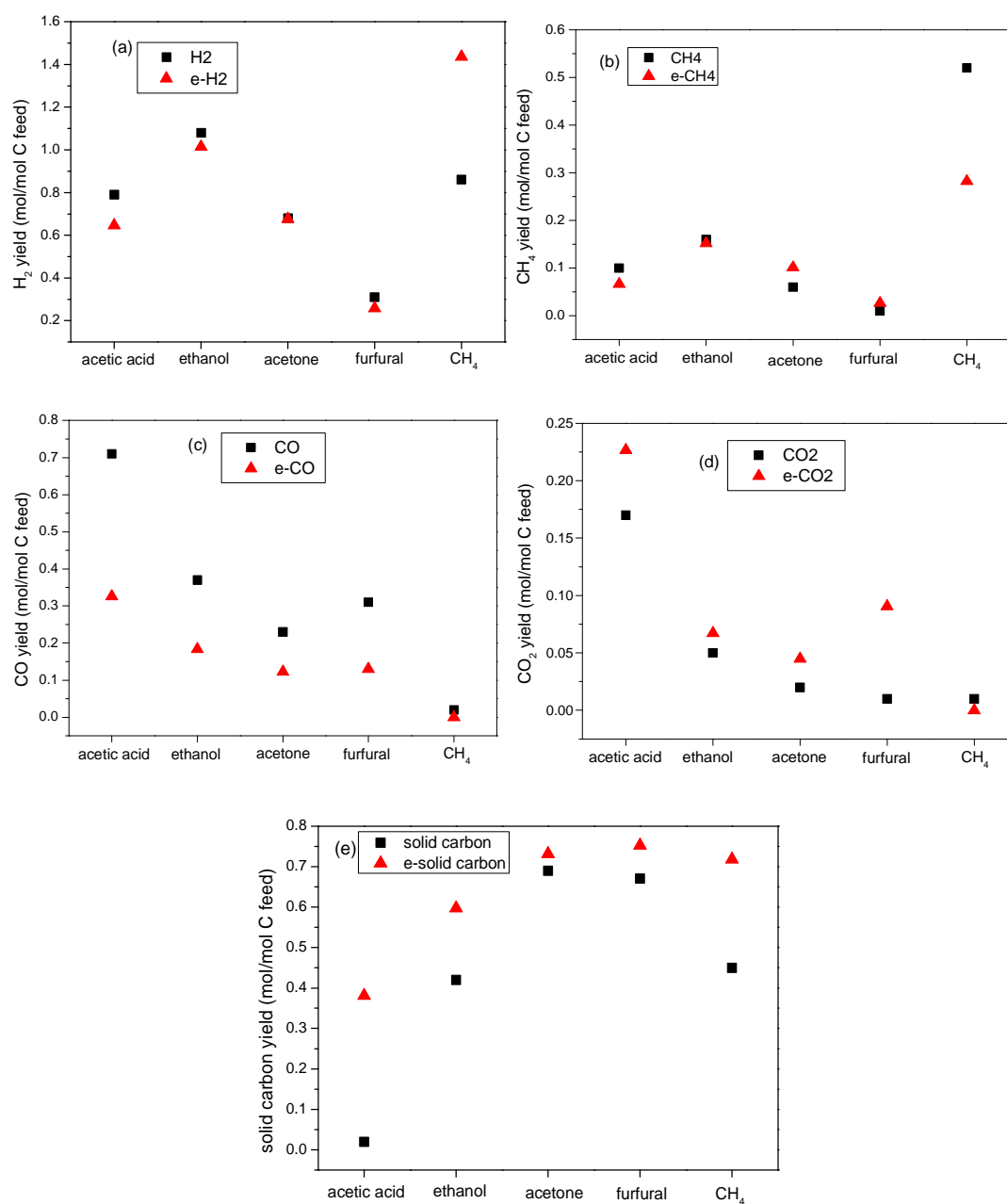
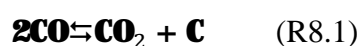


Figure 8.10 Comparison of pyrolysis product yields obtained by experiments at 650 °C (black solid square) with the equilibrium data (red solid triangle): (a) H₂ yield, (b) CH₄ yield, (c) CO yield, (d) CO₂ yield, and (e) solid carbon yield

The yields of pyrolysis products were compared with the data obtained at thermodynamic equilibrium (**Figure 8.10**). For the bio-compounds (acetic acid, ethanol, acetone and furfural), the H₂ yield and the CH₄ yield experimentally

observed were in a good agreement with their corresponding equilibrium data (**Figure 8.10a** and b). Larger CO yields and smaller CO₂ yields as well as smaller solid carbon yields were obtained in experiments compared to their equilibrium values (**Figure 8.10c-e**). This result could be interpreted as Boudouard reaction (R8.1) was kinetically restricted under the present experimental condition. For the pyrolysis of CH₄, neither CO nor CO₂ was detected in the product as expected. Both H₂ yield and solid carbon yield were considerably below the equilibrium value and consequently the amount of CH₄ in the product was higher than the equilibrium value. This result indicated that the CH₄ pyrolysis (R8.2) suffered kinetic limitation as well. In a summary, these two reactions for carbon formation were not kinetically favoured at the present experimental condition.



8.5 Effects of S/C

8.5.1 Feedstock conversion

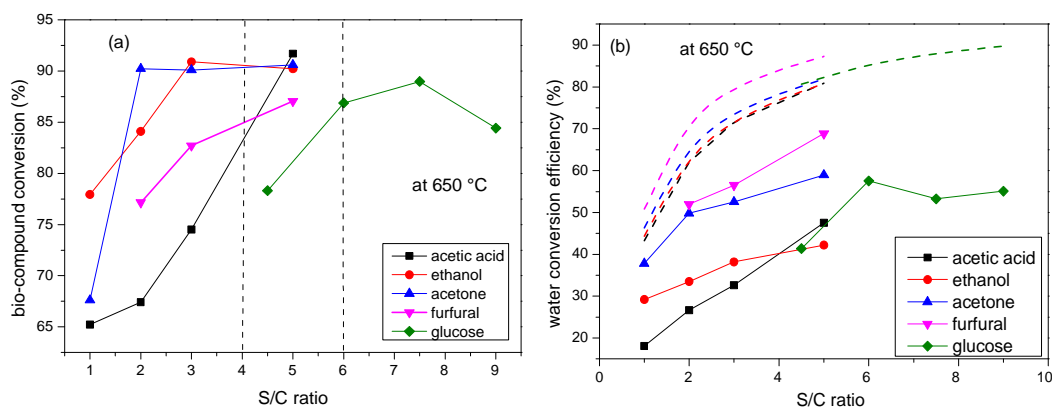


Figure 8.11 Effects of S/C on (a) fuel conversion and (b) water conversion efficiency at 650 °C (the water conversion efficiency at equilibrium was also shown in dashed line)

Water conversion was defined as the amount of water converted divided by the amount of water input. For different S/C, the water conversions are not comparable because the amounts of water input are different. Therefore, the amount of water consumed divided by the stoichiometric value required for the same amount of fuel input (according to the complete SR reaction equations in Chapter 4) was employed as an indicator of water utilization (denoted as water conversion efficiency).

High steam content in the feedstock (high S/C) was in favour of both WGS and SR reactions. As a result, the fuel conversion and water conversion efficiency kept increasing as the S/C increased for SR of acetic acid and furfural (**Figure 8.11**). For ethanol and acetone, the fuel conversions also underwent a significant increase as the S/C increased to 3 and 2, respectively. Further addition of water would not increase their fuel conversions. The slight increase in their water conversion efficiencies was caused by the shift of WGS equilibrium. For glucose, due to the limitation of glucose solubility, the S/C range studied was from 4.5 to 9. As the S/C increased, the glucose conversion increased first and then decreased. The maximum conversion was achieved at S/C =7.5. Beyond S/C=7.5, the water molecules may cover active sites of catalyst and thus impair the adsorption of reforming fuel molecules on the active sites [218].

8.5.2 Gas product yields

(1) H₂ yield

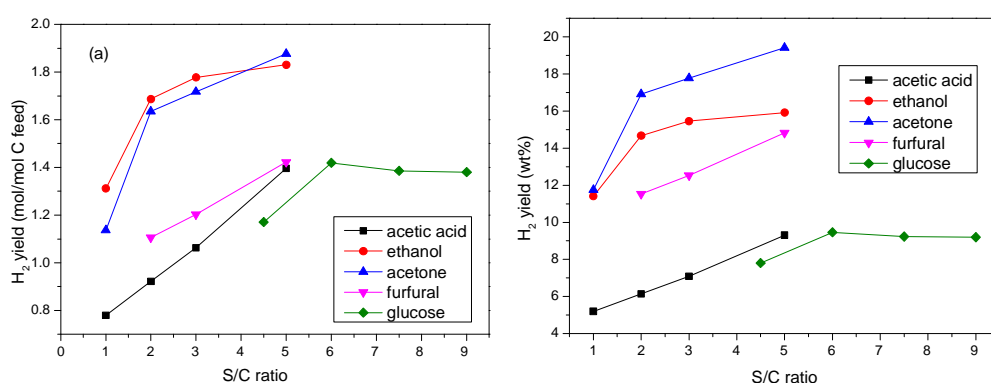


Figure 8.12 Variation of H₂ yield with S/C (a) in mol/mol carbon feed, and (b) in wt% of the bio-compound used

The variation of H₂ yield with respect to S/C was determined by both fuel conversion (**Figure 8.11a**) and water conversion efficiency (**Figure 8.11b**). As shown in **Figure 8.12a**, the H₂ yield from SR of furfural and acetic acid kept increasing as the S/C increased. The H₂ yield from SR of ethanol and acetone underwent a fast increase and then a slow increase. For glucose, the H₂ yield increased when S/C increased from 4.5 to 6 and then remained constant in the S/C range of 6 and 9. The H₂ yield in wt% of the fuel input is shown in **Figure 8.12b**. According to the H₂ yield in mol/mol C feed, the five bio-compounds could be classified into two groups: (1) ethanol and acetone with high H₂ yield and (2) furfural, acetic acid and glucose with low H₂ yield. Nonetheless, the H₂ yield from SR of glucose at 650 °C and S/C=6 was comparable with the result in ref [25] (67% of the stoichiometric potential).

(2) Yields of C-containing products

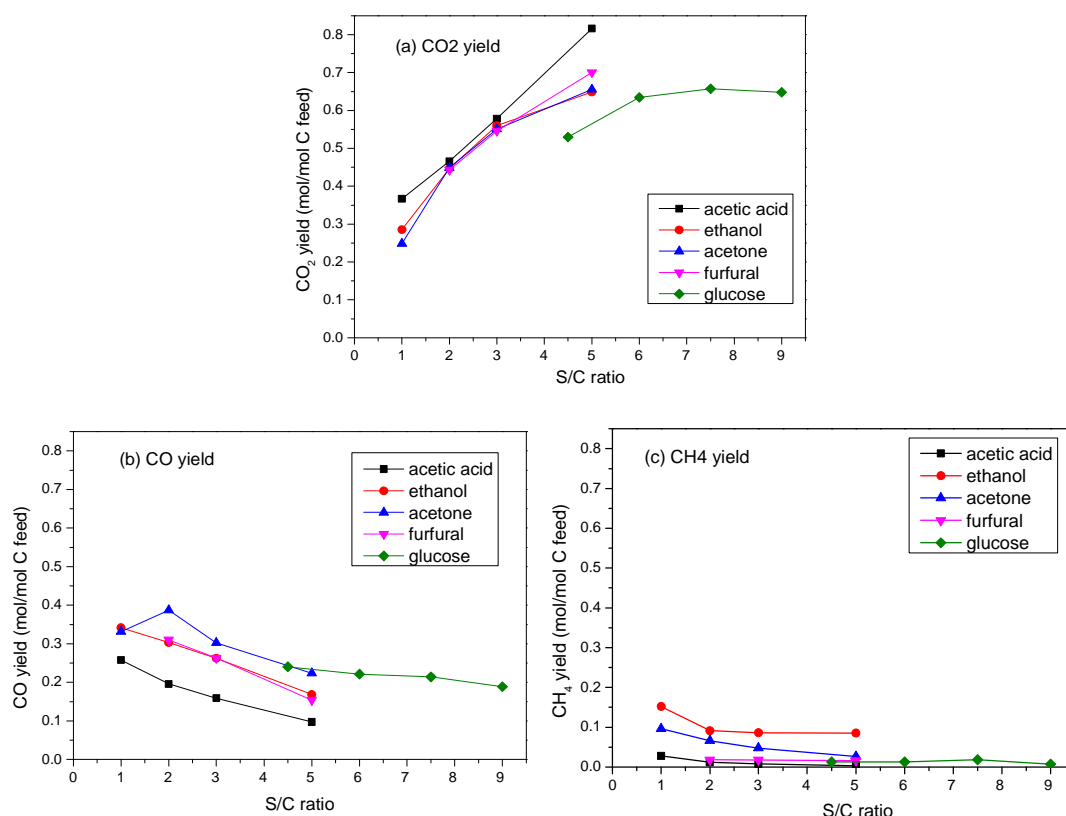


Figure 8.13 Carbon-containing product yields vs. S/C at 650 °C (a) CO₂, (b) CO and (c) CH₄

With increasing S/C, the CO₂ yield increased while the CO yield decreased because WGS reaction was favourable at high S/C ratio (**Figure 8.13a** and **b**). Higher S/C also shifted the equilibrium of CH₄ SR reaction in the direction of more CH₄ consumption. Thus, the CH₄ yield decreased (**Figure 8.13c**). The influence of S/C on the gas yields became less pronounced when the S/C ratio was above 6.

8.6 Characterisation of carbon deposits

8.6.1 CHN elemental analysis

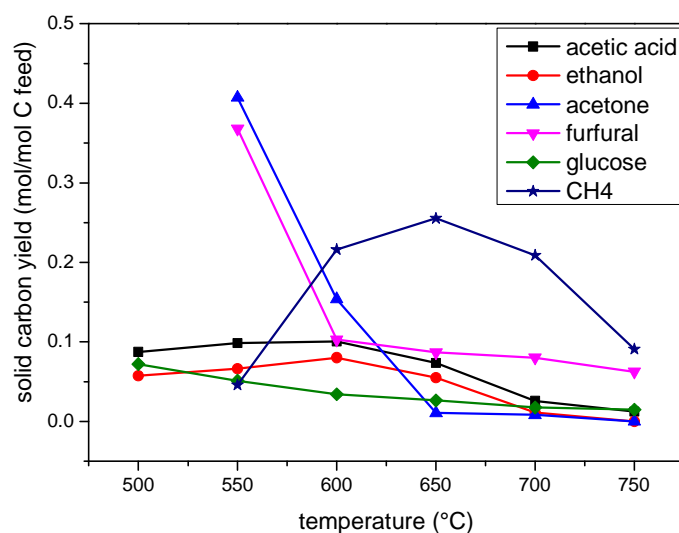


Figure 8.14 Yields of carbon deposits on the reacted catalyst at different temperatures with S/C=3 (for glucose, the S/C of 6 was used and the carbon yield calculation only considered the carbon deposited non-agglomerated catalyst particles)

For the bio-compounds, the amount of carbon deposited on the catalyst (in wt%) was measured by CHN elemental analysis. The solid carbon yield was calculated using Eq. 8.2.

$$C \text{ yield} = \frac{\text{catalyst mass} \times \text{carbon content (wt\%)} / 12}{\text{carbon feed} \left(\text{in } \frac{\text{mol}}{\text{s}} \right) \times \text{reaction duration}} \quad (\text{Eq. 8.2})$$

For the SR of CH₄, the solid carbon yield was calculated using Eq. 8.3.

$$C \text{ yield} = \frac{n_{CH_4,in} - n_{out,dry}(x_{CO} + x_{CO_2} + x_{CH_4})}{n_{CH_4,in}} \quad (\text{Eq. 8.3})$$

Where $n_{CH_4,in}$ is the flow rate of CH₄ feed, $n_{out,dry}$ is the total flow rate of dry outlet gas which is calculated based on nitrogen balance (see Chapter 3), x_i is the molar fraction of gas i in the dry outlet gas.

In the SR of CH₄, the yield of carbon deposits increased from 550 to 650 °C and then decreased (**Figure 8.14**). The maximum yield of carbon deposits was obtained at 650 °C. The increase in carbon yield with temperature resulted from the fact that the CH₄ pyrolysis was thermodynamically favourable at elevated temperature. As the temperature rose, the SR of CH₄ (endothermic) was also promoted, which competed with the pyrolysis of CH₄, resulting in the decrease in the solid carbon yield above 650 °C.

When using acetic acid and ethanol as reforming fuel, the carbon formation also increased first and then decreased as shown in **Figure 8.14**. The maximum carbon yield was obtained at 600 °C. Thermodynamic calculation (Figure 5.9 in Chapter 5) suggested that the carbon formation via pyrolysis and Boudouard reaction was suppressed at high temperatures. This could account for the decline occurring at high temperature region (600-750 °C). The negligible increase in the carbon yield from 500 to 600 °C was perhaps attributable to the promoted kinetics of carbon formation reactions. A peak value of carbon formation was also observed for SR of cresol by Wu and Liu [120]. A carbon deposition-carbon elimination kinetic model was proposed to explain the apparent carbon formation behaviour.

As **Figure 8.14** shows, the solid carbon yield from SR of acetone and furfural decreased dramatically as temperature increased and then levelled off above 650 °C and 600 °C, respectively. Compared to the other bio-compounds, the carbon deposition from SR of glucose was less severe if the agglomeration of catalyst particles was eliminated.

8.6.2 SEM imaging

8.6.2.1 Acetic acid, ethanol, acetone and furfural

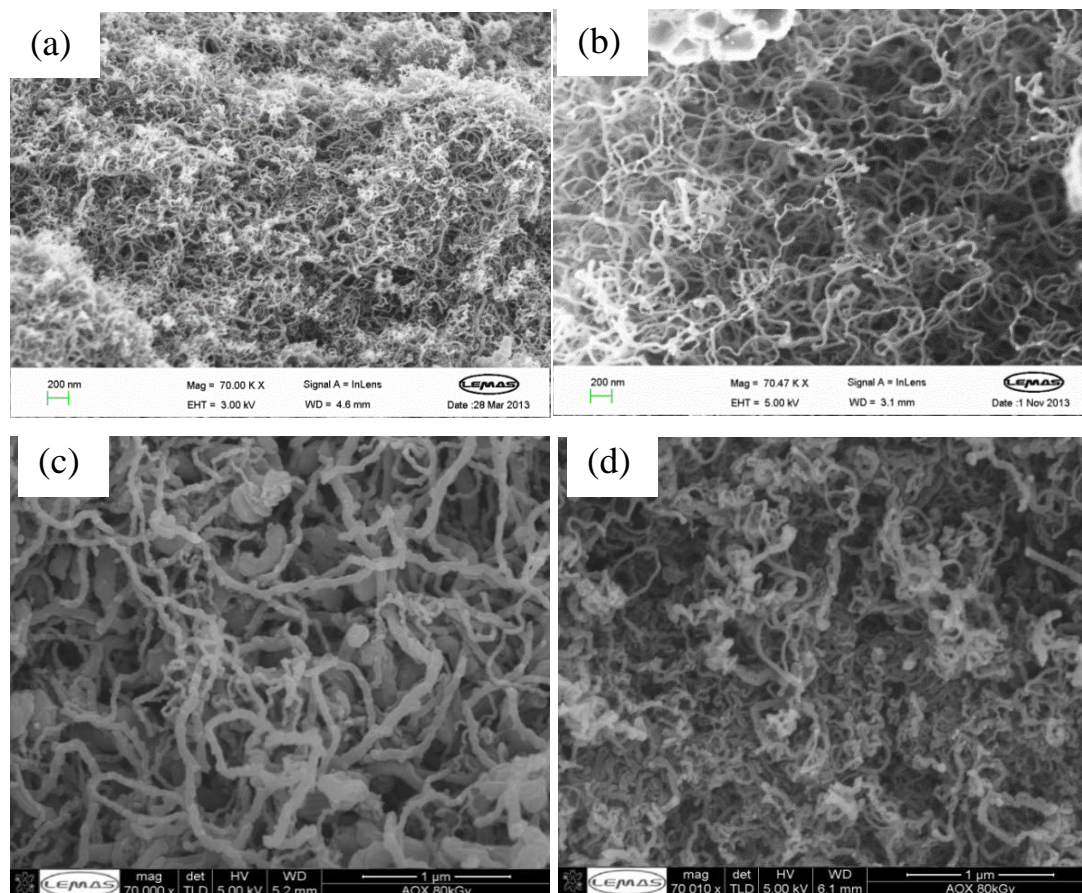


Figure 8.15 SEM images of reacted catalysts from steam reforming of (a) acetic acid, (b) acetone, (c) ethanol, and (d) furfural

As shown in **Figure 8.15**, carbon filaments were formed on the catalyst surface during SR of acetic acid [225], acetone, ethanol and furfural. There was a slight difference in the diameter and the denseness. Carbon filaments from SR of ethanol and furfural (50-100 nm in diameter) were thicker than those from SR of acetic acid and acetone (15-50nm in diameter). The carbon filaments from SR of acetic acid and furfural (**Figure 8.15a** and **d**) were much denser than those from SR of acetone and ethanol (**Figure 8.15b** and **c**).

8.6.2.2 Glucose

For SR of glucose, the carbon deposited on the agglomerated catalyst particles and on the non-agglomerated catalyst exhibited different textures. As **Figure 8.16(a-c)** shows, the carbon on the agglomerated catalyst particles was presented as large smooth flakes which coated the catalyst particles tightly (**Figure 8.16b**). The carbon that combined two particles together was in the form of porous honeycomb (**Figure 8.16c**), possibly resulting from the gas evolution during the decomposition of ‘sugar glue’. The morphology of carbon deposits on the non-agglomerated catalyst particles was not clear. EDX results (**Table 8.4**) suggested that the small particles on the catalyst surface were Ni crystallite clusters (e.g. sites A, E, and D in **Figure 8.16b** and d). A very thin layer of whisker carbon was shown on the catalyst surface (**Figure 8.16d**).

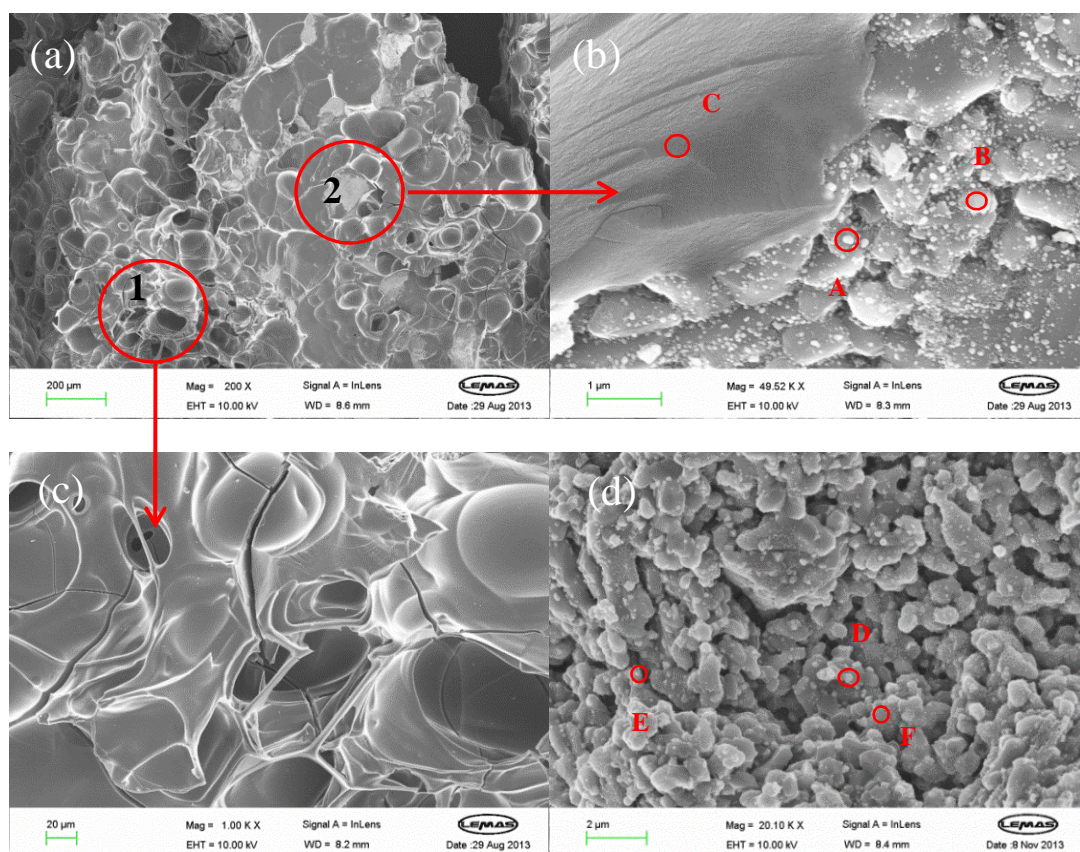


Figure 8.16 SEM images of (a-c) agglomerated catalyst particles and (d) non-agglomerated catalyst particles from steam reforming of glucose at 550 °C

Table 8.4 Elemental compositions (in wt%) of the sites marked in **Figure 8.16** determined by EDX

Sites	Al	O	Ni	C
A	27	0	42	31
B	51	5	3	41
C	0	6	0	94
D	14	17	58	10
E	28	18	49	5
F	57	41	0	2

8.6.2.3 Methane

The SEM instrument used in this project offered a variety of signal collection. Normally, secondary electron (SE) signals were collected for surface topography. Here, for the reacted catalyst from SR of CH₄, low angle back-scattered electron (LA-BSE) signals were collected. LA-BSE images are able to provide topographical information and composition contrast by brightness contrast. The heavier the element is, the brighter the corresponding site is in a LA-BSE image. **Figure 8.17** confirmed that the small particles with high brightness on the catalyst surface were Ni granules rather than carbon deposits, in accordance with the EDX analysis (**Table 8.4**).

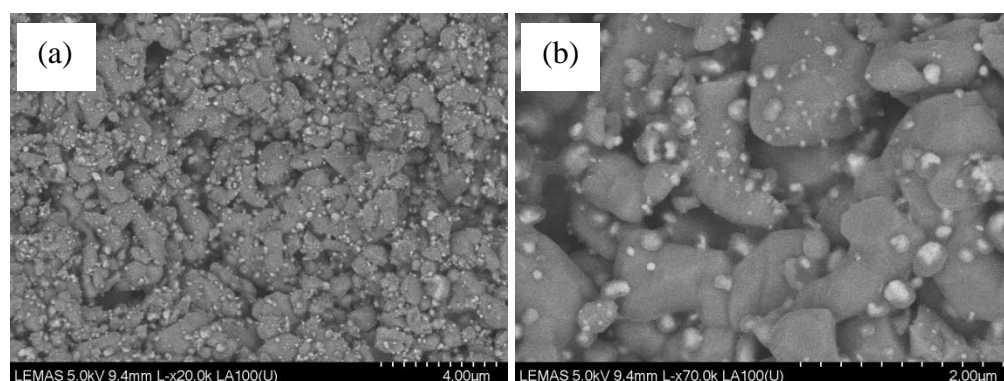


Figure 8.17 SEM images (LA-BSE signals) of the catalyst collected from steam reforming of CH₄ at 650 °C and S/C=3: (a) 20k magnification, (b) 70k magnification

CHN elemental analysis showed that a substantial amount of carbon (about 4 wt%) was deposited on the catalyst during SR of CH₄. However, the SEM imaging of the reacted catalyst (**Figure 8.17**) failed to show the morphology of carbon deposits. The carbon probably existed as a thin layer encapsulating the catalyst (layered carbon). Wu et al. [226] observed layered carbon formed from the decomposition of hydrocarbons by using focused ion beam/scanning electron microscopy (FIB/SEM). They suggested that layered carbon was the transition state to produce filamentous carbon. Chinthaginjala et al. [227] also reported that following the formation of layered carbon, filamentous carbon was formed on the top of layered carbon. Moreover, it was found that layered carbon could be gasified by steam more readily than filamentous carbon [228, 229].

8.7 Conclusions

The steam reforming (SR) performance of bio-compounds (acetic acid, ethanol, acetone, furfural and glucose) following catalyst auto-reduction was investigated. It was found that the SR performance using auto-reduced catalyst was close to that using H₂-reduced catalyst over a reaction duration of 45-60 min. The SR performance depended on the bio-compound used, the temperature and the molar steam to carbon ratio (S/C). In general, fuel conversion and H₂ yield were enhanced by raising temperature and S/C. The influence of temperature on water conversion was negligible. In contrast, water consumption was increased by increasing S/C. Above 650 °C, the H₂ yield in mol/mol C feed decreased in the order of ethanol > acetone > glucose > furfural > acetic acid (S/C=6 for glucose and S/C=3 for the other bio-compounds). The SR of ethanol achieved the largest H₂ yield (1.78 mol/mol C feed at 650 °C, 69% of the equilibrium potential) while the H₂ yield from SR of acetic acid was the lowest (1.06 mol/mol C feed at 650 °C, 61% of the equilibrium potential). The H₂ yield from SR of acetone was comparable to that from SR of ethanol, and even better if evaluating H₂ production by weight percentage of the bio-compound used. The discrepancy between experimental H₂ yields and equilibrium H₂ yields was ascribed to kinetic limitation on SR reaction. The WGS reaction seemed not to suffer significantly from kinetic resistance.

As a special case of S/C dependency study, catalytic pyrolysis of bio-compounds (i.e. S/C=0) was studied. H₂ and CO were the main pyrolysis products and their yield ratio depended on the H/O ratio in bio-compound molecules. For acetic acid and furfural with a H/O ratio of 2, the H₂ yield and the CO yield were close to each other. For ethanol and acetone with a H/O ratio of 6, the H₂ yield was approximately three times the CO yield. The comparison of experimental gas yields with equilibrium data indicated that Boudouard reaction and CH₄ pyrolysis were not kinetically favoured at 650 °C.

In summary, the main problem for SR of ethanol was a high CH₄ yield which may be contributed to ethanol pyrolysis. For SR of acetic acid, the H₂ yield obtained was relatively low probably due to the loss of active phase. Large amounts of carbon were formed on the catalyst at temperature below 650 °C, which was the main drawback for SR of acetone. The thermal stability of furfural limited SR of furfural at low temperatures. For SR of glucose, the severe agglomeration of catalyst particles at low temperatures was the main barrier. The temperatures for efficient SR of furfural and glucose were above 600 °C.

For the future work, the flow rate of reforming fuel and mass of catalyst need be properly designed to achieve a negligible external diffusion resistance for auto-reduction while providing sufficient catalyst for subsequent SR. Moreover, it is desirable to find out the cyclic performance of catalyst between oxidation and auto-reduction/SR.

Chapter 9

Reduction of nickel catalyst using solid bio-compounds glucose and citric acid

9.1 Introduction

Isothermal reduction of NiO/ α -Al₂O₃ catalyst with the five bio-compounds selected has been investigated in a steam reforming environment (Chapter 7). These bio-compounds were fed to the reactor in the form of aqueous solution or pure liquid and assumed to be vaporized prior to contact with the catalyst. This chapter studies the non-isothermal reduction of this catalyst with solid bio-compounds (glucose and citric acid) using TGA-FTIR technique. The direct reduction of iron ore with biomass (e.g. sawdust [145], palm kernel shell [146]) or biomass derivatives (e.g. char from biomass pyrolysis [32]) have been reported in the literature aiming at a sustainable metallurgical operation [145], in which biomass is used as a substitution of fossil fuel-based reductant. However, few studies have been devoted on the reduction of nickel oxide using biomass or compounds derived from biomass. Previous NiO reduction studies were mainly carried out in reducing gas atmospheres (H₂ [157, 216], syngas [41], CH₄ [130, 230]) or with solid carbon [231-233]. In the present work, the feasibility of reducing NiO with solid bio-compounds is examined. Herein, glucose and citric acid are chosen as representatives of solid bio-compounds as glucose is the basic building block of cellulose (a major biomass component) and citric acid naturally exists in a variety of fruits and vegetables. Impregnation is employed to load glucose or citric acid into the NiO/ α -Al₂O₃ catalyst. The issues addressed in this chapter include whether the NiO reduction occurs, the nature of the actual reductant (original feedstock, pyrolysis intermediates or carbonaceous residues), the reduction mechanism and kinetics.

9.2 Experimental

9.2.1 Sample preparation

2 g of NiO/ α -Al₂O₃ particles with a size of 0.85-2 mm were impregnated with glucose or citric acid aqueous solution (20 ml, 10 g/L) overnight at room temperature without stirring. The particles were then dried at 80 °C in an oven for 12 hours and denoted as 'NiO-G' and 'NiO-CA', respectively. In control experiments, α -Al₂O₃ particles were treated following the same procedure as the NiO/ α -Al₂O₃ particles. The α -Al₂O₃ samples impregnated with glucose and citric acid are referred to as 'Al₂O₃-G' and 'Al₂O₃-CA', respectively. The NiO/ α -Al₂O₃ particles without impregnation are referred to as 'fresh NiO'.

9.2.2 Temperature programmed reduction (TPR)

TPR experiments were performed on a TGA-FTIR instrument. Related working principles and instrument model were described in Chapter 3. NiO-G or NiO-CA samples (200 mg) were placed in the TGA crucible and heated from ambient temperature to 900 °C at 5 °C/min in a N₂ flow (50 ml/min). The N₂ flow acted as carrier gas flushing volatile products to the FTIR cell. OMNIC software was used to analyse the FTIR spectra obtained and create chemigrams (evolution profile against time or temperature) of volatile products. Wavenumber ranges set for creating chemigram of a specific compound were shown in Appendix D. TGA alone was used to carry out the TPR experiments with different heating rates for kinetics study. In this kinetics study, the temperature ramp rate was always 5 °C/min for the stage of bio-compound pyrolysis. When it came to the stage of NiO reduction, the heating rate was changed to different values (3, 7, 10, 15 °C/min). The TPR of fresh catalyst with H₂ was also performed in the TGA instrument as follows. 20 mg of fresh catalyst was heated to 150 °C at 20 °C/min under a N₂ flow and then maintained at this temperature for 3 hours to remove adsorbed moisture and air. After this, the sample was heated to 900 °C at 5 °C/min under a H₂ flow (50 ml/min) followed by naturally cooling down under N₂ flow.

9.2.3 Sample characterization

A series of TGA experiments were conducted under N₂ with a heating rate of 5 °C/min and terminated at different temperatures (420, 530, 670, 770 and 900 °C for the NiO-G sample, and 280, 400, 480, 530, 640, 740 and 900 °C for the NiO-CA sample) to obtain intermediate products. These samples were denoted as ‘NiO-G-T’ or ‘NiO-CA-T’, where ‘T’ is the end temperature of TGA experiments in °C. These samples were characterised by XRD and CHN elemental analysis. In addition, temperature programmed oxidation (TPO) experiments were performed on NiO-G-420, NiO-CA-400 and fresh NiO samples using the TGA-FTIR instrument. During TPO experiments, about 150 mg of samples were placed in the TGA crucible and heated from ambient temperature to 900 °C at 5 °C/min in an air flow of 50 ml/min. The surface topography and element distribution of samples were characterised by SEM-EDX technique. The pyrolysis of pure glucose or citric acid (100 mg) was also performed in TGA under N₂ (50 ml/min) from room temperature to 900 °C at a heating rate of 5 °C/min.

9.3 Results and discussion

9.3.1 TPR of glucose-impregnated NiO/ α -Al₂O₃ (NiO-G)

The TGA-FTIR results of NiO-G under N₂ at a heating rate of 5 °C /min are presented in **Figure 9.1**, and compared with those of Al₂O₃-G. With the temperature increasing, both samples underwent several mass losses as shown in **Figure 9.1a-b**. The main volatile products were identified as CO₂, H₂O and formic acid (see Appendix D). Their evolution profiles are shown in **Figure 9.1c-e**.

Up to 420 °C (henceforth termed ‘Section A’), both NiO-G and Al₂O₃-G exhibited similar mass change pattern which was an obvious mass loss over 150-240 °C followed by a less pronounced mass loss. The mass losses occurring in Section A corresponded to the formation of CO₂, H₂O and formic acid, resulting from glucose pyrolysis [234]. Moreover, the product profile of NiO-G below 420 °C was the same as that of Al₂O₃-G, suggesting NiO took no or negligible part in glucose pyrolysis.

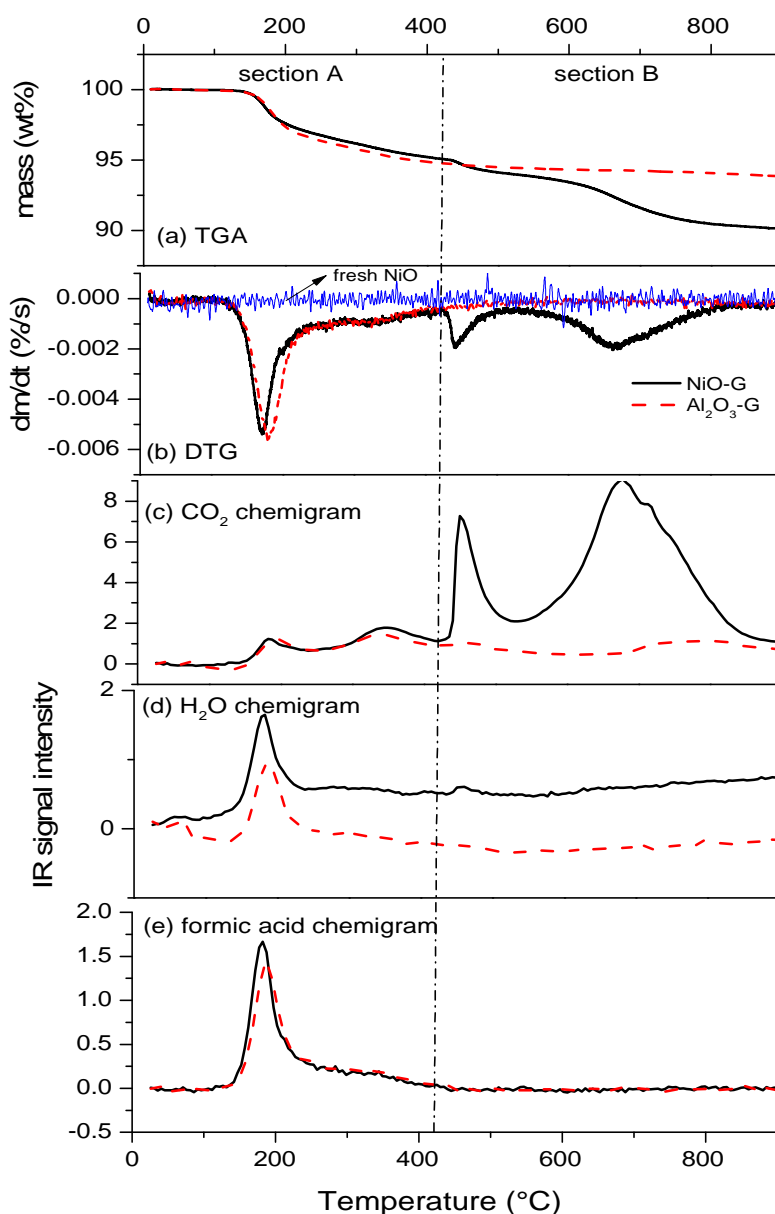


Figure 9.1 TGA-FTIR results of NiO-G (solid line) and Al₂O₃-G (dashed line) under N₂ at the heating rate of 5 °C/min: (a) TGA curve, (b) DTG curve, (c) CO₂ evolution profile, (d) H₂O evolution profile and (e) formic acid evolution profile. DTG of fresh NiO is also shown in (b)

From 420 °C to 900 °C (Section B), NiO-G had two additional mass loss phases around 442 °C and 665 °C while Al₂O₃-G showed a negligible mass change. These two mass losses specific to NiO-G were attributable to CO₂ production as CO₂ was the only carbon product detected by the FTIR (**Figure 9.1b** and c). Some water

vapour also evolved during this phase, as shown in the H₂O chemigram (**Figure 9.1d**). Hence, it is reasonable to believe that NiO reduction took place in Section B and CO₂ was the main reduction product. Sharma et al. [233] reported that both CO₂ and CO were primary products when reducing NiO with graphite in temperature range of 900-1000 °C. However, CO was not detected in this work probably due to the relatively low reaction temperature (below 900 °C). The CO production from NiO reduction by carbon (NiO + C → Ni + CO) is thermodynamically favoured at elevated temperatures (Appendix D).

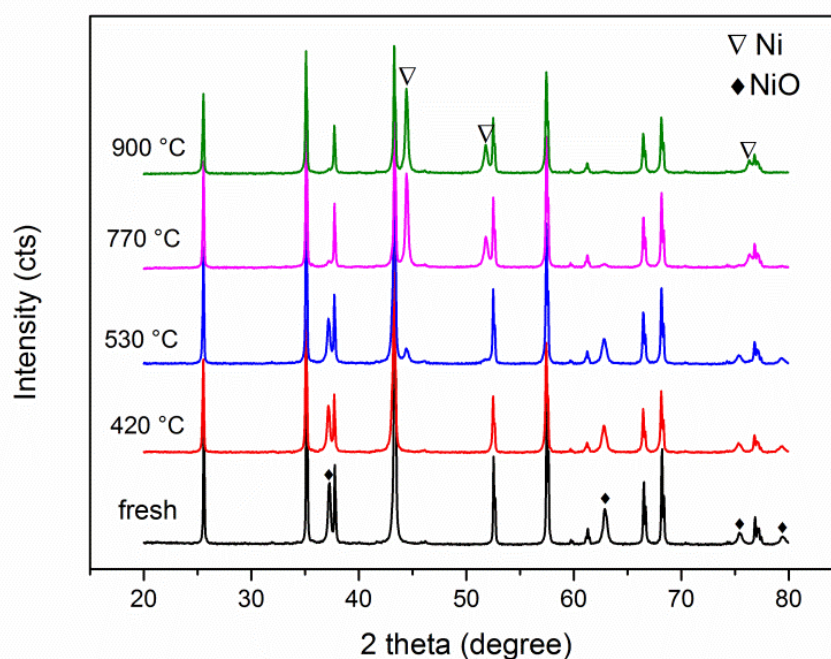


Figure 9.2 XRD patterns of NiO-G-T samples and fresh NiO sample (T=420, 530, 770, 900 °C, unmarked peaks are attributed to α -Al₂O₃)

To verify the occurrence of NiO reduction in the TGA-FTIR experiment above, XRD patterns of NiO-G samples obtained at different stages of the TPR process are presented in **Figure 9.2**. The characteristic peaks of metallic Ni were not observed at 420 °C but clearly appeared at 530 °C. The XRD result along with the TGA-FTIR result (**Figure 9.1**) indicated that the start temperature of NiO-G reduction was

420 °C. As the reduction proceeded, the intensity of NiO peaks decreased whereas the intensity of Ni peaks increased. When the temperature was raised to 900 °C, the NiO reduction was completed as shown by the entire disappearance of NiO peaks.

9.3.2 TPR of citric acid-impregnated NiO/ α -Al₂O₃ (NiO-CA)

The TGA-FTIR results of NiO-CA and Al₂O₃-CA under N₂ at a heating rate of 5 °C /min are compared in **Figure 9.3**. From ambient temperature to 280 °C, both NiO-CA and Al₂O₃-CA exhibited one mass loss peak around 180 °C (**Figure 9.3b**). This mass loss was attributed to the pyrolysis of citric acid [235, 236], which generated H₂O, CO₂ and other volatiles, such as itaconic anhydride and citraconic anhydride (**Figure 9.3c-e**, FTIR spectra and the pyrolysis process are given in Appendix D). Further mass losses above 280 °C only took place on NiO-CA. However, as metallic Ni was not detected by XRD until 480 °C (**Figure 9.4**), the onset temperature of NiO-CA reduction was considered at 400 °C rather than 280 °C. Like NiO-G, the TPR of NiO-CA was divided into two sections: below 400 °C and above. The first section (Section A in **Figure 9.3**) was associated with citric acid pyrolysis producing carbonaceous residue (coke). The second was NiO reduction by the coke (Section B in **Figure 9.3**). In Section B, three mass loss peaks (around 420 °C, 500 °C, and 640 °C) coincided with three CO₂ evolution peaks (**Figure 9.3b,c**), implying CO₂ is the main reduction product. As the temperature increased, the mass of the NiO-CA sample continuously decreased until 740 °C, above which further mass loss was not observed (**Figure 9.3a and b**). The Rietveld refinement of the XRD data for the NiO-CA-740 yielded the composition 84.4 wt% α -Al₂O₃, 9.8 wt% Ni and 5.8 wt% NiO, which was very close to that for the NiO-CA-900 (see Appendix D). This suggested that for NiO-CA, the extent of reduction had reached its maximum at 740 °C and did not proceed beyond that. The incomplete conversion of NiO to Ni (68.3%) was probably caused by the insufficiency of reductant. Negligible carbon content in the NiO-CA-740 sample detected by CHN analysis (see **Figure 9.5**) supported this argument. To achieve a complete reduction, a larger loading of citric acid on the catalyst would be required.

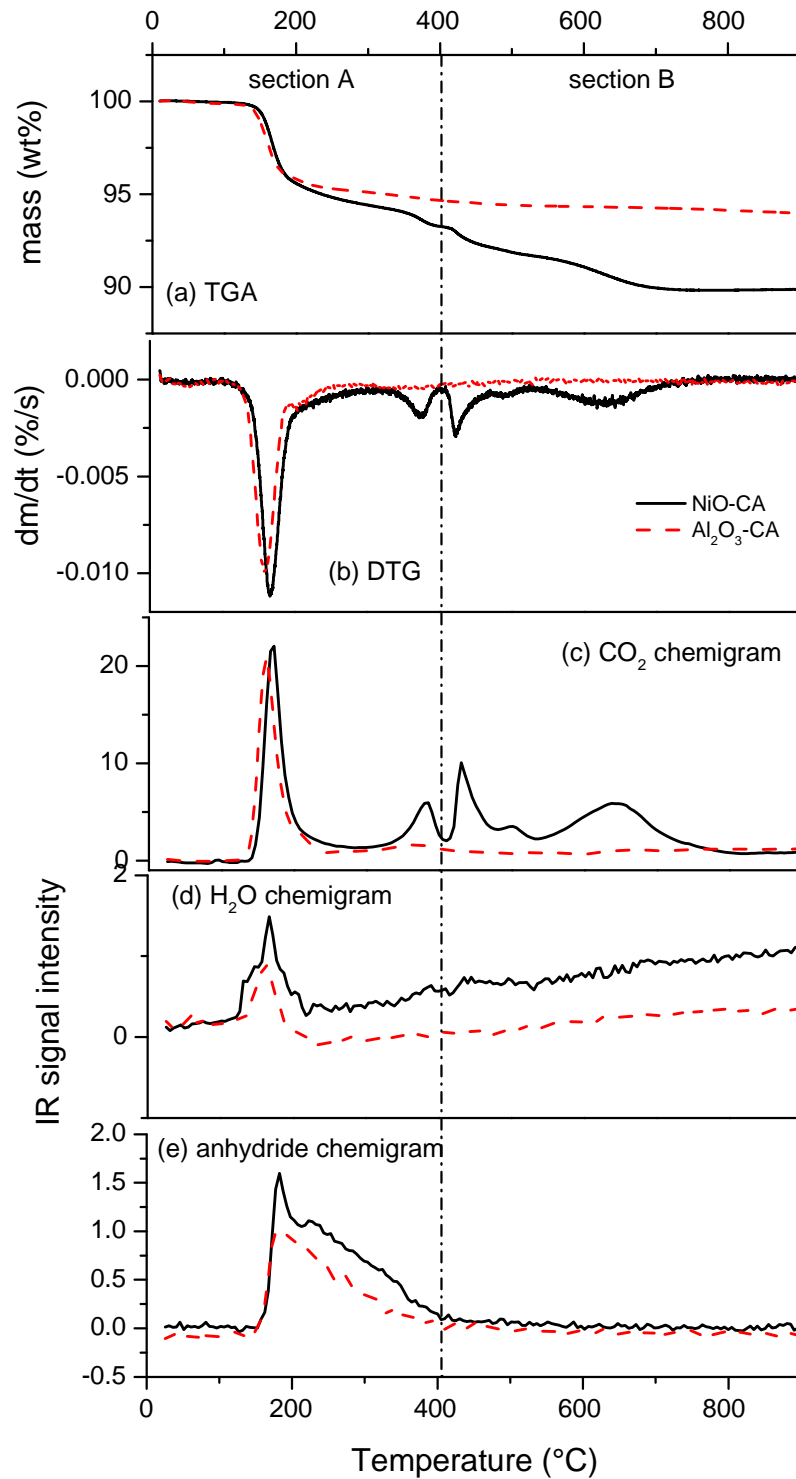


Figure 9.3 TGA-FTIR results of NiO-CA (solid line) and Al₂O₃-CA (dashed line) under N₂ at the heating rate of 5 °C/min: (a) TGA curve, (b) DTG curve, (c) CO₂ evolution profile, (d) H₂O evolution profile and (e) anhydride evolution profile

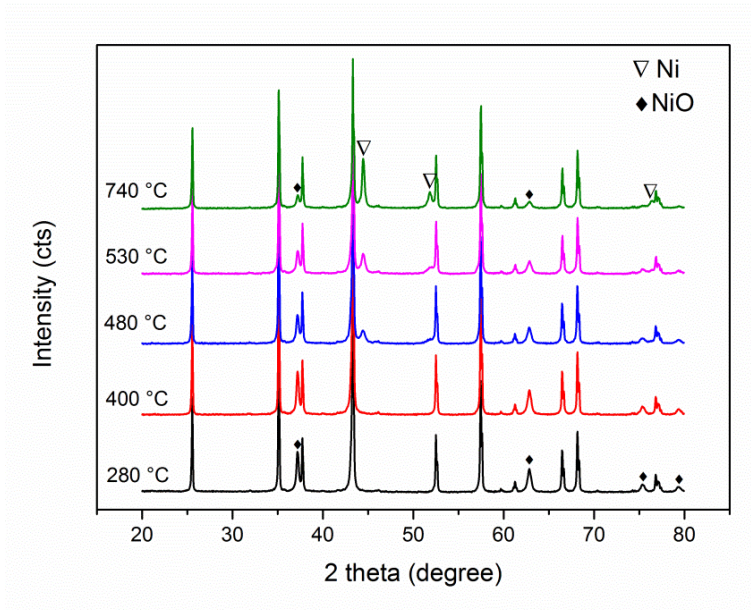


Figure 9.4 XRD patterns of NiO-CA-T samples ($T=280, 400, 480, 530$ and 740 °C, unmarked peaks are attributed to $\alpha\text{-Al}_2\text{O}_3$)

9.3.3 Coke characterisation

9.3.3.1 Carbon and hydrogen content during TPR (CHN results)

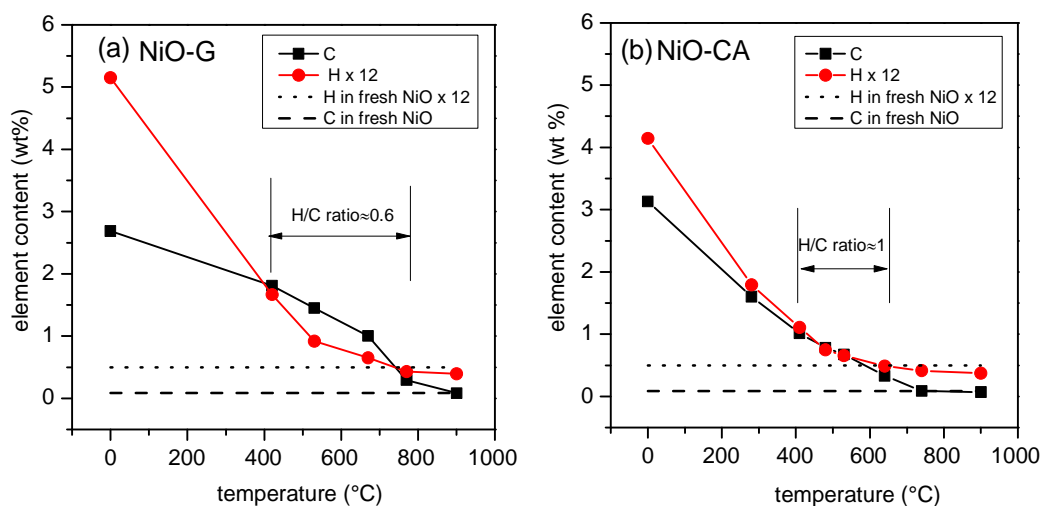


Figure 9.5 Carbon and hydrogen contents (wt%) from CHN analysis in (a) NiO-G-T samples and (b) NiO-CA-T samples, 'T' is the end temperature of TGA experiments, hydrogen content is multiplied by 12

Carbon and hydrogen content of the NiO-G-T samples (T=420, 530, 670, 770 and 900 °C) and the NiO-CA-T samples (T=280, 400, 480, 530, 640, 740 and 900 °C) are shown in **Figure 9.5**. The composition of initial NiO-G and NiO-CA samples (before thermal treatment) is represented by the far left point in **Figure 9.5a** and **b**, respectively.

(1) Carbon content

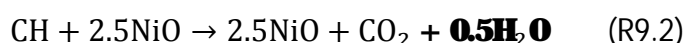
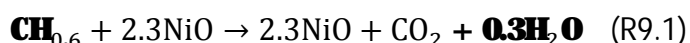
The CHN elemental analysis showed that the initial carbon loadings achieved by impregnation method were 2.69 wt% and 3.13 wt% for NiO-G and NiO-CA, respectively (T=0 in **Figure 9.5**). As the TPR proceeded, the amount of carbon decreased gradually until it was depleted at 900 °C for NiO-G (**Figure 9.5a**) and at 740 °C for NiO-CA (**Figure 9.5b**). At the end of pyrolysis and the beginning of NiO reduction, the carbon content in NiO-G (1.72 wt%, T=420 °C) was higher than that in NiO-CA (0.95 wt%, T=400 °C), indicating more carbon could be used for the subsequent NiO reduction of NiO-G compared to the case of NiO-CA. The ‘carbon deposition efficiency’, defined as the ratio of carbon formed during pyrolysis to the amount present in the feedstock, for NiO-G and NiO-CA were estimated to be 64% and 30%, respectively. The difference in carbon deposition efficiency between NiO-G and NiO-CA was probably due to the difference in charring characteristics of the bio-compounds concerned. Pyrolysis experiments of pure glucose and pure citric acid in absence of catalyst under N₂ indicated that their carbon deposition efficiencies were 49.7% and 15.3%, respectively. The presence of solid support significantly enhanced the carbon deposition efficiency of both glucose and citric acid during pyrolysis. High carbon deposition efficiency is a favourable property for achieving complete reduction in the absence of other reducing agents. The low carbon deposition efficiency of NiO-CA resulted in its incomplete NiO reduction as shown in Section 9.3.2, although the initial carbon loading of NiO-CA was larger than that of NiO-G.

(2) Composition of coke

In order to calculate the molar ratio of hydrogen to carbon (H/C ratio) of the coke, the weight percentage of hydrogen was multiplied by 12 (molar mass of carbon) and then compared with the weight percentage of carbon as shown in **Figure 9.5**. The

initial H/C ratios of 1.92 and 1.32 (at T='0' in **Figure 9.5**) were in good agreement with the expected values of 2.00 and 1.33 for pure glucose and citric acid respectively. After the thermal decomposition and throughout the reduction (Section B), the coke formed on the NiO/ α -Al₂O₃ corresponded to the formula CH_n, where n \approx 0.6 for NiO-G and n \approx 1 for NiO-CA. The coke composition reported here was similar to that deposited on bi-functional catalysts during steam reforming of naphtha with n varying from 0.5 to 1 [205].

For complete reduction, the stoichiometric molar ratio of CH_n to NiO was 0.43 for NiO-G and 0.4 for NiO-CA according to R9.1 and R9.2, respectively. However, the actual molar ratios of CH_n to NiO were 0.61 and 0.33, derived from the carbon content in NiO-G-420 and NiO-CA-400 as well as the NiO content of 18 wt% in fresh catalyst. Therefore, the amount of reductant was theoretically sufficient for complete NiO-G reduction, a feature verified by the lack of NiO peaks in the XRD spectra of NiO-G-900 (**Figure 9.2**). Excess carbon was expected to remain in the NiO-G-900 sample. However, CHN analysis (**Figure 9.5a**) showed that little carbon or hydrogen was detected on this sample. For NiO-CA, the amount of reductant could ensure a maximum of 82% conversion from NiO to Ni. Yet, Rietveld refinement of the XRD data indicated that the reduction extent was only 68.3%. A possible reason is that the carbonaceous material formed through bio-compound pyrolysis had some volatility/reactivity besides the reduction mechanism.



9.3.3.2 Oxidation temperature of coke (TPO results)

TPO experiments combined with FTIR analysis of the evolved gas were carried out on NiO-G-420 and NiO-CA-400 samples. A main mass loss peak accompanied by one CO₂ evolution peak was observed (**Figure 9.6a, b**), implying that only one type of coke existed on the NiO/ α -Al₂O₃. The oxidation temperature of the coke was around 385 °C and 360 °C respectively for NiO-G and NiO-CA, much lower than that of carbon black (670 °C, **Figure 9.6c**). The oxidation temperature may relate with the coke composition. H/C ratios of the coke from glucose pyrolysis and citric

acid pyrolysis are 0.6 and 1 while carbon black contains more than 97% elemental carbon. As expected, the carbonaceous material with a higher H content was more easily oxidised.

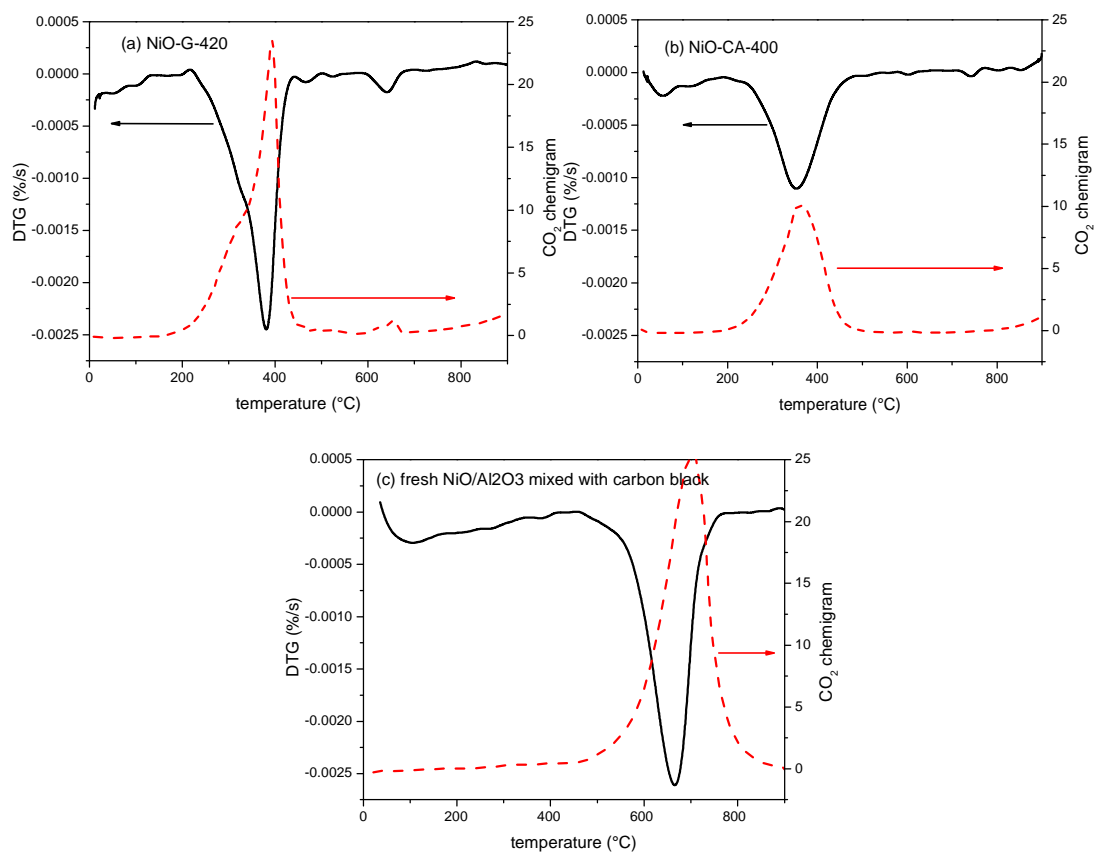


Figure 9.6 TPO-FTIR results of (a) NiO-G-420, (b) NiO-CA-400, and (c) fresh NiO/ α -Al₂O₃ catalyst mixed with carbon black in air (50 ml/min) at a heating rate 5 °C/min

9.3.3.3 Distribution of coke in NiO/ α -Al₂O₃ (SEM-EDX)

(1) Fresh catalyst

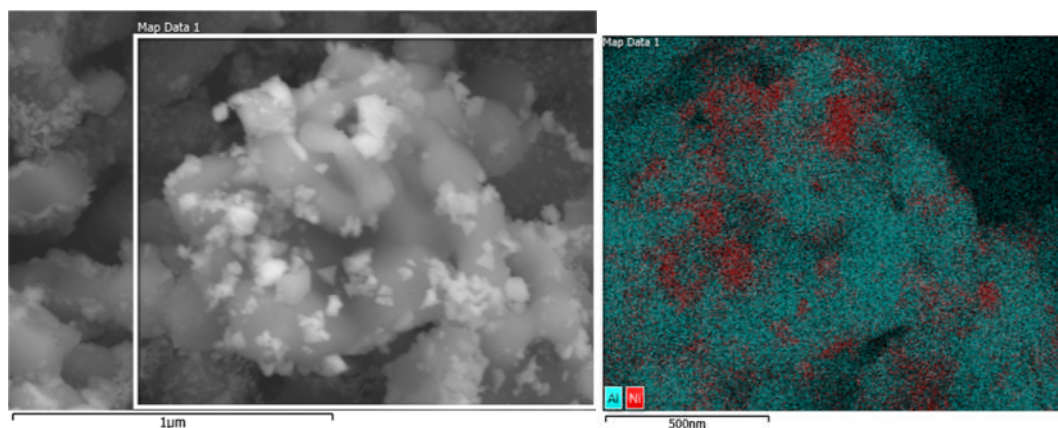


Figure 9.7 SEM image (left) and EDX mapping result (right) of fresh NiO/ α -Al₂O₃ catalyst

As shown in **Figure 9.7**, EDX mapping of the fresh catalyst confirmed that small particles on the catalyst surface were NiO (red colour for Ni element in contrast to the blue for Al element). Rietveld refinement of the XRD data indicated that the mean size of NiO crystallites was around 40 nm. The NiO particles observed on the catalyst surface show these crystallites accumulated into clusters of much larger size.

(2) NiO-G-420 sample

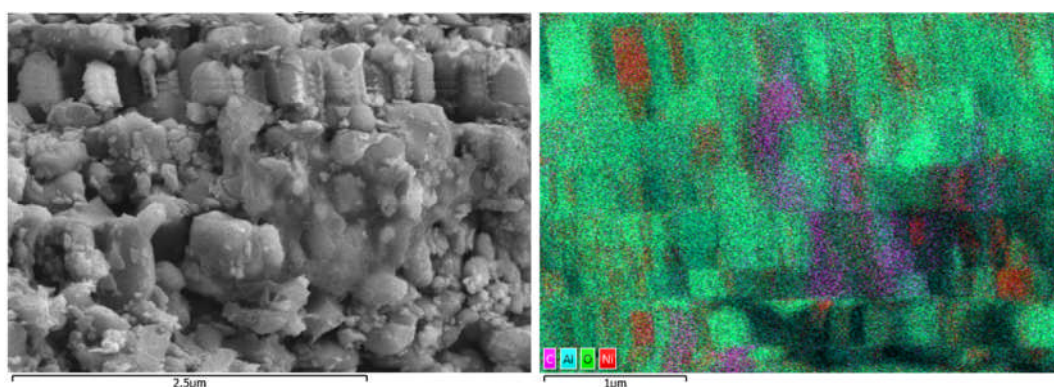


Figure 9.8 SEM image (left) and EDX mapping result (right) of the NiO-G-420 sample which was obtained by heating NiO-G under N₂ at 5 °C/min up to 420 °C

A large thin film of carbon was observed on the surface of NiO-G-420 sample by SEM imaging and EDX mapping (pink colour for carbon element in **Figure 9.8**-right). The catalyst surface was not completely covered by the carbon film and some NiO sites were bare.

9.3.4 Reduction mechanism

As shown in Section 9.3.1 and 9.3.2, two or three reduction peaks were observed during the NiO/ α -Al₂O₃ reduction by coke from glucose or citric acid pyrolysis. The existence of different NiO species (free NiO, and the NiO strongly combined with Al₂O₃, i.e. NiAl₂O₄) [99, 135] and the heterogeneity of coke were two common reasons for the occurrence of multiple reduction phases. However, these two explanations did not work in this study as (1) only one reduction peak was observed when reducing the fresh catalyst with H₂ (**Figure 9.9**) and (2) only one type of coke was detected during TPO of the NiO-G-420 and the NiO-CA-400 (**Figure 9.6**).

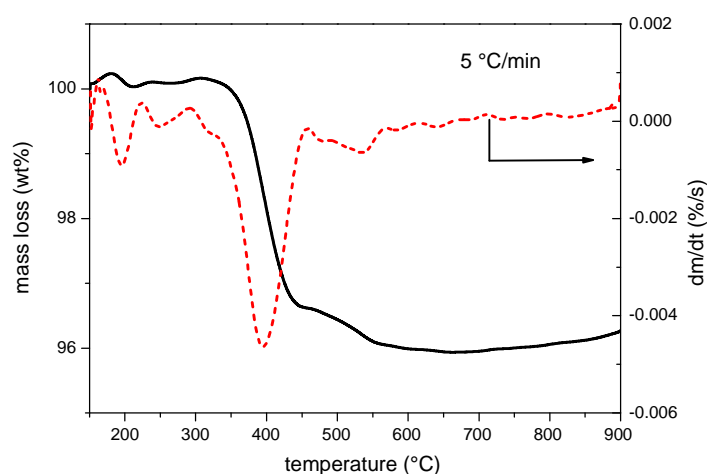
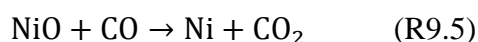
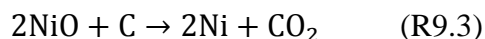


Figure 9.9 TGA and DTG curves of the NiO/ α -Al₂O₃ catalyst under H₂ flow at a heating rate of 5 °C/min

Two reduction stages were also observed by El-Guindy and Davenport for ilmenite reduction with graphite [45]. In their study, the first reduction stage was assigned to the solid-solid reaction at the contact points between reactants. The second reduction stage occurring at a higher temperature was attributed to the gaseous reduction with CO which was regenerated via R9.4. Pan et al. [30] suggested the direct reduction

of CuO by coal char took place with onset temperature as low as 500 °C. As the temperature increased, the reactivity of char gasification (R9.4) was improved and the gasification product, CO, became the main reducing agent for CuO reduction. In the present work, the reduction of the NiO/ α -Al₂O₃ catalyst with the coke also underwent a similar mechanism which is described as follows.



The first reduction phase observed over 400-530 °C was attributed to the direct reduction of NiO by the coke deposited on NiO sites (R9.3). As the reduction proceeded, the quantity of contact points between NiO and coke decreased resulting in the slowing down of the reduction rate. When the temperature increased to above 500 °C, carbon gasification by CO₂ via R9.4 was initiated. As a result, the coke deposited on Al₂O₃ sites was converted to CO, which acted as the reducing agent (R9.5) for the second reduction phase observed over 530-900 °C. Thermodynamic calculation (Appendix D) also indicated that R9.4 did not occur until 500 °C. The gaseous reduction mechanism made it possible that the bare NiO particles (shown in **Figure 9.8**) were reduced as well. In the second reduction stage, the CO₂ formed via R9.5 reacted with coke in return and produced more CO via the reverse Boudouard reaction (R9.4). A regeneration cycle of CO and CO₂ was established as shown in **Figure 9.10**. Therefore, it could be interpreted as the reductant was transported from Al₂O₃ sites to NiO sites with CO₂ as carrier.

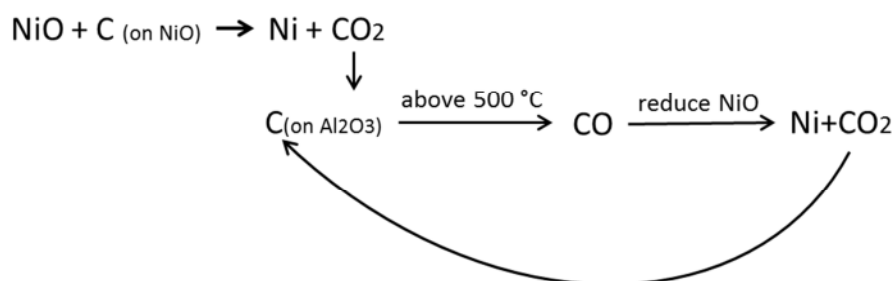


Figure 9.10 Mechanism diagram of NiO/ α -Al₂O₃ reduction with the coke deposited on both NiO sites and Al₂O₃ sites

The reduction mechanism mentioned above was supported by a TPR experiment of NiO-G with excess glucose being loaded (the weight ratio of glucose and the catalyst is 1:1.4) under N₂. Since the glucose was in excess, the catalyst was expected to be entirely covered by coke from glucose pyrolysis. Consequently, all the NiO particles could be directly reduced by the coke in contact with them. This argument was corroborated by the experimental evidence that only one reduction peak over 420-530 °C was observed during the TPR process of the excess glucose experiment (**Figure 9.11**). According to the reduction mechanism proposed in this study, the CO₂ produced from NiO reduction would react with the residual coke producing CO when temperature was above 500 °C. That was why the evolution of CO was observed following the reduction as shown in the chemigram of **Figure 9.12**.

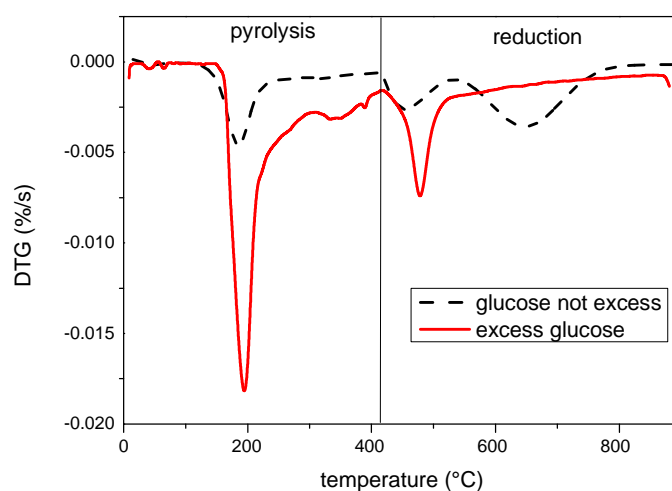


Figure 9.11 DTG of NiO-G under N₂ with excess glucose (the weight ratio of glucose and NiO/ α -Al₂O₃ is 1:1.4 in contrast to the ratio of 1:10 in the case of glucose not excess)

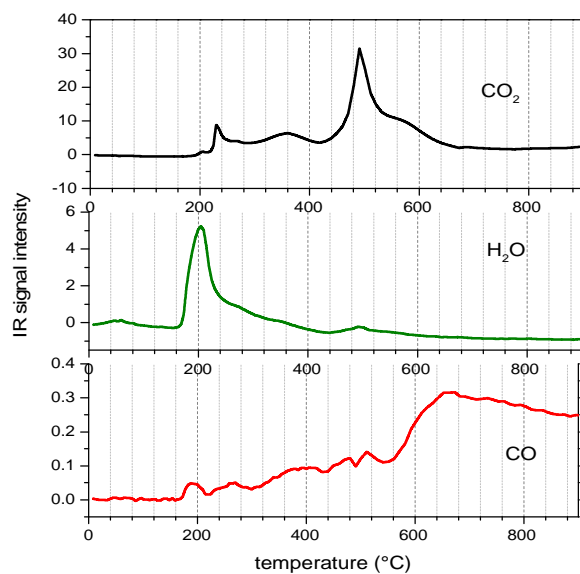


Figure 9.12 Evolution profiles of CO₂, H₂O and CO with respect to temperature for TPR of NiO-G with excess glucose under N₂

9.3.5 Reduction kinetics

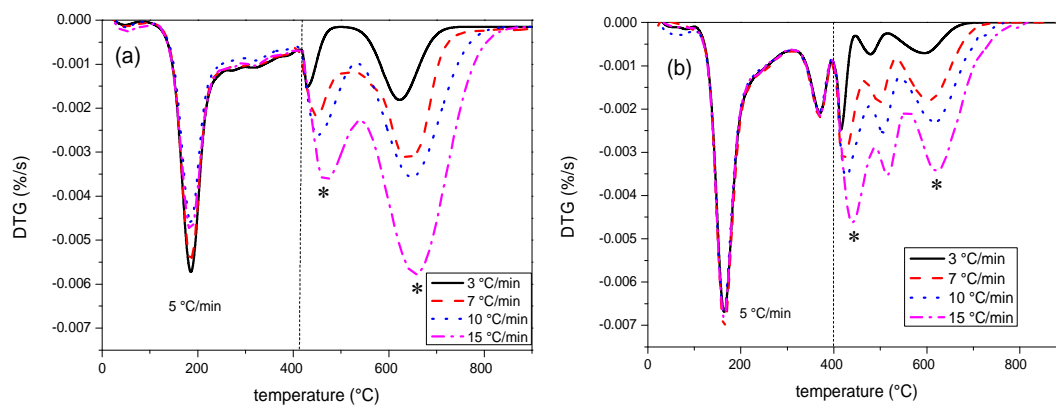


Figure 9.13 DTG of (a) NiO-G and (b) NiO-CA under N₂ at different heating rates (*these reduction peaks are used for kinetics calculation)

Reduction kinetics of NiO/ α -Al₂O₃ by coke from in situ pyrolysis of glucose or citric acid was investigated by TPR at four different heating rates (3, 7, 10 and 15 °C/min) under N₂. The heating rate for pyrolysis stage was maintained at

5 °C/min. As shown in **Figure 9.13**, the reduction peaks shift slightly to higher temperature as the heating rate was increased. Two reduction peaks are clearly identified for NiO-G and three reduction peaks for NiO-CA. For each reduction peak, the peak maximum corresponds to the largest mass loss rate and thus the largest reduction rate. Based on the dependence of the absolute temperature for the peak maximum (T_m) on heating rate (β), the apparent activation energy (E_a) of NiO reduction was estimated using Kissinger method [237]. The Kissinger method is able to calculate kinetic parameters of a solid state reaction without knowing the reaction mechanism (model-free method). This was done according to the equation:

$$\ln\left(\frac{\beta}{T_m^2}\right) = -\frac{E_a}{RT_m} + \ln\left(\frac{AR}{E_a}\right)$$

where R is the gas constant and A is the pre-exponential factor in the Arrhenius equation. The E_a and pre-exponential factor A could be derived from the slope and intercept of the Kissinger plot, which is $\ln(\beta/T_m^2)$ versus $(1/RT_m)$.

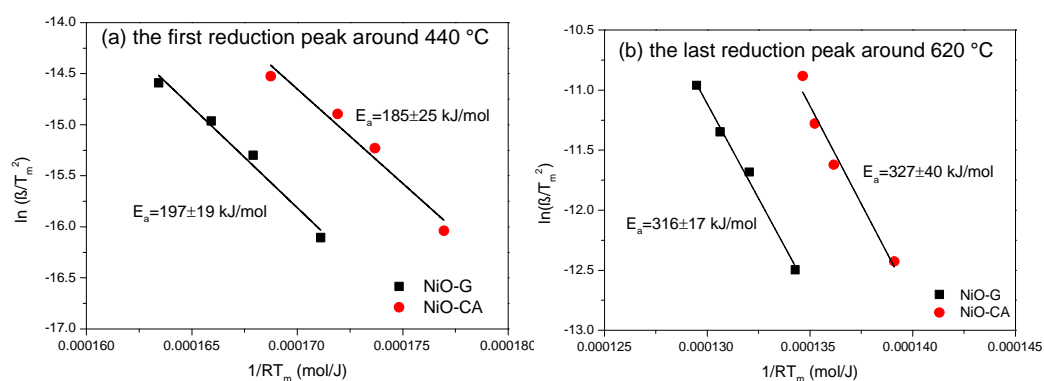


Figure 9.14 Kissinger plots of NiO reduction by coke (a) the first reduction peak and (b) the last reduction peak

Kissinger plots of the first and the last reduction peaks are presented in **Figure 9.14**. Satisfactory linear fits were achieved, indicating the applicability of the Kissinger method in the studied reaction. For the first reduction peak (**Figure 9.14a**), E_a was found to be 197 ± 19 kJ/mol for NiO-G and 185 ± 25 kJ/mol for NiO-CA, which were close to each other yielding an average of 190 kJ/mol. For the last reduction peak

(Figure 9.14b), E_a of NiO-G also approximated to that of NiO-CA, giving an average value of 320 kJ/mol. E_a values of NiO reduction calculated in this study are significantly larger than the 90 kJ/mol and 114 kJ/mol obtained when using H_2 [157, 160, 162, 237, 238] and CH_4 [130] as reductants. This is probably because the first reduction phase belongs to solid-solid reaction (generally slower than solid-gas reaction) and the last reduction phase was limited by the production of reducing agent via carbon gasification. The literature [233] reported the E_a value of bulk NiO reduction with natural graphite was 314 kJ/mol, much larger than the value (190 kJ/mol) obtained in this study for the reduction of supported NiO with the coke from bio-compound pyrolysis. This discrepancy was probably attributed to two factors. First, the reduction mechanism of supported NiO is different from that of bulk NiO. For the reduction of bulk NiO, a product layer is formed coating the unreacted NiO core, which impedes the diffusion of reductant to the NiO [45]. In contrast, during the reduction of supported NiO, Ni atoms liberated from NiO reduction migrate across the support to another site for nucleation and nuclei growth [160]. Hence, the lack of product layer diffusion resistance may contribute to the lower activation energy observed for the supported NiO reduction. Another possible reason is that the coke from bio-compound pyrolysis is more active than the graphite used in the literature [233].

For both the first and the last reduction peaks, the Kissinger plot of NiO-G was below that of NiO-CA, indicating NiO-G had a smaller pre-exponential factor and thus a lower frequency of reactant collision. The difference in their pre-exponent factor may be attributed to the difference in the elemental composition of their reductants. The carbonaceous material produced from glucose pyrolysis ($CH_{0.6}$) was more dehydrogenated than that from citric acid pyrolysis (CH), as analysed in 9.3.3. The densification of coke may constrain the movement of reductant species and thus reduce their chance of coming into contact with the NiO molecules. Consequently, the reduction rate of NiO-G would be slower than that of NiO-CA although they have similar activation energy.

9.4 Conclusions

It is feasible to reduce NiO/ α -Al₂O₃ catalyst with solid bio-compounds (glucose and citric acid) in batch pyrolysis mode. Glucose and citric acid were deposited on the catalyst by impregnation (denoted as NiO-G and NiO-CA, respectively) prior to the temperature programmed reduction (TPR) under N₂. As the temperature increased, NiO-G or NiO-CA underwent first the pyrolysis of glucose or citric acid to produce coke and then NiO reduction by the carbonaceous material. The reduction started at 420 °C and 400 °C respectively, with CO₂ as the main reduction product. A complete reduction was achieved for NiO-G while the conversion of NiO to Ni was only 68.3% for NiO-CA. Given that their initial carbon loading (in the form of bio-compound molecules) was similar to each other, the different extent of reduction was contributed to the different carbon deposition efficiency during bio-compound pyrolysis (64% vs. 30%). Glucose exhibited better charring characteristics than citric acid. TPO results indicated that only one type of coke was formed on NiO-G or NiO-CA. The coke existed as a large thin film unevenly covering the catalyst with some NiO particles being exposed. A two-step reduction mechanism was proposed to explain the multiple reduction peaks observed. The direct reduction of NiO by the coke deposited on NiO sites took place first to produce CO₂. As the reduction proceeded, the coke on NiO sites was depleted which led to the decrease in the reduction rate. When the temperature was increased to above 500 °C, the coke on Al₂O₃ sites was gasified by CO₂ to produce CO, which reduced those bare NiO particles (not in direct contact with coke). For both NiO-G and NiO-CA, the apparent activation energy of the first reduction peak (around 440 °C) was 190 kJ/mol and the last reduction peak (620 °C) was 320 kJ/mol. The pre-exponential factor of NiO-G was smaller than that of NiO-CA, which may relate to the fact that the coke on NiO-G (H/C ratio of 0.6) was more dehydrogenated than that on NiO-CA (H/C ratio of 1).

The utilization of bio-compounds in metal oxide reduction is a promising way to decrease fossil fuel consumption, although some problems need to be addressed in the future, e.g. how to control the deposition of bio-compounds to achieve complete reduction with little coke residue, and how to implement the process under bio-

compound constant feed rather than relying on batch impregnation of the metal oxide.

Chapter 10 Conclusions and future work

10.1 Conclusions

To exploit the potential of bio-derived fuels for H₂ production via chemical looping reforming (CLR), five bio-compounds (acetic acid, ethanol, acetone, furfural and glucose) as well as CH₄ (a commonly used fuel for CLR) were investigated in a process combining catalyst reduction and subsequent steam reforming (SR), which together represent half a cycle in CLR. A reforming catalyst, 18 wt% NiO/ α -Al₂O₃, was selected as model catalyst. Both a thermodynamic study using the CEA program and an experimental investigation in a packed bed reactor were performed. In addition, the reduction of this catalyst with solid bio-compounds (glucose and citric acid) was studied using TGA-FTIR technique. The main conclusions are as follows.

10.1.1 NiO catalyst reduction with bio-compounds (auto-reduction)

10.1.1.1. Thermodynamic study

It is thermodynamically feasible to reduce NiO with the five bio-compounds at temperatures at and above 200 °C. The reduction is an irreversible reaction and hardly affected by temperature, pressure, and the presence of steam. If the amount of NiO is insufficient to completely oxidize the bio-compounds, other products (carbon, CH₄, CO, and H₂) are generated in addition to Ni, H₂O and CO₂. The formation of carbon depends on temperature and the availability of NiO. The tendency to form carbon during NiO reduction at 650 °C increases in this order: acetic acid \approx glucose < ethanol < furfural < acetone < CH₄, related to the O/C ratio in bio-compound molecules.

Considering the total enthalpy change (from the reactants in normal state at 25 °C to equilibrium products at reaction temperature), NiO reduction with furfural requires a less energy input (53 kJ per mol NiO reduced at 650 °C), while a large amount of energy (89 kJ at 650 °C) is needed to reduce the same amount of NiO with acetic acid. The energy demand for NiO reduction with the other bio-compounds (glucose,

ethanol, and acetone) is close to that with CH₄ (77 kJ per mol of NiO reduced at 650 °C).

10.1.1.2 Kinetic investigation

The thermodynamic study above indicated that in a common temperature range (450-850 °C) and for a system consisting of NiO catalyst, steam and bio-compounds, the bio-compounds would preferably reduce NiO rather than react with steam or decompose. However, experiments showed that SR of bio-compounds took place as soon as metallic Ni was produced from NiO reduction probably because the SR reaction was kinetically promoted by metallic Ni. Hence, the auto-reduction was a complicated process due to the variety of reducing species (e.g. bio-compound itself, decomposition intermediates, reforming products H₂ and CO) and the competition from SR. A complete reduction was achieved at 650 °C for ethanol and 550 °C for the other bio-compounds.

Kinetic modelling was performed within the reduction extent of 0-50% as it was difficult to obtain valid data in the full conversion range. A two-dimensional nuclei growth model (A2) fitted the reduction kinetics very well except for glucose, which was fitted with A1.5 model. Similar apparent activation energies (30-40 kJ/mol) were obtained for the NiO reduction with different bio-compounds in the temperature range of 550-750 °C and with S/C of 3 (S/C=6 for glucose). Their pre-exponential factors decreased in this order: CH₄ > ethanol ≈ acetone > acetic acid > furfural > glucose, probably due to the different activities of reducing species they produced. Apart from the type of reductants and temperature, the steam content present in the reaction system also affected the reduction rate. With the S/C increasing, the rate constant increased first and then decreased. The optimal S/C for reduction kinetics at 650 °C was located between 1 and 2. When the S/C was low, carbon accumulated on Ni sites and impaired the dissociation of bio-compounds on Ni sites. When the S/C was large, excess water retarded the reduction probably by scavenging radicals and suppressing the nucleation and nuclei growth of Ni atoms. Compared to the other bio-compounds, ethanol exhibited a larger reduction rate constant and a lower optimal S/C, probably because its carbon radicals had a higher activity.

10.1.2 SR of bio-compounds following the auto-reduction

10.1.2.1 Thermodynamic study

H₂ yield increased with temperature and a maximum was obtained at around 650 °C if S/C=3 was used, above which the H₂ yield underwent a negligible decrease. An increase in S/C also enhanced the production of H₂, but the improvement beyond S/C =3 was not as significant as that raising the S/C from 0 to 3. The equilibrium yields of H₂, CH₄, CO and CO₂ at S/C of 3 and 650 °C (CH₄ yield at 500 °C) were successfully fitted as a linear function of the H/C and O/C ratios in feedstock molecules (equations are as shown below). The suitability of these fitted equations for other oxygenated hydrocarbons was checked. The numerical determination of the relationship between the equilibrium yields and the feedstock's molecular composition is useful for predicting the potential of various feedstocks in H₂ production, without doing repeated simulation work.

$$X_1 = H/C - 1.7 \times O/C$$

$$Y(H_2) = 0.4027X_1 + 1.5876 \quad \text{with } R^2 = 0.999$$

$$X_2 = H/C - 2.7 \times O/C$$

$$Y(CH_4) = 0.0771X_2 + 0.2524 \quad \text{with } R^2 = 0.9997$$

$$X_3 = O/C - 0.25 \times H/C$$

$$Y(CO_2) = 0.1764X_3 + 0.6375 \quad \text{with } R^2 = 0.9994$$

$$Y(CO) = -0.1208X_3 + 0.3323 \quad \text{with } R^2 = 0.9826$$

H₂ production from the bio-compound/steam system with S/C=3 was energy efficient (with significantly lower enthalpy balance than thermal water splitting) above 450 °C. At 650 °C, the ranking of feedstock according to their energy efficiency was CH₄ > ethanol > acetone > furfural > glucose > acetic acid. If the energy required by SR process was supplied by bio-compounds/NiO auto-reduction (autothermal CLR), the amount of moles of oxygen carrier NiO for one mole of H₂ produced from SR of furfural and ethanol was the smallest (0.74), which is slightly higher than that when using CH₄ as feedstock (0.69).

10.1.2.2 Experimental investigation

The SR performance using auto-reduced catalyst was close to that using H₂-reduced catalyst for ethanol, acetone, and furfural while a slight decrease was shown for acetic acid. For the different bio-compounds, fuel conversion and H₂ yield were generally enhanced by raising temperature and S/C. At 650 °C, the H₂ yield in mol/mol C feed decreased in the order of ethanol > acetone > glucose > furfural > acetic acid (S/C=6 for glucose and S/C=3 for the other bio-compounds). The SR of ethanol achieved the largest H₂ yield (1.78 mol/mol C feed, 69% of the equilibrium potential) while the H₂ yield from SR of acetic acid was the lowest (1.06 mol/mol C feed, 61% of the equilibrium potential). The discrepancy between experimental H₂ yields and equilibrium H₂ yields was ascribed to the kinetic limitation on SR reaction. The WGS reaction seemed not to suffer significantly from kinetic resistance. The comparison of gas yields experimentally obtained from catalytic pyrolysis of bio-compounds (S/C=0 at 650 °C) with equilibrium data indicated that Boudouard reaction and CH₄ pyrolysis were kinetically suppressed under the present experimental condition.

In summary, the main problem for SR of ethanol was a high CH₄ yield which may be attributed to ethanol pyrolysis. For SR of acetic acid, the H₂ yield obtained was relatively low probably due to the loss of active phase. Large amounts of carbon were formed on the catalyst at temperatures below 650 °C, which was the main drawback for SR of acetone. The thermal stability of furfural limited SR of furfural at low temperatures while the severe agglomeration of catalyst particles was the main barrier for SR of glucose. The temperatures for efficient SR of furfural and glucose were above 600 °C.

10.1.3 Reduction of NiO catalyst with solid bio-compounds

It is feasible to reduce the NiO/ α -Al₂O₃ catalyst with solid bio-compounds (glucose and citric acid) in batch pyrolysis mode. Glucose and citric acid were deposited on the catalyst by impregnation (denoted as NiO-G and NiO-CA, respectively) prior to the temperature programmed reduction (TPR) under N₂. As the temperature increased, NiO-G or NiO-CA underwent bio-compound pyrolysis to form carbonaceous material (coke), which acted as the actual reductant for NiO reduction.

The reduction extent depended on the initial loading of bio-compounds and the carbon deposition efficiency during pyrolysis (64% and 30% for glucose pyrolysis and citric acid pyrolysis, respectively).

A two-step reduction mechanism was proposed to explain the multiple reduction peaks observed. The direct reduction of NiO by coke deposited on NiO sites took place first to produce CO₂. As the reduction proceeded, the coke on NiO sites was depleted which led to the decrease in the reduction rate. When the temperature was increased to above 500 °C, the coke on Al₂O₃ sites was gasified by CO₂ to produce CO, which reduced those bare NiO particles which were not in direct contact with coke. For both NiO-G and NiO-CA, the apparent activation energy of the first reduction peak (around 440 °C) was 190 kJ/mol and the last reduction peak (620 °C) was 320 kJ/mol. The pre-exponential factor of NiO-G was smaller than that of NiO-CA, which may relate to the fact that the coke on NiO-G (H/C ratio of 0.6) was more dehydrogenated than that on NiO-CA (H/C ratio of 1).

10.2 Future work

(1) Mediate between auto-reduction and SR

As observed in Chapter 7, the optimal S/C range for reduction kinetics were below the S/C commonly used for SR (e.g. S/C=2-3). A rise in the S/C would increase SR performance but lead to a decreased reduction rate. Hence, a varying S/C regime may be required in the future for such an integrated catalyst reduction and SR process.

As discussed in Chapter 8, the amount of catalyst used in this work was the limiting factor of SR process. In other words, the SR performance would be enhanced if more catalyst was used or the feed of bio-compounds was decreased. However, a large flow rate of bio-compounds and small mass of catalyst were necessary for eliminating external diffusion resistance of auto-reduction. In future work, the flow rate of reforming fuel and mass of catalyst need to be properly designed to achieve negligible external diffusion resistance for auto-reduction while providing sufficient catalyst for subsequent SR. A varying feed rate of bio-compounds to the reactor is recommended.

(2) Further characterizations such as H₂ chemisorption to obtain nickel surface area and XPS to detect carbon species on the reacted catalyst surface are desirable in order to investigate the influence of auto-reduction on active metal dispersion and explain the different reducing activities the five bio-compounds exhibited.

(3) The cyclic performance of catalyst between oxidation and auto-reduction/SR needs to be investigated to further check the feasibility of bio-compounds in a CLR process. In addition, it is of significance to study the interaction between bio-compounds and CO₂ sorbent since the incorporation of in situ CO₂ adsorption into CLR has attracted growing attention due to the advantages of high H₂ yield and H₂ purity.

(4) In this study, the five bio-compounds were investigated individually as feedstock for catalyst reduction and subsequent SR. It is also of importance to find out the interaction between these bio-compounds during this process as bio-derived fuel normally exists as a complex mixture of various bio-compounds.

(5) For metal oxide reduction with solid bio-compounds, future work will be carried out on quantitatively controlling the deposition of bio-compounds to achieve complete reduction with little coke residue.

List of references

- [1] Lund H. Renewable energy strategies for sustainable development. *Energy*. 2007;32:912-9.
- [2] Renewables 2013 global status report. REN 21; 2013.
- [3] Lipman TE. What will power the hydrogen economy? Present and future sources of hydrogen energy. Institute of Transportation Studies University of California–Berkeley and Institute of Transportation Studies University of California–Davis. 2004. Report no. UCD-ITS-RR-04-10.
- [4] Logan BE. Peer reviewed: extracting hydrogen and electricity from renewable resources. *Environmental Science & Technology*. 2004;38:160A-7A.
- [5] Rostrup-Nielsen J, Rostrup-Nielsen T. Large-scale hydrogen production. *CATTECH*. 2002;6:150-9.
- [6] Bion N, Epron F, Duprez D. Bioethanol reforming for H₂ production. A comparison with hydrocarbon reforming. *Catalysis: Volume 22: The Royal Society of Chemistry*; 2010. p. 1-55.
- [7] Rostrup-Nielsen T. Manufacture of hydrogen. *Catalysis Today*. 2005;106:293-6.
- [8] Ridler DE, Twigg MV. Steam reforming. In: Twigg MV, editor. *Catalyst Handbook*. London: Manson Publishing Limited; 1996.
- [9] Chaubey R, Sahu S, James OO, Maity S. A review on development of industrial processes and emerging techniques for production of hydrogen from renewable and sustainable sources. *Renewable and Sustainable Energy Reviews*. 2013;23:443-62.
- [10] International Energy Outlook 2013. U. S. Energy Information Administration; 2013.
- [11] IPCC. Summary for Policymakers. In: Stocker DQ, Plattner GK, Tignor M, Allen SK, editor. *Climate Change 2013: The Physical Science Basis*. Cambridge UK and New York USA;2013. p. 11-4.
- [12] Mattisson T, Lyngfelt A. Capture of CO₂ using chemical-looping combustion. *Scandinavian-Nordic Section of Combustion Institute*. 2001:163-8.
- [13] Hossain MM, Lasa de HI. Chemical-looping combustion (CLC) for inherent separations—a review. *Chemical Engineering Science*. 2008;63:4433-51.
- [14] Zafar Q, Mattisson T, Gevert B. Integrated hydrogen and power production with CO₂ capture using chemical-looping reforming-redox reactivity of particles of CuO, Mn₂O₃, NiO, and Fe₂O₃ using SiO₂ as a support. *Industrial & Engineering Chemistry Research*. 2005;44:3485-96.
- [15] de Diego LF, Ortiz M, García-Labiano F, Adánez J, Abad A, Gayán P. Hydrogen production by chemical-looping reforming in a circulating fluidized bed reactor using Ni-based oxygen carriers. *Journal of Power Sources*. 2009;192:27-34.

- [16] Dupont V, Ross A, Knight E, Hanley I, Twigg M. Production of hydrogen by unmixed steam reforming of methane. *Chemical Engineering Science*. 2008;63:2966-79.
- [17] Pimenidou P, Rickett G, Dupont V, Twigg MV. High purity H₂ by sorption-enhanced chemical looping reforming of waste cooking oil in a packed bed reactor. *Bioresource technology*. 2010;101:9279-86.
- [18] Dou B, Song Y, Wang C, Chen H, Yang M, Xu Y. Hydrogen production by enhanced-sorption chemical looping steam reforming of glycerol in moving-bed reactors. *Applied Energy*. 2014;130:342-9.
- [19] Lyon RK, Cole JA. Unmixed combustion: an alternative to fire. *Combustion and Flame*. 2000;121:249-61.
- [20] Broda M, Manovic V, Imtiaz Q, Kierzkowska AM, Anthony EJ, Müller CR. High-purity hydrogen via the sorption-enhanced steam methane reforming reaction over a synthetic CaO-based sorbent and a Ni catalyst. *Environmental Science & Technology*. 2013;47:6007-14.
- [21] Saxena RC, Adhikari DK, Goyal HB. Biomass-based energy fuel through biochemical routes: A review. *Renewable and Sustainable Energy Reviews*. 2009;13:167-78.
- [22] Ni M, Leung DY, Leung MKH, Sumathy K. An overview of hydrogen production from biomass. *Fuel Processing Technology*. 2006;87:461-72.
- [23] Zheng X, Yan C, Hu R, Li J, Hai H, Luo W, et al. Hydrogen from acetic acid as the model compound of biomass fast-pyralysis oil over Ni catalyst supported on ceria–zirconia. *International Journal of Hydrogen Energy*. 2012;37:12987-93.
- [24] Dou B, Dupont V, Rickett G, Blakeman N, Williams PT, Chen H, et al. Hydrogen production by sorption-enhanced steam reforming of glycerol. *Bioresource technology*. 2009;100:3540-7.
- [25] Marquevich M, Czernik S, Chornet E, Montané D. Hydrogen from biomass: steam reforming of model compounds of fast-pyrolisis oil. *Energy & Fuels*. 1999;13:1160-6.
- [26] Wang D, Czernik S, Montane D, Mann M, Chornet E. Biomass to hydrogen via fast pyrolysis and catalytic steam reforming of the pyrolysis oil or its fractions. *Industrial & Engineering Chemistry Research*. 1997;36:1507-18.
- [27] Pimenidou P, Rickett G, Dupont V, Twigg M. Chemical looping reforming of waste cooking oil in packed bed reactor. *Bioresource Technology*. 2010;101:6389-97.
- [28] Lea-Langton A, Zin RM, Dupont V, Twigg MV. Biomass pyrolysis oils for hydrogen production using chemical looping reforming. *International Journal of Hydrogen Energy*. 2012;37:2037-43.
- [29] Cao Y, Pan W-P. Investigation of Chemical Looping Combustion by Solid Fuels. 1. Process Analysis. *Energy & Fuels*. 2006;20:1836-44.
- [30] Cao Y, Casenas B, Pan W-P. Investigation of Chemical Looping Combustion by Solid Fuels. 2. Redox Reaction Kinetics and Product Characterization with

Coal, Biomass, and Solid Waste as Solid Fuels and CuO as an Oxygen Carrier. *Energy & Fuels*. 2006;20:1845-54.

- [31] Abd Rashid RZ, Mohd Salleh H, Ani MH, Yunus NA, Akiyama T, Purwanto H. Reduction of low grade iron ore pellet using palm kernel shell. *Renewable Energy*. 2014;63:617-23.
- [32] Yunus NA, Ani MH, Salleh HM, Rashid RZA, Akiyama T, Purwanto H. Reduction of Iron Ore/Empty Fruit Bunch Char Briquette Composite. *ISIJ International*. 2013;53:1749-55.
- [33] Trane R, Dahl S, Skjøth-Rasmussen MS, Jensen AD. Catalytic steam reforming of bio-oil. *International Journal of Hydrogen Energy*. 2012;37:6447-72.
- [34] Hu X, Lu GX. Investigation of the steam reforming of a series of model compounds derived from bio-oil for hydrogen production. *Applied Catalysis B-Environmental*. 2009;88:376-85.
- [35] Ramos MC, Navascues AI, Garcia L, Bilbao R. Hydrogen production by catalytic steam reforming of acetol, a model compound of bio-oil. *Industrial & Engineering Chemistry Research*. 2007;46:2399-406.
- [36] Wu C, Liu RH. Sustainable hydrogen production from steam reforming of bio-oil model compound based on carbon deposition/elimination. *International Journal of Hydrogen Energy*. 2011;36:2860-8.
- [37] Comas J, Marino F, Laborde M, Amadeo N. Bio-ethanol steam reforming on Ni/Al₂O₃ catalyst. *Chemical Engineering Journal*. 2004;98:61-8.
- [38] Wang D, Montane D, Chornet E. Catalytic steam reforming of biomass-derived oxygenates: Acetic acid and hydroxyacetaldehyde. *Applied Catalysis A-General*. 1996;143:245-70.
- [39] Richardson J, Lei M, Turk B, Forster K, Twigg MV. Reduction of model steam reforming catalysts: NiO/ α -Al₂O₃. *Applied Catalysis A: General*. 1994;110:217-37.
- [40] Richardson JT, Scates R, Twigg MV. X-ray diffraction study of nickel oxide reduction by hydrogen. *Applied Catalysis A: General*. 2003;246:137-50.
- [41] Abad A, García-Labiano F, de Diego LF, Gayán P, Adánez J. Reduction kinetics of Cu-, Ni-, and Fe-based oxygen carriers using syngas (CO+ H₂) for chemical-looping combustion. *Energy & Fuels*. 2007;21:1843-53.
- [42] Sharma S, Vastola F, Walker Jr P. Reduction of nickel oxide by carbon: I. Interaction between nickel oxide and pyrolytic graphite. *Carbon*. 1996;34:1407-12.
- [43] Sharma S, Vastola F, Walker Jr P. Reduction of nickel oxide by carbon: II. Interaction between nickel oxide and natural graphite. *Carbon*. 1997;35:529-33.
- [44] Sharma S, Vastola F, Walker Jr P. Reduction of nickel oxide by carbon: III. Kinetic studies of the interaction between nickel oxide and natural graphite. *Carbon*. 1997;35:535-41.
- [45] El-Guindy M, Davenport W. Kinetics and mechanism of Ilmenite reduction with graphite. *Metallurgical Transactions*. 1970;1:1729-34.

- [46] Syed-Hassan SSA, Li C-Z. NiO reduction with hydrogen and light hydrocarbons: Contrast between SiO₂-supported and unsupported NiO nanoparticles. *Applied Catalysis A: General*. 2011;398:187-94.
- [47] Hu X, Dong D, Zhang L, Lu G. Steam reforming of bio-oil derived small organics over the Ni/Al₂O₃ catalyst prepared by an impregnation–reduction method. *Catalysis Communications*. 2014;55:74-7.
- [48] de Diego LF, Ortiz M, Adánez J, García-Labiano F, Abad A, Gayán P. Synthesis gas generation by chemical-looping reforming in a batch fluidized bed reactor using Ni-based oxygen carriers. *Chemical Engineering Journal*. 2008;144:289-98.
- [49] Dueso C, Ortiz M, Abad A, García-Labiano F, de Diego LF, Gayán P, et al. Reduction and oxidation kinetics of nickel-based oxygen-carriers for chemical-looping combustion and chemical-looping reforming. *Chemical Engineering Journal*. 2012;188:142-54.
- [50] Zafar Q, Mattisson T, Gevert B. Integrated hydrogen and power production with CO₂ capture using chemical-looping reforming redox reactivity of particles of CuO, Mn₂O₃, NiO, and Fe₂O₃ using SiO₂ as a support. *Industrial & engineering chemistry research*. 2005;44:3485-96.
- [51] Maschio G, Koufopoulos C, Lucchesi A. Pyrolysis, a promising route for biomass utilization. *Bioresource technology*. 1992;42:219-31.
- [52] Bridgwater AV, Meier D, Radlein D. An overview of fast pyrolysis of biomass. *Organic Geochemistry*. 1999;30:1479-93.
- [53] Butler E, Devlin G, Meier D, McDonnell K. A review of recent laboratory research and commercial developments in fast pyrolysis and upgrading. *Renewable and Sustainable Energy Reviews*. 2011;15:4171-86.
- [54] Yaman S. Pyrolysis of biomass to produce fuels and chemical feedstocks. *Energy Conversion and Management*. 2004;45:651-71.
- [55] Braimakis K, Atsonios K, Panopoulos KD, Karellas S, Kakaras E. Economic evaluation of decentralized pyrolysis for the production of bio-oil as an energy carrier for improved logistics towards a large centralized gasification plant. *Renewable and Sustainable Energy Reviews*. 2014;35:57-72.
- [56] Stevens C, Brown RC. *Thermochemical processing of biomass: conversion into fuels, chemicals and power*: John Wiley & Sons; 2011.
- [57] Udomsirichakorn J, Salam PA. Review of hydrogen-enriched gas production from steam gasification of biomass: The prospect of CaO-based chemical looping gasification. *Renewable and Sustainable Energy Reviews*. 2014;30:565-79.
- [58] Tijmensen MJA, Faaij APC, Hamelinck CN, van Hardeveld MRM. Exploration of the possibilities for production of Fischer Tropsch liquids and power via biomass gasification. *Biomass and Bioenergy*. 2002;23:129-52.
- [59] Abu El-Rub Z, Bramer E, Brem G. Review of catalysts for tar elimination in biomass gasification processes. *Industrial & engineering chemistry research*. 2004;43:6911-9.

- [60] Min Z, Yimsiri P, Asadullah M, Zhang S, Li C-Z. Catalytic reforming of tar during gasification. Part II. Char as a catalyst or as a catalyst support for tar reforming. *Fuel*. 2011;90:2545-52.
- [61] Reddy SN, Nanda S, Dalai AK, Kozinski JA. Supercritical water gasification of biomass for hydrogen production. *International Journal of Hydrogen Energy*. 2014;39:6912-26.
- [62] Czernik S, Bridgwater AV. Overview of applications of biomass fast pyrolysis oil. *Energy & Fuels*. 2004;18:590-8.
- [63] Sinclair DS. Fast pyrolysis processor which produces low oxygen content, liquid bio-oil. Google Patents; 2013.
- [64] Yang SI, Hsu TC, Wu CY, Chen KH, Hsu YL, Li YH. Application of biomass fast pyrolysis part II: The effects that bio-pyrolysis oil has on the performance of diesel engines. *Energy*. 2014;66:172-80.
- [65] Garcia-Perez M, Shen J, Wang XS, Li CZ. Production and fuel properties of fast pyrolysis oil/bio-diesel blends. *Fuel Processing Technology*. 2010;91:296-305.
- [66] Czernik S, Johnson DK, Black S. Stability of wood fast pyrolysis oil. *Biomass and Bioenergy*. 1994;7:187-92.
- [67] Garcia-Perez M, Chala A, Pakdel H, Kretschmer D, Roy C. Characterization of bio-oils in chemical families. *Biomass & Bioenergy*. 2007;31:222-42.
- [68] Remón J, Broust F, Valette J, Chhiti Y, Alava I, Fernandez-Akarregi AR, et al. Production of a hydrogen-rich gas from fast pyrolysis bio-oils: Comparison between homogeneous and catalytic steam reforming routes. *International Journal of Hydrogen Energy*. 2014;39:171-82.
- [69] Lehto J, Oasmaa A, Solantausta Y, Kytö M, Chiaramonti D. Review of fuel oil quality and combustion of fast pyrolysis bio-oils from lignocellulosic biomass. *Applied Energy*. 2014;116:178-90.
- [70] Chiaramonti D, Oasmaa A, Solantausta Y. Power generation using fast pyrolysis liquids from biomass. *Renewable and Sustainable Energy Reviews*. 2007;11:1056-86.
- [71] Oehr K. Acid emission reduction. USA: U.S. Patent 5458803 A; 1995.
- [72] Elliott DC. Historical Developments in Hydroprocessing Bio-oils. *Energy & Fuels*. 2007;21:1792-815.
- [73] Beckman D, Elliott DC. Comparisons of the yields and properties of the oil products from direct thermochemical biomass liquefaction processes. *The Canadian Journal of Chemical Engineering*. 1985;63:99-104.
- [74] Marchetti JM, Miguel VU, Errazu AF. Possible methods for biodiesel production. *Renewable and Sustainable Energy Reviews*. 2007;11:1300-11.
- [75] Balat M. Potential importance of hydrogen as a future solution to environmental and transportation problems. *International Journal of Hydrogen Energy*. 2008;33:4013-29.
- [76] Rahimpour MR, Jafari M, Iranshahi D. Progress in catalytic naphtha reforming process: A review. *Applied Energy*. 2013;109:79-93.

- [77] Pregger T, Graf D, Krewitt W, Sattler C, Roeb M, Möller S. Prospects of solar thermal hydrogen production processes. *International Journal of Hydrogen Energy*. 2009;34:4256-67.
- [78] Baykara SZ. Experimental solar water thermolysis. *International Journal of Hydrogen Energy*. 2004;29:1459-69.
- [79] Steinfeld A. Solar thermochemical production of hydrogen—a review. *Solar Energy*. 2005;78:603-15.
- [80] Azwar M, Hussain M, Abdul-Wahab A. Development of biohydrogen production by photobiological, fermentation and electrochemical processes: A review. *Renewable and Sustainable Energy Reviews*. 2014;31:158-73.
- [81] Sehested J. Four challenges for nickel steam-reforming catalysts. *Catalysis Today*. 2006;111:103-10.
- [82] Reijers HTJ, Valster-Schiermeier SE, Cobden PD, van den Brink RW. Hydrotalcite as CO₂ sorbent for sorption-enhanced steam reforming of methane. *Industrial & Engineering Chemistry Research*. 2006;45:2522-30.
- [83] Gallucci F, Basile A. Pd–Ag membrane reactor for steam reforming reactions: a comparison between different fuels. *International Journal of Hydrogen Energy*. 2008;33:1671-87.
- [84] Steinberg M, Cheng HC. Modern and prospective technologies for hydrogen production from fossil fuels. *International Journal of Hydrogen Energy*. 1989;14:797-820.
- [85] Li B, Maruyama K, Nurunnabi M, Kunimori K, Tomishige K. Temperature profiles of alumina-supported noble metal catalysts in autothermal reforming of methane. *Applied Catalysis A: General*. 2004;275:157-72.
- [86] Nurunnabi M, Mukainakano Y, Kado S, Miyazawa T, Okumura K, Miyao T, et al. Oxidative steam reforming of methane under atmospheric and pressurized conditions over Pd/NiO–MgO solid solution catalysts. *Applied Catalysis A: General*. 2006;308:1-12.
- [87] Pérez-Moreno L, Soler J, Herguido J, Menéndez M. Stable hydrogen production by methane steam reforming in a two zone fluidized bed reactor: Experimental assessment. *Journal of Power Sources*. 2013;243:233-41.
- [88] Herguido J, Menéndez M, Santamaría J. On the use of fluidized bed catalytic reactors where reduction and oxidation zones are present simultaneously. *Catalysis Today*. 2005;100:181-9.
- [89] Xiao X, Meng X, Le DD, Takarada T. Two-stage steam gasification of waste biomass in fluidized bed at low temperature: Parametric investigations and performance optimization. *Bioresource Technology*. 2011;102:1975-81.
- [90] Sattar A, Leeke GA, Hornung A, Wood J. Steam gasification of rapeseed, wood, sewage sludge and miscanthus biochars for the production of a hydrogen-rich syngas. *Biomass and Bioenergy*. 2014;69:276-86.
- [91] Ayalur Chattanathan S, Adhikari S, Abdoulmoumine N. A review on current status of hydrogen production from bio-oil. *Renewable and Sustainable Energy Reviews*. 2012;16:2366-72.

- [92] Wu C, Sui M, Yan YJ. A comparison of steam reforming of two model bio-oil fractions. *Chemical Engineering & Technology*. 2008;31:1748-53.
- [93] Wang D, Montane D, Chornet E. Catalytic steam reforming of biomass-derived oxygenates: acetic acid and hydroxyacetaldehyde. *Applied Catalysis A: General*. 1996;143:245-70.
- [94] Takanahe K, Aika K-i, Seshan K, Lefferts L. Catalyst deactivation during steam reforming of acetic acid over Pt/ZrO₂. *Chemical Engineering Journal*. 2006;120:133-7.
- [95] Li Z, Hu X, Zhang L, Liu S, Lu G. Steam reforming of acetic acid over Ni/ZrO₂ catalysts: Effects of nickel loading and particle size on product distribution and coke formation. *Applied Catalysis A: General*. 2012;417-418:281-9.
- [96] Mackie JC, Doolan KR. High-temperature kinetics of thermal decomposition of acetic acid and its products. *International Journal of Chemical Kinetics*. 1984;16:525-41.
- [97] Basagiannis A, Verykios X. Catalytic steam reforming of acetic acid for hydrogen production. *International Journal of Hydrogen Energy*. 2007;32:3343-55.
- [98] Hu X, Lu G. Comparative study of alumina-supported transition metal catalysts for hydrogen generation by steam reforming of acetic acid. *Applied Catalysis B: Environmental*. 2010;99:289-97.
- [99] Hu X, Lu G. Inhibition of methane formation in steam reforming reactions through modification of Ni catalyst and the reactants. *Green Chemistry*. 2009;11:724-32.
- [100] Bengaard HS, Nørskov JK, Sehested J, Clausen BS, Nielsen LP, Molenbroek AM, et al. Steam Reforming and Graphite Formation on Ni Catalysts. *Journal of Catalysis*. 2002;209:365-84.
- [101] Thaicharoensutcharittham S, Meeyoo V, Kitiyanan B, Rangsunvigit P, Rirksomboon T. Hydrogen production by steam reforming of acetic acid over Ni-based catalysts. *Catalysis Today*. 2011;164:257-61.
- [102] Kugai J, Velu S, Song C. Low-temperature reforming of ethanol over CeO₂-supported Ni-Rh bimetallic catalysts for hydrogen production. *Catalysis Letters*. 2005;101:255-64.
- [103] Vaidya PD, Rodrigues AE. Insight into steam reforming of ethanol to produce hydrogen for fuel cells. *Chemical Engineering Journal*. 2006;117:39-49.
- [104] Ni M, Leung DY, Leung MK. A review on reforming bio-ethanol for hydrogen production. *International Journal of Hydrogen Energy*. 2007;32:3238-47.
- [105] Sahoo DR, Vajpai S, Patel S, Pant KK. Kinetic modeling of steam reforming of ethanol for the production of hydrogen over Co/Al₂O₃ catalyst. *Chemical Engineering Journal*. 2007;125:139-47.
- [106] Subramani V, Song C. Advances in catalysis and processes for hydrogen production from ethanol reforming. *Catalysis: Volume 20: The Royal Society of Chemistry*; 2007. p. 65-106.

- [107] Fatsikostas AN, Verykios XE. Reaction network of steam reforming of ethanol over Ni-based catalysts. *Journal of Catalysis*. 2004;225:439-52.
- [108] Frusteri F, Freni S, Spadaro L, Chiodo V, Bonura G, Donato S, et al. H₂ production for MC fuel cell by steam reforming of ethanol over MgO supported Pd, Rh, Ni and Co catalysts. *Catalysis Communications*. 2004;5:611-5.
- [109] Mattos LV, Jacobs G, Davis BH, Noronha FbB. Production of hydrogen from ethanol: review of reaction mechanism and catalyst deactivation. *Chemical reviews*. 2012;112:4094-123.
- [110] Haga F, Nakajima T, Miya H, Mishima S. Catalytic properties of supported cobalt catalysts for steam reforming of ethanol. *Catalysis Letters*. 1997;48:223-7.
- [111] Mavrikakis M, Barteau MA. Oxygenate reaction pathways on transition metal surfaces. *Journal of Molecular Catalysis A: Chemical*. 1998;131:135-47.
- [112] Rass-Hansen J, Christensen CH, Sehested J, Helveg S, Rostrup-Nielsen JR, Dahl S. Renewable hydrogen: Carbon formation on Ni and Ru catalysts during ethanol steam-reforming. *Green Chemistry*. 2007;9:1016-21.
- [113] Mariño F, Baronetti G, Jobbagy Ma, Laborde M. Cu-Ni-K/ γ -Al₂O₃ supported catalysts for ethanol steam reforming: Formation of hydrotalcite-type compounds as a result of metal-support interaction. *Applied Catalysis A: General*. 2003;238:41-54.
- [114] Vizcaíno AJ, Carrero A, Calles JA. Hydrogen production by ethanol steam reforming over Cu-Ni supported catalysts. *International Journal of Hydrogen Energy*. 2007;32:1450-61.
- [115] Han SJ, Bang Y, Yoo J, Seo JG, Song IK. Hydrogen production by steam reforming of ethanol over mesoporous Ni-Al₂O₃-ZrO₂ xerogel catalysts: Effect of nickel content. *International Journal of Hydrogen Energy*. 2013;38:8285-92.
- [116] Han SJ, Bang Y, Yoo J, Park S, Kang KH, Choi JH, et al. Hydrogen production by steam reforming of ethanol over P123-assisted mesoporous Ni-Al₂O₃-ZrO₂ xerogel catalysts. *International Journal of Hydrogen Energy*. 2014.
- [117] Serrano DP, Coronado JM, de la Pena O'Shea VA, Pizarro P, Botas JA. Advances in the design of ordered mesoporous materials for low-carbon catalytic hydrogen production. *Journal of Materials Chemistry A*. 2013;1:12016-27.
- [118] Hu X, Lu G. Investigation of the steam reforming of a series of model compounds derived from bio-oil for hydrogen production. *Applied Catalysis B: Environmental*. 2009;88:376-85.
- [119] Ramos MC, Navascués AI, García L, Bilbao R. Hydrogen production by catalytic steam reforming of acetol, a model compound of bio-oil. *Industrial & engineering chemistry research*. 2007;46:2399-406.

- [120] Wu C, Liu R. Carbon deposition behavior in steam reforming of bio-oil model compound for hydrogen production. *International Journal of Hydrogen Energy*. 2010;35:7386-98.
- [121] Khzouz M, Wood J, Pollet B, Bujalski W. Characterization and activity test of commercial Ni/Al₂O₃, Cu/ZnO/Al₂O₃ and prepared Ni–Cu/Al₂O₃ catalysts for hydrogen production from methane and methanol fuels. *International Journal of Hydrogen Energy*. 2013;38:1664-75.
- [122] Wu C, Liu R. Hydrogen production from steam reforming of m-cresol, a model compound derived from bio-oil: green process evaluation based on liquid condensate recycling. *Energy & Fuels*. 2010;24:5139-47.
- [123] Mattisson T, Lyngfelt A. Applications of chemical-looping combustion with capture of CO₂. *Second Nordic Minisymposium on CO₂ Capture and Storage*, Göteborg, Sweden. 2001.
- [124] Ryden M, Lyngfelt A, Mattisson T. Chemical-looping combustion and chemical-looping reforming in a circulating fluidized-bed reactor using Ni-based oxygen carriers. *Energy & Fuels*. 2008;22:2585-97.
- [125] de Diego LF, Ortiz M, Garcia-Labiano F, Adanez J, Abad A, Gayan P. Hydrogen production by chemical-looping reforming in a circulating fluidized bed reactor using Ni-based oxygen carriers. *Journal of Power Sources*. 2009;192:27-34.
- [126] de Diego LF, Ortiz M, Adanez J, Garcia-Labiano F, Abad A, Gayan P. Synthesis gas generation by chemical-looping reforming in a batch fluidized bed reactor using Ni-based oxygen carriers. *Chemical Engineering Journal*. 2008;144:289-98.
- [127] Giannakeas N, Lea-Langton A, Dupont V, Twigg MV. Hydrogen from scrap tyre oil via steam reforming and chemical looping in a packed bed reactor. *Applied Catalysis B: Environmental*. 2012;126:249-57.
- [128] Garcia-Labiano F, De Diego L, Adánez J, Abad A, Gayán P. Reduction and oxidation kinetics of a copper-based oxygen carrier prepared by impregnation for chemical-looping combustion. *Industrial & engineering chemistry research*. 2004;43:8168-77.
- [129] Zafar Q, Abad A, Mattisson T, Gevert B, Strand M. Reduction and oxidation kinetics of Mn₃O₄/Mg–ZrO₂ oxygen carrier particles for chemical-looping combustion. *Chemical Engineering Science*. 2007;62:6556-67.
- [130] Zafar Q, Abad A, Mattisson T, Gevert B. Reaction kinetics of freeze-granulated NiO/MgAl₂O₄ oxygen carrier particles for chemical-looping combustion. *Energy & Fuels*. 2007;21:610-8.
- [131] Cabello A, Gayán P, García-Labiano F, de Diego LF, Abad A, Izquierdo MT, et al. Relevance of the catalytic activity on the performance of a NiO/CaAl₂O₄ oxygen carrier in a CLC process. *Applied Catalysis B: Environmental*. 2014;147:980-7.
- [132] Rydén M, Lyngfelt A, Mattisson T. Chemical-looping combustion and chemical-looping reforming in a circulating fluidized-bed reactor using Ni-based oxygen carriers. *Energy & Fuels*. 2008;22:2585-97.

- [133] Cho P, Mattisson T, Lyngfelt A. Comparison of iron-, nickel-, copper-and manganese-based oxygen carriers for chemical-looping combustion. *Fuel*. 2004;83:1215-25.
- [134] Jin H, Okamoto T, Ishida M. Development of a Novel Chemical-Looping Combustion: Synthesis of a Looping Material with a Double Metal Oxide of CoO–NiO. *Energy & Fuels*. 1998;12:1272-7.
- [135] Hossain MM, de Lasa HI. Reactivity and stability of Co-Ni/Al₂O₃ oxygen carrier in multicycle CLC. *AIChE journal*. 2007;53:1817-29.
- [136] Siriwardane RV, Ksepko E, Tian H, Poston J, Simonyi T, Sciazko M. Interaction of iron–copper mixed metal oxide oxygen carriers with simulated synthesis gas derived from steam gasification of coal. *Applied Energy*. 2013;107:111-23.
- [137] Dupont V, Ross AB, Hanley I, Twigg MV. Unmixed steam reforming of methane and sunflower oil: A single-reactor process for -rich gas. *International Journal of Hydrogen Energy*. 2007;32:67-79.
- [138] Siriwardane R, Tian H, Miller D, Richards G, Simonyi T, Poston J. Evaluation of reaction mechanism of coal–metal oxide interactions in chemical-looping combustion. *Combustion and Flame*. 2010;157:2198-208.
- [139] Adanez J, Abad A, Garcia-Labiano F, Gayan P, de Diego LF. Progress in chemical-looping combustion and reforming technologies. *Progress in Energy and Combustion Science*. 2012;38:215-82.
- [140] Siriwardane R, Tian H, Richards G, Simonyi T, Poston J. Chemical-looping combustion of coal with metal oxide oxygen carriers. *Energy & Fuels*. 2009;23:3885-92.
- [141] Cho P, Mattisson T, Lyngfelt A. Carbon formation on nickel and iron oxide-containing oxygen carriers for chemical-looping combustion. *Industrial & Engineering Chemistry Research*. 2005;44:668-76.
- [142] Rydén M, Lyngfelt A, Mattisson T. Synthesis gas generation by chemical-looping reforming in a continuously operating laboratory reactor. *Fuel*. 2006;85:1631-41.
- [143] Alizadeh R, Jamshidi E, Ale-Ebrahim H. Kinetic study of nickel oxide reduction by methane. *Chemical Engineering & Technology*. 2007;30:1123-8.
- [144] Liu G-s, Strezov V, Lucas JA, Wibberley LJ. Thermal investigations of direct iron ore reduction with coal. *Thermochimica Acta*. 2004;410:133-40.
- [145] Strezov V. Iron ore reduction using sawdust: Experimental analysis and kinetic modelling. *Renewable Energy*. 2006;31:1892-905.
- [146] Abd Rashid RZ, Mohd. Salleh H, Ani MH, Yunus NA, Akiyama T, Purwanto H. Reduction of low grade iron ore pellet using palm kernel shell. *Renewable Energy*. 2014;63:617-23.
- [147] Goodman DR. Handling and using catalysts in the plant. In: Twigg MV, editor. *Catalyst Handbook*. London: Manson Publishing Limited; 1996.
- [148] Kung HH. *Transition metal oxides: surface chemistry and catalysis*: Elsevier; 1989.

- [149] Khawam A, Flanagan DR. Solid-state kinetic models: basics and mathematical fundamentals. *The Journal of Physical Chemistry B*. 2006;110:17315-28.
- [150] Szekeley J, Lin CI, Sohn HY. A structural model for gas-solid reactions with a moving boundary-V an experimental study of the reduction of porous nickel-oxide pellets with hydrogen. *Chemical Engineering Science*. 1973;28:1975-89.
- [151] Kanervo JM, Krause AOI. Kinetic Analysis of Temperature-Programmed Reduction: Behavior of a $\text{CrO}_x/\text{Al}_2\text{O}_3$ Catalyst. *The Journal of Physical Chemistry B*. 2001;105:9778-84.
- [152] Avrami M. Kinetics of Phase Change. II Transformation-Time Relations for Random Distribution of Nuclei. *The Journal of Chemical Physics*. 1940;8:212-24.
- [153] Avrami M. Kinetics of Phase Change. I General Theory. *The Journal of Chemical Physics*. 1939;7:1103-12.
- [154] Hossain MM, de Lasa HI. Reduction and oxidation kinetics of Co-Ni/ Al_2O_3 oxygen carrier involved in a chemical-looping combustion cycles. *Chemical Engineering Science*. 2010;65:98-106.
- [155] Benton AF, Emmett PH. The reduction of nickelous and ferric oxides by hydrogen. *Journal of the American Chemical Society*. 1924;46:2728-37.
- [156] Ishida M, Jin H, Okamoto T. A fundamental study of a new kind of medium material for chemical-looping combustion. *Energy & Fuels*. 1996;10:958-63.
- [157] Utigard TA, Wu M, Plascencia G, Marin T. Reduction kinetics of Goro nickel oxide using hydrogen. *Chemical Engineering Science*. 2005;60:2061-8.
- [158] Richardson JT, Lei M, Forster K, Twigg MV. Reduction of Model Steam Reforming Catalysts - NiO/ $\alpha\text{-Al}_2\text{O}_3$. *Applied Catalysis A-General*. 1994;110:217-37.
- [159] Richardson JT, Turk B, Twigg MV. Reduction of model steam reforming catalysts: Effect of oxide additives. *Applied Catalysis A-General*. 1996;148:97-112.
- [160] Richardson JT, Scates RM, Twigg MV. X-ray diffraction study of the hydrogen reduction of, NiO/ $\alpha\text{-Al}_2\text{O}_3$ steam reforming catalysts. *Applied Catalysis A-General*. 2004;267:35-46.
- [161] Ostrovski O, Zhang GQ. Reduction and carburization of metal oxides by methane-containing gas. *Aiche Journal*. 2006;52:300-10.
- [162] Richardson JT, Scates R, Twigg MV. X-ray diffraction study of nickel oxide reduction by hydrogen. *Applied Catalysis A-General*. 2003;246:137-50.
- [163] Quah EBH, Li C-Z. Roles of desorbed radicals and reaction products during the oxidation of methane using a nickel mesh catalyst. *Applied Catalysis A: General*. 2004;258:63-71.
- [164] Lee WJ, Li C-Z. Coke formation and reaction pathways of catalyst-surface-generated radicals during the pyrolysis of ethane using Ni mesh catalyst. *Applied Catalysis A: General*. 2007;316:90-9.

- [165] Syed-Hassan SSA, Lee WJ, Li C-Z. Positive and negative catalytic effects of a nickel mesh catalyst for the partial oxidation of ethane. *Chemical Engineering Journal*. 2009;147:307-15.
- [166] Syed-Hassan SSA, Li CZ. NiO reduction with hydrogen and light hydrocarbons: Contrast between SiO₂-supported and unsupported NiO nanoparticles. *Applied Catalysis A-General*. 2011;398:187-94.
- [167] Liu G-s, Strezov V, Lucas JA, Wibberley LJ. Thermal investigations of direct iron ore reduction with coal. *Thermochimica Acta*. 2004;410:133-40.
- [168] Zin RM, Lea-Langton A, Dupont V, Twigg MV. High hydrogen yield and purity from palm empty fruit bunch and pine pyrolysis oils. *International Journal of Hydrogen Energy*. 2012;37:10627-38.
- [169] Pimenidou P, Rickett G, Dupont V, Twigg MV. Chemical looping reforming of waste cooking oil in packed bed reactor. *Bioresource Technology*. 2010;101:6389-97.
- [170] Kabo GJ, Voitkevich OV, Blokhin AV, Kohut SV, Stepurko EN, Paulechka YU. Thermodynamic properties of starch and glucose. *The Journal of Chemical Thermodynamics*. 2013;59:87-93.
- [171] Molinder R, Comyn T, Hondow N, Parker J, Dupont V. In situ X-ray diffraction of CaO based CO₂ sorbents. *Energy & Environmental Science*. 2012;5:8958-69.
- [172] McBride BJ, Gordon S. Computer program for calculation of complex chemical equilibrium compositions and applications: II. Users manual and program description. NASA reference publication. 1996;1311:84-5.
- [173] Gordon S, McBride BJ. Computer program for calculation of complex chemical equilibrium compositions and applications. Part 1: Analysis. 1994.
- [174] Guénadou D, Lorcet H, Peybernès J, Catoire L, Osmont A, Gökalp I. Plasma thermal conversion of bio-oil for hydrogen production. *International Journal of Energy Research*. 2012;36:409-14.
- [175] Kelley K. US Bureau of Mines Bulletin 584. US Government Printing Office, Washington, DC. 1960:46.
- [176] Keem J, Honig J. Selected Electrical and Thermal Properties of Undoped Nickel Oxide. DTIC Document; 1978.
- [177] Dupont V, Twigg MV, Rollinson AN, Jones JM. Thermodynamics of hydrogen production from urea by steam reforming with and without in situ carbon dioxide sorption. *International Journal of Hydrogen Energy*. 2013;38:10260-9.
- [178] Chen W-H, Lin M-R, Yu A, Du S-W, Leu T-S. Hydrogen production from steam reforming of coke oven gas and its utility for indirect reduction of iron oxides in blast furnace. *International Journal of Hydrogen Energy*. 2012;37:11748-58.
- [179] Huang Z, He F, Feng Y, Zhao K, Zheng A, Chang S, et al. Biomass char direct chemical looping gasification using NiO-modified iron ore as an oxygen carrier. *Energy & Fuels*. 2013;28:183-91.

- [180] Kale GR, Kulkarni BD, Bharadwaj K. Chemical looping reforming of ethanol for syngas generation: A theoretical investigation. *International Journal of Energy Research*. 2013;37:645-56.
- [181] Subramani V, Song C. Advances in catalysis and processes for hydrogen production from ethanol reforming. *Catalysis*. 2007;20:65-106.
- [182] Jozwiak WK, Kaczmarek E, Maniecki TP, Ignaczak W, Maniukiewicz W. Reduction behavior of iron oxides in hydrogen and carbon monoxide atmospheres. *Applied Catalysis A: General*. 2007;326:17-27.
- [183] Pineau A, Kanari N, Gaballah I. Kinetics of reduction of iron oxides by H₂: Part II. Low temperature reduction of magnetite. *Thermochimica Acta*. 2007;456:75-88.
- [184] Basagiannis AC, Verykios XE. Reforming reactions of acetic acid on nickel catalysts over a wide temperature range. *Applied Catalysis A: General*. 2006;308:182-93.
- [185] Grashinsky C, Giunta P, Amadeo N, Laborde M. Thermodynamic analysis of hydrogen production by autothermal reforming of ethanol. *International Journal of Hydrogen Energy*. 2012;37:10118-24.
- [186] Vagia EC, Lemonidou AA. Thermodynamic analysis of hydrogen production via steam reforming of selected components of aqueous bio-oil fraction. *International Journal of Hydrogen Energy*. 2007;32:212-23.
- [187] Sun S, Yan W, Sun P, Chen J. Thermodynamic analysis of ethanol reforming for hydrogen production. *Energy*. 2012;44:911-24.
- [188] Adhikari S, Fernando S, Gwaltney SR, Filip To S, Mark Bricka R, Steele PH, et al. A thermodynamic analysis of hydrogen production by steam reforming of glycerol. *International Journal of Hydrogen Energy*. 2007;32:2875-80.
- [189] Garcia E, Laborde M. Hydrogen production by the steam reforming of ethanol: thermodynamic analysis. *International Journal of Hydrogen Energy*. 1991;16:307-12.
- [190] Vasudeva K, Mitra N, Umasankar P, Dhingra S. Steam reforming of ethanol for hydrogen production: thermodynamic analysis. *International Journal of Hydrogen Energy*. 1996;21:13-8.
- [191] Fishtik I, Alexander A, Datta R, Geana D. A thermodynamic analysis of hydrogen production by steam reforming of ethanol via response reactions. *International Journal of Hydrogen Energy*. 2000;25:31-45.
- [192] Milne T, Agblevor F, Davis M, Deutch S, Johnson D. A review of the chemical composition of fast-pyrolysis oils from biomass. *Developments in thermochemical biomass conversion*: Springer; 1997. p. 409-24.
- [193] McCusker LB, Von Dreele RB, Cox DE, Louer D, Scardi P. Rietveld refinement guidelines. *Journal of Applied Crystallography*. 1999;32:36-50.
- [194] Giannakeas N, Lea-Langton A, Dupont V, Twigg MV. Hydrogen from scrap tyre oil via steam reforming in a packed bed reactor. *Applied Catalysis B-Environmental*. 2012;126:249-57.

- [195] Khawam A, Flanagan DR. Solid-state kinetic models: Basics and mathematical fundamentals. *Journal of Physical Chemistry B*. 2006;110:17315-28.
- [196] Hancock JD, Sharp JH. Method of comparing solid-state kinetic data and its application to decomposition of Kaolinite, Brucite, and BaCO₃. *Journal of the American Ceramic Society*. 1972;55:74-7.
- [197] Go KS, Son SR, Kim SD. Reaction kinetics of reduction and oxidation of metal oxides for hydrogen production. *International Journal of Hydrogen Energy*. 2008;33:5986-95.
- [198] Hancock J, Sharp J. Method of Comparing solid-state kinetic data and its application to the decomposition of Kaolinite, Brucite, and BaCO₃. *Journal of the American Ceramic Society*. 1972;55:74-7.
- [199] Gardner RA. Kinetics of silica reduction in hydrogen. *Journal of Solid State Chemistry*. 1974;9:336-44.
- [200] Szekely J, Lin CI, Sohn HY. Structural model for gas-solid reactions with a moving boundary 5. Experimental study of reduction of porous Nickel-Oxide Pellets with Hydrogen. *Chemical Engineering Science*. 1973;28:1975-89.
- [201] Hossain MM, de Lasa HI. Reactivity and stability of Co-Ni/Al₂O₃ oxygen carrier in multicycle CLC. *Aiche Journal*. 2007;53:1817-29.
- [202] Kanervo JM, Krause AOI. Characterisation of supported chromium oxide catalysts by kinetic analysis of H₂-TPR data. *Journal of Catalysis*. 2002;207:57-65.
- [203] Abad A, Garcia-Labiano F, de Diego LF, Gayan P, Adanez J. Reduction kinetics of Cu-, Ni-, and Fe-based oxygen carriers using syngas (CO + H₂) for chemical-looping combustion. *Energy & Fuels*. 2007;21:1843-53.
- [204] Hardiman KA, Hsu CH, Ying TT, Adesina AA. The influence of impregnating pH on the postnatal and steam reforming characteristics of a Co-Ni/Al₂O₃ catalyst. *Journal of Molecular Catalysis A-Chemical*. 2005;239:41-8.
- [205] Barbier J. Deactivation of reforming catalysts by coking - a review. *Applied Catalysis*. 1986;23:225-43.
- [206] Duprez D, Demicheli MC, Marecot P, Barbier J, Ferretti OA, Ponzi EN. Deactivation of steam-reforming model catalysts by coke formation 1. Kinetics of the formation of filamentous carbon in the hydrogenolysis of cyclopentane on Ni/Al₂O₃ catalysts. *Journal of Catalysis*. 1990;124:324-35.
- [207] Basagiannis AC, Verykios XE. Reforming reactions of acetic acid on nickel catalysts over a wide temperature range. *Applied Catalysis A-General*. 2006;308:182-93.
- [208] Trane R, Dahl S, Skjoth-Rasmussen MS, Jensen AD. Catalytic steam reforming of bio-oil. *International Journal of Hydrogen Energy*. 2012;37:6447-72.
- [209] Takanabe K, Aika K, Seshan K, Lefferts L. Catalyst deactivation during steam reforming of acetic acid over Pt/ZrO₂. *Chemical Engineering Journal*. 2006;120:133-7.

- [210] Basagiannis AC, Verykios XE. Catalytic steam reforming of acetic acid for hydrogen production. *International Journal of Hydrogen Energy*. 2007;32:3343-55.
- [211] An L, Dong CQ, Yang YP, Zhang JJ, He L. The influence of Ni loading on coke formation in steam reforming of acetic acid. *Renewable Energy*. 2011;36:930-5.
- [212] Hu X, Lu GX. Inhibition of methane formation in steam reforming reactions through modification of Ni catalyst and the reactants. *Green Chemistry*. 2009;11:724-32.
- [213] McCusker L, Von Dreele R, Cox D, Louer D, Scardi P. Rietveld refinement guidelines. *Journal of Applied Crystallography*. 1999;32:36-50.
- [214] Dow W-P, Wang Y-P, Huang T-J. Yttria-stabilized zirconia supported copper oxide catalyst: I. Effect of oxygen vacancy of support on copper oxide reduction. *Journal of Catalysis*. 1996;160:155-70.
- [215] Ryu HJ, An GT. Chemical-looping hydrogen generation system: Performance estimation and process selection. *Korean Journal of Chemical Engineering*. 2007;24:527-31.
- [216] Richardson J, Scates R, Twigg M. X-ray diffraction study of the hydrogen reduction of NiO/ α -Al₂O₃ steam reforming catalysts. *Applied Catalysis A: General*. 2004;267:35-46.
- [217] Chiron F-X, Patience GS. Kinetics of mixed copper-iron based oxygen carriers for hydrogen production by chemical looping water splitting. *International Journal of Hydrogen Energy*. 2012;37:10526-38.
- [218] Gardner RA. The kinetics of silica reduction in hydrogen. *Journal of solid state chemistry*. 1974;9:336-44.
- [219] Benton AF. The reduction of nickelous and ferric oxides by hydrogen. *Journal of the American Chemical Society*. 1924;46:2728-37.
- [220] Giannakeas N, Lea-Langton A, Dupont V, Twigg MV. Hydrogen from scrap tyre oil via steam reforming and chemical looping in a packed bed reactor. *Applied Catalysis B: Environmental*. 2012;126:249-57.
- [221] Fagerson IS. Thermal degradation of carbohydrates; a review. *Journal of Agricultural and Food Chemistry*. 1969;17:747-50.
- [222] Kato K, Takahashi N. Pyrolysis of cellulose
Part II. Thermogravimetric analyses and determination of carbonyl and carboxyl groups in pyrocellulose. *Agricultural and Biological Chemistry*. 1967;31:519-24.
- [223] Sugisawa H, Edo H. The thermal degradation of sugars I. Thermal polymerization of glucose. *Journal of Food Science*. 1966;31:561-5.
- [224] Örsi F. Kinetic studies on the thermal decomposition of glucose and fructose. *Journal of Thermal Analysis*. 1973;5:329-35.
- [225] Vagia EC, Lemonidou AA. Investigations on the properties of ceria-zirconia-supported Ni and Rh catalysts and their performance in acetic acid steam reforming. *Journal of Catalysis*. 2010;269:388-96.

- [226] Wu C, Williams PT. Investigation of coke formation on Ni-Mg-Al catalyst for hydrogen production from the catalytic steam pyrolysis-gasification of polypropylene. *Applied Catalysis B: Environmental*. 2010;96:198-207.
- [227] Chinthaginjala JK, Thakur DB, Seshan K, Lefferts L. How carbon-nano-fibers attach to Ni foam. *Carbon*. 2008;46:1638-47.
- [228] Trimm DL. Catalysts for the control of coking during steam reforming. *Catalysis Today*. 1999;49:3-10.
- [229] Kroll VCH, Swaan HM, Mirodatos C. Methane reforming reaction with carbon dioxide over Ni/SiO₂ catalyst: I. Deactivation studies. *Journal of Catalysis*. 1996;161:409-22.
- [230] Alizadeh R, Jamshidi E, Ale Ebrahim H. Kinetic study of nickel oxide reduction by methane. *Chemical Engineering & Technology*. 2007;30:1123-8.
- [231] Sharma SK, Vastola FJ, Walker PL. Reduction of nickel oxide by carbon 1. Interaction between nickel oxide and pyrolytic graphite. *Carbon*. 1996;34:1407-12.
- [232] Sharma SK, Vastola FJ, Walker PL. Reduction of nickel oxide by carbon 2. Interaction between nickel oxide and natural graphite. *Carbon*. 1997;35:529-33.
- [233] Sharma SK, Vastola FJ, Walker PL. Reduction of nickel oxide by carbon .3. Kinetic studies of the interaction between nickel oxide and natural graphite. *Carbon*. 1997;35:535-41.
- [234] Orsi F. Kinetic studies on thermal-decomposition of glucose and fructose. *Journal of Thermal Analysis*. 1973;5:329-35.
- [235] Barbooti MM, Alsammerrai DA. Thermal-decomposition of citric-acid. *Thermochimica Acta*. 1986;98:119-26.
- [236] Wyrzykowski D, Hebanowska E, Nowak-Wicz G, Makowski M, Chmurzynski L. Thermal behaviour of citric acid and isomeric aconitic acids. *Journal of Thermal Analysis and Calorimetry*. 2011;104:731-5.
- [237] Jankovic B, Adnadevic B, Mentus S. The kinetic study of temperature-programmed reduction of nickel oxide in hydrogen atmosphere. *Chemical Engineering Science*. 2008;63:567-75.
- [238] Ishida M, Jin HG, Okamoto T. A fundamental study of a new kind of medium material for chemical-looping combustion. *Energy & Fuels*. 1996;10:958-63.

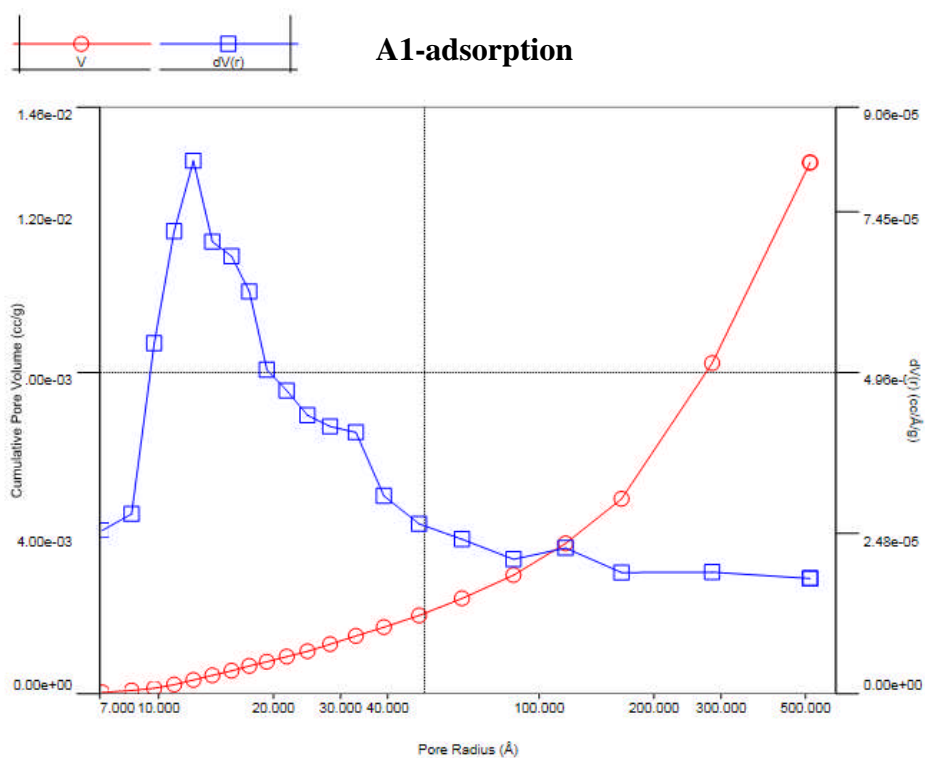
Appendix A

Surface area and pore size of fresh catalyst obtained by isotherm analysis

1. Summary

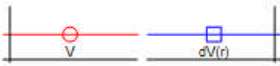
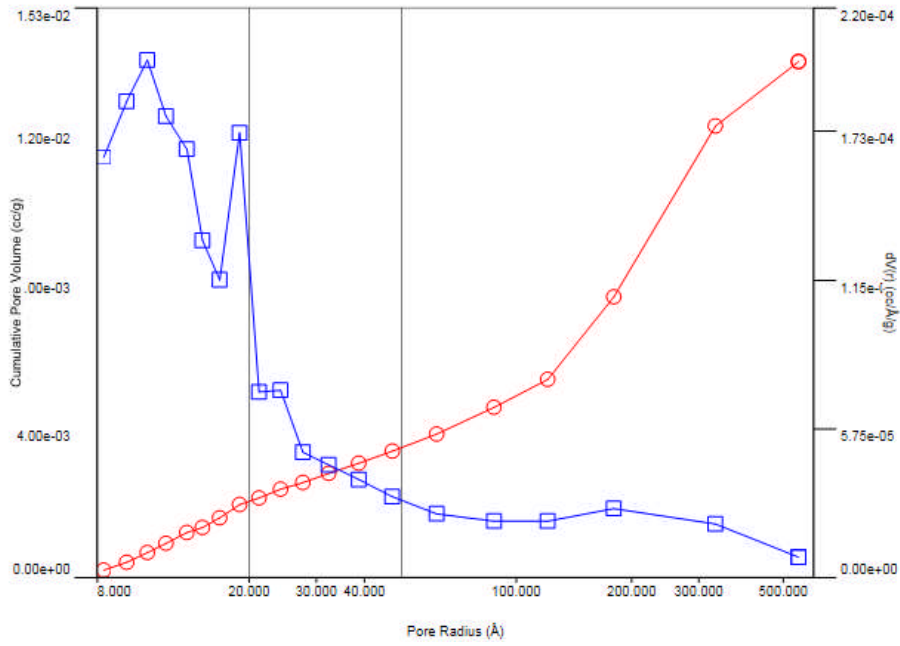
sample no.	pore radius (Å) by BJH		surface area by BET (m ² /g)
	adsorption	desorption	
A1	12.329	10.797	2.504
B2	12.312	10.771	2.533

2. BJH graphs

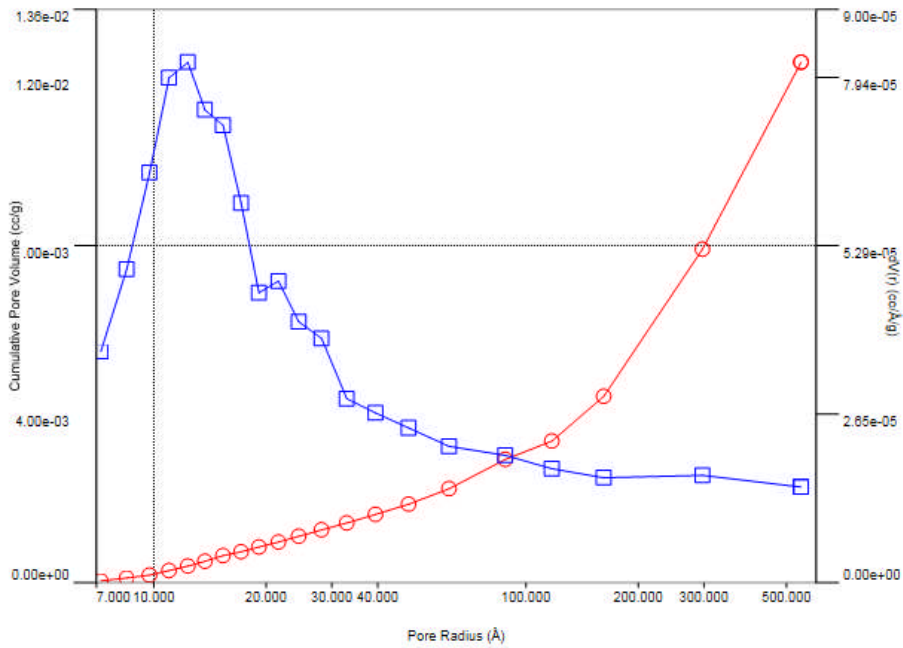




A1-desorption

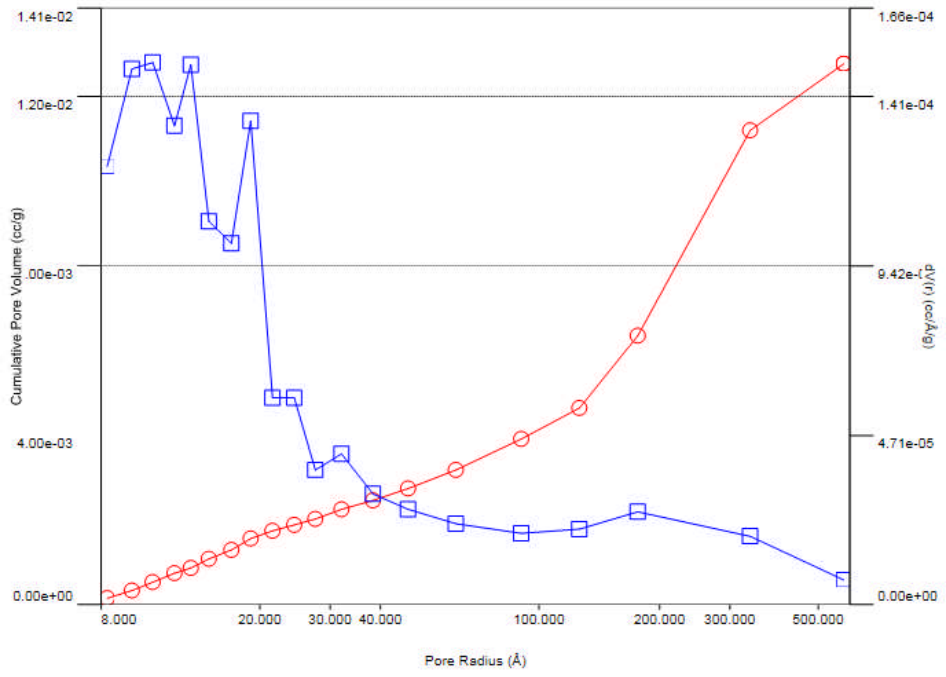


B2-adsorption





B2-desorption



Appendix B

1. Derivation of NASA polynomial coefficients for crystal NiO

(1) A set of C_p° in J/(mol K) in the temperature range of 298-2000 K was obtained from the literature (Bulletin United States Bureau of Mines 548 (1960): Contributions to the data on theoretical metallurgy). The reliability of these data was checked by comparing them with the other data source (J. E. Keem and J. M. Hoing. Selected electrical and thermal properties of undoped nickel oxide. CINDAS report 52, 1978: p41-45) as shown in Figure 1.

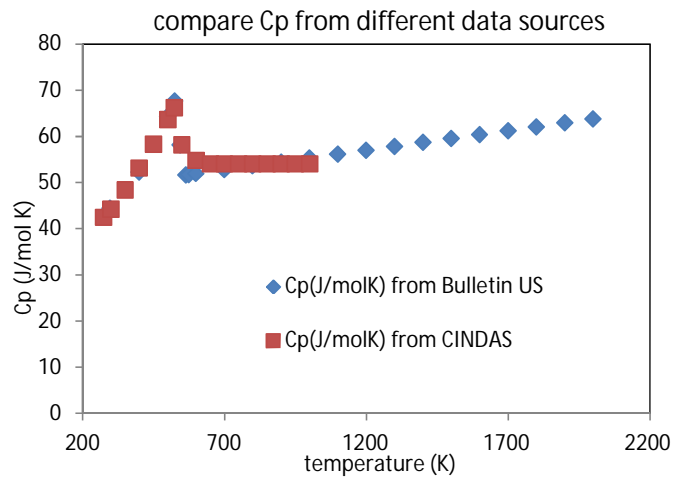


Figure 1

(2) It was found that the whole temperature range can be divided into three segments (298-525K, 525-565K, 565-2000K). For each segment, the plot of C_p° vs T was fitted into polynomials to obtain coefficients a_1 - a_7 according to Eq. 3.9 (see Chapter 3). Coefficients (e.g. a_1 and a_2) that were not shown in fitted polynomials were assumed to be zero. $H^\circ(298K)$, $H^\circ(525K)$, and $H^\circ(565K)$ were plugged into Eq. 3.10 to obtain coefficient b_1 for each segment. $S^\circ(298K)$, $S^\circ(525K)$, and $S^\circ(565K)$ were plugged into Eq. 3.11 to obtain coefficient b_2 for each segment.

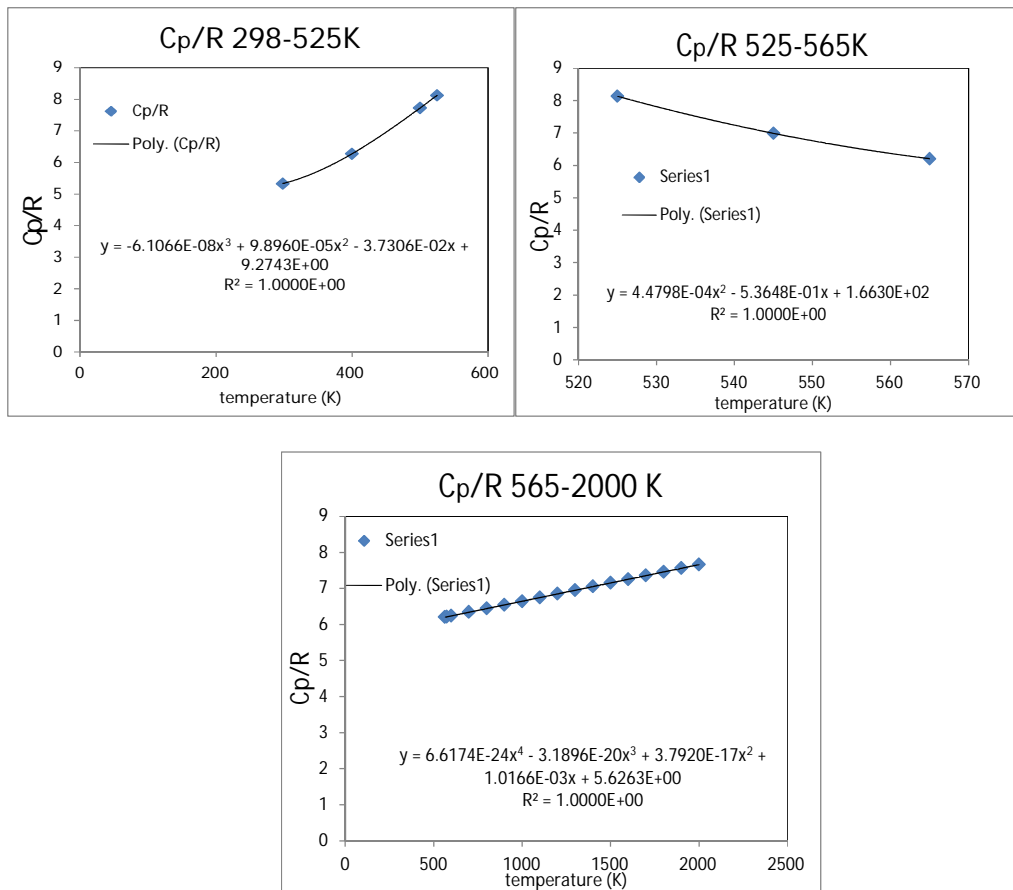


Figure 2

(3) To check the accuracy of these coefficients obtained, the H° and S° values obtained through the NASA polynomial equations (Eq. 3.10-3.11) were compared with the data provided by the literature (Bulletin United States Bureau of Mines 548 (1960): Contributions to the data on theoretical metallurgy). They were in good agreement with each other as shown in Figure 3.

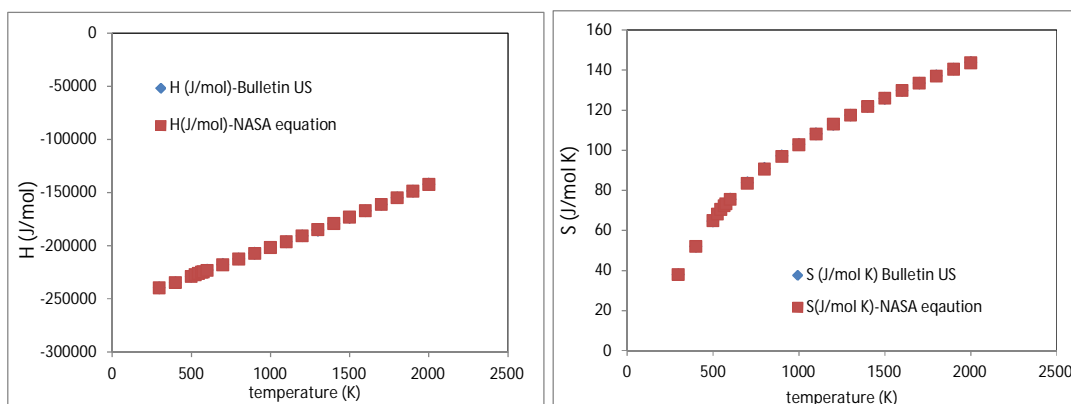


Figure 3

2. Derivation of NASA polynomial coefficients for glucose

The nine coefficients for glucose were obtained using the same procedure as NiO(cr). Thermodynamic data of glucose were retrieved from the ref. (Thermodynamic properties of starch and glucose. The Journal of Chemical Thermodynamics. 2013;59:87-93). This work was done by Dr. Valerie Dupont.

3. Formatted thermodynamic data of furfural, glucose, and NiO(cr) for the use in CEA program

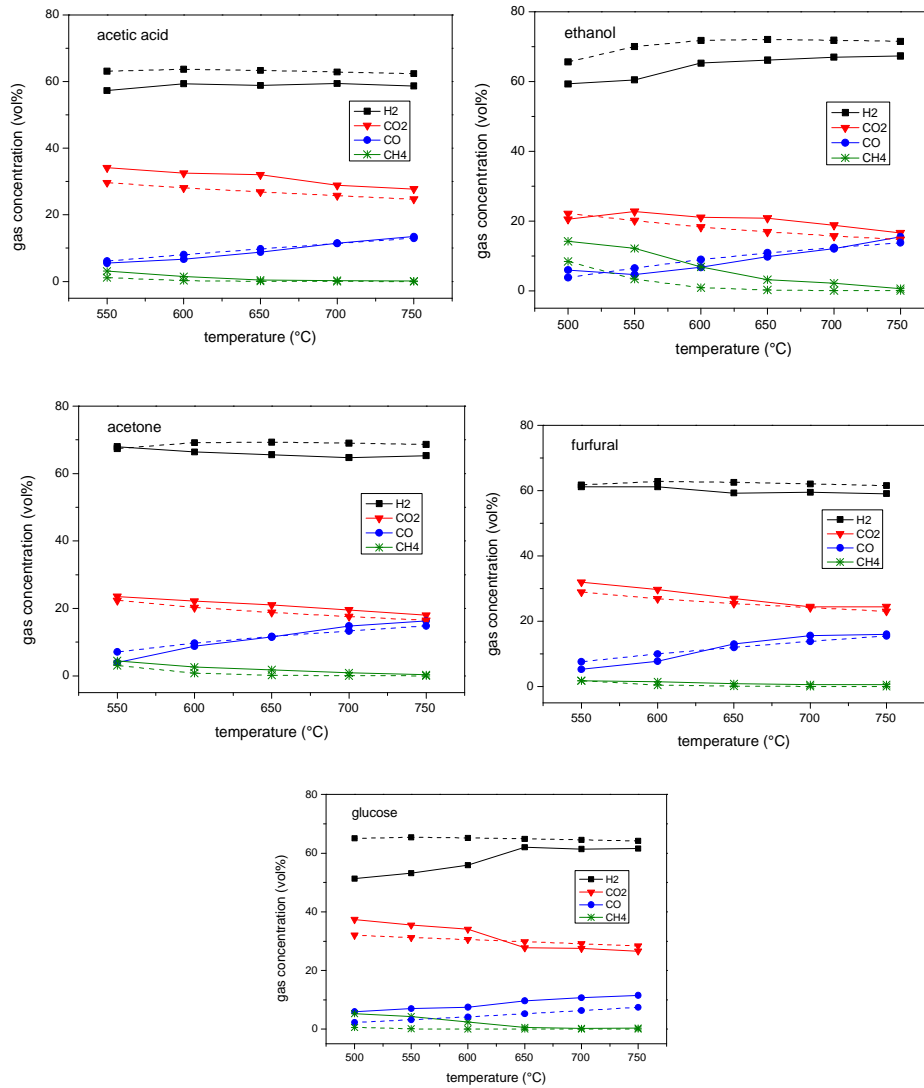
```
C5H4O2,furfura 2-furaldehyde aka furfural Catoire 2008 Guenadou 2011
2 C 5.00H 4.00O 2.00 0.00 0.00 0 96.0900000 -165686.400
300.000 1000.0007 -2.0 -1.0 0.0 1.0 2.0 3.0 4.0 0.0 14788.139
0.000000000D+00 0.000000000D+00 1.012017650D-01 4.124540440D-02-4.840793250D-06
-2.440848800D-08 1.231203620D-11 -2.170609920D+04 2.592313660D+01
1000.000 6000.0007 -2.0 -1.0 0.0 1.0 2.0 3.0 4.0 0.0 14788.139
0.000000000D+00 0.000000000D+00 1.142683940D+01 1.968709370D-02-8.119687040D-06
1.521681030D-09-1.065660120D-13 .. .. -2.515843870D+04-3.465257810D+01
```

```
C6H12O6,gluco glucose j chem thermo 2013(59)87-93.
1 jct/13 C 6.00H 12.00O 6.00 0.00 0.00 0 180.1600000 -1133962.000
200.000 1300.0007 -2.0 -1.0 0.0 1.0 2.0 3.0 4.0 0.0 36197.000
0.000000000D+00 0.000000000D+00 1.825877760D+00 9.211188420D-02-2.434948060D-05
-4.125823400D-08 2.530870150D-11 -1.407426170D+05 1.950523710D+01
```

```
NiO(cr) united states bureau of mines bulletin 548(1960).
3 g/60 NI 1.000 1.00 0.00 0.00 0.00 1 74.6928000 -239743.200
298.150 525.000 7 -2.0 -1.0 0.0 1.0 2.0 3.0 4.0 0.0 6757.000
0.000000000D+00 0.000000000D+00 9.274300000D+00-3.730600000D-02 9.896000000D-05
-6.106600000D-08 0.000000000D+00 -3.069700000D+04-4.100300000D+01
525.000 565.000 7 -2.0 -1.0 0.0 1.0 2.0 3.0 4.0 0.0 6757.000
0.000000000D+00 0.000000000D+00 1.663000000D+02-5.364800000D-01 4.479800000D-04
0.000000000D+00 0.000000000D+00 -6.233800000D+04-8.135000000D+02
565.000 2000.0007 -2.0 -1.0 0.0 1.0 2.0 3.0 4.0 0.0 6757.000
0.000000000D+00 0.000000000D+00 5.626300000D+00 1.016600000D-03 3.792000000D-17
-3.189600000D-20 6.617400000D-24 -3.041800000D+04-2.752700000D+01
```


Appendix C

Dry gas composition from steam reforming of bio-compounds



Dry gas composition (in vol%) from steam reforming of bio-compounds at 1 atm with S/C of 6 for glucose and S/C of 3 for the rest (solid line: experimental data, dashed line: equilibrium data).

Appendix D

Supplementary documents for Chapter 9

SD1:

(a) IR transmittance spectrum of volatile products during the TGA-FTIR experiment (a heat ramp of 5 °C/min under N₂ flow) of NiO-G at 31.79 min (corresponding to 183.6 °C). (b)-(d) The standard IR spectra of H₂O, formic acid and CO₂.

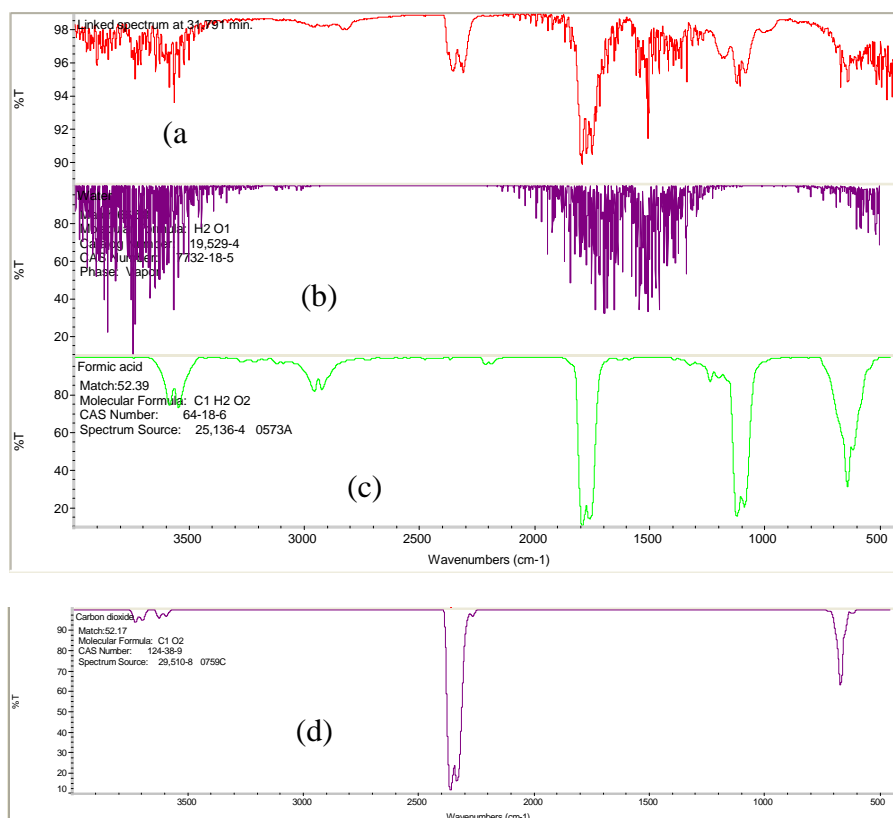


Table 1. Wavenumber ranges set for collecting chemigrams of volatile products from TPR of NiO-G under N₂

component	Region(cm ⁻¹)	Baseline(cm ⁻¹)
CO ₂	2250-2400	2250-2400
CO	2000-2200	2000-2200
H ₂ O	1300-1600	1300-1600
Formic acid	900-1250	900-1250

SD2:

IR transmittance spectra of volatile products during the TGA-FTIR experiment (a heat ramp of 5 °C/min under N₂ flow): (a) pure citric acid at 213°C, (b) Al₂O₃-CA at 188°C, and (c) NiO-CA at 208°C.

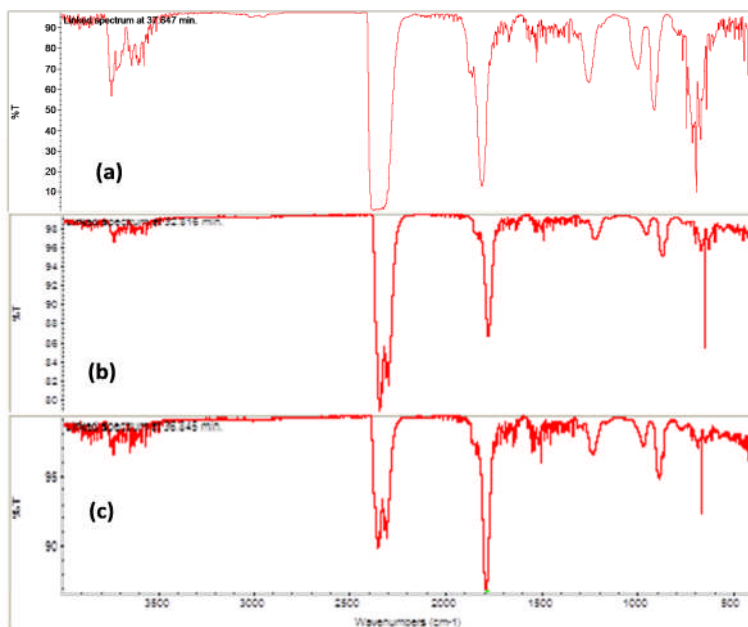


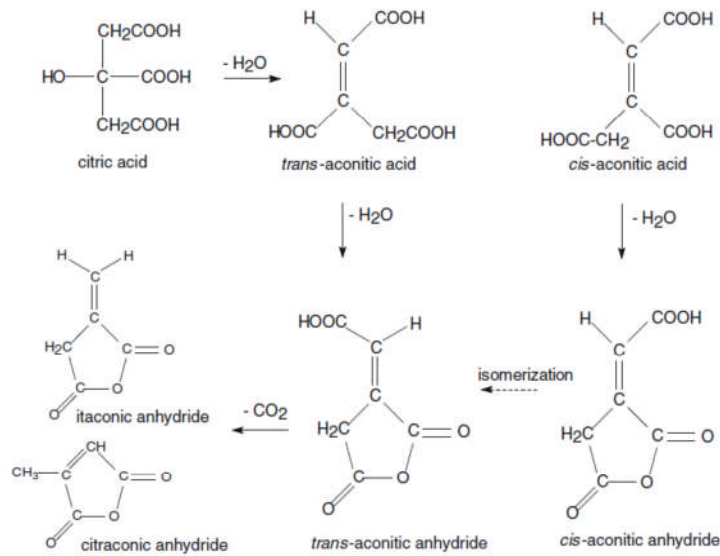
Table 2. IR bands in the above FTIR spectra and their assignment

IR band wavenumber (cm ⁻¹)	assignment
4000-3400	H ₂ O
2250-2400	CO ₂
1700-1900	C=O stretching vibration of anhydrides
1600-1300	H ₂ O
1250	C-O stretching vibration of anhydrides
900, 970	=CH & =CH ₂ bending vibration of anhydrides
600-750	CO ₂

Table 3. Wavenumber ranges set for collecting chemigrams of volatile products from TPR of NiO-CA under N₂

component	Region(cm ⁻¹)	Baseline(cm ⁻¹)
CO ₂	2250-2400	2250-2400
CO	2000-2200	2000-2200
H ₂ O	1300-1600	1300-1600
anhydride	800-1100	800-1100

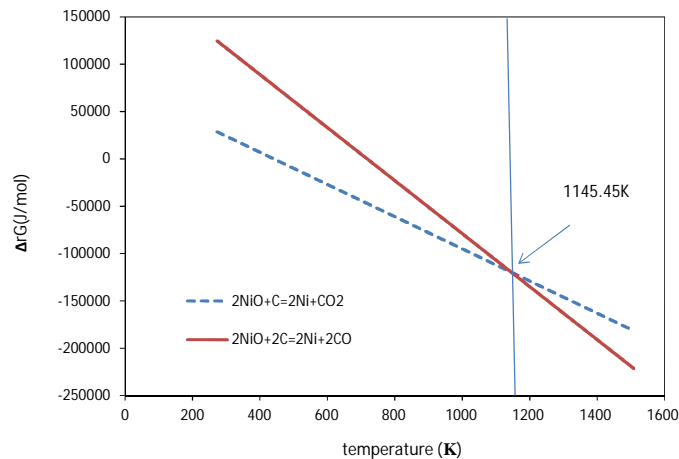
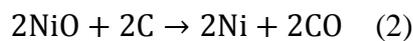
Thermal decomposition process of citric acid in N₂ or Ar atmosphere (adapted from ref. 1-2)



[1] Barbooti MM, Alsammerrai DA. Thermal-decomposition of citric-acid. *Thermochimica Acta*. 1986;98:119-26.

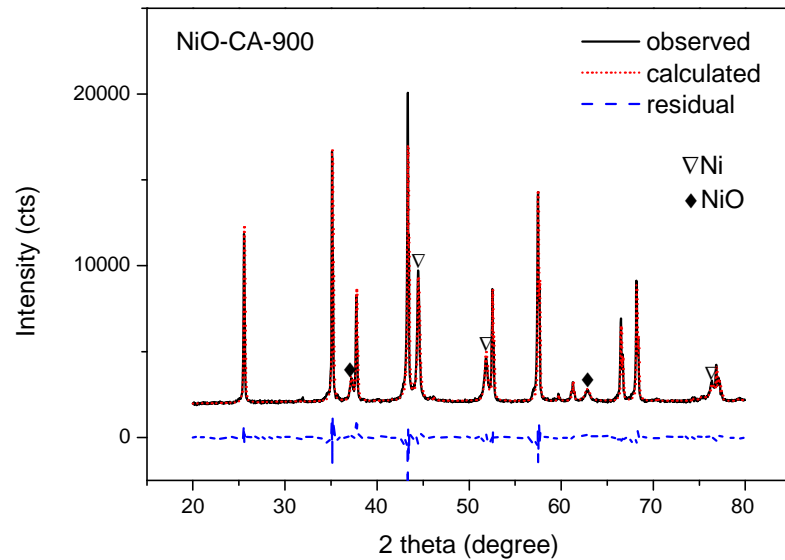
[2] Wyrzykowski D, Hebanowska E, Nowak-Wicz G, Makowski M, Chmurzynski L. Thermal behaviour of citric acid and isomeric aconitic acids. *Journal of Thermal Analysis and Calorimetry*. 2011;104:731-5.

SD3: Gibbs free energy change for the two reactions below. It was found that reaction (2) (CO production) became more thermodynamically favourable than reaction (1) (CO₂ production) when the temperature increased to above 1145.45K.



SD4:

XRD profile of the NiO-CA-900 sample and its Rietveld refinement result (around 84.4% α -Al₂O₃, 9.8% Ni and 5.8% NiO, weighted R profile (R_{wp}) is 4.10 and goodness of fitting is 4.34) (ICDD reference code for α -Al₂O₃: 04-005-4505, for NiO: 04-013-0890, for Ni: 04-010-6148).



SD 5: The equilibrium composition of reaction $C + CO_2 \rightleftharpoons 2CO$ at 1 atm with 0.5 mol of CO₂ and 0.5 mol of graphite as initial reactants was obtained using CEA program. As shown, this reaction did not occur until 500 °C.

